



THÈSE

En vue de l'obtention du
DOCTORAT DE L'UNIVERSITÉ DE TOULOUSE
Délivré par l'Université Toulouse 3 - Paul Sabatier

Présentée et soutenue par

Philippe COLLIN

Le 03 novembre 2020

**Design, taking into account the partial discharges
phenomena, of the Electrical Insulation System (EIS) of
high power electrical motors for hybrid electric propulsion
of future regional aircrafts**

Ecole doctorale : **GEET – Génie Electrique Electronique et Télécommunications :**
du système au nanosystème

Spécialité : **Génie Electrique**

Unité de recherche :
LAPLACE - Laboratoire PLAsma et Conversion d'Energie - CNRS-UPS-INPT

Thèse dirigée par
David MALEC et Yvan LEFEVRE

Jury

Stéphane DUCHESNE, *Professeur au LSEE– Université d'Artois*, Rapporteur
Olivier GALLOT-LAVALLEE, *Maître de conférence HDR au G2ELab – Université Grenoble-Alpes*, Rapporteur
Anca PETRE, *Maître de conférences au SIAME – Université de Pau et des Pays de l'Adour*, Examinatrice
Pierre BIDAN, *Professeur au LAPLACE – Université de Toulouse*, Examineur
David MALEC, *Professeur au LAPLACE – Université de Toulouse*, Directeur de thèse
Yvan LEFEVRE, *Chargé de recherche HDR au CNRS – LAPLACE*, Co-directeur de thèse
Thierry LEBEY, *Responsable des recherches sur la haute tension et les technologies associées – SAFRAN*, Invité
Laurent ALBERT, *Project Manager – IRT Saint-Exupéry*, Invité
Jean François ALLIAS, *R&T Program Engineer – AIRBUS*, Invité

Résumé

La réduction des émissions de CO₂ est un enjeu majeur pour l'Europe dans les années à venir. Les transports sont en effet aujourd'hui à l'origine de 24% des émissions mondiales de CO₂. L'aviation ne représente cependant que 2-3% des émissions globales de CO₂ mais le trafic aérien est en pleine expansion et, déjà, des inquiétudes apparaissent légitimement. A titre d'exemple, en Suède, depuis les années 1990, les émissions de CO₂ dues au trafic aérien ont augmenté de 61%. Ce constat explique l'apparition du mouvement « Flygskam » qui se reprend dans de plus en plus de pays Européens.

C'est dans ce contexte que l'Union Européenne a lancé en septembre 2016 le projet **Hybrid Aircraft academic reSearch on Thermal and Electrical Components and Systems (HASTECS)**. Le consortium regroupe différents laboratoires ainsi que l'avionneur Airbus. Ce projet s'inscrit dans le programme « H2020 Clean Sky 2 » qui vise à développer une *aviation plus verte*. L'objectif ambitieux est de réduire de 20% les émissions de CO₂ ainsi que le bruit produit par les avions, d'ici 2025. Pour cela, le consortium a décidé d'étudier une architecture hybride de type série. La propulsion est assurée par une motorisation électrique pour laquelle deux cibles ont été définies. En 2025, les moteurs devront en effet atteindre une densité de puissance de 5kW/kg, système de refroidissement inclus. En 2035, cette densité de puissance devra être doublée (10kW/kg). Pour atteindre ces cibles, le niveau de tension sera considérablement augmenté, probablement au-delà du kilovolt. Le risque d'apparition de décharges électriques dans les stators des moteurs électriques sera considérablement accru et doit être pris en compte dès la phase de conception du moteur.

L'objectif de cette thèse est de mettre au point un outil d'aide au design du Système d'Isolation Electrique (SIE) primaire du stator des moteurs électriques qui seront pilotés par convertisseurs. Le manuscrit qui synthétise les travaux effectués est découpé en cinq parties.

La première partie commencera par préciser les enjeux et défis d'une aviation plus verte. La constitution du SIE d'un stator de moteur électrique sera ensuite développée. Enfin, les contraintes qui s'appliquent sur le SIE dans l'environnement aéronautique seront identifiées.

La deuxième partie présentera les différents types de décharges électriques que l'on peut retrouver dans les dispositifs électriques. Le principal risque vient des Décharges Partielles (DP) qui détériorent peu à peu le SIE. Le principal mécanisme permettant d'expliquer l'apparition des DP est l'avalanche électronique. Le critère de Paschen permet d'évaluer le Seuil d'Apparition des Décharges Partielles (SADP). Différentes techniques permettent de détecter et mesurer l'activité des DP. Des modèles numériques permettent d'évaluer le SADP.

La troisième partie présentera une méthode originale pour déterminer les lignes de champ électrique dans un problème électrostatique. Elle n'utilisera qu'une formulation en potentiel scalaire.

La quatrième partie présentera une étude expérimentale pour établir une correction du critère de Paschen. En effet, un bobinage de moteur électrique est très loin des hypothèses dans lesquelles ce critère a été originellement défini.

Enfin, la cinquième partie sera consacrée à l'élaboration de l'outil d'aide au design du SIE. Des abaques seront construits afin de fournir des recommandations sur le dimensionnement des différents isolants dans une encoche de stator. Une réduction du SADP due à une variation combinée de la température et de la pression sera également prise en compte.

Mots clefs : Décharges partielles, théorie de Paschen, Modélisation, Eléments finis, Champ électrique, Dimensionnement, Diélectriques, Isolation électrique, SADP.

Abstract

Reducing CO₂ emissions is a major challenge for Europe in the forthcoming years. Nowadays, transport represents 24% of the world CO₂ emissions. Aviation accounts for only 2-3% of these world CO₂ emissions. However, air traffic is booming and concerns are legitimately emerging. As an example, CO₂ emissions from air traffic have increased by 61% in Sweden since the 90s. This explains the emergence of the "Flygskam" movement which is spreading in more and more European countries.

It is in this context that the European Union launched in September 2016 the project **Hybrid Aircraft academic reSearch on Thermal and Electrical Components and Systems (HASTECS)**. The consortium brings together different research laboratories and Airbus. This project is part of the program "H2020 - Clean Sky 2" which aims to develop a *greener aviation*. Its ambitious goal consists in reducing CO₂ emissions and noise produced by aircraft by 20%, by 2025. To do that, the consortium has decided to study a serial hybrid architecture. Propulsion is provided by electric motors. Two targets have been defined. In 2025, the engines must reach a power density of 5kW/kg, including the cooling system. In 2035, this power density of the engines will have to be doubled (10kW/kg). To reach these targets, the voltage level will be considerably increased, probably beyond one kilovolt. The electric discharges appearance risk will be considerably increased and need to be considered right from the motor design stage. The objective of this thesis is then to develop a tool in order to help the designer of electric motors fed by a converter when he will deal with its primary Electrical Insulation System (EIS). This manuscript is organized into five parts.

The first part will begin by clarifying both issues and challenges of a greener aviation. The EIS composition in electric motors will then be developed. Finally, the constraints withstood by the EIS in an aeronautical environment will be identified.

The second part will present the different types of electric discharges that can be found in electric devices. The main risk comes from Partial Discharges (PD) which gradually deteriorate the EIS. The main mechanism for explaining the appearance of PD is the electronic avalanche. The Paschen criterion makes it possible to evaluate the Partial Discharge Inception Voltage (PDIV). Different techniques may be used to detect and measure the activity of these PD. Numerical models may also be used to evaluate the PDIV.

The third part will present an original method for determining the electric field lines in an electrostatic problem. It only uses a scalar potential formulation.

The fourth part will present an experimental study to establish a correction of the Paschen criterion. Indeed, an electric motor winding is very far from the assumptions in which this criterion was originally defined.

Finally, the fifth part will be devoted to the development of the SIE design aid tool. Graphs will be generated to provide recommendations on the sizing of the various insulators in a stator slot. A reduction in the PDIV due to a combined variation in temperature and pressure will also be taken into account.

Keywords: Partial discharges, Paschen, Modelling, Finite elements, Electric field, Sizing, Dielectrics, Electrical insulation, PDIV.

Remerciements

Ces travaux de thèse ont été réalisés au laboratoire LAPLACE (Laboratoire PLASMA et Conversion d'Énergie). Ils ont été financés par l'Union Européenne dans le cadre du programme H2020.

Je tiens tout d'abord à grandement remercier mes deux directeurs de thèse David Malec et Yvan Lefevre. Ils m'ont accompagné tout au long de cette aventure tant humaine que scientifique. Je garde de très bons souvenirs de nos escapades aux cours des différentes conférences auxquelles j'ai eu la chance de participer. Je suis très heureux de l'amitié qui nous lie désormais. Également merci aux membres des deux équipes du laboratoire qui m'ont accueilli chaleureusement : le MDCE sur le site université Paul Sabatier et le GREM 3 sur le site INPT-ENSEEIH.

Je tiens à remercier Stéphane Duchesne (LSEE, Université d'Artois) et Olivier Gallot-Lavallee (G2ELab, Université Grenoble-Alpes) d'avoir accepté d'être rapporteurs de ma thèse. Merci également aux autres membres du jury, Anca Petre (SIAME, Université de Pau et des Pays de l'Adour), Pierre Bidan (LAPLACE, Université de Toulouse) pour l'évaluation de ce travail en tant qu'examinateurs. Merci à Thierry Lebey (SAFRAN), Laurent Albert (IRT Saint-Exupéry) et Jean François Allias (AIRBUS) d'avoir pris part au jury en tant que membres invités. Je vous suis très reconnaissant d'avoir pris le temps pour évaluer mon travail et pour la richesse des échanges que nous avons eu lors de la soutenance de cette thèse.

Je voudrais remercier Sorin Dinculescu, Zarel Valdez-Nava, Vincent Bley, Céline Combettes, Benoit Lantin, Benoit Schlegel, Pierre Hernandez et Nofel Merbahi pour leur aide à la réalisation de mes travaux expérimentaux.

Merci également à tous les doctorants, post-doctorants et stagiaires qui ont fait un passage dans le bureau porte 102 du bâtiment 3R3 : Mallys Banda, Fernando Pedro, Riccardo Albani, Kemas M Tofani, Imadeddine Benfridja, Youcef Kemari, Pawel Piotr Pietrzak, Trong Trung Le et bien d'autres ! Il y a toujours eu une bonne ambiance dans ce bureau !

Un grand merci aussi aux doctorants et docteurs du troisième étage sur le site ENSEEIH : Maxime Bonnet, Théo Carpi, Mateus Carvalho Costa, Jessica Neumann, Jordan Stekke, Youness Rtimi. C'était toujours un plaisir de passer vous dire bonjour et de squatter un siège et votre café !

Merci à tous mes collègues du projet HASTECS. Aux doctorants : Sarah Touhami, Najoua Erroui, Amal Zeaïter, Flavio Accorinti, Malik Tognan et Matthieu Pettes-Duler. J'ai passé d'excellents moments en votre compagnie ce qui a rendu mon travail encore plus agréable. Bon courage à toi Matthieu qui est le dernier à soutenir !

Je tiens à remercier tous mes compères de l'Association des Laplaciens (ADeL) que j'ai eu le plaisir de présider : Marjorie Morvan, Aurélien Pujol, Plinio Bau, Bojan Djuric et Matthieu Pettes-Duler (encore toi !). On a vraiment fait du bon boulot et on s'est bien éclaté !

Merci aussi aux nombreux doctorants et docteurs du PRHE avec lesquels j'ai passé beaucoup de bon temps : Cyril Van de Steen, Julien Cosimi, Maxime Bafail, Tristan Gouriou, Aurélie Marches, Eléna Griseti, Valentin Ferrer. Je pense aussi à d'autres gens bien sympas : Maxime Castelain, Aurélie Tokarski, Benoit Prochet, Nicolas Millet, Davin Guedon, Andréa Al Haddad.

Remerciements

Merci à mes anciens camarades de l'ENSEEIH : Thomas Longchamps, Etienne Farman, Yoann Scotto, Baptiste Genet et tous les autres pour les très bons moments passés même après l'obtention de notre diplôme d'ingénieur.

Je remercie ma famille étendue (les Collin et les Chauvin) pour leur soutien pendant ces années de thèse.

Enfin je dédie mes derniers remerciements à ma compagne Julie Chauvin. Tu es toujours à mes côtés pour me supporter et pour me donner la force d'aller de l'avant. Je t'aime!

Table of contents

Résumé.....	3
Abstract	4
Remerciements	5
General Introduction.....	13
Chapter 1: Toward full-electric transportation	17
1 Implications and challenges	19
1.1 Sustainable transportation.....	19
1.1.1 International context.....	19
1.1.2 European and France contexts.....	21
1.2 The “Flygskam” movement	21
2 Toward more electric aircrafts	22
2.1 Classic aircraft architecture	22
2.1.1 Pneumatic network	22
2.1.2 Hydraulic network	22
2.1.3 Mechanical power	23
2.1.4 Electrical network.....	23
2.2 Projects of more electric aircrafts	24
2.2.1 E-FanX.....	25
2.2.2 CityAirbus	26
3 HASTECS project.....	26
3.1 Targets.....	26
3.2 Serial hybrid configuration	27
3.3 Work packages	27
3.3.1 Work Package 1 (WP1)	28
3.3.2 Work Package 2 (WP2)	29
3.3.3 Work Package 3 (WP3)	30
3.3.4 Work Package 4 (WP4).....	32
3.3.5 Work Package 5	33
3.3.5.1 DC busbar	33
3.3.5.2 Motor Electrical Insulation System (EIS)	35
3.3.6 Work Package 6	35
4 Electric motors electrical insulation	36
4.1 Low voltage machine.....	36
4.1.1 Turn-to-turn insulation.....	38

4.1.2	Phase-to-phase insulation	41
4.1.3	Turn-to-slot insulation	41
4.1.4	Slot impregnation	42
4.2	High voltage machine	44
5	Thermal aspect	46
5.1	Cooling strategies	46
5.2	Thermally enhanced polymers	47
6	Impact of power electronics.....	49
6.1	Pulse Width Modulation (PWM) basis	49
6.2	Power feeding cable	51
6.3	Frequency increase.....	55
6.4	Voltage distribution.....	57
Chapter 2: Physics of Partial Discharges (PD).....		61
1	Different kinds of discharges.....	63
1.1	Discharges in non-vented cavities.....	64
1.2	Discharges in vented cavities	65
1.3	Discharges on the surface	66
1.4	Corona discharge.....	67
1.5	PD consequences on stator insulation	68
2	Physics of plasma.....	69
2.1	Townsend mechanism.....	69
2.1.1	First Townsend's coefficient.....	70
2.1.2	Second coefficient	73
2.2	Paschen's law	74
2.3	Impact of aeronautics conditions.....	75
2.3.1	Environmental variations	75
2.3.2	Impact of temperature	77
2.3.3	Impact of humidity	80
3	PD analysis.....	82
3.1	Experimental detection of PD activity.....	82
3.1.1	Radio-frequency detection.....	83
3.1.2	Optical detection	83
3.1.3	Power factor/capacitance tip-up test.....	84
3.1.4	Used electric detection.....	84
3.2	Parameters linked to PD.....	85
3.2.1	Partial Discharge Inception Voltage (PDIV)	85

3.2.2	Partial Discharge Extinction Voltage (PDEV)	86
3.2.3	Apparent charge	86
3.3	Statistical processing of the results	87
4	Degradation of the polymer insulation in aeronautic environment	90
4.1	Pressure	91
4.2	Humidity	92
4.3	Temperature	93
4.4	Frequency and voltage	94
4.5	Lifetime evaluation	96
5	Modelling partial discharges activity	98
5.1	Streamer criterion	98
5.2	Paschen's criterion	100
Chapter 3: Electric field lines computation		103
1	Introduction	105
2	The electrostatic problem	105
2.1	Presentation of the field of study	105
2.2	Electrostatic equations and formulations	106
2.3	Advantages and disadvantages of each formulation	108
2.3.1	Vector potential	108
2.3.2	Scalar potential	109
3	Electric field lines computation derived from a scalar potential formulation	109
3.1	Ballistic method	109
3.2	Flux tubes based method	113
4	Proposed method	116
4.1	Electric field and electric flux	116
4.2	Equipotential lines	118
4.3	Flux function	120
4.4	Illustrative examples	122
5	Another method using <i>Matlab</i> functions	124
5.1	Building the additional mesh	124
5.2	Electric field	125
5.3	Comparison with the proposed method	126
6	Conclusion	128
Chapter 4: Correction of the Paschen's criterion		129
1	Motivations	131
1.1	Configuration different from the initial one	131

1.2	Experimental observation	131
2	Experimental approach	133
2.1	Samples	133
2.2	Experimental protocol.....	135
3	Results	136
3.1	PDIV results	136
3.2	Dielectric constant measurements	139
4	Mixed experimental and numerical approaches.....	141
5	Single layer insulation.....	144
6	Secondary electron emission coefficients.....	146
6.1	Impact of the incoming angle of bombarding ions	147
6.2	Influence of the enamel chemistry	149
7	Additional experimentation	150
7.1	Set up.....	150
7.2	Results	152
8	Conclusions and perspectives	154
Chapter 5: Tool to predict PD activity in machine slot.....		157
1	Dielectric constant evolution with temperature and frequency	159
2	Partial Discharge Evaluation Criterion.....	160
3	Partial Discharge Inception Voltage (PDIV) decrease for a combined variation of temperature and pressure.....	161
4	Wire design graphs.....	162
4.1	Simple analytical model for electric field in air gap computation.....	162
4.2	Validation of Simple Analytical Model with finite elements.....	164
4.3	Enamel thickness as a function of applied voltage	165
4.4	Copper diameter as function of computed enamel thickness	167
4.5	Validation	168
5	Slot insulation design graphs.....	170
5.1	Simple analytical model for electric field in air gap computation.....	170
5.2	Validation of Simple Analytical Model with finite elements.....	171
5.3	Slot liner thickness as a function of applied voltage and insulation materials	172
5.3.1	First imbrication	173
5.3.2	Second imbrication.....	174
5.3.3	Third imbrication	175
5.4	Validation	175
6	Evaluation of the electric stresses under normal temperature and pressure conditions	176

6.1	Turn/turn electric stress.....	176
6.2	Turn/slot electric stress.....	178
7	Partial Discharge Evaluation Tool (PDET).....	178
7.1	PDET algorithm.....	179
7.2	Inputs.....	180
8	Illustrative example.....	181
9	Conclusion.....	186
	General conclusion and perspectives.....	189
	Publications.....	193
	Annex.....	195
	References:.....	197

General Introduction

Aircrafts manufacturers such as Airbus, Boeing and Bombardier are engaged in the competition to develop more- and full- electric aircrafts. That incoming revolution takes place in a context where more and more people and countries are expecting a much greener air transportation. The first step of this change is to progressively replace turboshafts by electric motors to ensure the propulsion of the aircraft. More and more on-board electric power is consequently required.

The risk of electric discharges in propelling electric motors will then increased, as the feeding voltage will probably be higher than one kilovolt. The Electric Insulation System (EIS) ensures the protection of a machine against electric hazards. It can be divided into two categories. Type I is used in low-voltage rotating machine. The International Electric Commission (IEC) considers a machine with a phase-to-phase voltage lower than $700 V_{rms}$ as a low-voltage machine. Type I insulation is almost exclusively made of polymer materials. These are also called organic materials. On the other hand, Type II insulation is used in machine with phase-to-phase voltage upper than $700 V_{rms}$. It uses inorganic materials such as fibber glass, mica, ceramics, composite materials,... These are more expensive materials which lifespan is increased in presence of electric discharges. Type I insulation is also used in machines fed by voltages higher than $700 V_{rms}$, as the EIS has been designed to be free from electric discharges.

Since the introduction of power electronic power supplies, that provides easy control of the machine rotational speed, the electrical insulation of such motors faces new hazards. Fast changing supply voltage, with high dV/dt , may cause the apparition of partial discharges (PD), that results in accelerated insulation aging and often leads to premature failure of the motors. In low voltage rotating machines, the stator insulation system is multi-level. Its first component (primary insulation) is the polymer enamel on the magnet wire, among the others: inter-phase insulation, slot insulation and impregnation varnish. Depending on the desired thermal properties, there are several types of polymers being used nowadays in enameled wires: polyamide (PA), polyamide-imide (PAI), polyester-imide (PEI) and polyimide (PI). Inorganic nano-particles (SiO_2 , Al_2O_3 , ZnO ,...) may also be used as fillers to obtained *corona-resistant* enamels. In random-wound stators powered by power inverters, in comparison with sinusoidal power supply, the magnet wire insulation is far more endangered. Hence, the objective is to concentrate on this primary insulation. Once the voltage exceeds the Partial Discharge Inception Voltage (PDIV), electronic avalanches will take place in the EIS, leading to:

- an ions bombardment of the insulator surfaces;
- an increase in temperature the the area submitted to PD;

- a chemical degradation of the insulators.

All these actions will strongly increase the insulator degradation rate. Usually, there are three ways used to avoid and/or to resist to such damage. Firstly, the use of corona-resistant enameled wires, especially formulated to increase the lifetime under PD attacks. Secondly, a suitable design of the primary electrical insulation: choice of right enamel wires (size and shape), insulation thickness (grade), choice of wires arrangement in the slots... Third, the use of both of these two solutions.

A non-closed motor embedded in an aircraft is submitted to severe environmental variations. These are mainly the temperature, the pressure, the humidity and vibration. These environmental parameters have a significant impact on the physics describing PD. It is for example known that a combined temperature increase and pressure decrease in dry air reduces the PDIV.

The objective of this thesis is to develop an automatic tool, based on PD physics, in order to help the machine designer to better design and size the EIS of rotating machines fed by inverters. The scope of investigation of the tool is limited to the stator slot. It considers only one phase per slot (an upgrade could be considered thereafter to treat more than one phase per slot). Therefore, the turn/turn and turn/slot electric stresses are studied. First, a criterion to evaluate PDIV in both configuration is established. It is a correction of the Paschen's criterion, taking into account the dielectric over-coating and a combined variation of temperature and pressure in micro gaps. Simple Analytical Models (SAM) are developed and validated with 2D-Finite Elements Models (2D-FEM). Graphs are derived from parametric studies to size the EIS in order to withstand electric stress without PD in turn/turn and turn/slot configurations.

This thesis is founded by the **Hybrid Aircraft reSearch on Thermal and Electrical Components and Systems (HASTECS)** project. It is part of the "H2020 - Clean Sky 2" European program. It is a consortium composed of public laboratories and Airbus. The PhD research work takes place in the Laboratory on PLAsma and Conversion of Energy (LAPLACE) in Toulouse. The works in LAPLACE were conducted in collaboration between 2 research teams: the *Dielectrics Materials in the Energy Conversion* (MDCE) group and the *Research Group in Electrodynamics* (GREM3). MDCE has provided the facilities for the experimental studies, whereas GREM3 has provided the license and expertise on Ansys finite elements software.

This PhD dissertation is divided into five chapters. A short description of each chapter is given in the following.

Chapter I: Toward full electric transportations

Chapter I will start by presenting the challenges on the road toward a green aviation, based on Worldwide and European scales. Then, a classic aircraft architecture will be detailed. Projects of more electric aircrafts will be introduced alongside the HASTECS project with its serial-hybrid electric architecture. Chapter I will continue with the explanation of a motor EIS composition for Type I and Type II machines. It will finish by identifying power electronics impacts on electric stresses occurring at the motor terminals.

Chapter II: Physics of Partial Discharges

Chapter II will begin with a presentation of the different kinds of electric discharges. The electronic avalanche will be identified as the main mechanism involved in PD. It will be described by the Paschen's law. The impact of aeronautical conditions on Paschen's law will be detailed. Chapter II will then describe the experimental methods to detect and measure a PD activity in an electric device. The parameters impacting the insulation lifespan will be identified. Finally, two main numerical models to evaluate PD activity will be introduced; each of them uses a different criterion.

Chapter III: Electric field lines computation

This chapter will be dedicated to the electrostatic problem composed by two enamelled round wires in close contact. The formulations in both vector and scalar potential will be presented. It will come that the scalar formulation is the easiest to handle. It will be consequently used to propose an original method to compute field lines. The proposed method will be compared to a ballistic method implanted in Matlab software. The field lines geometry and the scalar potential distribution are required for the application of the PDIV evaluation criterion based on Paschen's law.

Chapter IV: Correction of Paschen's criterion

Paschen's criterion has been experimentally established for a configuration which is completely different from the ones found in a machine stator slot. Therefore, the validity of this criterion will be investigated. Experimental observations of PD degradation between enamelled round wires in close contact has revealed that the Paschen's law shape is conserved. The dielectric over-coating has been found to simply increase the PDIV level. An experimental study coupled with a 2D-FEM will be performed to evaluate the secondary electron coefficient value in the presence of a dielectric over-coating.

Chapter V

This chapter will present in detail the tool to implement the EIS design in order to avoid any PD in stator slots. It will start by giving the assumptions used in the different models. A focus will be on turn/turn and turn/slot configurations. Parametric studies on the impacting parameters will be realized using SAM. Sizing graphs will be derived from these studies. These graphs will then be implanted in a Partial Discharge Evaluation Tool (PDET). The interest and efficiency of the developed PDET will finally be proved with an illustrative example.

Finally, conclusions as well as perspectives for future works will be proposed.

Chapter 1: Toward full-electric transportation

1 IMPLICATIONS AND CHALLENGES

1.1 SUSTAINABLE TRANSPORTATION

1.1.1 International context

The role of transportation in the world sustainable development was firstly pointed out during the 1992 United Nation's Earth Summit at Rio de Janeiro [1]. Since then, the strong role of transportation in climate change, raw material depletion, human health and ecosystems equilibrium is as important as ever. Indeed, the transportation sector:

- is responsible of 24% of world CO₂ emissions [2]. Every person on our planet produces, on average, 1.5t of CO₂ emissions per year, just for being on the move [3]. Both passengers and freight road vehicles are responsible of 74% of the total transportation CO₂ emissions, while both aviation and shipping reach 22% and rail 1.3%;
- remains the largest consumer of oil : 57% of the global demand [4], i.e. : 55.8 Mb/day where road represents 78.1%, air 11.4%, sea 7.3% and rail 3.2% ;
- is responsible of 12-70% of the total tropospheric air pollution mix [5]; Asia, Africa and the Middle East suffer more due to the use of old and inefficient vehicles. Outdoor air pollution (O₃, NO_x, SO₂, CO, PM₁₀, PM_{2.5},...) kills more than 8 million people across the world every year. Transportations, mainly road ones, *would be* responsible of almost 50% of these premature deaths [6] ;
- is responsible of direct and indirect damages, or major changes, on ecosystems (air, marine and earth), which are often unpredictable [7].

In order to identify guidelines, different scenarii such as the *Sustainable Development Scenario* (SDS), the *Clean Air Scenario* and the *Future is Electric Scenario* have been established by using the World Energy Model developed by the International Energy Agency [8]. As an example, Figure 1 shows the CO₂ emissions SDS targets versus transportation sectors ; direct transport emissions must peak around 2020 and then fall by more than 9% by 2030.

Chapter 1: Toward full-electric transportation

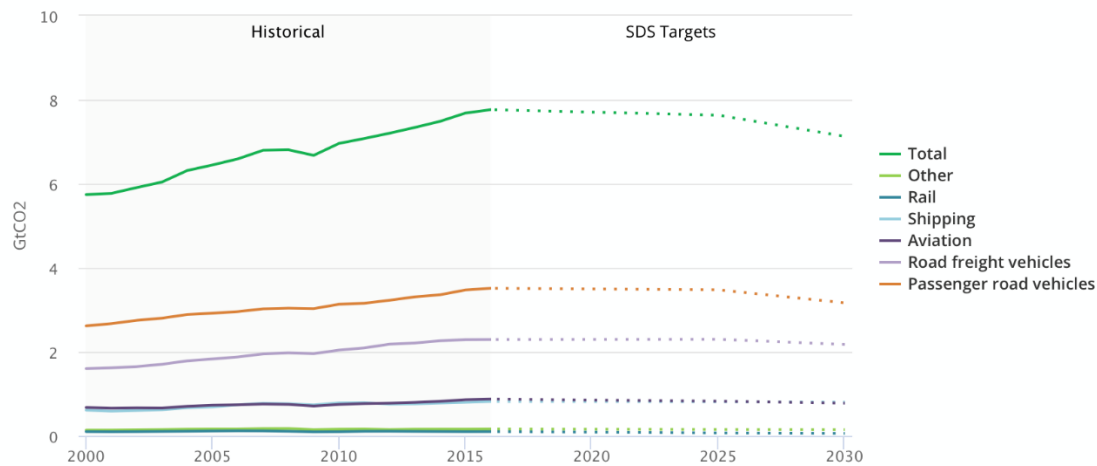


Figure 1: CO₂ emissions versus transportation sectors (past evolution and SDS targets) [2]

In order to put global warming, human health and environmental impacts of transportation on track to meet all 2030 goals, different efforts must be undertaken or pursued in all kind of transport by increasing even more:

- 1) the efficiency of existing ICE (Internal Combustion Engine) powertrains: lower fuel consumption, use of bio- or low carbon- fuels, better decontamination of exhaust gas,... ;
- 2) the electrification of ICE powertrains: hybridization or full electrification;
- 3) the capacity, the efficiency, the lifetime and the hybridization of embedded power sources;
- 4) the efficiency of existing powertrains, traditionally electric ;
- 5) the good consumer's behaviours (better transportation planning, carpooling,...) and the voluntary city transport policies.

The transportation sector has now entered a critical transition period where existing measures listed below must be deepened and extended in order to reach the environmental goals, whereas in the meantime the need in this sector is continuously growing. This process will need to be set in motion over the next decade. Any delay would require stricter measures beyond 2030, which could noticeably increase the cost of reaching environmental and health targets. This must be accompanied, of course, by the power sector decarbonisation since 41% of world CO₂ emissions is due to electricity generation [2]. Among all the measures listed below, items 2), 3), 4) and 1) for electric-assisted solutions, are essentially dependent on R&D efforts in the field of both Electrical and Electrochemical (-applied to energy) Engineering.

1.1.2 European and France contexts

In the European Union (EU), more and more societies aim to be greener; fossils energies are more and more substituted by sustainable ones. As an example, in France, the proportion of sustainable energy into the total energy consumption has increased by about 69% from 1990 to 2016 [9]. It represents 16% of the total consumption of energy in France in 2018. With the *Accord de Paris* and the *Climate Plan*, EU aims to increase this proportion up to 27% in 2030 [9].

There are several motivations for the energy transition. It is first economic. Nowadays, fossil energies still represent 81.7% of total energy consumption in the World. Oil remains the most used [10]. It mainly comes from the Middle East. Due to both repeated politic tensions and commercial monopoly, the oil barrel price is unstable. Figure 2 presents the evolution of the oil barrel cost (in US \$) from 1970 to 2015 [11].

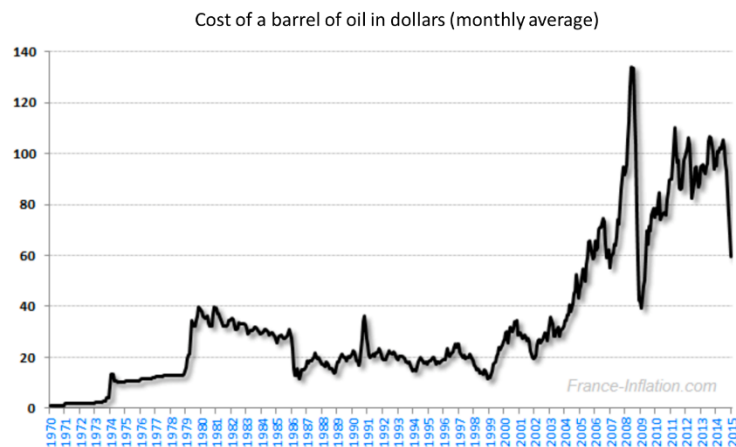


Figure 2: Evolution of the oil barrel cost (in US dollars) [11]

The second motivation is the society awareness on both contamination and climate change. Political actions are undertaken to reduce carbon emissions, especially in the transportation field. As an example, the EU Horizon 2020 project aims to a 23% reduction of greenhouse gas emissions from road transport in 2030 compared to 2005 [12]. In 2016, road transport represented nearly 21% of EU's total emissions of carbon dioxide [12].

1.2 THE "FLYGSKAM" MOVEMENT

Aviation is only responsible of 2-3% of global CO₂ emissions according to the International Air Transport Association (IATA) [13]. It represents 11-12% of the total emission due to transportation [14]. There, the total CO₂ emissions have decreased by 24% from 1990 while the emissions due to aviation have increased by 61% [14]. These data have particularly rang a bell in Sweden where people are

increasingly abandoning air planes for internal trips; internal flights have decreased by 3% from January to September 2018 [14]. This movement that has received the name “Flygskam”, literally *the shame to take the plane*, is growing in other countries.

2 TOWARD MORE ELECTRIC AIRCRAFTS

2.1 CLASSIC AIRCRAFT ARCHITECTURE

Multiple sources of energy are present in an aircraft. It includes mechanical, electrical, hydraulic and pneumatic energies. Figure 3 illustrates the implantation of a conventional power distribution [15].

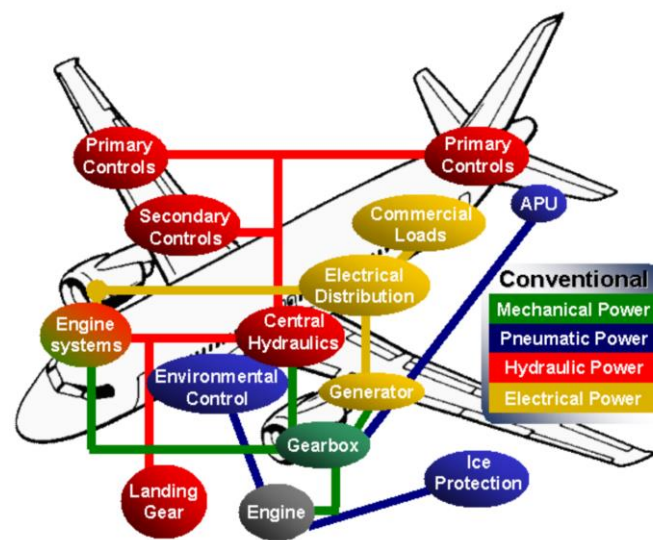


Figure 3: Schematic of a conventional power distribution in aircrafts [15]

2.1.1 Pneumatic network

The pneumatic power is bled from the engine high-pressure compressor. It is commonly used to power the Environmental Control System (ECS). It also supplies hot air for Wing Ice Protection System (WIPS). The major drawback of air bleeding from the engine is that it reduces thrust efficiency.

2.1.2 Hydraulic network

The hydraulic power is provided by a central hydraulic pump. The power is transferred to actuation systems (primary and secondary flight control), landing gears, engine actuation, thrust reversal system and several other auxiliary systems.

Chapter 1: Toward full-electric transportation

As an example, the A320 hydraulic system is composed of three fully independent circuits: Green, Yellow and Blue (see Figure 3). The normal hydraulic source on the blue circuit is the electrical pump. The auxiliary source is the Ram Air Turbine (RAT), used in case of a huge electrical power failure. On the green and yellow circuits, the normal hydraulic source is the Engine Driven Pump (EDP). The auxiliary source is the Power Transfer Unit (PTU). It is a hydraulic motor pump which transfers hydraulic power between the green and yellow systems without transfer of fluid [16].

The main drawback of a hydraulic power is the economic cost in maintenance due to the system complexity.

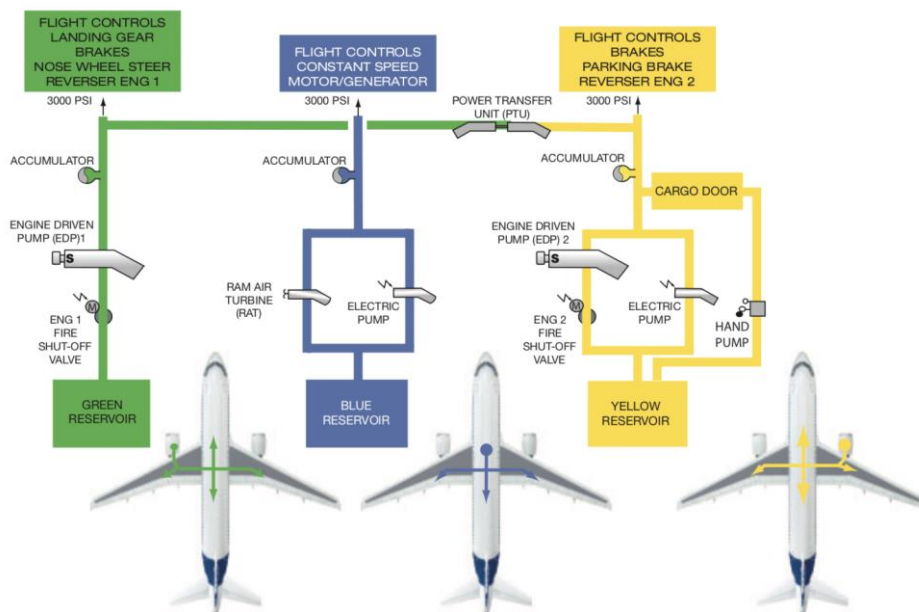


Figure 4: Green, Blue and Yellow A320 hydraulic circuits [16]

2.1.3 Mechanical power

The gearbox is the heart of the mechanical power transmission. It transfers the power from the engines to central hydraulic pumps, to local pumps for engine equipment, to other mechanically driven subsystems and to the main electrical generator [15].

2.1.4 Electrical network

The proportion of on board electric power has continuously increased in aircrafts. The electric power tends to replace more and more systems which were powered by either pneumatic or hydraulic power. Figure 5 illustrates the increasing of inboard electrical equipment demand in commercial aviation [17].

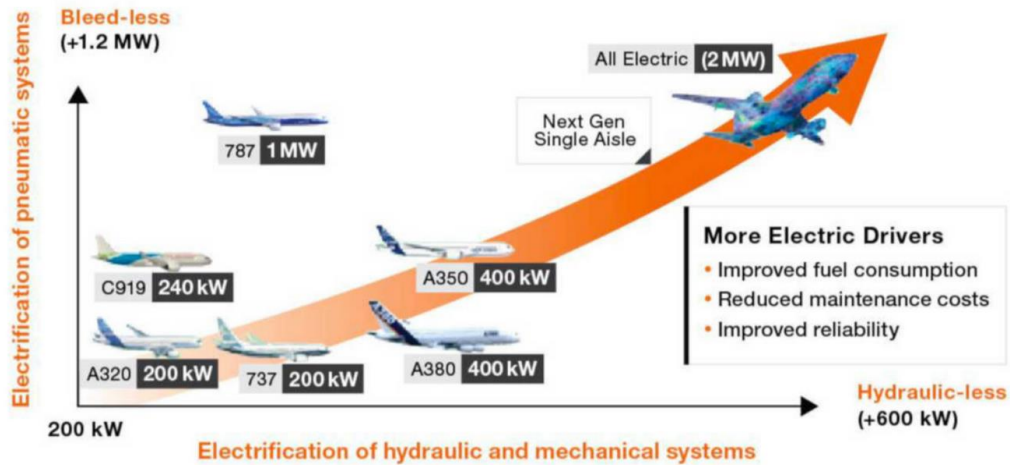


Figure 5: Increasing on board electrical equipment demand in commercial aviation [17]

The former on board electric bus first provided both constant voltage and frequency to the aircrafts devices. An Integrated Drive Generator (IDG) was used to change the variable speed of the jet engine to constant speed [18]. Between 1936 and 1946, the voltage supply has increased from 14.25 VDC to 28 VDC [19].

In recent aircrafts such as Airbus A380, Airbus A350 and Boeing 787, there is no more IDG. A gearbox is used to directly couple the engine generator to the jet engine. An alternative voltage of 115/200 VAC is produced with a frequency range from 350 to 800 Hz [18].

The interest to replace pneumatic and hydraulic system with electric ones is mainly economic. Moreover, electric aircrafts have a lower maintenance cost.

2.2 PROJECTS OF MORE ELECTRIC AIRCRAFTS

Almost ten years ago, focusing in EU, Airbus revealed its first full electric aircraft. Up to now, new demonstrators try to develop and optimize the electric propulsion technology.

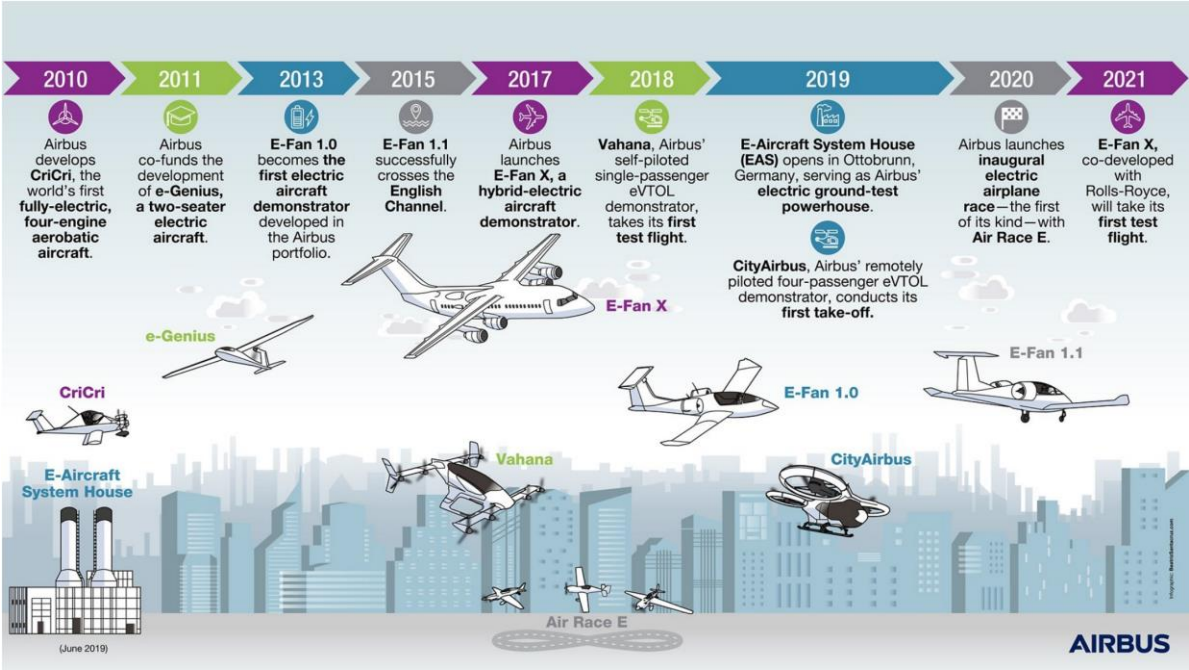


Figure 6: A timeline of Airbus's achievement in electric propulsion [20]

2.2.1 E-FanX

The E-FanX is the last Airbus-Rolls Royce project dealing with airplanes electrification. The objective is to develop a flight demonstrator testing a 2MW hybrid-electric propulsion system on a 100 seat regional jet. One of the four jet engines will be replaced with a 2 MW electric motor fed by a 3 kVDC electrical distribution. The flight testing should have started by the end of 2020 but, due to the corona virus pandemic, it has been stopped until further notice [21].



Figure 7: Airbus-Rolls Royce E-FanX (in green : the electric propeller) [21]

2.2.2 CityAirbus

The CityAirbus is an all-electric four-seat multicopter vehicle demonstrator. It is an electric Vertical Take-Off and Landing vehicle (eVTOL). It is remotely piloted. The CityAirbus demonstrator first take-off happened in May 2019. This vehicle produces less noise and zero emission compared to a classic helicopter.



Figure 8: CityAirbus technical data [22]

3 HASTECS PROJECT

3.1 TARGETS

The Hybrid Aircraft academic reSearch on Thermal and Electrical Components and Systems (**HASTECS**) is part of the “H2020 - Clean Sky 2” program. It is a heavy EU aeronautics research program which aims to reduce by 20% the CO₂ emissions and the noise produced by airplanes by 2025. It regroups several laboratories, including LAPLACE, in partnership with Airbus Toulouse.

HASTECS objectives are to identify the most promising technological breakthrough solutions and to develop tools to considerably increase the efficiency of the electric hybrid powertrain systems. The final objective is to obtain both fuel consumption and noise contamination significant saves as it is currently the case for road vehicles (cars, buses, trucks). To successfully achieve such objectives, the specific powers will have to be increased.

HASTECS consortium aims to double the specific power of electric motors including cooling system. The targets are 5 kW/kg by 2025 and 10kW/kg by 2035. Concerning the power electronics, the specific power, including cooling, aims to be 15kW/kg by 2025 and 25kW/kg by 2035. These targets are to be achieved despite challenging environmental conditions such as harsh environmental conditions.

This technological breakthrough should reduce by 1.8 ton the weight of a 1.5MW inverter-motor powertrain. Consequently, 3.5% fuel save should be achieved on a 300 nautical miles' regional flight.

The kick-off meeting on September 13th 2016 has marked the start of HASTECS project for five years. It involves six PhD students and two post-doctoral students for a total founding of 1.5 M€ [23].

3.2 SERIAL HYBRID CONFIGURATION

There are several possible architectures for an electric hybrid powertrain [24]. HASTECS consortium has retained the serial hybrid one. It has mainly been selected because it is the architecture of the future Airbus demonstrator eFanX [21]. It is illustrated in Figure 9.

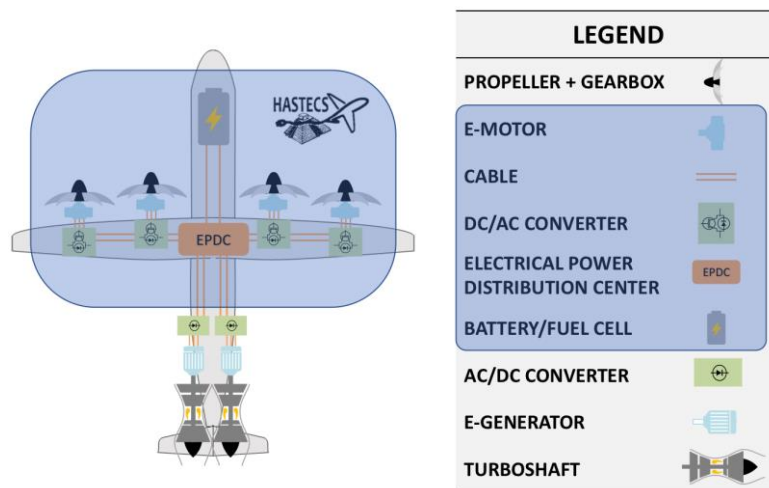


Figure 9: Serial hybrid powertrain [25]

Gas turboshafts driving electric generators are the main sources of power. Rectifiers supply an ultra-high DC voltage. Bus voltages are in the range of kVs [26]. The power is directed toward the Electrical Power Distribution Center (EPDC). Auxiliary power is delivered by batteries and/or fuel cells. The power supplies inverter fed motors. The propellers are driven through gearboxes.

HASTECS perimeter is composed of the batteries/fuel cells, the high voltage DC bus, the power electronics and the inverter fed motors. The tasks are dispatched between six Work Packages (WP).

3.3 WORK PACKAGES

Figure 10 below illustrates the tasks carried by each WP and the possible interactions.

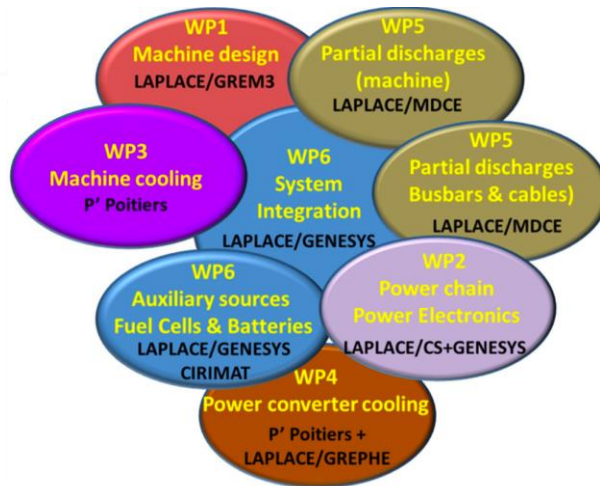


Figure 10: HASTECS work packages [23]

3.3.1 Work Package 1 (WP1)

This WP focuses on the electromechanical sizing of the electric motors. The first target for 2025 is a 5 kW/kg specific power, including cooling. The second target for 2035 is to reach 10 kW/kg. WP1 strongly interacts with WP3 (thermal study) and WP5 (partial discharges study). To choose the motor architecture, an analytic calculation tool has been developed [27]. It makes quick trade-offs of high specific torque electric motors using the loadability concepts developed by designers. The loadability concepts are mainly the electric, magnetic and thermal loads (see Table 1). Such loads are introduced in the tool as inputs to get the main sizes, weight and performances of the electric motor. The main interest is that there is no need to specify neither the stator winding configuration, nor the rotor structure. Additional inputs data such as the mechanical power or the rotational speed are required [28].

Load	Parameter	Description	Constraint
Magnetic loading	B_m	Magnetic flux in air gap	Magnetic materials
Electric loading	K_m	Surface current density	Insulation materials Cooling technology
Electromagnetic loading	$\sigma_t = \frac{B_m * K_m}{2}$ $T_{em} = 2 * \sigma_t * \pi * R^2 * L$	σ_t : tangential stress in airgap T_{em} : maximum electromagnetic torque R: inner stator radius L: motor active length	Magnetic materials Insulation materials Cooling technology

Table 1: Electric machine loads [28]

3.3.2 Work Package 2 (WP2)

The task of this WP is to develop a tool to facilitate high-power converters design in a limited time to analyse and compare several conversion topologies to power the motorization system. The first objective for 2025 is to size a 15 kW/kg power converter, including cooling. The second objective for 2035 is to increase this value to 25 kW/kg. To reach such high values, the power converter losses have to be minimized.

First, this WP determines an optimal DC bus voltage. This key parameter is determinant in both machine sizing and partial discharges study. The efficiency and power density of different multileveled topologies are investigated using a developed tool and real semiconductors datasheets (Figure 11).

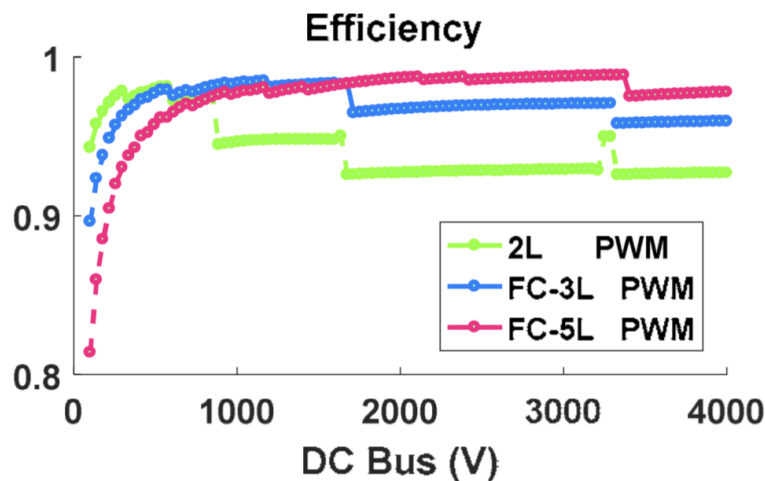


Figure 11: Power electronics efficiency for several topologies using available database components [29]. 2L PWM: 2 Layers Pulse Wide Modulation, FC-3L PWM: Flying Cap-3 Layers Pulse Wide Modulation, FC-5L PWM: Flying Cap-5 Layers Pulse Wide Modulation

This WP carried out a work to develop a simulation tool for pre-sizing converters. It makes it possible to size a converter from a chosen topology. Parametric studies by varying the DC bus voltage, the requested power or the modulation index make it possible to determine the optimum operating point. An algorithm was developed to select the best suited component for both desired voltage and current values [29]. The performances are being computed based on analytical calculations of the losses in the semiconductors components for multiple multilevel architectures. Pulse Width Modulation (PWM) control is mainly considered [29].

Discontinuities in the results (see Figure 10) are due to discontinuities in component calibres and have been overcome by generating virtual components with continuous calibres. Components parameters

variation laws are identified as a function of the voltage or current-voltage product calibres and then applied to the desired one [29]. Figure 12 illustrates the efficiency as a function of DC bus voltage for a real two layers PWM components versus the generated ones [29] .

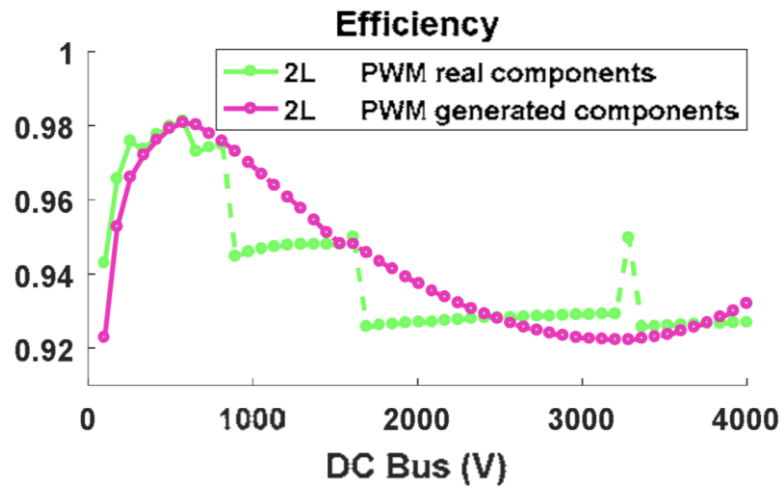


Figure 12: Real versus generated components efficiencies for adapted voltage and current calibres [29]

3.3.3 Work Package 3 (WP3)

This WP deals with the electric motors cooling technology. Thermal limitations are mainly imposed by both magnetic components and insulation materials. Besides, there are multiple losses in the electric motor that increase its temperature [30], [31]:

- iron losses in both stator and rotor laminations;
- Joule's losses in windings and end-windings;
- aero-thermal losses in air-gap;
- mechanical losses in the bearings.

An analytically Lumped Parameter Thermal Model (LPTM) has been used. It enables a quick parametric study. The motor is discretized in nodes (Figure 13); the thermal energy balance on each nodes is computed [30].

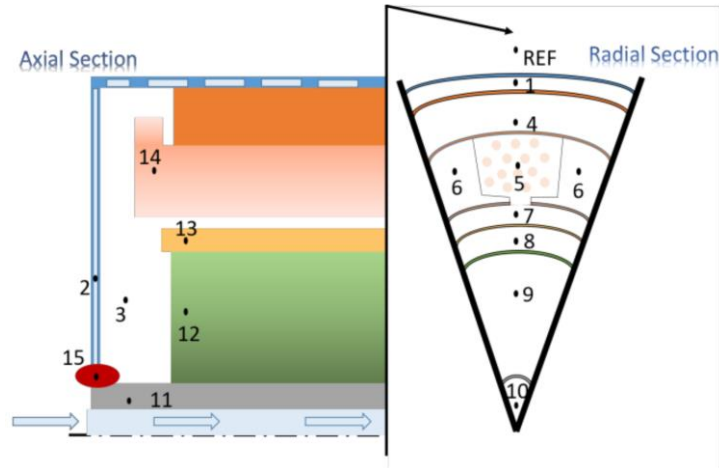


Figure 13: Motor nodes locations in axial and radial sections [30]

The connections between nodes (Figure 14) depends on material properties such as thermal conductance.

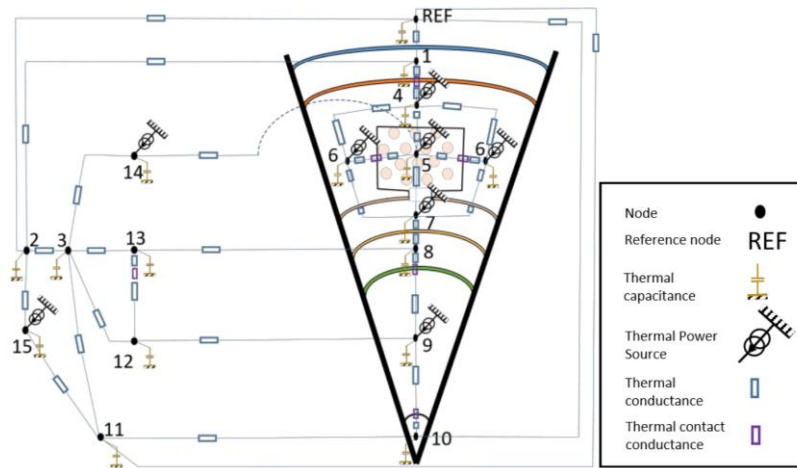


Figure 14: Motor nodal network [30]

As an example, for a motor configuration similar to the Lexus 2008 [32] and considering a water jacket cooling solution [30], the hot spots have been identified (see Figure 15):

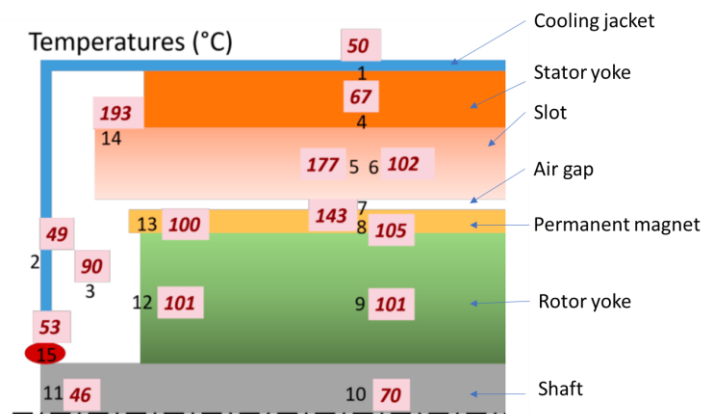


Figure 15: Resulting temperatures in different locations inside a motor. Adapted from [30].

The hot spots are located in the winding and end-winding where the thermal conductivities are the lowest [30], [32].

3.3.4 Work Package 4 (WP4)

This WP aims to design and to optimize solutions to cool the electric power converters. The cooling solution also has to provide a constant operating temperature for the whole mission of the aircraft. Climb and descent stages are the most stressful. The temperature difference between ground and flight can reach 40 °K [33]. The Capillary Pumped Loop for Integrated Power (CPLIP) cooling solution has been chosen. It suits the Power electronics In the Nacelle (PIN) configuration. Figure 16 illustrates the CPLIP concept [33]:

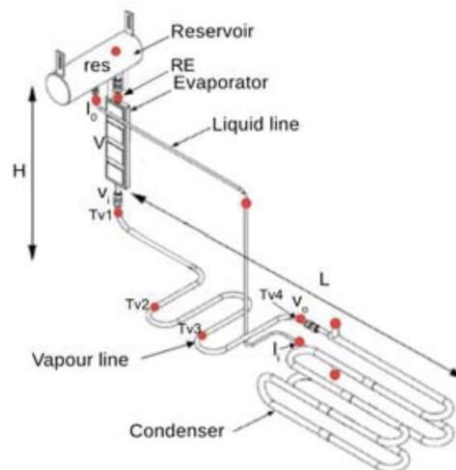


Figure 16: CPLIP concept schema [33]

The power electronic is set up around the evaporator wall. A tank delivers the liquid at ambient temperature to the evaporator. In this porous component, there is a heat exchange occurring between the power electronics and the fluid. The fluid then turns to vapour and is directed toward the condenser through the vapour line. In the condenser, the vapour is cooled and turns back to liquid. The liquid is sent back to the reservoir through the liquid line.

The choice of the design point is particularly sensitive as it influences the weight of the cooling system. It has been chosen at the beginning of the take-off and climb stage [33]. Whatever the selected power converter topology, the energy to be evacuated during the take-off and climb stage represent 44% to 45% of the energy to be evacuated in the cruise stage but in a much smaller amount of time [33].

Figure 17 gives the results obtained from an experimental test in a mission profile of a single-phase fed power converter [33]. The maximal losses to be evacuated are Q_{max} greater than 15 kW. It can be seen that the power converter temperature (evaporator wall) is maintained lower than 150 °C which is the highest temperature the components can withstand.

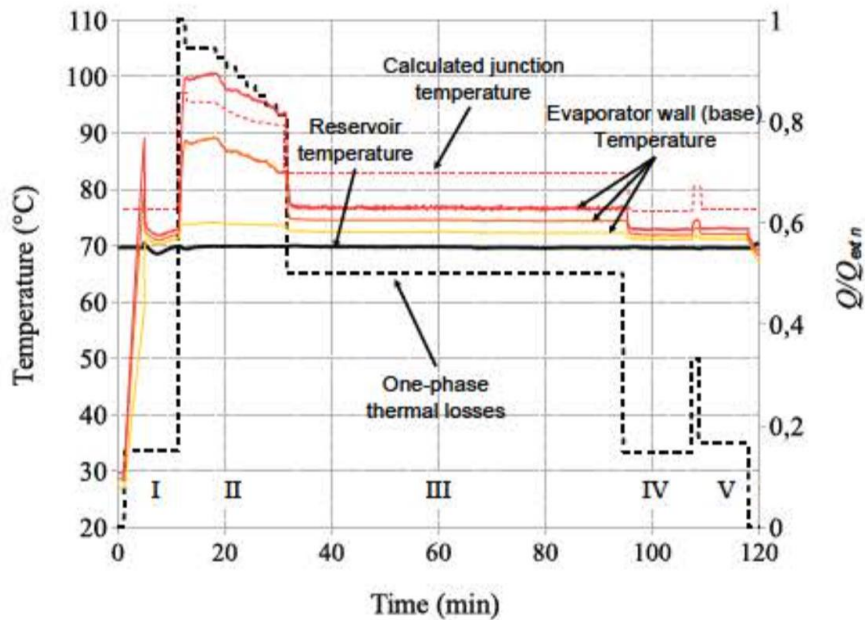


Figure 17: Diagram resulting from an experimental test in a mission profile of a single-phase fed power converter. Stages: taxi out (I), take-off and climb (II), cruise (III), descent and landing (IV), taxi in (V) [33]

3.3.5 Work Package 5

This WP deals with partial discharges (PD) that may occur. Two systems are studied by this WP: the Electrical Insulation System (EIS) of the DC busbar powering the power electronic and the motor EIS design.

3.3.5.1 DC busbar

Concerning the EIS busbar design, the main results/achievements are:

- the evidence that the risk of PD appearance in busbars is high at triple points areas;
- simulations to evaluate and to prevent the PD appearance.

The power converter topology is based on a design provided by WP2. It is made of seven busbars slats. The DC bus voltage is 2.5 kV and the insulation is made of Polytetrafluoroethylen (PTFE) film located between the slats [34]. Such configuration results in multiple triple points busbars/PTFE/air interfaces. PD are more likely to appear at these points due to a local electric field reinforcement. Figure 18 is a schematic view of power busbars embedded inside a power converter [34].

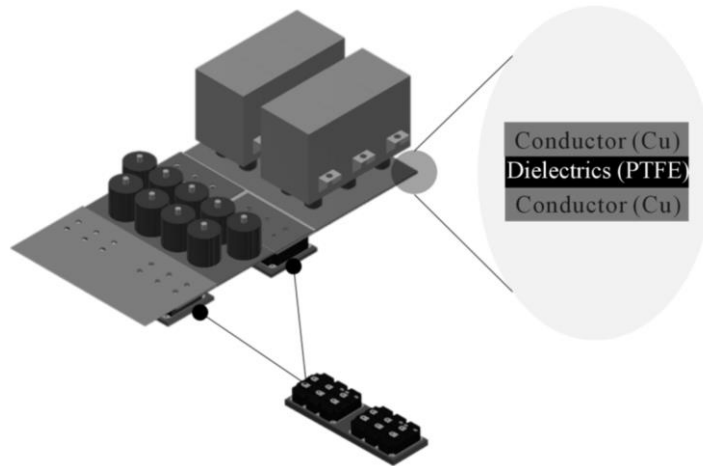


Figure 18: Schematic view of power busbars embedded inside a power electronics converter; example of triple point [34]

2D-finite elements study of a characteristic triple point has been done. It has pointed out the sensitivity of the charge accumulation in the dielectric interfaces on the air gap electric field. There are two possible scenarios:

- firstly, the charges accumulated in the insulator near the interfaces have the same sign than the conductor polarities: these are so called homo-charges. The electric field in the triple point is then reduced. The gaps are larger than 1 mm, thus the air will breakdown if the electric field exceeds 3kV/mm. Figure 19 displays the numerical results for a configuration without any dielectric charge density and with an homo-charges absolute charge density of 1 C/m³ [34].

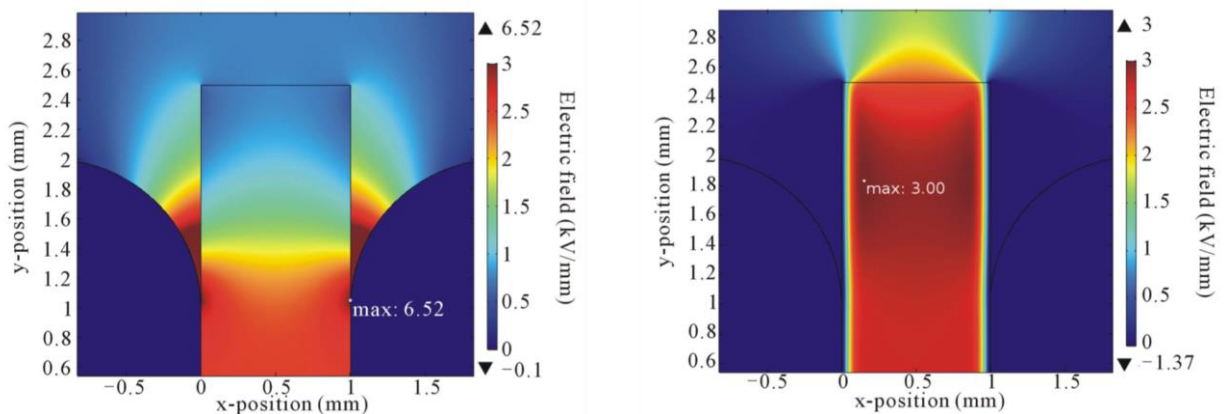


Figure 19: Simulated electric field associated to homo-charges; left) Absolute charge density of 0 C/m³; right) Absolute charge density of 1 C/m³ [34]

With the dielectric uncharged (left) the electric field in the triple point reaches the air breakdown threshold (3kV/mm). PD are more likely to occur. However, with the dielectric charged with homo-charges with an absolute density of 1 C/m³, the electric field in the triple point areas is decreased under

the breakdown threshold. The electric field is reinforced inside the dielectric. However, such material has a higher dielectric strength than air: classical values are 60-100 kV/mm.

- The other scenario is that the charges accumulated in the insulator near the interfaces are of opposite signs than the conductors. These are so called hetero-charges. In such case, the numerical results are less optimistic concerning PD in the triple points (Figure 20).

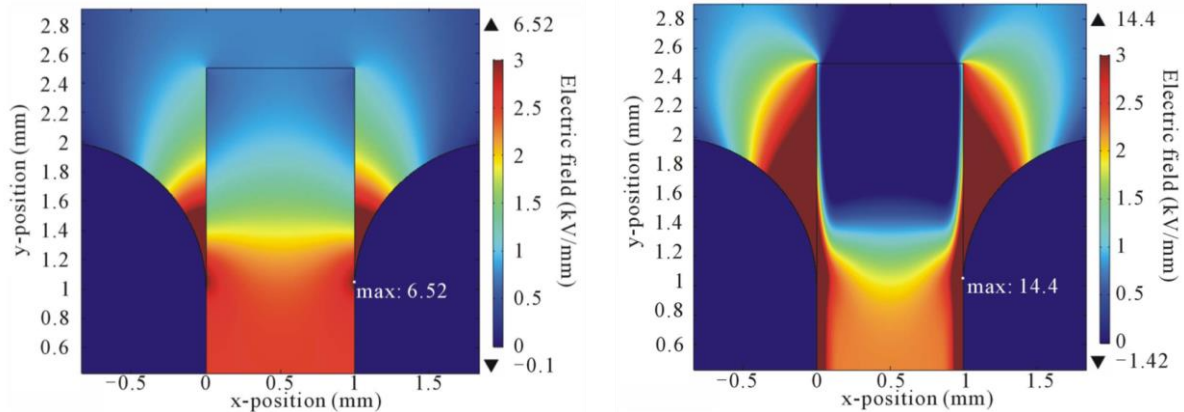


Figure 20: Simulated electric field associated to hetero-charges; left) Absolute charge density of 0 C/m^3 ; right) Absolute charge density of 1 C/m^3 [34]

In such case, the electric field is reinforced in the triple points area and the electric field exceeds the breakdown threshold.

This work has shown that the charging of the dielectric has hazardous consequences on the electric field at triple points areas. One conclusion is the special care to design a non-charged insulation system, for example by using insulators well known to accumulate a low amount of charges.

3.3.5.2 Motor Electrical Insulation System (EIS)

This task is the research subject of this PhD dissertation. The aim is to provide a tool to help the machine designers to avoid or to reduce PD that may occur in the EIS of inverter fed motors. The work has mainly been focused on the Paschen's criterion application in the context of electric motor working under aeronautics conditions.

3.3.6 Work Package 6

This WP centralises the multiple models developed by the others WP. It realizes the global optimization of the whole powertrain. From an input data set and given environmental conditions (temperature, pressure, aircraft speed,...) "surrogate" models are used to quickly assess the efficiencies and masses

from each devices to the whole powertrain. The regional aircraft structure is fixed, only the propulsive system can be modified thanks to an implicit loop as pictured in Figure 21.

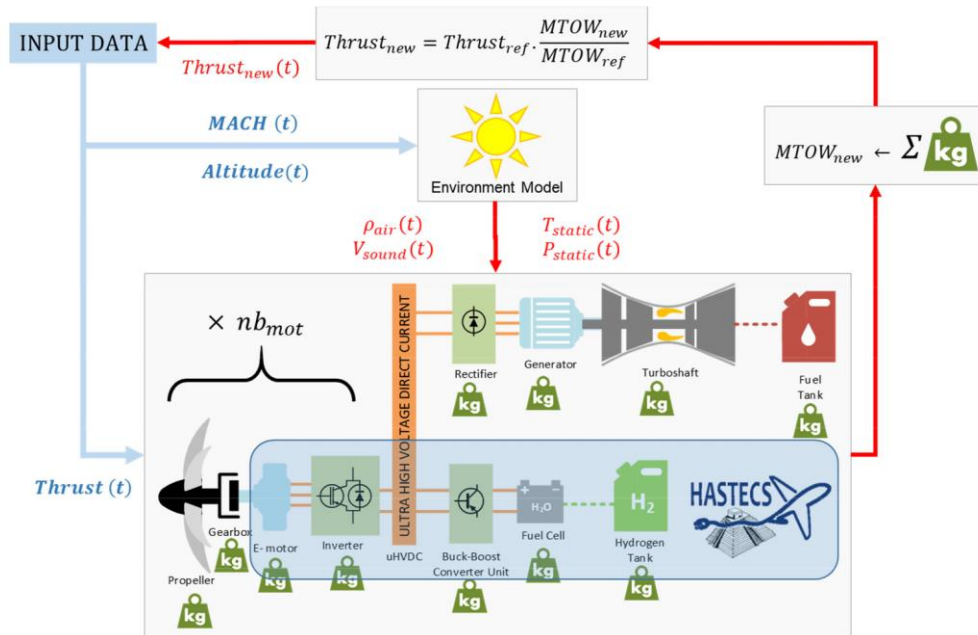


Figure 21: Implicit looped integrated process [26]

This WP has also realized a state of the art and prospects on auxiliary sources (batteries and fuel cells).

4 ELECTRIC MOTORS ELECTRICAL INSULATION

4.1 LOW VOLTAGE MACHINE

The electric insulation of electric motors is generally made of organic materials. These are the polymers; they are mainly found in the motor as foils, papers, varnishes and resins.

The primary electrical insulation of Low Voltage (LV) rotating machine stators is composed of three main insulation layers. These are the turn-to-turn, turn-to-ground and phase-to-phase insulations.

Figure 22 is a sketch of the three insulation layers of a stator.

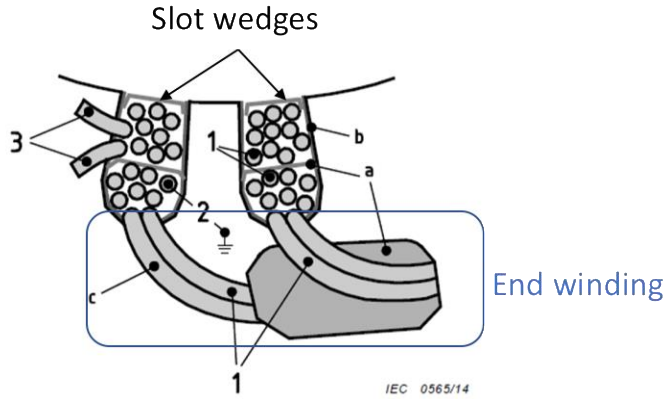


Figure 22: Electric stresses: 1) phase-to-phase, 2) turn-to-ground, 3) turn-to-turn
 Insulation layer: a) phase separator, b) slot liner, c) enamelled turn – adapted from [35]

The slot is impregnated with a resin and generally closed with edges. The end winding insulation is reinforced. The following table gives some common materials used for the electric insulation of LV motors:

Component	Insulation Material
Enamelled wire	<ul style="list-style-type: none"> • Polyurethane • Polyether • Polyester-imide • Polyamide-imide • Poly-imide • With Self-bonding overcoat • Litz wires (for HF applications)
End winding tape	<ul style="list-style-type: none"> • Glass cloth • Polyester • Silicon Carbide Coating
Slot insulation	<ul style="list-style-type: none"> • Impregnated PET felt/film/felt • Impregnated polyaramid paper • PET film/mica/PET film
Impregnating resin	<ul style="list-style-type: none"> • Epoxy • Silicone • Polyester-imide • Polyamide-imide • Poly-imide
Wedges/closure	<ul style="list-style-type: none"> • Glass mat with epoxy resin • Glass fabric bonded with epoxy resin

Table 2: Insulating materials for low-voltage motors based on [19][36]

The choice of the material is determined by four criteria. They are given in order of importance:

- 1) Dielectric strength. Usually expressed in [kV/mm]. It represents the maximum electric field amplitude the material is able to endure. Most of the organic materials of dozens of micrometers in thickness have dielectric strength of the order of 100 kV/mm.
- 2) Maximum working temperature. It defines the maximum temperature at which the material ensures its insulating function. The best organic materials have maximum working temperature up to 240 °C.
- 3) Mechanical properties for the implementation of the material inside the stator slot.
- 4) Thermal conductivity. It characterises the ability of the material to evacuate the heat flux toward the cooling system. Organic materials have thermal conductivity of the order of 0.1-0.3 W.m⁻¹.K⁻¹.

4.1.1 Turn-to-turn insulation

It is made with a polymer enamel coating the conductor core, generally made of copper. The thickness of the enamel varies from some micro-meters to dozens of micro-meters for turn copper diameter up to 5mm [37].

Anton [38] detailed the enamel technology and realized a comparative study of the common polymers used as enamel.

The enamel is the result of a varnish being cured. The varnish is a complex mix in which are present: the solvent, a polymer precursor, the cross-linking agents and some additives.

The solvent prevents the polymer precursor from polymerizing. It represents between 60-80% of the total solution. It is mainly composed of a mix of phenol and cresylic acid. The solvent is evaporated during the curing process. Some additives such as naphtha or xylene are added to the solvent to adjust the viscosity of the varnish. The polymer precursors represent 18-40% of the solution.

The enamel overcoat is made of multiple layers which are successively polymerized at high temperature in an oven. The first layers (i.e.: the closest to the copper) goes much more in the oven than the external layers. The cross-linking is therefore not uniform in the whole enamel thickness. The process to get an enamelled wire is illustrated in Figure 23.

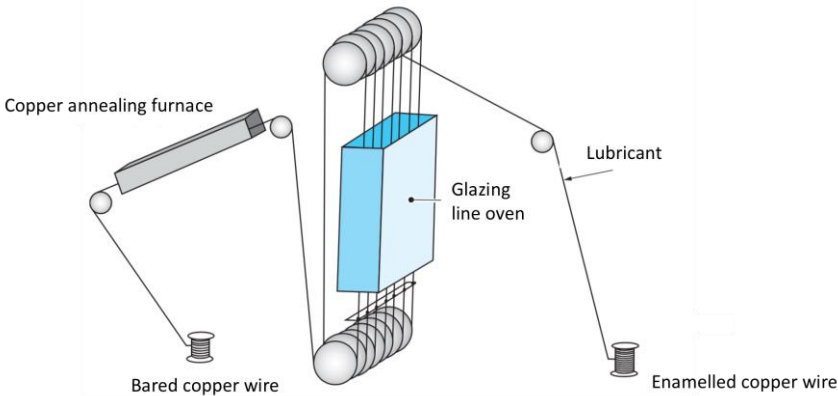


Figure 23: Enamelled wires glazing line process [38]

Multiple polymers are generally found in the enamel coating. The enamel has to resist the biggest thermal stress present in a motor slot due to its location just over the copper wire, which is the main heat source. Besides, it is surrounded by the resin which impregnates the whole slot. The choice of the polymers thus strongly depends on the temperature and the chemical compatibility with the impregnation resin. The insulation power of polymers is highly affected by the temperature. They are distributed into thermal classes. They define the higher temperature at which the polymer is able to ensure its insulation function up to 20 000 hours. Some are presented in Table 3.

Thermal class	Y	A	E	B	F	H	N	-	-	-
Temperature (°C)	90	105	120	130	155	180	200	220	240	280*

Table 3: Some thermal classes [39]

(*) 280°C thermal class is obtained by adding non-organic nano-fillers in a PI matrix [40]

Here are the different materials commonly used:

- Polyvinyl formal: thermal class 120 °C, they have very good mechanical properties. They are particularly used on big round wires or flat wires in transformer application due to their good resistance to hydrolysis.
- Polyurethane (PUR): thermal class 180 °C, they are used on thin wires (from 0.02 to 2 mm). One can find them in household appliances, television or phone.
- Polyester imide (PEI): thermal class 180 °C, they are very flexible and they have a good grip on copper. They are applied on wires from 0.03 to 0.8 mm.
- Polyester THEIC (TriHydroxyEthyl IsoCyanurate): thermal class 200 °C. They are usually used as undercoat of polyamides imides in order to improve their mechanical properties (flexibility, grip) while keeping a good heat resistance. They are used on diameter from 0.5 to 5 mm.

Chapter 1: Toward full-electric transportation

- Polyester imide THEIC: thermal class 200 °C, they have a good heat resistance and a good chemical resistance. They are also used as undercoat of polyamides imides.

- Polyamide imide (PAI): they have a very good thermal stability, a very good resistance to thermal shock and very good mechanical properties. Used as full coat, they have a thermal class of 220 °C and are used with diameters from 0.1 to 1.3 mm. Because of their high cost, they are generally used as upper layer of polyester imides THEIC to get wires of thermal class of 200 °C with diameters from 0.1 to 5 mm.

- Polyimide (PI): they have a very good heat resistance (up to 240 °C) and a very good resistance to thermal shock. They are used on wires from 0.05 to 6 mm diameter.

These properties are summarized in Table 4.

Properties	Formal	PUR	PEI	PET-THEIC + PAI	PEI-THEIC + PAI	PAI	PI
Thermal class [°C]	120	155	180	200	200	220	240
Copper diameters [mm]	0.6 - 5	0.02 - 2	0.05 - 2	0.05 - 5	0.1 - 5	0.1 – 1.3	0.05 – 6
Electric strength (EIC V/μm)	170	180	175	180	180	180	180
Abrasion	(2)		(3)	(2)	(2)	(2)	(5)
Grip	(2)		(2)	(1)	(2)		
Flexibility	(2)					(2)	(2)
Solvent resistance	(3)			(2)	(2)	(2)	
Thermal conductivity [W.m ⁻¹ .K ⁻¹]	Mainly between 0.1-0.3 [41]						
Properties: (1): excellent, (2): very good, (3) good, (5): very bad							

Table 4: Main properties of standard enamel wires adapted from [38]

The thermal conductivity characterizes the behaviour of a material to a heat flux. The lowest this value, the more difficult the heat flux cross over and evacuation from the winding. For comparison, the thermal conductivity of iron is 80 W.m⁻¹.K⁻¹. Conductivity values of standards enamel materials are very low compared to iron.

4.1.2 Phase-to-phase insulation

The phase-to-phase insulation ensures the electrical insulation between different phases in the end winding and/or into the slots (if there is more than one phase by slot). Depending on the number of different phases which overlaps and the winding configuration, such insulation has to resist up to twice a phase peak voltage.

It is mainly composed of porous fabric from aramid fibers. This porous material is impregnated with resin, during the winding impregnation step. Aramid fibers have also good both heat and humidity resistances [42].

4.1.3 Turn-to-slot insulation

The slot insulation ensures the electrical insulation between the winding and the stator slot. Mainly, the stator frame is grounded. This insulation has to be able to resist the whole phase peak voltage.

It is inserted inside the slot before the winding operation. It also protects the wires during their insertion in the slot against stator abrasion. Slot insulation is mainly formed with paper, film or flexible materials. It is also used to ensure a physical separation between the end winding and the stator slot. The common materials used are mica and/or aramid. Slot wedges are an additional protection which increases the mechanical handling of the winding.



Figure 24: Slot wedges and phase insulation seen with the winding in place; one wedge is partially inserted [43]

		Tensile strength [N/mm ²]	Operation temp. [°C]	Moisture absorb. (% by weight)	Chemical strength; Graded 0-4			Voltage strength [kV/mm]	Trade names
					Acid s	Alkali s	Organic solvent		
Insulating foils	Polyester PETP	140-160	130	0.5	2	1	4	150	Mylar Melinex Hostaphan
	Polyimide	180	220	3	3	0	4	280	Kapton
	Polysulphone PS	90	180	1.1	3	3	1	175	Folacron PES
Fiber insulator	Cotton fibers	250-500	105 (impregnated)	10	1	2	4	-	-
	Polyester fibers	500-600	155	0.4	2	1	4	-	-
	Glass fibers	1000-2000	130-200 (depending the impregnant)	-	4	3	4	-	-
	Aramid paper	1250	210	7-9	3	3	4	20 (1min, 50Hz test)	Nomex

Table 5: Characteristics of foils and fiber insulators [39]

4.1.4 Slot impregnation

The slot is filled with a resin. It aims to electrically insulate the whole slot. It also holds the winding in place and improve the heat dissipation toward the stator cylinder head. Impregnation resins are mainly composed of both solvent and polymer precursor. The solvent prevents the precursor from polymerizing. That is the reason why it is necessary to heat the resin during impregnation. The solvent evaporates and the precursors assembles to form the polymer.

The main function of the resin is to mechanically hold the winding in place (to avoid damage due to friction between the winding and the core) and to protect it against moisture, pollution and dust in the case of an open motor. It is not in direct contact with the copper so it does not have to resist such a high temperature as the enamel. It has to be chemically stable.

Several process exist to fix the resin. They have been documented by [44] in his PhD dissertation:

- **drop by drop method.** The resin is slowly deposited on the winding so that it impregnates the winding by capillarity. It is the most employed method in the industry. However, it is quite possible that some parts of the winding may not well be impregnated.

- **brush method.** The impregnation is done during the manufacturing of hand-made windings. The resin is repeatedly applied with a brush. The repartition of the resin is more uniform than the one obtained with the drop by drop method. The resin is directly put in the middle of the winding. This method is only applied to specific machine for small series production.

- **soaking method.** The machine is slowly lowered in a tank full of resin. It stays here a while so that the air trapped between the wires is extracted. The machine is then slowly pulled up and drained.

- **Vacuum Pressure Impregnation (VPI) method.** It is composed of different steps:

- Preheating: the motor is placed in an oven that heats it and allows moisture to evaporate. This will also help the resin better penetrate the material;

- Dry Vacuuming: the motor is removed from the oven and placed into a vacuum chamber to remove air and any remaining moisture;

- Filling: the chamber is filled with resin, coating the part and filling in all the gaps of the EIS;

- Wet Vacuuming: the vacuum levels is reduced and hold it for a set period of time;

- Pressure: the pressure is increased within the chamber using dry air (nitrogen for example) to allow deeper penetration of the resin;

- Draining: the pressure is vented and the motor is removed;

- Curing: the motor is finally placed into an oven to cure the impregnating resin.

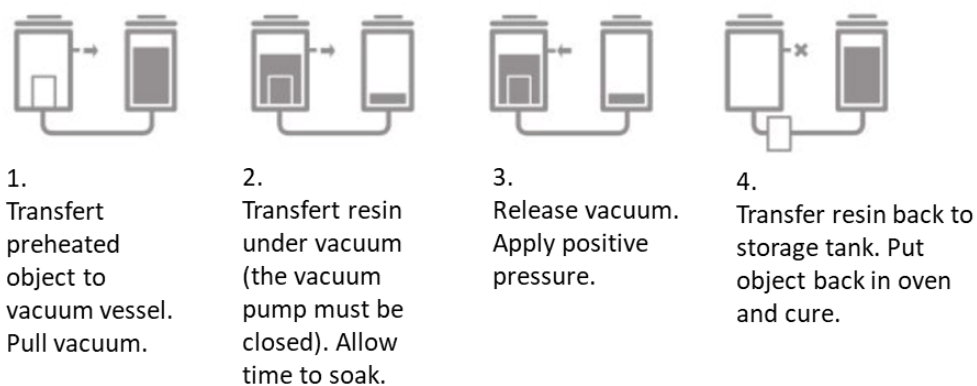


Figure 25: Vacuum impregnation steps given by Von Roll [45]

This method is found to be better than the others.

Chapter 1: Toward full-electric transportation

- double VPI: the vacuum impregnation steps are done twice to reinforce the holding of the winding. It is used when a high quality of impregnation is required.

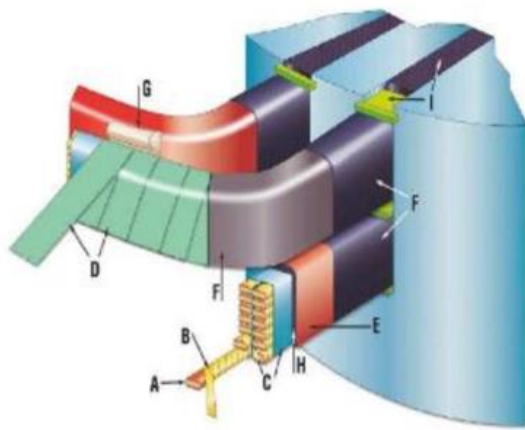
Table 6 gives the common varnishes characteristics.

	Mechanical strength; Grades 0-4	Operation temperature [°C]	Moisture resistance; Grades 0-4	Chemical strength; Grades 0-4	Typical materials
Impregnating varnishes	3	155	3	3	Alkyd polyester
	1	180	3	3	Silicone epoxy
Impregnating resins	3	155	3	3	Polyester alkyd Epoxy
	4	180	4	4	Polyester Epoxy
Coating (surface) varnishes	2	130	3	3	Alkyd Polyurethane
	2	155	4	4	Alkyd Polyurethane
	1	180	4	3	Alkyd Silicone Epoxy

Table 6: Characteristics of varnishes and resins [39]

4.2 HIGH VOLTAGE MACHINE

Machines powered with a phase to phase voltage higher than 700Vrms are considered as high voltage machines [35]. When the applied voltage is more than a few kV, these machines have to work doubtless with partial discharges. Their EIS is consequently reinforced by using non-organic materials. Figure 26 illustrates a classical EIS used in such high voltage machines.



- Winding wire (A)
- Conductor insulation (B)
- Stack insulation (C)
- Main wall insulation: Mica tape (D) + VPI resin (H)
- Conductive paint or tape (F)
- Stress grading paint or tape (F)
- Finishing or sealing tapes (E)
- Bracing materials (G)
- Slot wedging materials (I)

Figure 26: High voltage machine electrical insulation system [46]

In most high voltage motors the winding is composed of enamelled copper bars. It is well organized in the slot. Bars reduce the end winding congestion outside the slot. For high frequency application, the bars are subdivided. This is to prevent frequency losses such as skin and proximity effects.

Some specifications for high voltage motor insulation are given in [39]. Mica tape wound is widely used in layers around the conductors due to its very good partial discharge resistance. On the end windings, stress grading tapes are applied on the bars extremity close to the slot end. The most common stress grading materials are a semi-conductive silicon carbide tape or paint. It aims to progressively reduce the electric field at the area where the stator cylinder head, the insulation tape and the surrounding air meet together (triple point). That is a weak spot in the system which is susceptible to easily lead to electric discharges [34].

The groundwall insulation is usually made out from natural resins and mineral used as fillers. The resins include refined petroleum oils, waxes, asphalts, etc. Minerals include mica, asbestos or quartz [47].

In this PhD dissertation, we consider that the level of the applied voltage (i.e.: 2.5 kV) allows to find solution leading to PD-free working conditions. This is the reason why the following chapters will deal with an organic EIS. However, if partial discharges appear, the methodology that will be developed may be applied just by changing both size and permittivity of the EIS components.

5 THERMAL ASPECT

5.1 COOLING STRATEGIES

There are two main strategies to cool an electric motor. The first one consists in evacuating the heat on the stator cylinder head. A thermal exchange takes place between the hot stator cylinder head and the coolant. The coolant can either be a gas such as air or a liquid such as water. In the case of a high power density electric motor for aeronautical application, a water jacket seems to be the best suited solution [30]. An example of water jacket configuration extracted from [48] is presented in Figure 27. The housing oil channel is used to deliver the oil to the stator oil channels. After running in the channels, the oil is cooled at the end windings and goes back to the tank.

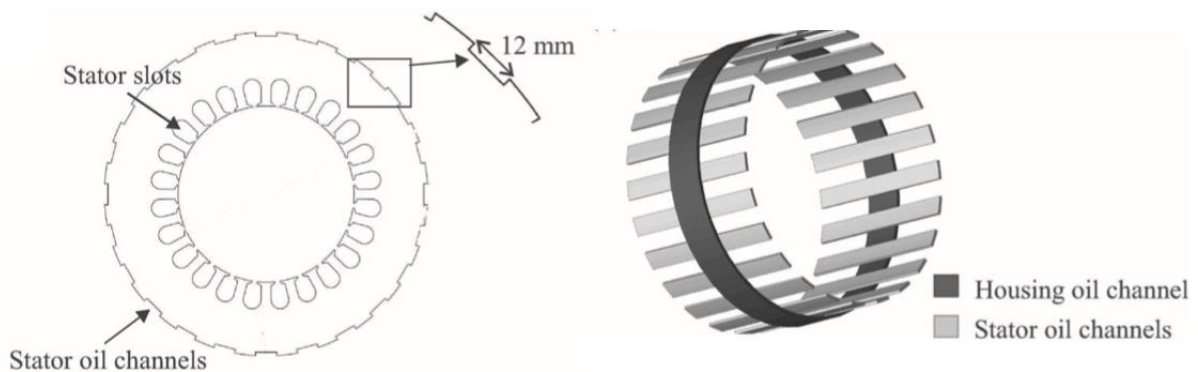


Figure 27: Left) Stator design; right) Cooling system structure [48]

The thermal conductivity of polymers used in the electrical insulation of motors is mainly between $0.1\text{-}0.5\text{ W}\cdot\text{m}^{-1}\cdot\text{K}^{-1}$. That represents a real difficulty when using external cooling system such as water jacket. The heat flux has to cross the enamel overcoat, the impregnation resin and the slot liner. Such low thermal conductive materials retain the heat inside the slot and then reduce the cooling efficiency.

Another strategy consists in directly cooling the conductors inside the slot. The authors in [49] presented a Direct Winding Heat eXchangers (DWHX) made using a 3D printer (see Figure 28).

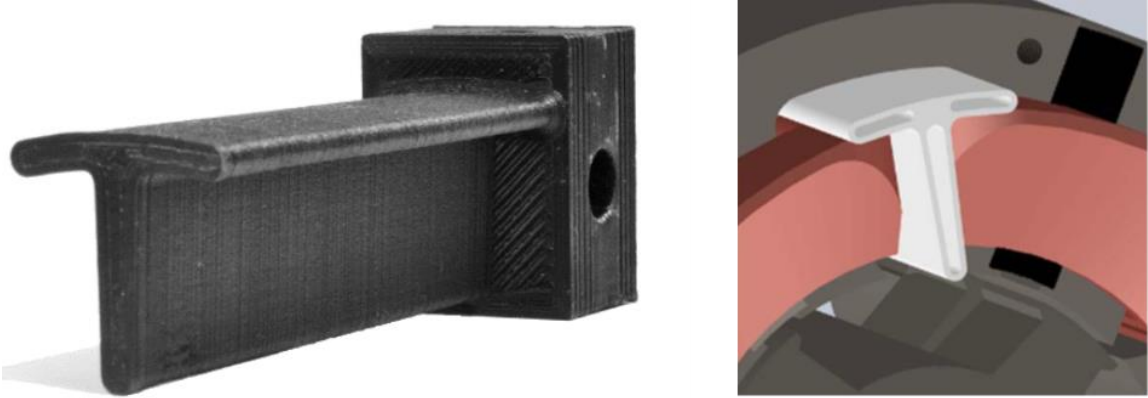


Figure 28: left) 3D-DWHX CF-Nylon prototype for heat transfer testing; right) 3D-DWHX shown in the stator slot of a motor equipped with permanent magnets [49]

The numerical results of the maximum temperature in several spots obtained by using only water jacket, only the 3D-DWHX and the combination of both are presented on Table 7:

	Maximum Temperature [°C]		
	Winding	Stator iron	Magnet
Water Jacket	30.1	22.5	21.1
3D-DWHX	58.1	67.6	37.3
Combined	16.9	15	18.6

Table 7: Comparison of stator cooling strategies involving 3D-DWHX [49]

The worst performance is obtained by using 3D-DWHX alone. This can be explained by the low thermal conductivity of the Nylon constituting the DWHX and of the winding. However, significant temperature reduction is obtained combining both cooling solutions, especially in the winding.

5.2 THERMALLY ENHANCED POLYMERS

Hitachi and Hitachi Chemical has developed an enhanced thermal epoxy resin [50]. They change the amorphous molecular structure into a crystal-like structure (see Figure 28). These liquid crystal molecules are called *mesogens*. They form a highly ordered structure which increase both thermal conductivity and flexibility of the resin. The enhanced thermal conductivities can reach $0.96 \text{ W.m}^{-1}.\text{K}^{-1}$, which is up to 5 times greater than classic epoxy resin.

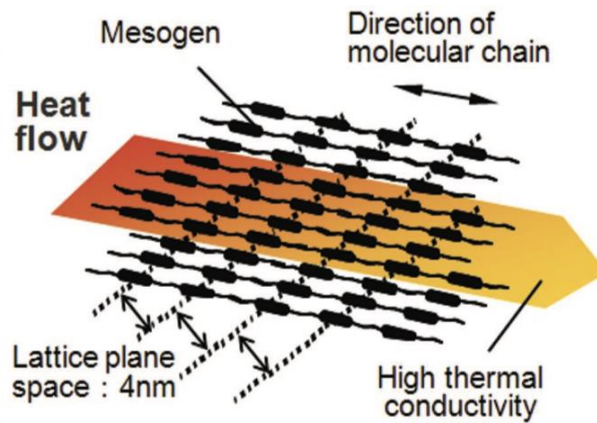


Figure 29: Structure of a new high thermal properties epoxy resin [50]

The authors in [48] compared the maximal temperature in a water cooled machine using three different impregnation materials. The main thermal and electric properties are summarized in Table 8.

Materials	Varnish	Epoxylite	SbTCM
Thermal conductivity [W.m ⁻¹ .K ⁻¹]	0.25	0.85	3.20
Dielectric strength [kV/mm]	80	20	10

Table 8: Materials used by [48]

SbTCM stands for silicone-based thermally conductive material. The simulation results obtained for a coolant flow rate of 2.5 L/min are presented on Figure 30. The temperature decrease compared to classic varnish at 3.2 A is of around 20% for Epoxylite and 30% for SbTCM. The current amplitude is at the stator winding.

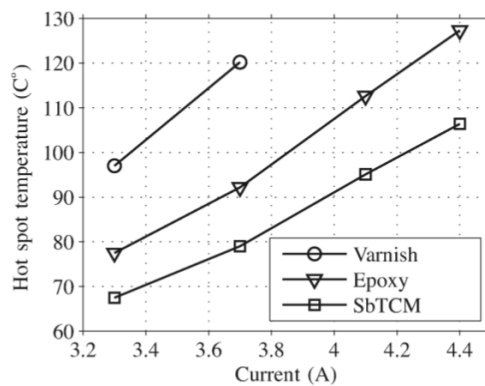


Figure 30: Simulation results: comparison between the hot spot temperature in electric machines using different impregnation materials at different current magnitude (at the stator winding). The inlet coolant flow rate is assumed to be 2.5L/min [48]

Chapter 1: Toward full-electric transportation

The drawback of such efficient thermal properties for SbTCM is a reduction of a factor 8 of the dielectric strength compared to classic varnish. SbTCM looks attractive but for some application, such as high power density motors, its dielectric strength may be too low.

Other high thermal conductivity composites have been reported by [51] (Table 9).

Properties	PA 66		PPS		PPA		LCP		PEEK	
	Std	Enh	Std	Enh	Std	Enh	Std	Enh	Std	Enh
Thermal conductivity [W.m ⁻¹ .K ⁻¹]	0.24	20-32	0.08-0.29	10-20	0.15	20	0.0837	20	0.25	10
Tensile strength [MPa]	95	65-117	48-86	45-70	76	44-83	110-186	80	70-103	70
Elongation %	15-90	0.75-1.5	1-6	0.31-0.75	30	0.6-1	1.3-4.5	0.25	30-150	0.5

Table 9: Comparison of standard (Std) versus thermally enhanced (Enh) polymer composites material properties [51]

As shown in Table 9, very high thermal conductivity are reached. However, the enhanced composites are much more mechanically fragile than the standard ones: the elongation is much lower. The enhanced materials are closer to ceramics than polymers.

On the other hand in [52] the Direct Current electric properties of polyimide/boron nitride (PI/BN) nano-composites for a large range of nanoparticle size and filler content have been investigated. It was shown that an efficient control of the charge carrier mobility allows a huge enhancement of the insulating properties of PI films.

6 IMPACT OF POWER ELECTRONICS

6.1 PULSE WIDTH MODULATION (PWM) BASIS

Power electronic offers a wide range of possibilities in machine control. AC motors now replace DC motors in application that require to control the machine rotation speed. AC motors are less expensive in particular due to less wearing parts. However, the power has to be converted from DC to AC. This is done via an inverter. Figure 31 illustrates such a classic electromechanical chain.

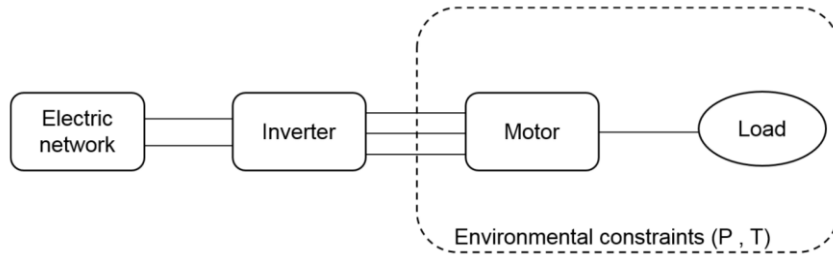


Figure 31: Diagram of an electromechanical chain [53]

If one considers the application of an electric aircraft, the load would be a fan. In case the motor is not pressurized, the group composed of the motor and the fan will be submitted to pressure (P) and temperature (T) variations.

An example of classic three phase inverter architecture is presented in Figure 32.

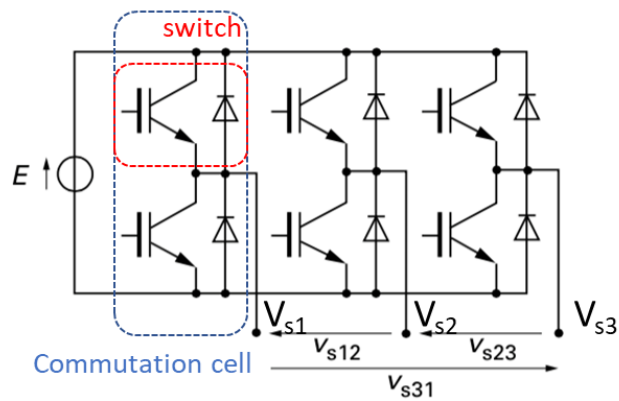


Figure 32: Classic three-phase inverter based from [54]

It is composed of three commutation cells. One cell is made of two switches. A switch is composed of a switching semi-conductive component, such as MOSFET or IGBT, and its anti-parallel diode. The two switches composing a cell are complementary. When the one at the top is ON (i.e.: the electric current can flow through it) the one below is OFF (i.e.: the electric current cannot pass). A commutation function f_m is defined. It equal either 0 or 1 depending on which switch is ON or not. So, for the commutation cell on phase 1, the output voltage is:

$$V_{s1} = f_{m1} * E$$

One of the most common command of PWM is the intersepective one. It consists in comparing the modulant to a carrier signal. The modulant defines the shape of the wanted output signal. The carrier generally has a triangular shape. Its frequency is much higher than the modulant frequency. Figure 33 illustrates the principle of three-phase sinusoidal PWM.

Chapter 1: Toward full-electric transportation

Two sinusoidal waveform modulant signals are represented. These are the ideal voltage on phases 1 and 2. The phase shift between the two signals is 120° . The output of f_{m1} is equal to 1 if the phase 1 modulant has a larger amplitude than the one of the carrier and 0 otherwise. It is the same for f_{m2} but comparing the phase 2 modulant to the carrier. The frequency of f_{m1} and f_{m2} pulses is constant. Only the width of the pulse changes. The phase to phase voltage is simply the difference of the cells output voltages. So, the resulting modulated phase to phase voltage between phase 1 and 2 is obtained by subtracting the f_{m1} and f_{m2} signals.

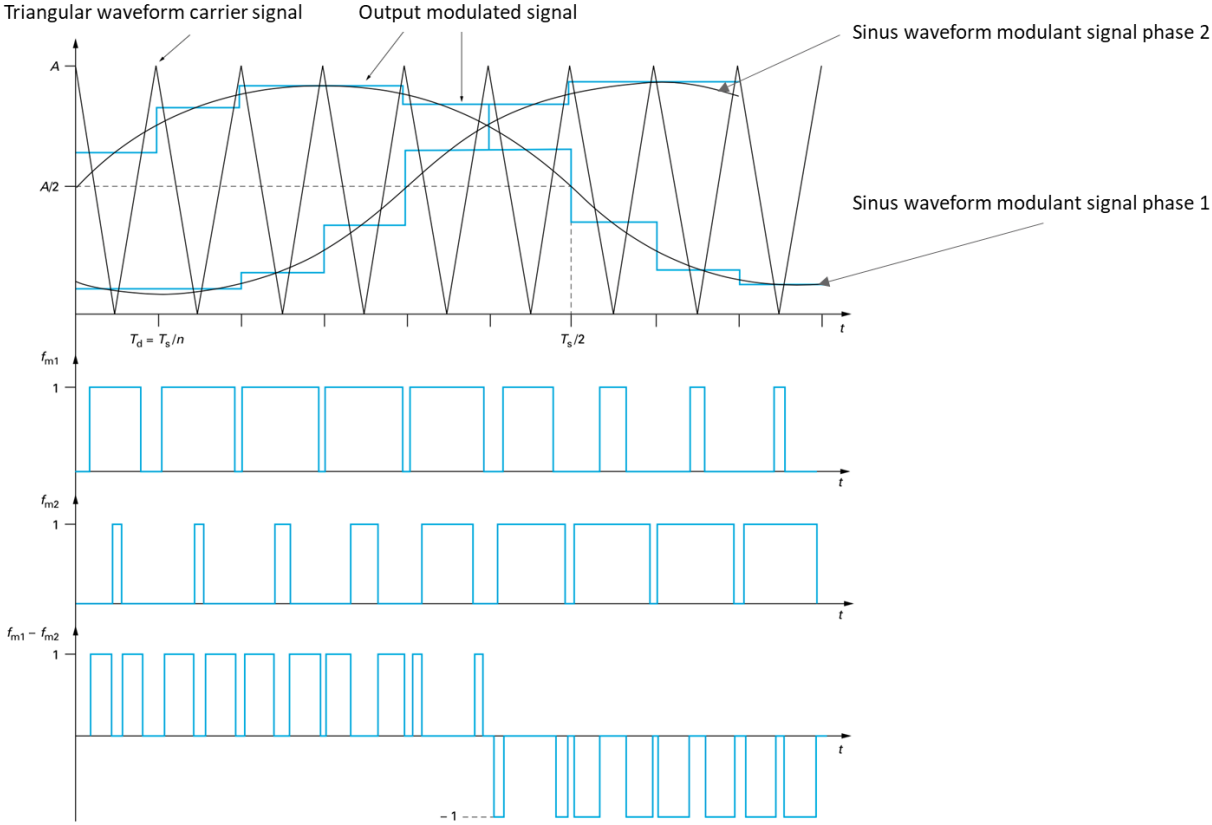


Figure 33: Example of three-phase sinusoidal PWM based from [54]

6.2 POWER FEEDING CABLE

The power cable connects the inverter to the motor. It has an impact on the overshoot that happen at the motor terminals. This cable is generally modelled using a transmission line harness [53],[55].

Figure 34 illustrates the single conductor transmission line model. It corresponds to a phase-to-ground connection. It is a repetition of infinitesimal elements. The number of elements to used depend on the line length and the frequency of the output inverter signal.

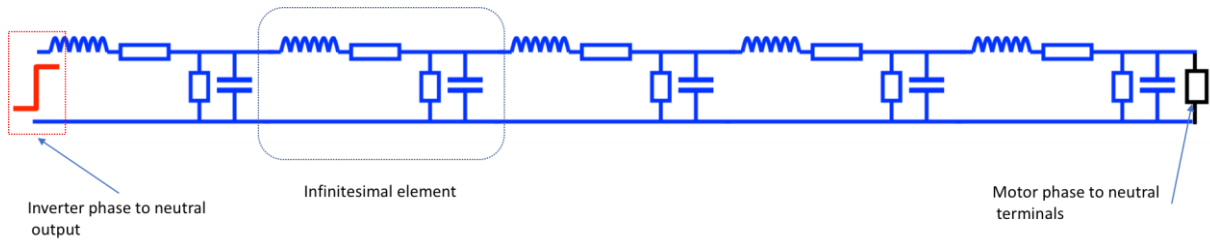


Figure 34: Transmission line phase to neutral model

Figure 35 details the constitutive elements of an infinitesimal line element. The line behaves as a global inductive behaviour modelled with a per-unit-length inductance ($L \cdot dx$). Joule's losses are modelled by a per-unit-length resistance ($R \cdot dx$) in serial with the per-unit-length inductance. The capacitive coupling between the line and the ground is modelled connecting a per-unit-length capacitor ($C \cdot dx$). The dielectric losses in the insulation of the line are modelled with a per-unit-length resistance ($G \cdot dx$) in parallel with the line capacitor.

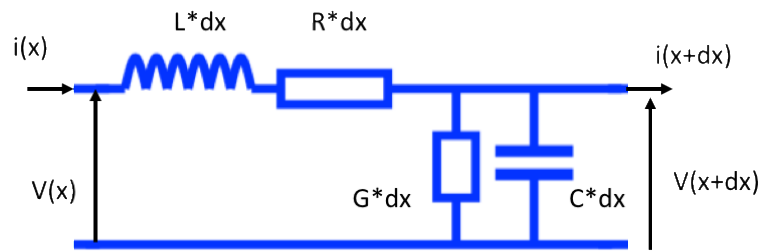


Figure 35: Transmission line elementary cell

Let us designate by Z_c , Z_m and Z_i the impedances of respectively the power cable, the motor and the inverter. As these three impedances are different, there are reflexions of the input voltage waveform in the cable. At each time step, the voltage at a point along the cable is the sum of the reflected voltage waveforms toward the inverter and toward the motor. The reflexion of the voltage waveform toward the inverter output is characterized by the reflexion coefficient Γ_{ri} :

$$\Gamma_{ri} = \frac{Z_i - Z_c}{Z_i + Z_c} \tag{Eq 1}$$

The reflexion of the voltage waveform toward the motor is similarly characterized by the reflexion coefficient Γ_{rm} :

$$\Gamma_{rm} = \frac{Z_m - Z_c}{Z_m + Z_c} \tag{Eq 2}$$

The impedance of the cable Z_c is function of its dimensions. It can be computed from both its per-unit-length inductance L (H/m) and per-unit-length capacity C (F/m):

$$Z_c = \sqrt{\frac{L}{C}} \tag{Eq 3}$$

The voltage at the motor terminals is submitted to damped oscillations. The first oscillation has the biggest amplitude. Figure 36 adapted from [56] presents the phase-to-ground and first stator coil maximum voltage amplitudes. It can be seen in this example that the overshoot can reach 1.5 the DC voltage bus for a cable of 25m.

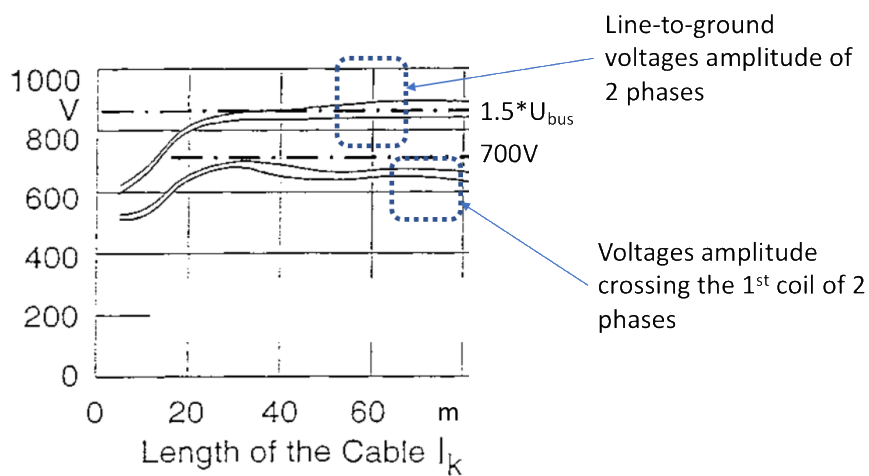


Figure 36: Maximum motor terminal voltage during PWM inverter operation depending on the cable length. Pulse frequency 9kHz, $U_{bus}=560V$, 4kW induction motor, rise time $t_r=100ns$. Adapted from [56]

The authors in [57] has proposed an improved model for computing the phase-to-phase voltage overshoots at a motor terminals. An equivalent two phase model of the electromechanical chain (inverter+cable+motor) is considered (Figure 37), where j is the complex operator and w is the angular frequency. The model is composed of classic RLCG($j\omega$) elements and a propagation function $\gamma_c(jw)$.

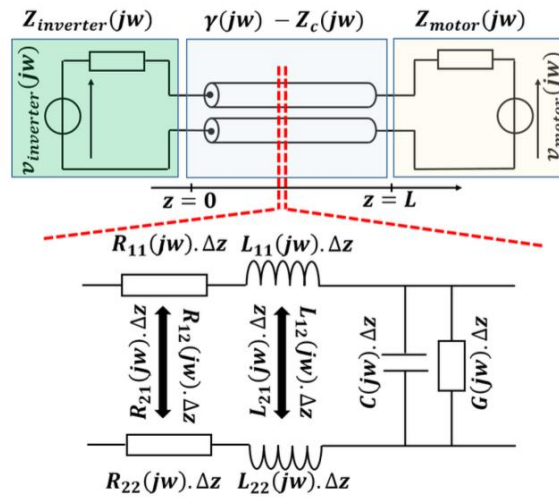


Figure 37: Proposed equivalent two-phase model of an electromechanical chain [57]

Figure 38 presents the computed phase-to-phase motor terminals overshoots as a function of the cable length. Different transistor gate resistance (R_g) values were used. This resistance modulates the output rising time. The biggest the R_g value, the slowest the rising time. It can be seen that the phase-to-phase voltage overshoot increases considerably for cable length higher than 2 m. For the biggest R_g values, it happens for length superior to 3 m. Besides, compared to Figure 36, the phase-to-phase high overshoots occur for cable length much shorter than in the case of phase-to-ground or coil-to-ground overshoot. For phase-to-phase, one can consider a critical cable length of 2 m whereas for phase-to-ground and coil-to-ground the critical cable length is about 20 m.

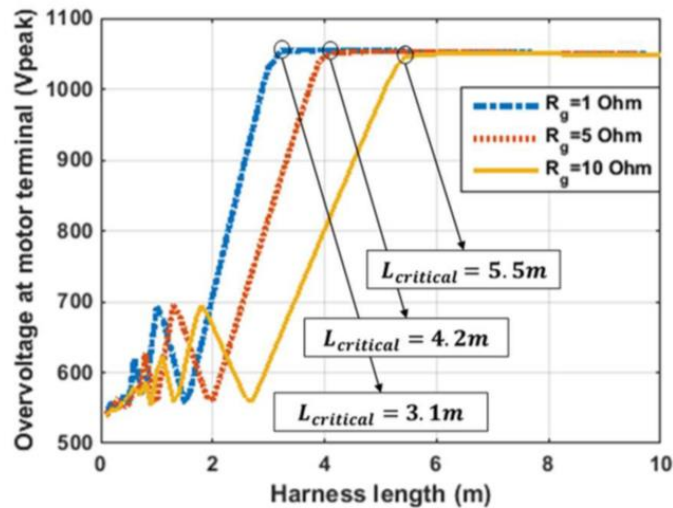


Figure 38: Maximal overvoltage at motor terminals for different harness lengths, obtained by simulation using trapezoidal inverter waveforms [57]

6.3 FREQUENCY INCREASE

New semi-conductive components based on SiC and GaN technologies permit power electronics to switch higher levels of voltage in shorter time than classic silicon components [58]. Besides, SiC components have a bigger energy gap. That means that at a fixed temperature, an electron in a SiC components will need more energy to cross the gap than in a silicon component. Therefore, SiC technology enables to work at higher temperature [59].

The rise of inverters switching frequencies lead to faster rising time on the machine terminals. It is the time interval in which the voltage amplitude goes from 10% to 90% of the peak voltage. Figure 39 illustrates an incoming voltage front wave at motor terminals fed by a PWM inverter.

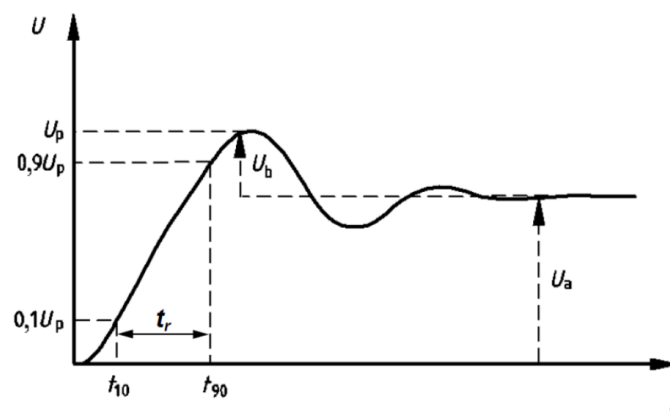


Figure 39: Voltage front wave at a machine terminal fed with PWM inverter [35]

The author in [60] has investigated the impact of the voltage front coming from an inverter over the overshoot at the stator winding. A 41 turns coil has been powered by a pulse generator with rising times of 10 ns and 85 ns. The results are displayed in Figure 40. It can be seen that for the front of 10 ns the overshoot is 1.73 times the DC bus voltage. However, there is barely no overshoot for a slower rising time of 85 ns.

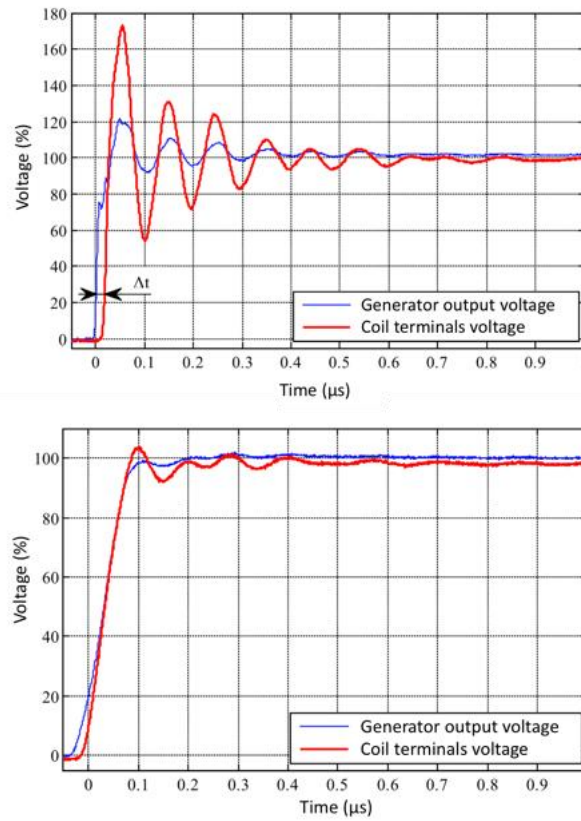


Figure 40: Voltage at a 41 turns coil terminals; top) rising time 10ns; below) rising time 85ns [60]

An evaluation of the overvoltage at the motor terminals as a function of both rising time and cable length is proposed in EIC Standard (60034-18-41). On Figure 41, the overvoltage factor defined by the ratio of the phase-to-phase peak voltage over the pulse voltage is given versus cable length and rising time. The results obtained by [57] on Figure 38 are coherent with the EIC Standard evaluation.

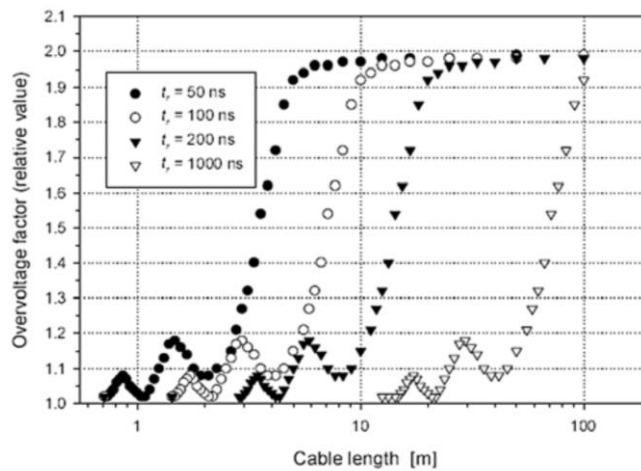


Figure 41: Overvoltage ratio in function of cable length and rising time proposed in EIC Standard (60034-18-41)

However, it is no more the case when considering fast switching frequency of a SiC inverter. A complex ringing phenomena may happen for cable length lower than 3 m [61]. This ringing phenomena is attenuated with the increase in the power cable length. Figure 42 illustrates the overvoltage at the motor terminals powered with a silicium based inverter (dashed blue lines) versus a SiC inverter (red line).

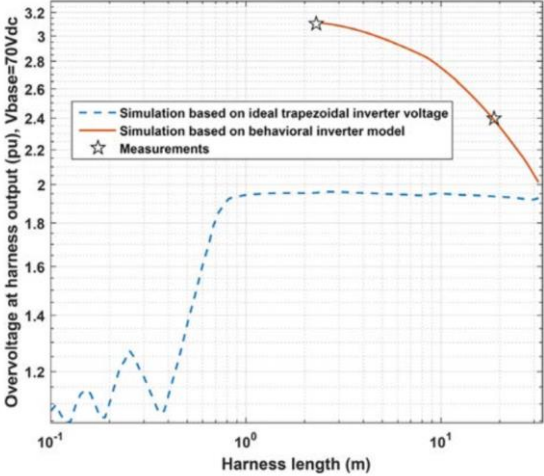


Figure 42: Overvoltage ratio as a function of both cable length and rising time (dashed blue curve: $tr=50ns$, red curve: $tr=8ns$) [61]

6.4 VOLTAGE DISTRIBUTION

Figure 43 presents the voltage waveforms measured between 5 coils constituting one phase. A step voltage amplitude E has been used. The coil number one is the first to receive the incoming voltage front. The first coil receives a much bigger overshoot (top). After the transient regime the voltage is uniformly distributed between the coils (below). However, during transient, the voltage between the coils can be of the same magnitude than the step voltage.

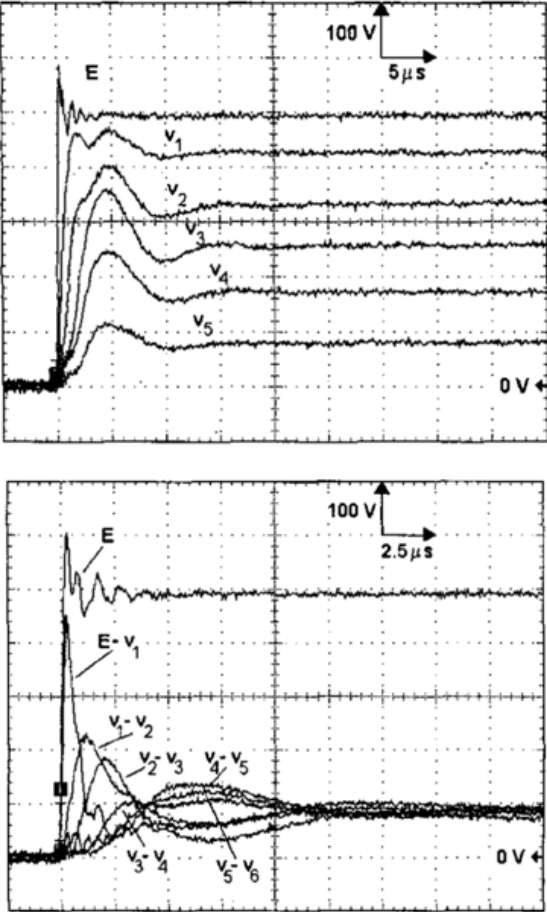


Figure 43: Overvoltage measured in a stator coils. Top) voltage distribution; Below) voltage between coils turns [62]

The voltage crossing the first coil as a function of the incoming front rising time has been investigated by [56]. It is expressed as a percentage of the phase-to-neutral motor terminal voltage. Figure 44 shows that for rising time lower than 50 ns, the first coil is susceptible to get more than 70% of the maximum phase-to-neutral motor voltage.

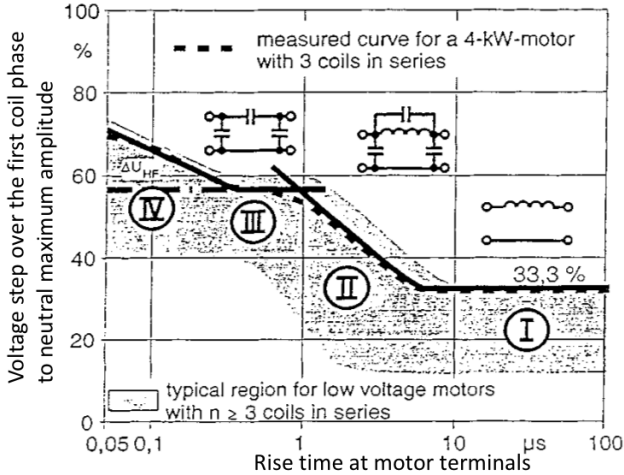


Figure 44: Percentage of the voltage across the first coil as a function of the rise time [56]

Works have been done to evaluate the non linear voltage repartition within the winding. The author in [60] modelled a coil by using a RLC circuit model. The parameters have been determined either by experimental measurements or 2D-finite elements computation. Figure 45 compares the results obtained with the RLC circuit and the experimental measurements. A 41 turns coil is considered. It is powered by a 300V DC bus voltage. The top figure shows the response of the coil terminals to a voltage front. The bottom picture represents the maximal turn to turn voltage drop obtained between turns 4 and 9. The RLC model provides a good evaluation of the first peak.

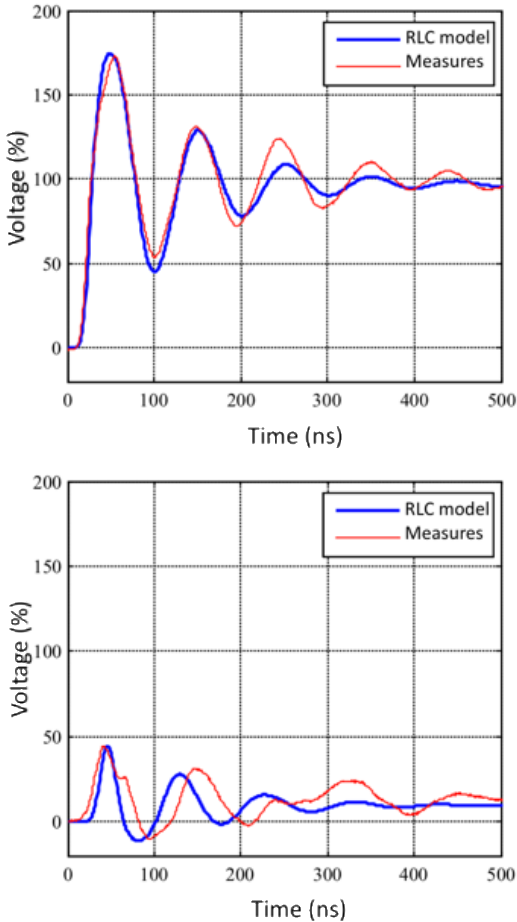


Figure 45: top) voltage at a 41 turns coil; below) voltage drop between turns 4 and 9 (% of 300V DC bus voltage) [60]

Both motor terminal overshoots and non linear voltage distribution within stator winding in transient regimes are the main cause of partial discharges (PD) appearance. In the next chapter, the behaviour of PD will be investigated. It aims to a better understanding of the phenomenon in order to evaluate PD on stator winding of inverter fed motors.

This chapter has presented the implication and challenges for more electric aircrafts. It has introduced the serial hybrid architecture under study for the HASTECS project. The insulation of the stator of an electric machine has been detailed. The impact of power converter switching frequency and of the power harness length on the voltage distribution in the winding has been pointed out. The next chapter presents the partial discharges and how they are affected by the components of the powertrain.

Chapter 2: Physics of Partial Discharges (PD)

This chapter is dedicated to Partial Discharges (PD). It will start with the definition of a PD and the explanation of the mechanism which ignites it. Then, the experimental techniques to detect and measure PD activity will be presented. The effect of aeronautical environment on PD will be then considered. Finally, the principle of common numerical models to evaluate PD will be introduced.

1 DIFFERENT KINDS OF DISCHARGES

There are different ways to classify electric discharges. For instance in [63] the discharges were classified depending on their nature. The nature of the discharge varies depending on the voltage and current characteristics.

Another way to sort discharges is to classify them by the location where they take place. In [64] the discharges are sorted in four main categories: inner discharges, surface discharges, corona discharges and treeings. Treeings take place during ageing, so that this kind of discharge will not be considered in our study. Figure 46 illustrates the three kinds of discharges that may take place in machines during a PDIV measurement.

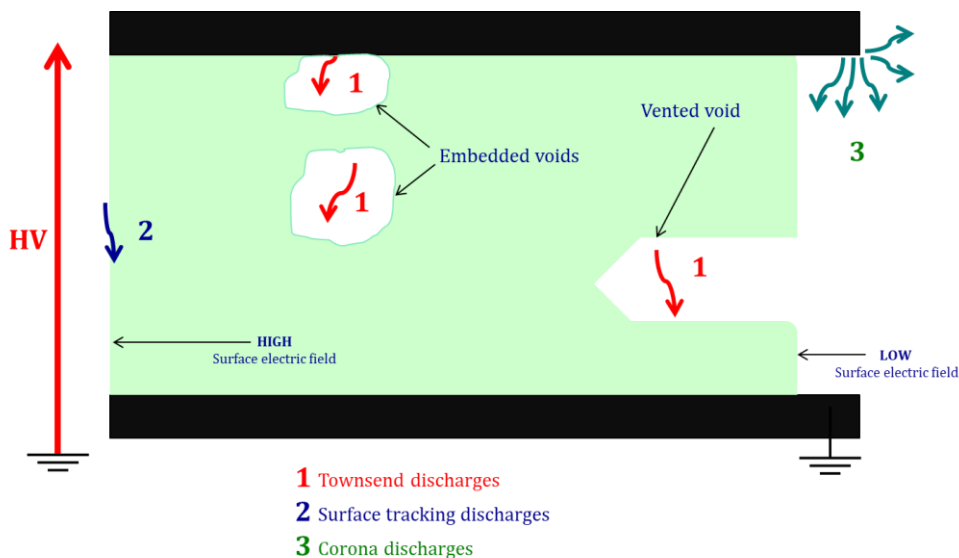


Figure 46: Different kinds of discharges depending on their location: 1) Townsend discharges in both embedded and vented voids, 2) surface tracking discharges, 3) corona discharges

In this paragraph the discharges sorted in the way of [64] are developed.

1.1 DISCHARGES IN NON-VENTED CAVITIES

These discharges happen inside the insulation material. It is due to the presence of defects in the insulator (Figure 47). These defects can be introduced during the manufacturing process (air bubbles) or during the polymer aging (delamination).. Additional defects may be introduced during the winding operation mainly because of mechanical stress. Besides, at working conditions, there can be displacement of insulating materials due to both vibration and thermal cyclings. Air gaps are then introduced between insulators and metallic parts of the EIS. As these gaps are not vented (they are embedded inside the EIS), PD are not sensitive to the environmental working conditions (temperature, humidity, dust, fluids, ...).

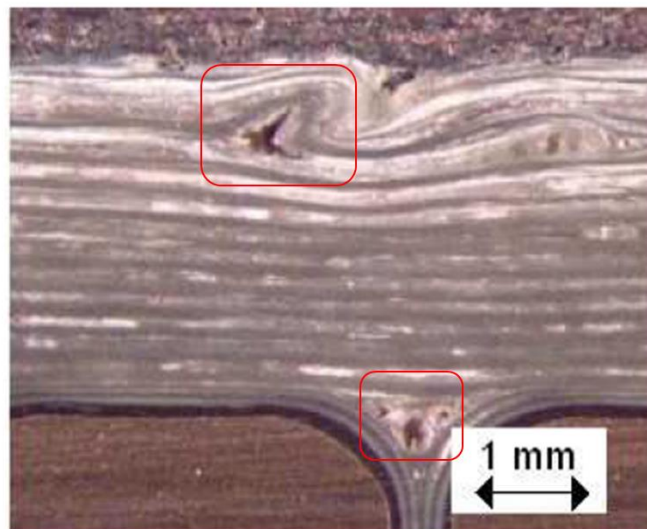


Figure 47: Mica insulation showing various defects (red rectangles) – adapted from [65]

The PD activity causes the insulator structure damage by ions bombardments, heat, physico-chemical attacks, UV and other radiations effects. With the repetition of PD, electrical trees can grow inside the polymer (Figure 48). At term, some branches go through the whole insulator thickness, leading to its electric breakdown.

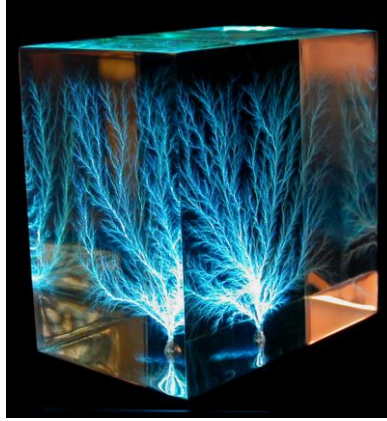


Figure 48: 3D electrical treeing in a block of clear acrylic [66]

In the presence of humidity inside a hydrophilic insulator, so called water treeing are ignited at much lower electric field amplitude. The author in [67] reported an amplitude around 10 kV/mm for water treeing and around 100 kV/mm for normal treeing.

1.2 DISCHARGES IN VENTED CAVITIES

Most of electric motors are not hermetic. That means that the air is free to circulate all over the stator winding and that it is submitted to the external air. The authors in [68] investigate the impact of air flow on a two-dimensional array of integrated coaxial micro-hollow coplanar DBD in air at atmospheric pressure. It is shown that the discharge is considerably impacted by the air flow as presented on Figure 49, as this air flow modifies the physics on the insulator surface.

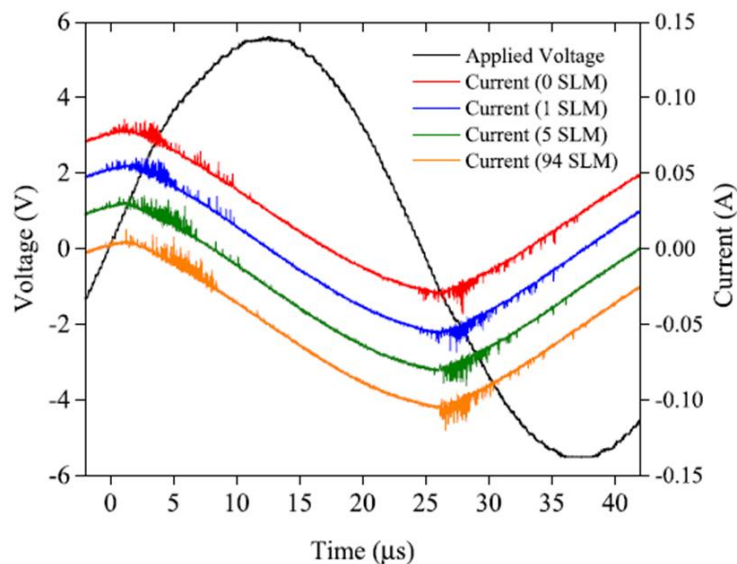


Figure 49: Typical current and voltage waveforms of the 2D-micro-discharges in air. The peak-to-peak applied voltage is identical for all the flow rates [68]

In [69] the impact of pressure on the stator winding PDIV was investigated. Figure 50 indicates a decrease of PDIV when the pressure decreases.

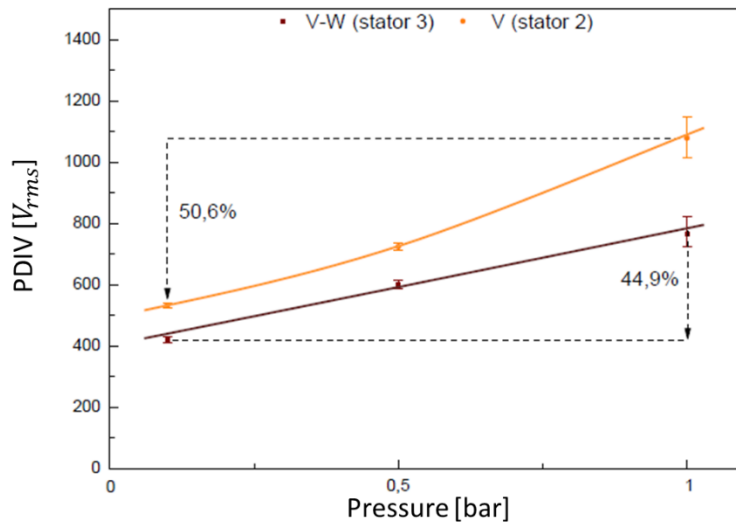


Figure 50: PDIV as a function of pressure (temperature 25°C, relative humidity 50%) - 2 stators are tested [69]

In our research project, an open motor will be considered. So the impact of environmental conditions on PDIV have to be taken into account. These are detailed further.

1.3 DISCHARGES ON THE SURFACE

These kind of discharges occur when a high tangential electric field appear at the insulator surface (surface tracking PD type). If contaminants, moisture,... are present on the insulator surface, discharges can be triggered with lower electric field. This phenomenon may be increased when it takes place at a triple point (in an area where air, polymer and metal are present). The partial surface discharges propagate on the insulator surface and cause damage on it (Figure 51). When the propagation link two conductors, the discharge switches from a partial to a total one.

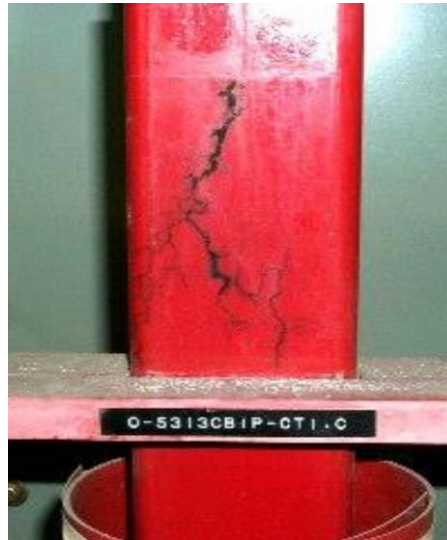


Figure 51: Example of surface tracking discharges effects on an insulator due to contamination/humidity [70]

The end windings of high voltage electric motors are more susceptible to trigger such surface discharges. It is possible to limit such discharges by a suitable design, the choice of insulators having high surface resistivity and by adding a semi-conductive paint on the winding close to the stator slot edge [71]. This additional overcoat will gradually decrease the electric field.

1.4 CORONA DISCHARGE

This kind of discharges takes place in strongly non uniform electric field zone. These are needle-plane or cylinder wire–plane configuration. The electric field is very high in a small region directly surrounded the needle, the wire, the busbar, the junction... and remains weak in the rest of the domain. The size of the electrodes has to be very small compare to the gap between electrodes. They represent a great deal on high voltage power line design (Figure 52).

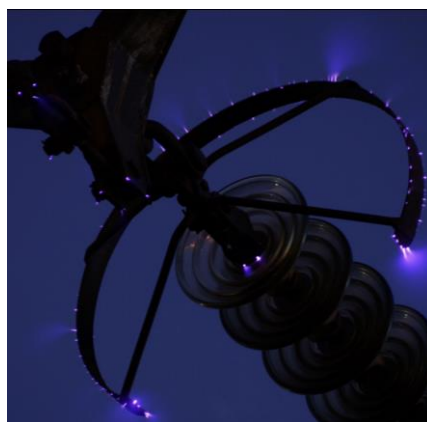


Figure 52: Corona discharge on an insulator string of a 500 kV overhead power line [72]

1.5 PD CONSEQUENCES ON STATOR INSULATION

Three types of solid insulator dielectric breakdown due to high electric field can be distinguished. These can combine each other:

- Electromechanical breakdown: an electrostatic pressure is applied by the conductors on the insulators. This leads to a decrease of the slot insulation thickness or a creation of cracks in it. This phenomenon can lead to an irreversible electromechanical rupture of the material. Moreover, initial cracks existing in the insulator (defects) may lead to a filamentary electromechanical breakdown.

- Thermal breakdown: it occurs when the material conductivity increases due to a high current density. That causes additional losses and therefore heating by Joule's effect. Thermal runaway can then cause a dielectric breakdown, call thermal breakdown. As for electromechanical breakdown, filamentary thermal breakdown may take place in insulators.

- Electronic breakdown: a sufficiently high electric field may cause different breakdown mechanisms, each initiated by electrons: electronic avalanche, field effect emission, free volume effect. These phenomena all lead to the breakdown by generating a large amount of electrons that transform the insulator in a conductor.

PD activity is responsible of premature failure. A PD generates erosion (by ions bombardment), heat but also ozone. Ozone rapidly attack polymers and reduce its lifetime [73]. This PD activity slowly degrade the insulators and at term can lead to a complete failure of the motor.

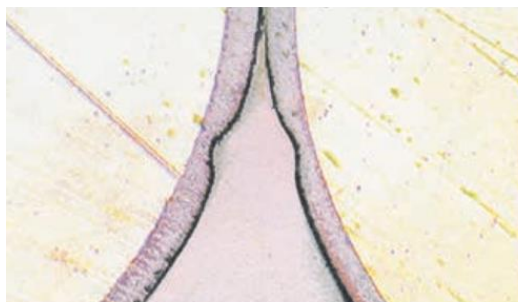


Figure 53: Consequences of PD on a stator winding insulation; left) Corroded enamel layer [40]; right) Slot liner flashover [74]

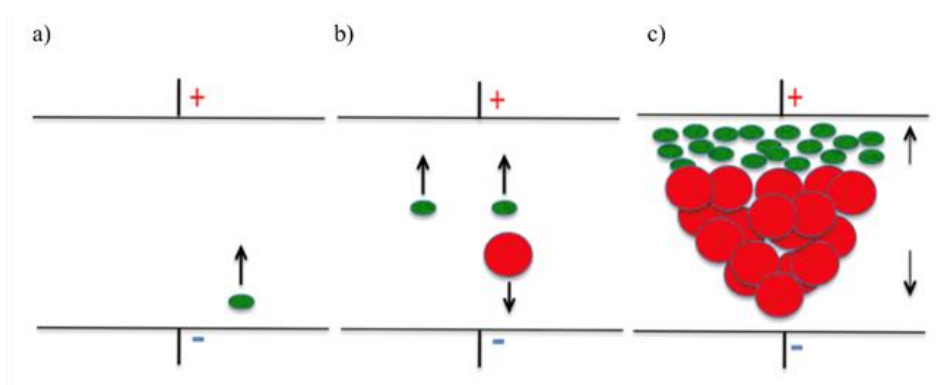
2 PHYSICS OF PLASMA

Townsend type PD happen in cavities (embedded bubble, delamination) inside the polymer or in the surrounding air submitted to a high electric field (vented voids). If the field intensity exceeds a critical value, the air is ionized. Negatively and positively charged particles are then present in such proportion that the air remains electrically neutral. The air is in an another physical state: it is a so called plasma.

The evaluation of the PD activity is extremely dependent on the formation of this plasma. In this paragraph, the predominant mechanism, supposed to take place in our motors EIS, will be presented.

2.1 TOWNSEND MECHANISM

It describes the ionization of a gas between two metallic plane electrodes. It was established by John Townsend in 1901, following the empirical discovery by Friedrich Paschen in 1889 [75]. The electric breakdown of the gas results from an electronic avalanche (Figure 54). It requires that an initial free electron is present in the gas gap (the germ electron). This electron is submitted to an uniform electric field produced by the voltage applied to the electrodes. The electron is accelerated by this electric field. During its motion in the gas gap, impacts occur with gas neutral particles. Additional electrons are then pulled from the impacted particles. The neutral particles then turn to positive ions. If the electric field is strong enough, there is an electronic flow toward the positive electrode and a positive ionic flow toward the negative electrode. An electric current is established in the gas gap. This leads consequently to the gas electric breakdown.



Electronic avalanche process: a) electron acceleration, b) ionization collision, c) electronic avalanche

Figure 54: Electronic avalanche mechanism; green circles are electrons, red circles are positive ions [76]

Two coefficients mainly impact on the described mechanism, as described below.

2.1.1 First Townsend's coefficient

The first Townsend's coefficient is commonly designated as α . It represents the quantity dn of electrons generated by n electrons moving along a distance dx during the avalanche process (4). The solution of Eq 4 is of the form given by Eq 5.

$$dn = \alpha \cdot n \cdot dx \tag{Eq 4}$$

$$n = n_0 \cdot \exp(\alpha \cdot x) \tag{Eq 5}$$

With n_0 being the initial number of electrons at $x = 0$.

The α coefficient describes the formation of additional electrons by the collision of a single initial electron with the other particles in the gas. It is mainly dependent from the chemical composition of the gas and the energy of the incoming electron. Different outputs may result from a collision. In some cases, an additional electron is generated but in others it is simply absorbed by the impacted particle. Table 10 summarizes some reactions which happen in the plasma between gas particles (A and B) and colliding electrons (e^-).

Process	Reactions
Ionization by electronic collision	$e^- + A \rightarrow 2e^- + A^+$
Excitation by electronic collision	$e^- + A \rightarrow e^- + A^*$
Radiative recombination	$e^- + A^+ \rightarrow A + h\nu$
Three corpses recombination	$e^- + A^+ + B \rightarrow B + A^*$
Detachment by electronic collision	$e^- + A^- \rightarrow 2e^- + A$
Three corpses attachment	$e^- + A + B \rightarrow B^- + A$
Dissociative ionization	$e^- + AB \rightarrow 2e^- + A + B^+$
Dissociation by electronic collision	$e^- + AB \rightarrow e^- + A + B$

Table 10: Main collision reactions in a plasma. Adapted from [76] [75]; * symbol designates an excited state of the particle, $h\nu$ indicates light emission

Collisions are characterised by the notion of effective cross-section. Let us consider an electron moving at the speed v toward N particles contained in an elementary volume of gas designated by the product $\sigma \cdot dx$. The particles are moving at a speed much slower than the electron one (v). Let's define v_r as the relative speed of the electron compared to the particles speed. Thus, the surface σ is dependent of the relative speed v_r and the species in interaction [77]. The surface σ is the so called effective cross-section.

Figure 55 illustrates the concept of effective cross-section.

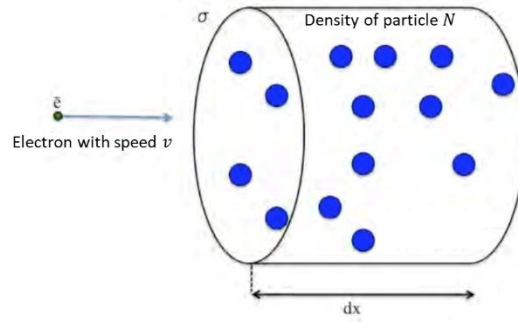


Figure 55: Effective cross-section.

The number of collision n_c is defined as:

$$n_c = N \cdot \sigma \cdot dx \quad \text{Eq 6}$$

The density N of the gas can be derived from the perfect gas law:

$$p = N \cdot k \cdot T \quad \text{Eq 7}$$

With p the gas pressure, k the Boltzmann's constant and T the gas temperature.

The electron mean free path λ is a notion derived from the number of collision n_c and the travelled length in the plasma dx :

$$\lambda = \frac{dx}{n_c} = \frac{1}{N \cdot \sigma} \quad \text{Eq 8}$$

Let us consider one electron ($n = 1$) travelling over the distance dx and doing one single collision ($n_c = 1$) which generates one electron ($dn = 1$). Combining Eq 4, Eq 6 and Eq 8 one gets:

$$\alpha = \frac{1}{\lambda} \quad \text{Eq 9}$$

The diminution of the number of free paths dn_λ travelled through a unit of length dx due to n_c collisions is expressed by Eq 10. The solution is given by Eq 11.

$$dn_\lambda = -n_\lambda \cdot n_c = -n_\lambda \cdot N \cdot \sigma \cdot dx \quad \text{Eq 10}$$

$$dn_\lambda = -\frac{1}{\lambda} \cdot n_\lambda \cdot dx$$

$$n_{\lambda} = n_{\lambda,0} \cdot \exp\left(\frac{-x}{\lambda}\right) \quad \text{Eq 11}$$

With $n_{\lambda,0}$ the total number of free path.

Let us consider that an electron which ionizes an atom starts with a zero speed in the direction of the electric field between two collisions. The electron then transfers all its kinetic energy to the impacted atom. The probability of ionizing the atom is taken as 1 as long as the electron kinetic energy is equal or above the atom ionizing energy. This is written as:

$$e \cdot E \cdot \lambda_i \geq e \cdot V_i \quad \text{Eq 12}$$

$$E \cdot \lambda_i \geq V_i$$

With e the electron's charge, E the electric field amplitude, λ_i the electron minimal free path, eV_i is the atom ionizing energy.

The probability for an electron free path being superior to the minimal free path λ_i is expressed as the variation of the number of free paths, which length is at least of λ_i , over dx compared to the total number of free paths $n_{\lambda,0}$. Combining Eq 10 and Eq 11 one gets:

$$\frac{n_{\lambda}(\lambda_i) - n_{\lambda}(\lambda_i + dx)}{n_{\lambda,0}} = -\frac{dn_{\lambda}(\lambda_i)}{n_{\lambda,0}} = \frac{1}{\lambda} \cdot \exp\left(\frac{-\lambda_i}{\lambda}\right) \cdot dx \quad \text{Eq 13}$$

By definition, this probability also represents the number of electrons generated by electronic avalanche per unit of length which is in fact the α coefficient itself. So Eq 13 can be written as:

$$\alpha = \frac{1}{\lambda} \cdot \exp\left(\frac{-\lambda_i}{\lambda}\right) \quad \text{Eq 14}$$

Combining Eq 8 and Eq 7, it has been demonstrated that the mean free path λ is proportional to the ratio T/p with T the plasma temperature and p the pressure. One can now get to the well-known formula:

$$\frac{\alpha}{p} = A \cdot \exp\left(\frac{-B \cdot p}{E}\right) \quad \text{Eq 15}$$

With:

$$\frac{1}{\lambda} = A(T) \cdot p$$

$$B = A(T) \cdot V_i$$

The authors in [78] gives the value of A and B, at normal temperature and pressure conditions, for different gases. The results are presented on Table 11:

Gas	A [Torr ⁻¹ .cm ⁻¹]	B [V.Torr ⁻¹ .cm ⁻¹]	Validity domain of E/p [V.Torr ⁻¹ .cm ⁻¹]
H ₂	5	130	150-600
N ₂	12	342	100-600
CO ₂	20	466	500-1000
Air	15	365	100-800
H ₂ O	13	290	150-1000
HCL	25	380	200-1000
He	3	34	20-150
Ne	4	100	100-400
Ar	14	180	100-600
Kr	7	240	100-1000
Xe	26	350	200-800
Hg	20	370	200-600

Table 11: A and B constants values for different gases [78]

2.1.2 Second coefficient

The second coefficient is commonly designated with γ . It characterises the emission of secondary electrons in the gap due to ions impacting the cathode (Figure 54.c). However, not all the electrons being ejected from the cathode will participate to the electronic avalanche. Some will be absorbed by atoms, others may be recaptured by the cathode and others may leave the gap [79].

In the Townsend's mechanism, the γ coefficient represents the part of electrons which are ejected from the cathode and which participate to the electronic avalanche over the number of ions bombing the cathode. For a metallic plane electrode in air, a common value found in the literature for this coefficient is $\gamma = 0.01$ [78] [55] [44]. The value of this coefficient strongly depend on the gas composition and the electrode geometry and chemical composition [80].

Let us consider an air gap of length d . Initially, only one electron is present in the gap ($n_0 = 1$). The total number of electrons present in the gap due to electronic avalanche is given by Eq 5. So, the number of electrons generated by electronic avalanche initialized by the one present electron is:

$$e^{\alpha \cdot d} - 1 \tag{Eq 16}$$

It is also the number of generated positive ions.

The Townsend’s mechanism considers the electronic avalanche to be self-maintained. The ions bombing the cathode have to eject at least one electron which will ignite another avalanche. This condition is expressed as:

$$\gamma \cdot (e^{\alpha \cdot d} - 1) = 1 \tag{Eq 17}$$

$$\alpha \cdot d = \ln\left(\frac{1}{\gamma} + 1\right)$$

2.2 PASCHEN’S LAW

In 1889, Friedrich Paschen investigated the breakdown of air located between two metallic plane electrodes [81]. The authors in [82] represented the Paschen’s curve in different gazes based on multiple data sources. The Paschen’s curve in air at normal temperature and humidity conditions is shown in Figure 56.

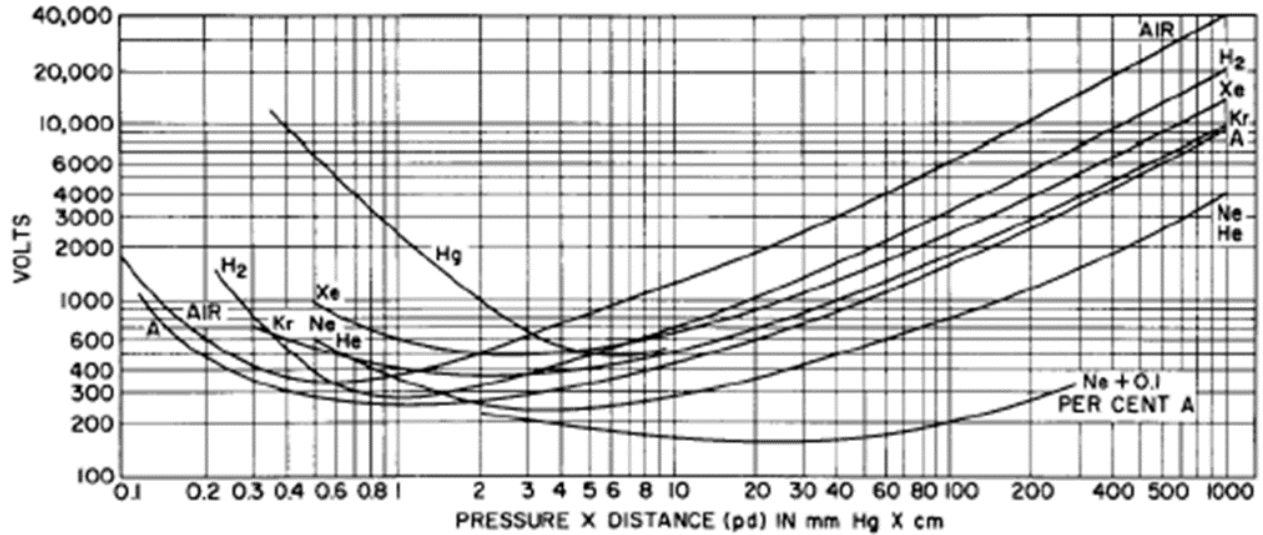


Figure 56: Paschen’s curve for various gases [83]

The abscissa axis corresponds to the product of the air pressure p times the gap length d . It is expressed in *torr.mm* in Figure 56. The ordinate axis indicates the voltage level (peak value, not rms value) at which the electric breakdown of the air gap due to a self-maintained electronic avalanche occurs. At such voltage level, the equation Eq 17 is verified.

The Paschen’s curves can be plot using the following equation:

$$V = \frac{B * p * d}{C + \ln(p * d)} \quad \text{Eq 18}$$

With:

$$C = \ln\left(\frac{A}{\ln\left(1 + \frac{1}{\gamma}\right)}\right)$$

The Paschen's curve is displayed in logarithmic scale. It presents a minimum voltage of about 306 V_{peak} for a product $pd=0.01\text{bar}\cdot\text{mm}$. The presence of this minimum can be explained by simply considering a fixed d gap length and keeping in mind that the electronic avalanche breakdown is the only mechanism represented by this curve. On the left of the minimum, the pressure p decreases. That means that the density of atoms decreases too. The less atoms in the gap, the more important the probability for an electron to cross the gap without impacting any atom. Thus, it is more difficult to get an electronic avalanche and consequently the breakdown voltage increases. On the right of the minimum, the pressure p increases and so does the density of atoms. The number of collisions increases but the energy of the electron between two collisions decreases. A higher energy is required for an electron to travel through the gap without being absorbed. So the breakdown voltage increases.

At air pressure of 1 bar the minimum is obtained for an air gap of 8 μm width. This correspond to the order of magnitude of big air bubbles trapped in the secondary insulation (impregnation resin) [31], [55].

2.3 IMPACT OF AERONAUTICS CONDITIONS

The aeronautics conditions impact on PD appearance have been studied in [1] and [11]. Thus, the results and figures displayed in the following paragraph are mainly extracted from these works.

2.3.1 Environmental variations

The Pashen's curve has originally been computed under normal condition of temperature and humidity [81] [82]. This means a temperature of 20 °C and an absolute humidity of 11 g/m³.

In the aeronautical context, the environmental conditions may change, especially for equipment located in non-pressurized areas of the fuselage, the wings, the landing gears and the nacelles. The ground temperature amplitude can go from – 40 °C (polar climate) up to + 50 °C (arid desert climate). During the aircraft climb, the temperature is considered to decrease of 2 °C per 300 m. At 15 000 m (about 49 000 ft) the external temperature is about - 60°C. However, the calculated temperature within

the winding in the HASTECS motors will be around 180 °C (result of motor Joule’s heating and cooling system). The DO160 standard provides test procedures to characterise an equipment for a given mission profile. Figure 57 illustrates the kind of considered temperature variations.

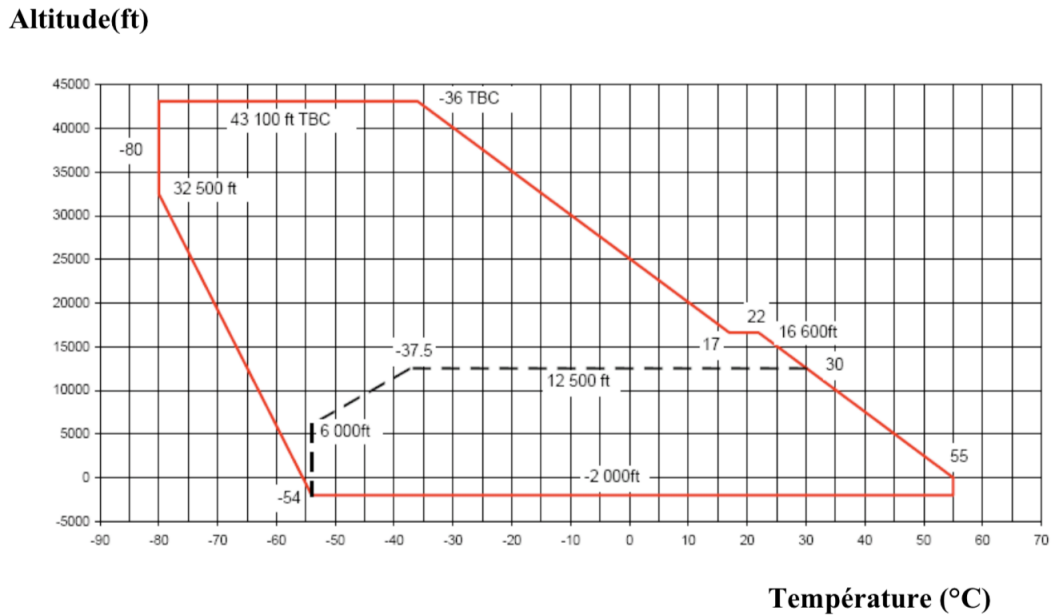


Figure 57: Temperature variation in aeronautic environment – DO160 [85]

Figure 58 displays the humidity variation as a function of the altitude. Multiple mission types are considered; Polar Mission (PM), Tropical Mission (TM), Allowable Maximum Hot Day (AMHD), Structural Maximum Hot Day (SMHD), Standard Day (SD). The humidity is defined by the ratio r of water quantity over dry air quantity. This ratio r is expressed in $[g/kg]$. The data were provided by Airbus.

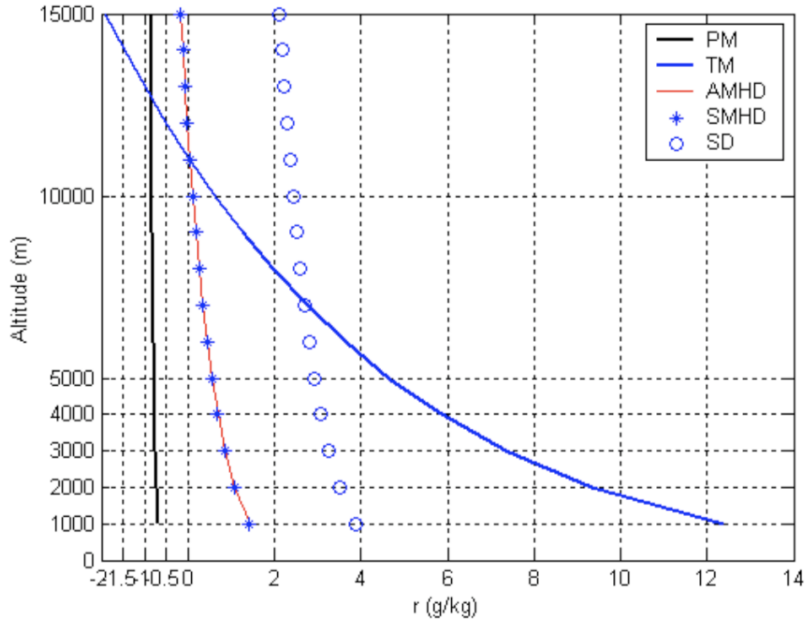


Figure 58: Humidity profile in altitude [76] [84]

For a tropical mission (TM), the humidity level changes significantly as a function of the altitude. For the other missions, the humidity can be considered as constant whatever the altitude.

2.3.2 Impact of temperature

Two main corrections are used to consider the impact of the temperature in dry air on the original Paschen's curves. These are the Peek's [86] and Dunbar's [87] corrections.

The Peek's correction introduces a factor δ . It is an image of the air density. The breakdown voltage level V for a considered temperature T and pressure p is deduced from the breakdown voltage V_0 at standard temperature $T_0= 293 K$ and pressure $p_0= 760 Torr$

$$V(p, T, H_{r0}) = \delta * V(p_0, T_0, H_{r0}) \quad \text{Eq 19}$$

$$\delta = \frac{293}{T[K]} * \frac{p[Torr]}{760}$$

With H_{r0} : the standard humidity rate 11 g/m³. Temperatures are expressed in K and pressures in Torr.

The Peek's correction moves the original Paschen's curve along the ordinate axis (Figure 59).

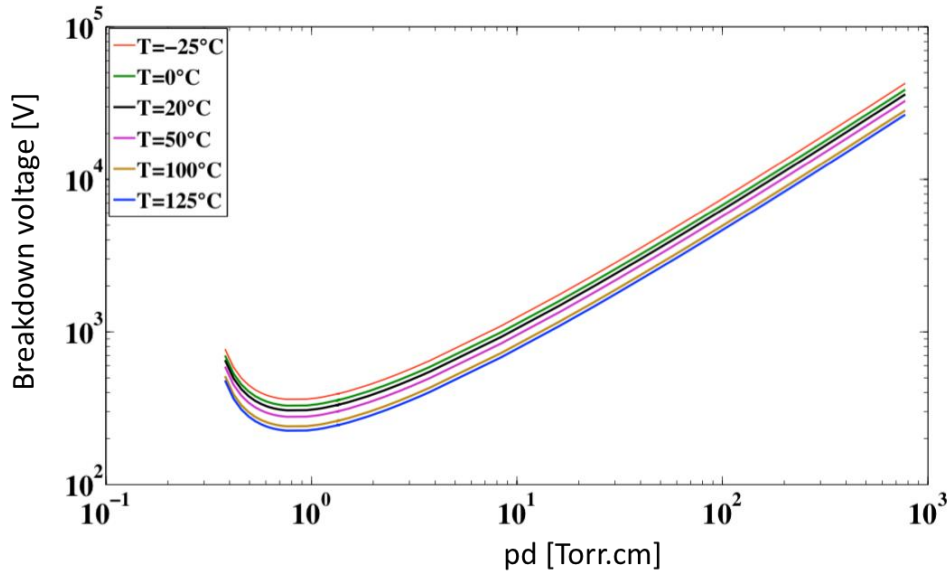


Figure 59: Corrected Paschen's curves computed with Peek's correction [76]

The higher the temperature, the lower the breakdown voltage. The temperature is an image of the particles energy. An electron in a 125 °C air gap is more energetic than one in a - 25 °C air gap. Due to that initial amount of energy, such electron requires less energy to ignite an electronic avalanche mechanism. Thus, a lower electric field is required in the air gap (i.e.: a lower voltage drop).

On the other hand, the correction proposed by Dunbar [87] is derived from the perfect gas law Eq 7. For a constant volume of air gap, the pressure is proportional to the temperature. It is then possible to extract an equivalent pressure p_{eq} in the air gap due to the temperature T starting from initial conditions (p_0, T_0) .

$$p_{eq} = p_0 * \frac{273 + T[^\circ C]}{273 + T_0[^\circ C]} \quad \text{Eq 20}$$

Where the temperatures are expressed in [°C].

The Dunbar's correction thus moves the original Paschen's curve along the abscissa axis because the impact of temperature is taken into account by defining the resulting equivalent pressure p_{eq} . It is displayed on Figure 60:

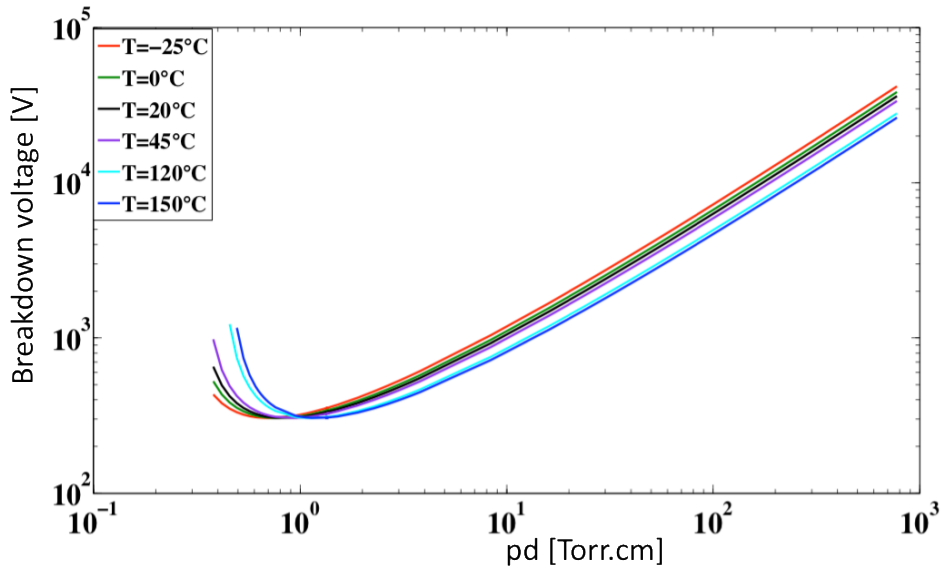


Figure 60: Corrected Paschen's curves computed with Dunbar's correction [76]

At higher temperature the curves are shifted to the right because it results in higher equivalent pressure in the air gap.

In her PhD work, Sili [76] identified the domain of validity of both Peek's and Dunbar's corrections. Peek's correction is validated for pressure or distance variations at temperatures lower than 25 °C. Dunbar's correction is validated for variations of distance at atmospheric pressure at temperatures upper than 25 °C. However, if both the temperature and pressure varies, Dunbar correction is no more validated. A new empirical formulation for breakdown voltage computation has then been proposed. This formulation is validated for temperatures upper than 35 °C.

Table 12 recaps the different corrections in temperatures and give their domains of validity.

Experimental conditions	Domain of validity	Correction
<ul style="list-style-type: none"> • p=760Torr • d varies or <ul style="list-style-type: none"> • p varies • d= 1 mm 	T<25°C	Peek: $V(p, T, H_{r0}) = \delta * V(p_0, T_0, H_{r0})$ $\delta = \frac{293}{T[K]} * \frac{p[Torr]}{760}$
<ul style="list-style-type: none"> • p=760Torr • d varies 	T>25°C	Dunbar: $p_{eq} = p_0 * \frac{273 + T[°C]}{273 + T_0[°C]}$

<ul style="list-style-type: none"> • p varies • d=1mm 	<p>T>35°C</p>	<p>Sili:</p> $V_T = \frac{V_{Paschen,mod}}{K_T}$ <p>With</p> <ul style="list-style-type: none"> ➤ $V_{Paschen,mod} = \begin{cases} \frac{B \cdot p \cdot d}{C + \ln(p \cdot d)} & \text{for } p \cdot d > p \cdot d_{min} \\ 306V & \text{for } p \cdot d < p \cdot d_{min} \end{cases}$ ➤ $K_T = a \cdot \delta^b$ ➤ $\begin{cases} a = 0.0226 \cdot T(K) - 6.13 \\ b = 0.0027 \cdot T(K) - 0.74 \end{cases}$
---	------------------	--

Table 12: Temperature corrections of the Paschen's curve

2.3.3 Impact of humidity

Figure 61 displays the evolution of the breakdown voltage of air as a function of the relative humidity [84]. Three temperatures have been considered: 10 °C, 20 °C and 30 °C.

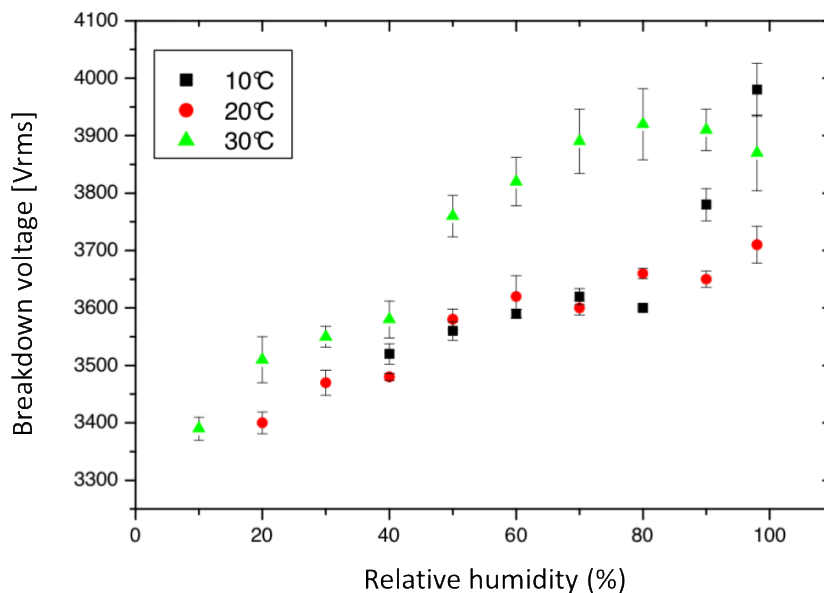


Figure 61: Impact of relative humidity versus air breakdown voltage for different temperatures [84]

Globally, an increase in humidity leads to an increase in breakdown voltage. Water molecules in the gap produce a screen effect. Thus, more energy is required for the electrons to ionize the particles.

One can also notice that, in presence of humidity, the breakdown voltage increases with the temperature. This observation is in opposition with the conclusions in dry air presented in the previous paragraph. This can be explained by other mechanisms which are now introduced by the presence of humidity and which dynamic may be dependant on the temperature [88].

A correction can be found in the literature to take into account the humidity alone in the Paschen's theory [89]:

$$V_h = V_{NCTP} * (1 + \frac{K_h}{100} * (h - h_{NCTP})) \tag{Eq 21}$$

With:

- V_h is the corrected breakdown voltage for an absolute humidity h compared to the standard absolute humidity $h_{NCTP} = 11 \text{ g/m}^3$.
- V_{NCTP} is the breakdown voltage under normal condition of temperature and pressure given by the IEC Publication 60 (1970).

The K_h coefficient is linked to the humidity. For a gap smaller than 1 m, IEC suggests that it does not depend on the gap length:

$$K_h = (1 + \frac{h - h_{NCTP}}{100}) \tag{Eq 22}$$

Table 13 gives the correspondence between some absolute humidity and the corresponding relative humidity at a fixed temperature (from Mollier's diagram):

Relative humidity %	Absolute humidity [g/m^3]
20%	4
40%	8.29
52.5%	11
60%	12.56
80%	16.7
90%	18

Table 13: Correspondence between absolute humidity and relative humidity at 25°C

Figure 62 displays the corrected breakdown voltages for absolute humidity of 4 g/m^3 , 11 g/m^3 and 18 g/m^3 [44].

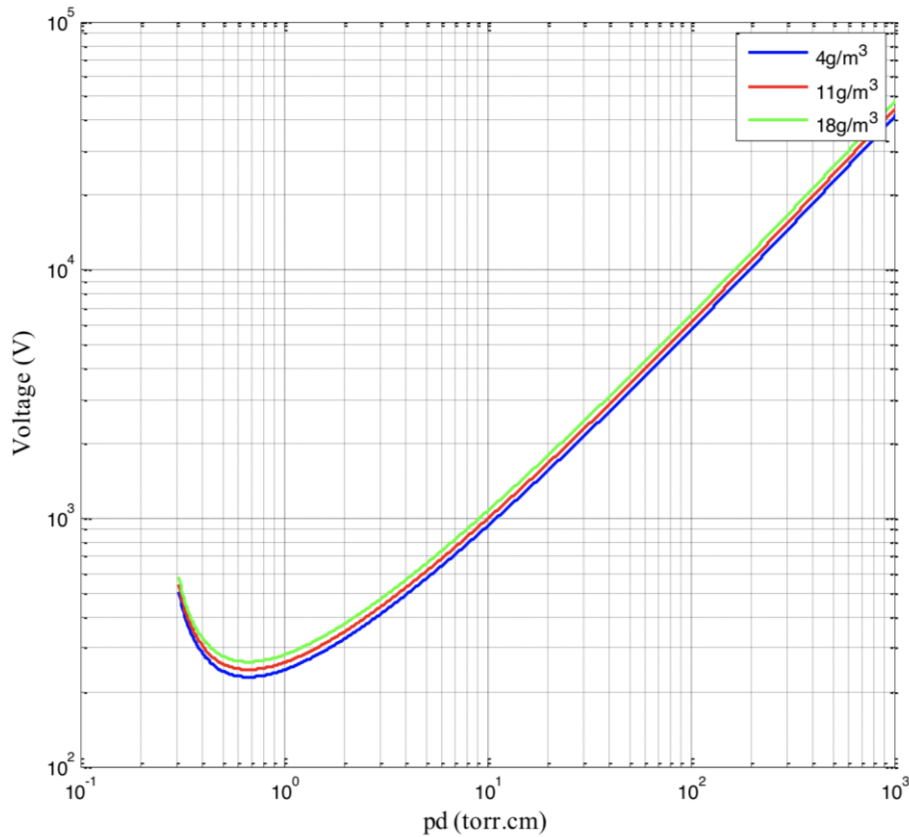


Figure 62: Corrected Paschen's curve versus absolute humidity values at atmospheric pressure and room temperature [44]

In the case of a closed motor (pressurized or not) the air may be considered as dry.

3 PD ANALYSIS

3.1 EXPERIMENTAL DETECTION OF PD ACTIVITY

Partial discharges (PD) consist in repetitive current pulses. These generate electromagnetic interferences, audible noise, light emission, chemical species (from gas breakdown), pressure waves, heat and dielectric losses [42]. PD detection methods consist in measuring variations of one or more of these quantities. They can be divided into two main categories: the indirect and direct methods. In an indirect method, the sensor is located outside the circuit where the sample/device is. In a direct method, the sample and the sensor are located in the same electric circuit.

In this paragraph, two main indirect commonly used PD detection methods will be introduced: radio-frequency detection and optical detection. Common electric direct detections will then be detailed.

3.1.1 Radio-frequency detection

It consists in capturing the electromagnetic PD induced interference by using an antenna. The signal can be visualised by connecting an oscilloscope. The main difficulty consists in separating the PD wave signature from surrounding electromagnetic interferences. Consequently, some devices use complex algorithms to recognize real partial discharges signatures [90]. This method cannot be used in electromagnetically polluted area.

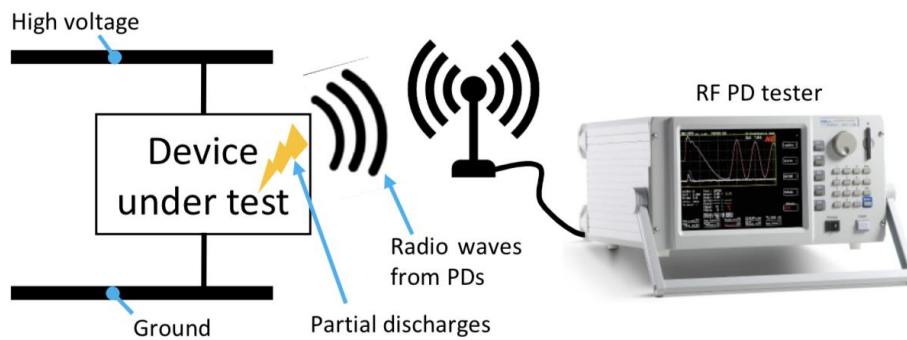


Figure 63: Setup for PD radio-frequency detection [91]

3.1.2 Optical detection

It is possible to detect PD occurring on the surface or in gas thanks to its induced light emission. It is measured using a photomultiplier tube using a photon-counting technique [42]. It results in a frequency distribution graph whose amplitude correspond to the total number of photon count per second collected by the optical sensor. The main advantage of this technique is that it is not perturbed by surrounding electromagnetic interferences. Its main disadvantage is that it cannot detect PD in embedded areas where no light may be detected from outside.

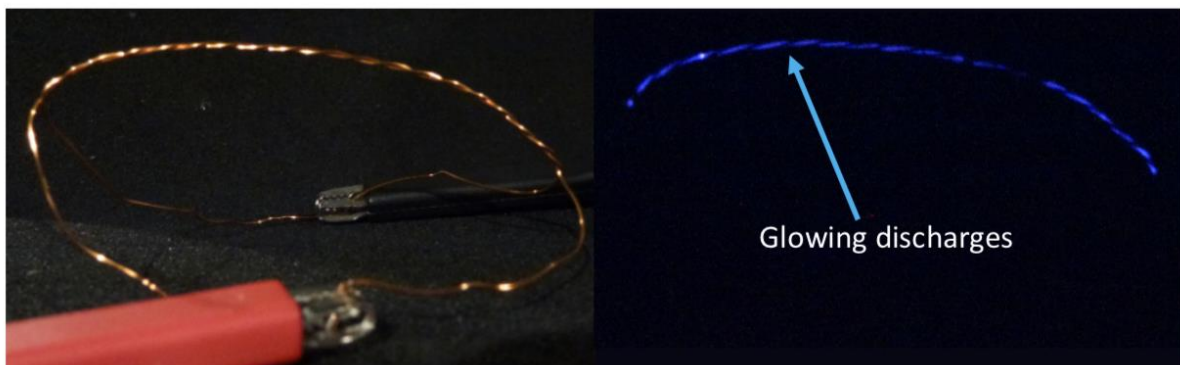


Figure 64: PD light emission (on the right) on a twisted pair made with two enamelled wires sample [91]

3.1.3 Power factor/capacitance tip-up test

This test is commonly used to determine the quality of a coil or a bar ground insulation. It uses the fact that the power factor (also called dissipation factor) or the capacity of such insulation will change with applied AC voltage if defects (voids, delaminations) exist. Indeed, when applying high voltage, PD will take place in these defects leading to an increase in the dissipation factor (PD induce losses) and a decrease in the capacity (PD short-circuit the defects). The difference between low and high voltage values gives an indication of how void-free that insulation is.

In high voltage machines, two measurements are performed at 25% and 100% of the rated line-to-ground voltage. For new coils, it is suggested that the power factor tip-up should be $< 0.5\%$ and the capacitance tip-up should be $< 1\%$ for new machines and $< 4\%$ for old generation machines [47].

3.1.4 Used electric detection

The detection is operated with a non-destructive electric measurements under a 50 Hz sine voltage. A high-pass RLC filter is employed, allowing the measurement of high frequency current pulses by considerably reducing the low frequency current signature from the power source.

Figure 65 illustrates the whole setup for a direct electric PD detection. A high voltage transformer (220 V / 20 kV - PD free) is used to applied high voltage to the sample. A low frequency generator (FX 1641A) coupled with a low frequency amplifier deliver the power to the high voltage transformer in order to be fully independent from the power network and its perturbations. The whole detection circuit is located inside a Faraday cage to avoid surrounding electromagnetic perturbations. The coupling capacity C_k associated with the measurement impedance Z_m are used to detect PD. For each PD occurring in the sample or in the air gap surrounding it, image charges at both sample electrodes are modified. As the external circuit (C_k, Z_m) has a very low high frequency impedance, these image charges change leads to a pulse current in the detection circuit. A voltage measurement is performed at the measurement impedance terminals. The acquisition is done on an oscilloscope.

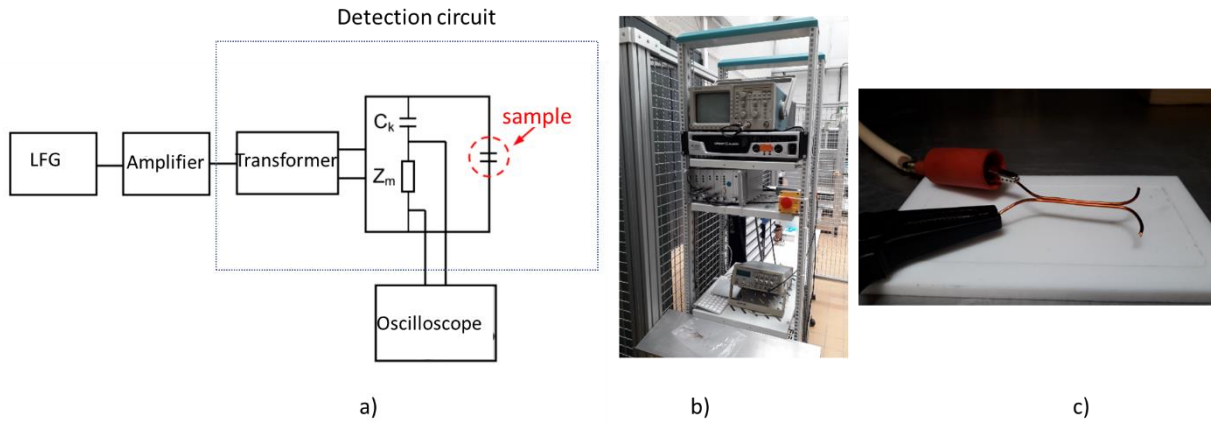


Figure 65: Setup for PD electric detection; a) Schematic of the PD measurement circuit, b) LFG: Low Frequency Generator, amplifier and oscilloscope, c) Sample inside the Faraday cage

3.2 PARAMETERS LINKED TO PD

3.2.1 Partial Discharge Inception Voltage (PDIV)

The PDIV is defined as the lowest voltage value at which PD are ignited and remain maintained. Indeed, during a first PDIV test, surface discharges may occur, corresponding to the ionization of dust, moisture or contaminant on the sample surface. These kind of PD quickly disappear and the corresponding voltage do not have to be considered as the PDIV. IEC standard recommends that the PDIV corresponds to the lowest voltage at which a measured quantity exceeds a predefined threshold. We will not use these definition but the one described before. Figure 66 illustrates a PD pattern obtained at the PDIV.

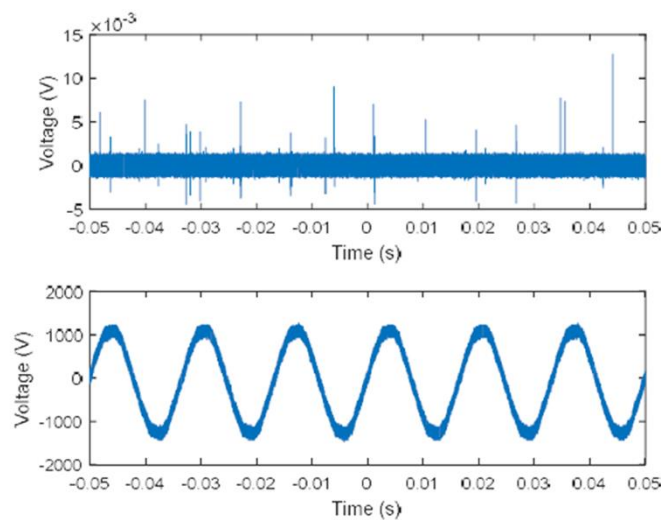


Figure 66: Illustration of PD detection; below) Applied voltage, top) PD signals [92]

3.2.2 Partial Discharge Extinction Voltage (PDEV)

The PDEV is the voltage at which PD disappear when progressively reducing the applied voltage from PDIV. Practically, PD continue to be maintained when the voltage is decreasing from the PDIV up a to a value from which they disappear.

3.2.3 Apparent charge

A PD between electrodes at different voltage results in a release of charges. The charges move in the gap between the electrodes. Such displacement of charges over the thickness of the electrodes induces either a transient voltage pulse at the electrodes terminals or a transient current pulse (this is our case). This phenomenon is attributed to the so called apparent charge. The evaluation of the apparent charge quantity is required for the PD quantification. However, the apparent charge does not correspond to the total charge locally released by the PD. It is affected by the electrodes geometries, the material properties, the measurement circuit impedance.... Thus, the real PD charge cannot be directly measured.

Considering the work in [93], it is possible to get the real charge from the measurable charge. Let us consider two plane parallel electrodes at a voltage V separated by air. A discharge occurs and results in a charge q being present in the gap. Figure 67 illustrates the considered configuration.

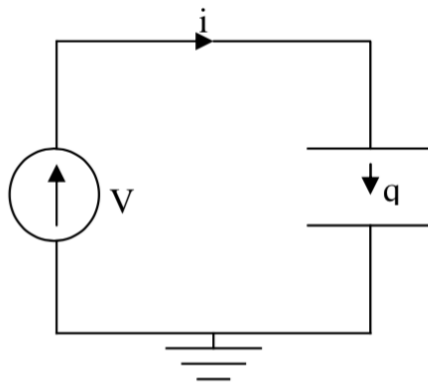


Figure 67: Charge circulation in an air gap between two plane parallel electrodes [84]

When travelling a dx length in the gap, the charge q submitted to the electric field E realise a work W . This work is provided by the power source.

$$W = q * E * dx = i * V * dt \tag{Eq 23}$$

$$\text{With } \begin{cases} E = E * u \\ dx = dx * u \\ \|u\| = 1 \end{cases}$$

Let us consider that a displacement of charge q over a length dx results in a voltage drop ΔV . The apparent charge q_{app} in the circuit is given by (24).

$$q_{app} = \int_0^{\Delta t} i * dt = \frac{q}{V} * \int_0^{\Delta x} E * dx \quad \text{Eq 24}$$

$$q_{app} = q * \frac{\Delta V}{V}$$

The apparent charge is only a part of the charge released by the PD.

3.3 STATISTICAL PROCESSING OF THE RESULTS

PDIV experimental evaluations always present dispersions in the results from one sample to another one. It comes from difference in the manufacturing process, dimensions tolerance and incertitude from the measurement equipment. Dispersion may also be expected when reproducing the same measurement successively on the same sample. This is due to the fact that PD do not exactly take place in the same area from one test to another. Despite the same breakdown mechanism (electronic avalanche), the PDIV values (and thus the breakdown electric field values) will consequently be different and need to be treated by a statistical analysis.

The Weibull's distribution, commonly used to treat dielectric strength data, has been used for the statistical processing of PDIV values. It is also applicable with lifetime data processing. First, the results are distributed into n_i intervals. A probability density $P(E)$ is defined. This function is obtained when the width of the n_i intervals tend to zero and when the number of intervals tend to the infinite. In other words, $P(E)$ is the continuous distribution of the discontinuous data. Figure 68 illustrates an example of data distribution and the associated $P(E)$ function.

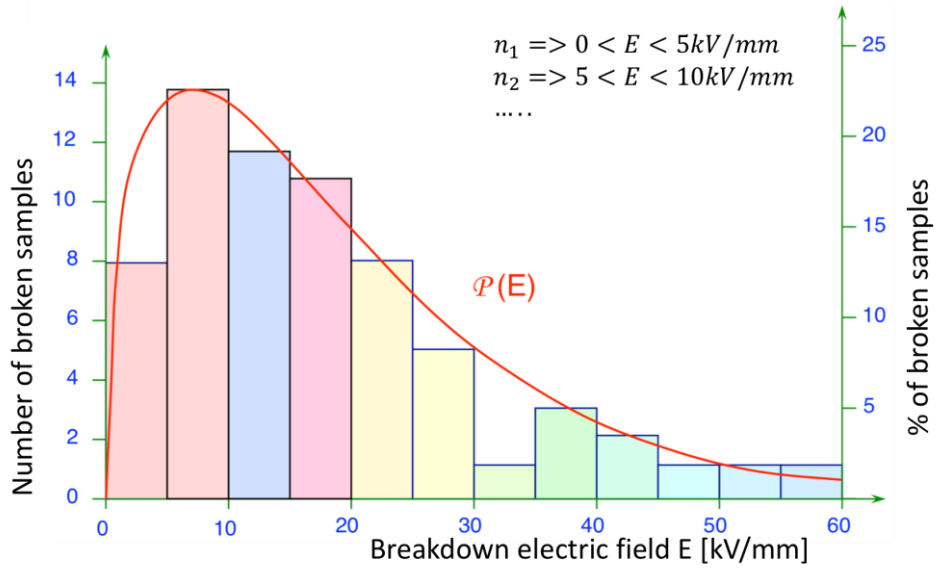


Figure 68: Illustration of PDIV data distribution

The cumulative probability density $P_C(E)$ is computed as follow:

$$P_C(E) = \int_0^E P(E) * dE \tag{Eq 25}$$

Figure 69 illustrates the P_C cumulative probability. It comes from different results than the one presented on Figure 68.

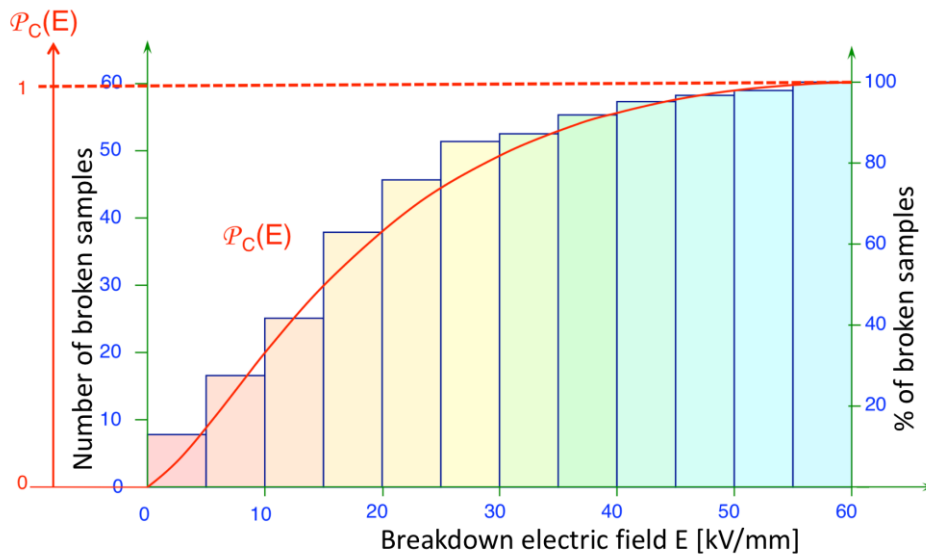


Figure 69: Example of P_C cumulative probability

A good and simple approximation of $P_C(E)$ is recommended by EIC 62539 standard and given by [94]:

$$P_C(i, n) = \frac{i - 0.44}{n + 0.25} \tag{Eq 26}$$

With

- i : breakdown value in ascendant order;
- n : total number of breakdown values.

Experimental PDIV data show that $P_C(E)$ is generally of the form:

$$P_C(E) = 1 - \left(\exp\left(\frac{E}{\alpha}\right)\right)^\beta \tag{Eq 27}$$

With β the shape parameter and α the characteristic breakdown field value such that:

$$P_C(\alpha) = 63.2\% \tag{Eq 28}$$

By manipulating Eq 27 with log operator on can gets:

$$\log\left(\log\left(\frac{1}{1 - P_C(E)}\right)\right) = \beta * \log(E) - \beta * \log(\alpha) \tag{Eq 29}$$

By taking an axis system $\log\left(\log\left(\frac{1}{1 - P_C(E)}\right)\right) = f(\log(E))$ the points can be interpolated with a slope β .

Figure 70 illustrates an example of $P_C(E)$ evolution in the particular axis system defined by Eq 29.

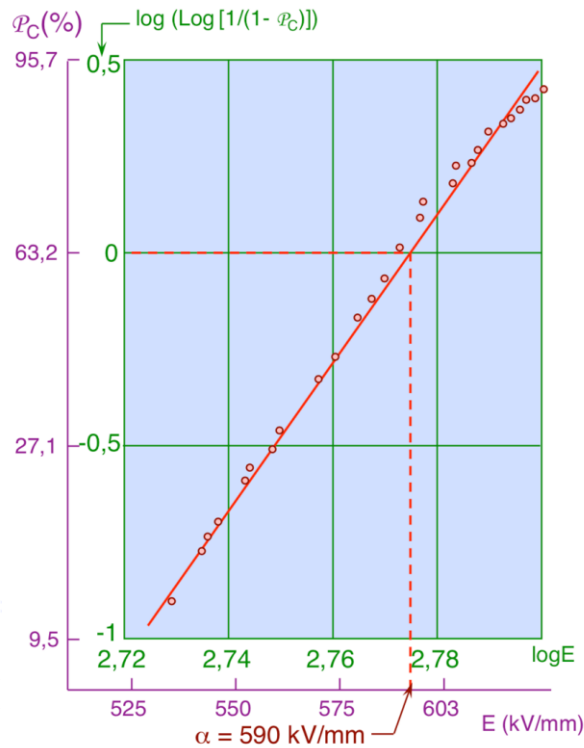


Figure 70: $P_C(E)$ evolution in the axis system defined by (26)

Another way to determine the α and β coefficients is through computation. This approach is based on least square regression and used weighting coefficients given by White in [95]. Let us apply the following change of variable:

$$X_i = \log(-\log(1 - P_C(i))) \quad \text{Eq 30}$$

$$Y_i = \log(E_i)$$

Where the index i refers to sample i .

First, the weighted averages of X_i and Y_i are computed Eq 31 and Eq 32. It is considered that all the samples are used: there is no sample excluded due any sample defect or artefact occurring during the experimental measurements.

$$X_m = \frac{\sum_{i=1}^n w_i * X_i}{\sum_{i=1}^n w_i} \quad \text{Eq 31}$$

$$Y_m = \frac{\sum_{i=1}^n w_i * Y_i}{\sum_{i=1}^n w_i} \quad \text{Eq 32}$$

With w_i the weighted coefficient associated to the broken sample i given by [95]. Samples are sorted in ascendant breakdown values.

The α and β coefficients are finally computed in Eq 33 and Eq 34:

$$\beta = \frac{\sum_{i=1}^n w_i * (X_i - X_m)^2}{\sum_{i=1}^n w_i * (X_i - X_m) * (Y_i - Y_m)} \quad \text{Eq 33}$$

$$\alpha = \exp(Y_m - \frac{X_m}{\beta}) \quad \text{Eq 34}$$

4 DEGRADATION OF THE POLYMER INSULATION IN AERONAUTIC ENVIRONMENT

There are different mechanisms which may impact the time to failure of dielectrics under an electric field [96]. The intrinsic failure of a polymer mainly results from electrical, thermal and mechanical mechanisms, sometimes acting simultaneously. A PD activity does not lead to an instantaneous breakdown of the polymer: the time to failure can goes from seconds to days. It is an extrinsic stress which degrades the polymer insulation progressively up to the final breakdown. The extrinsic time to failure, occurring above the PDIV, is always lower than the intrinsic one. It has been introduced in the

Chapter 2- §1 that some PD take place in cavities inside the polymer. The author in [67] have established a link between thermal and mechanical stresses over the apparition of cavities inside the polymer. This indicates that during its lifetime, PD may occur after ageing in initially healthy samples. This paragraph focuses on electric degradation of polymer in aeronautic environment.

4.1 PRESSURE

The impact of pressure on machine winding PD magnitude has been investigated in [97]. The measurements have been done on twisted pair samples. Figure 71 displays the evolution of the discharge magnitude as a function of the applied voltage at different pressure levels. The temperature value is not given.

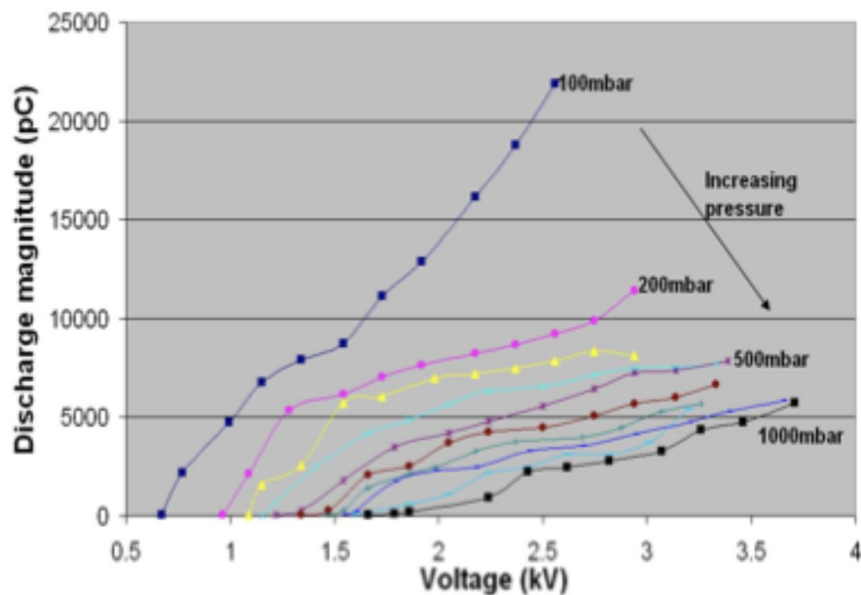


Figure 71: PD magnitudes at different voltage and pressure levels [97]

The discharges magnitude can be interpreted as a stress indicator. The higher the discharge magnitude level, the more stressed the polymer. At fixed voltage and temperature, the discharge magnitude increases when the pressure decreases. Thus, the stress on the polymer increases when the pressure decreases. A faster degradation of the polymer can be expected a low pressure.

4.2 HUMIDITY

Humidity changes the degradation of the polymer into two opposite directions whether considering surface discharges or inner discharges. The authors in [98] have investigated the effect of exposure to ambient relative humidity on the dielectric degradation. Figure 72 displays the evolution of the time to failure as a function of the electric field applied to the dielectric for different relative humidity exposure. The magnitudes are in arbitrary unit (AU).

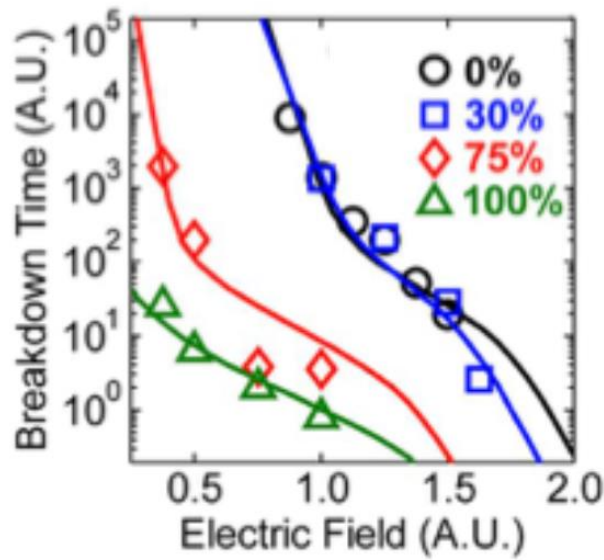


Figure 72: Time to failure as a function of the electric field for different humidity - 60Hz AC voltage [98]

In this experiment, samples have been exposed to different humidity levels for two weeks. The higher the humidity level, the higher the humidity inside the dielectric sample. At a fixed electric field amplitude, the time to failure decreases when the humidity inside the dielectric increases. This can be explained by a failure due to water treeing as presented by [67] and/or by the increase in dielectric losses due to humidity.

In [99] the degradation of polyethylene under corona discharges is studied at different external humidity level. Here, there is no humidity inside the dielectric. Figure 73 displays the obtained results.

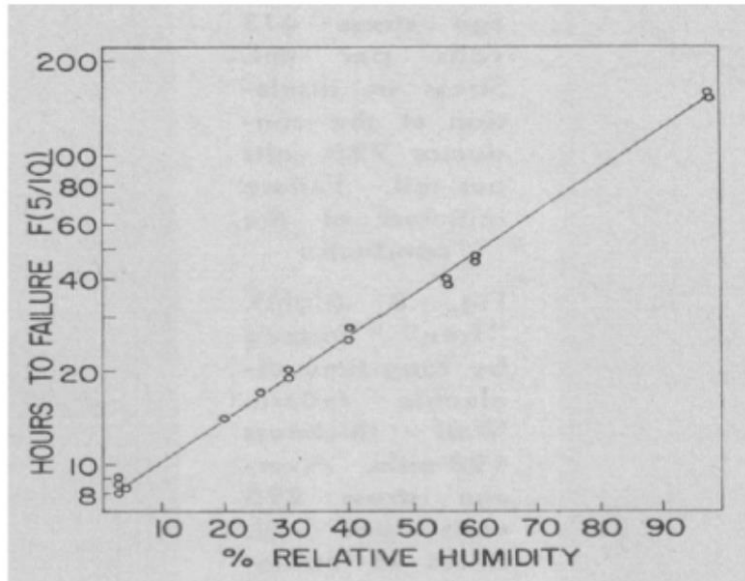


Figure 73: Polyethylene failure time as a function of the external relative humidity under corona discharges ($E=8\text{ kV/mm}$, $f=60\text{ Hz}$) [99]

In the case of corona discharge, the time to failure extends with the augmentation of the humidity. In fact, water particles act as a screen effect which shielded the polymer.

4.3 TEMPERATURE

The impact of temperature over electrical tree development inside a dielectric has been studied in [100]. Figure 74 presents the trees average growth rate in Low Density Polyethylene (LDPE) and branched LDPE (BPEQ) as a function of the applied voltage for temperatures ranging from 20 °C to 50 °C.

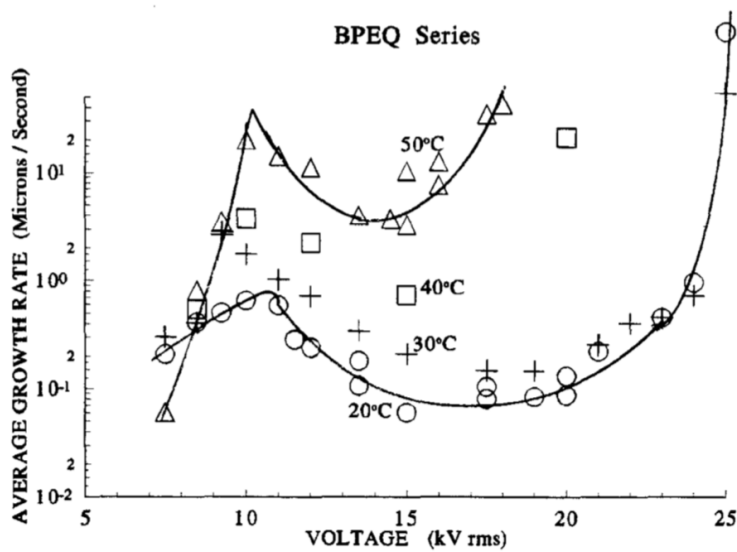


Figure 74: Average tree growth rate as a function of voltage and temperature in LDPE and branched LDPE (BPEQ) [100]

At a fixed voltage, the tree growth accelerates when the temperature increases. This can be explained by an increase of cavities formation inside the dielectric due to the temperature [67]. The time to failure of the dielectric due to tree is thus decreased.

It has been presented Chapter 2 §2.3 that an elevation of temperature reduces the PDIV level (at a fixed pressure). Due to that, PD are ignited at lower voltage and thus for a given voltage, the higher the temperature, the higher the dielectric degradation rate. Figure 75 displays the lifespan evolution of enamelled twisted pairs, showing the strong impact of temperature [101].

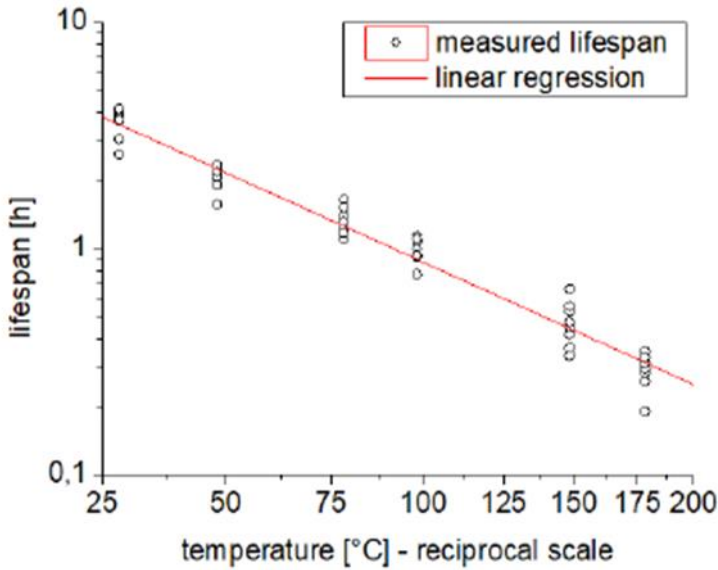


Figure 75: Lifespan of twisted pairs under PD versus temperature; copper diameter: 1.12mm, grade 2, PEI/PAI 200°C corona resistant magnet wire, V=1.75kV, f=10kHz [101]

4.4 FREQUENCY AND VOLTAGE

In Chapter 1 §6, it has been pointed out that power electronics increases the electric stress on the motor EIS, especially when overvoltages appear at the motor terminals. The level of the voltage, as well as the switching frequency of the converter, are stressful parameters [69], [101]. Figure 76 displays two examples of twisted pairs lifespan reduction due to an increase in voltage or frequency.

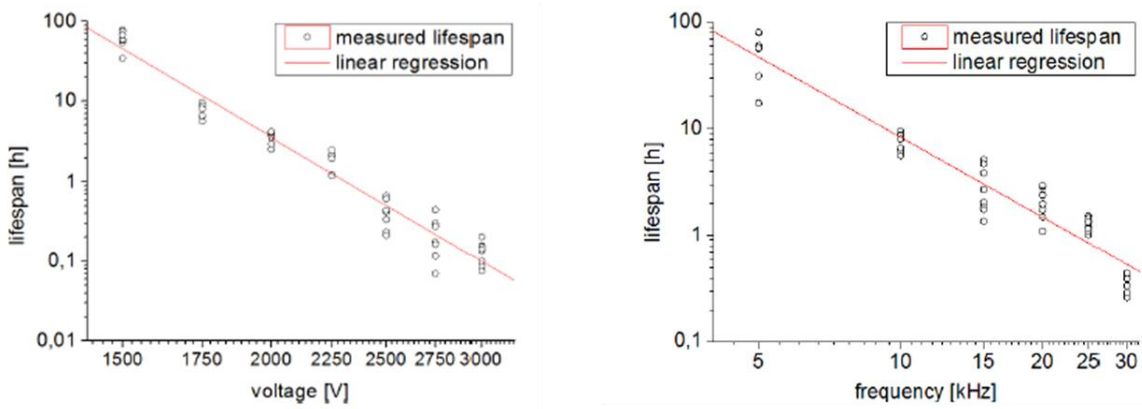


Figure 76: Lifespan of twisted pairs under P. Left) Lifespan versus voltage ($f=10\text{kHz}$, $T=30^\circ\text{C}$), Right) Lifespan versus frequency ($V=1.75\text{kV}$, $T=30^\circ\text{C}$); copper diameter: 1.12mm, grade 2, PEI/PAI 200°C corona resistant magnet wire [101]

Besides, the introduction of wide-band gap materials such as SiC or GaN rises some interrogation on the impact of the dV/dt slope on the dielectric ageing. The impact of all these parameters on the ageing of the electric insulation is investigated in [57], [61], [102].

In [102], two voltage signals were used: a sinusoidal one and a square-wave voltage. The applied voltage amplitudes, frequencies and duty cycles are the same for both signals. Figure 77 displays the main results. As expected, at a fixed frequency, the lifetime decreases when the voltage increases whereas at fixed voltage, the lifetime decreases when the frequency increases. Finally, the slope of the applied voltage seems to have no significant impact on the lifetime as under the same conditions, the measured lifetimes by applying a sine or a square wave voltage are very close together.

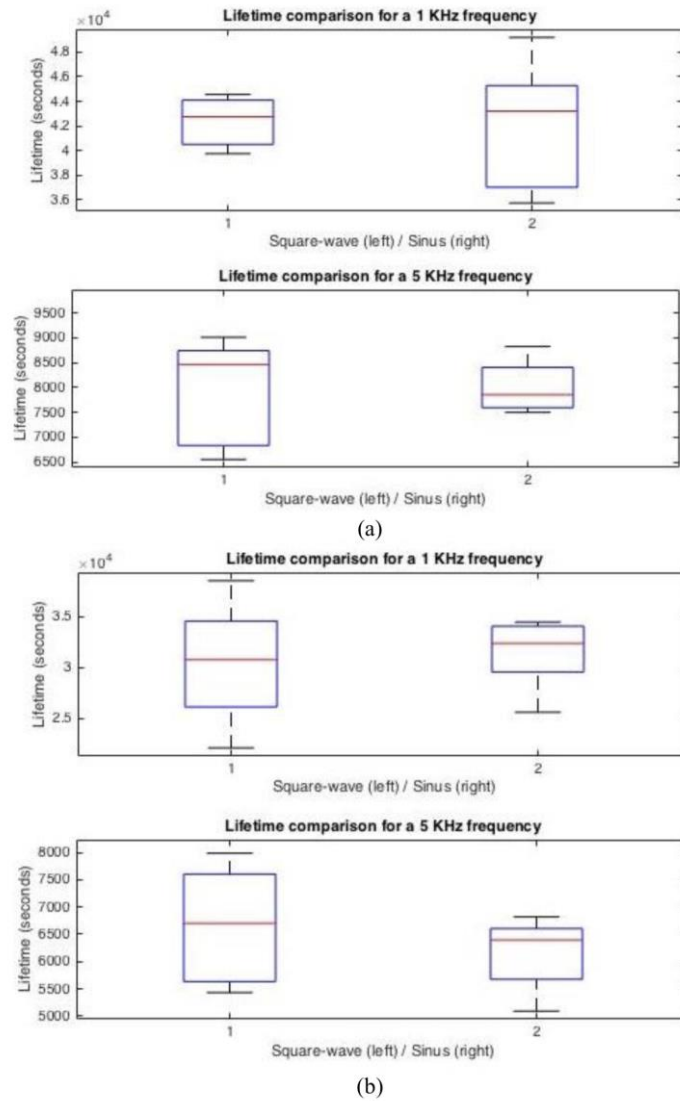


Figure 77: Comparison between square and sine voltage effect on lifetime under PD. Boxplots representing lifetimes (median, quartiles, extrema): (a) $V=1445 V_{peak}$ (50%) (b) $V=1540 V_{peak}$ (60%) [102]

4.5 LIFETIME EVALUATION

There are different models to predict the lifespan of a sample. The simplest ones take only one constraint into account. The commonly used are the Inverse Power Model and the Exponential Model [103]. Table 14 presents the equations used.

Model	Parameters	Equation
Inverse Power Model	L: time to failure at voltage V V: voltage k: constant N: constant	$L = k * V^{-N}$

Chapter 2: Physics of Partial Discharges (PD)

Exponential Model	<p>L : time to failure at voltage V</p> <p>V: voltage</p> <p>c: constant</p> <p>k: constant</p>	$L = c * \exp(-k * V)$
-------------------	---	------------------------

Table 14: Inverse power model and exponential model for lifetime under PD evaluation; adapted from [103]

The authors in [104] studied the combined impact of temperature, voltage and frequency on the lifetime. Concerning the electrical stresses (i.e.: voltage and frequency) an inverse power model was applied. For the temperature, an exponential model was applied.

Stress	Parameters	Model
Electrical	<p>E_V: constant derived from both the material and power law applied to voltage V</p> <p>V: voltage</p> <p>E_F: constant derived from both the material and power law applied to frequency F</p> <p>F: frequency</p> <p>L: time to failure</p>	$\begin{cases} \log(L) = E_V * \log(V) \\ \log(L) = E_F * \log(F) \end{cases}$
Thermal	<p>E_T and b: constants derived from the material and obtained from lifetime data under electro-thermal stress</p> <p>T: temperature</p>	$\log(L) = E_T * \exp(-b * T)$

Table 15: Lifetime models applied for electrical and thermal stresses; adapted from [104]

The model which couples the electrical and thermal stresses is expressed in Eq 35.

$$\begin{aligned} \log(L) \sim & M + E_V * \log(V) + E_F \\ & * \log(F) + E_T * \exp(-b * T) + E_{FV} \\ & * \log(V) * \log(F) + E_{VT} \\ & * \log(V) * \exp(-b * T) + E_{FT} \\ & * \log(F) * \exp(-b * T) + E_{VFT} \\ & * \log(V) * \log(F) * \exp(-b * T) \end{aligned} \quad \text{Eq 35}$$

The first four terms in Eq 35 correspond respectively to the averaged lifetime M , the impact of voltage alone, the impact of frequency alone and the impact of temperature alone. The terms five to seven coupled two by two temperature, voltage and frequency. For example, the constant E_{FV} is attached to the coupling frequency-voltage term. Finally, the last term couples all three parameters (i.e.: temperature, frequency and voltage).

The design of experiment regression has been applied to characterise the influence of each terms on the lifetime [104].

On board electrical motors are usually designed to have a lifetime of several ten thousand hours. It will be obviously too much money and time consuming to check its lifetime under nominal working conditions. An alternative is to use accelerated lifetime tests. It consists in testing the machine at higher stress levels. Stresses can be the voltage, frequency, current, temperature or pressure. Stresses level have to remain under maximum values defined by standards [105] [106] in order not to produce irrelevant degradation mechanisms (for example testing at a temperature above the thermal class). The results are then treated using regression methods. A survey of several regression methods is presented in [107]. These are the design of experiments, response surface, multilinear and robust regression. Each method has its advantages. As an example, design of experiments is accurate with a limited experimental cost.

5 MODELLING PARTIAL DISCHARGES ACTIVITY

5.1 STREAMER CRITERION

This approach considers that the mechanism at the origin of the discharge is the ionization of the gas. It introduces the effective ionization α_{eff} . It corresponds to the rate of net production of free electrons in the gas. This coefficient strongly depends on the electric field amplitude E . The function varies depending the gas. This function is given in air by [108]:

$$\alpha_{eff}(E) = p * \left[k * \left(\frac{E}{p} - \Lambda \right)^2 - A \right] \quad Eq 36$$

With $k = 1.6 \text{ mm.bar}/kV^2$, $\Lambda = 2.2 \text{ kV}/(\text{mm.bar})$ and $A = 0.3 \text{ 1}/(\text{mm.bar})$. p is the pressure in [bar]. $\alpha_{eff}(E) > 0$ for $E > 2.6 \text{ kV}/\text{mm}$. That is the critical field strength at which there is a net production of free electrons.

Figure 78 displays the evolution of this reduced coefficient as a function of the reduced electric field. Three different sets of experimental data points are used [108].

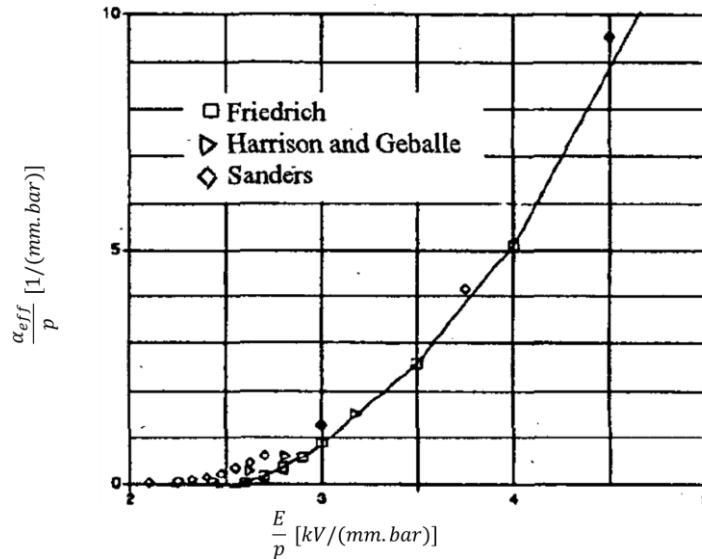


Figure 78: reduced effective ionization as a function of reduced electric field in air [108]

It is assumed that a streamer occurs along a field line on which the density of electrons is high enough for the electronic avalanche to happen. The condition of self-sustained avalanche is given in [109]:

$$\int \alpha_{eff}(E). dl > C_{crit} \quad Eq 37$$

The integral is computed along field lines on which $\alpha_{eff} > 0$. The critical value C_{crit} is usually in the range of 9-18 [108]–[110]. At this point two scenarios are possible:

- Firstly, $\alpha_{eff} > 0$ on the entire field line. The fulfilment of Eq 37 will lead to breakdown across the gap;
- Secondly, there are parts along the line where $\alpha_{eff} < 0$. It is still possible to go to breakdown if the electric field in front the streamer head is so high that it makes the streamer goes forward. This is kind of a suction effect. This is the so called streamer propagation. It requires that the average electric field $\langle E \rangle$ along the line satisfied the following equation given by [109]:

$$\langle E \rangle = \frac{U}{L} > \frac{U_0}{L} + E_0 \quad Eq 38$$

With U the voltage difference between electrodes, L the field line length, $U_0 \approx 10 - 30 kV$ is an empirical constant and $E_0 \approx 0.5 kV/mm$ for a discharge starting from positive electrode and $E_0 \approx 1.2 kV/mm$ for a discharge starting from the negative electrode [109].

This methodology has been implanted in COMSOL [110]. Figure 79 presents an application of COMSOL Particle Tracing Module for the evaluation of field lines starting from a positive electrode where Eq 37 is verified and on which a streamer is likely to appear.

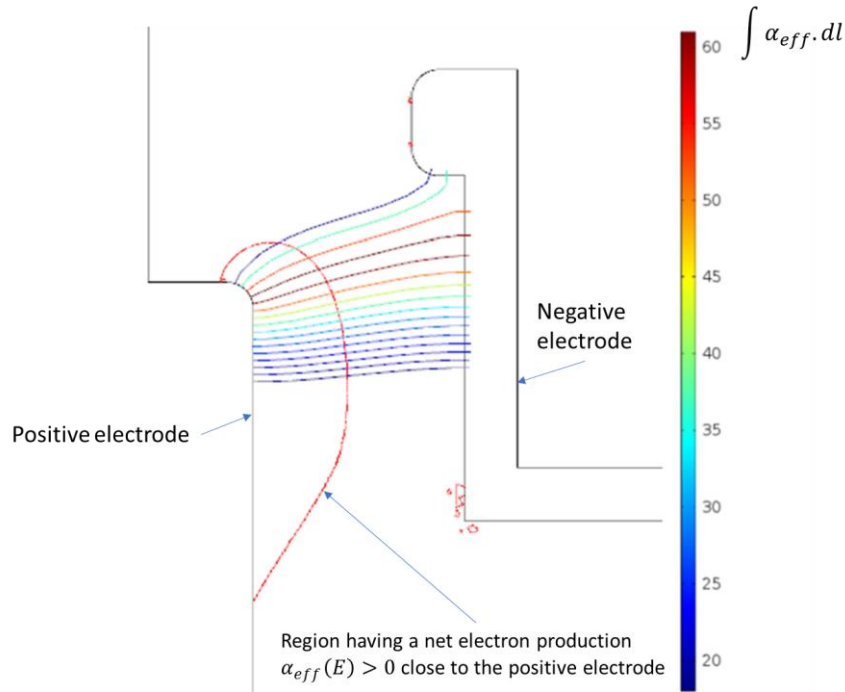


Figure 79: Field lines satisfying the streamer propagation condition (Eq 37) for discharges starting from the positive electrode [110]

The main advantage of this method is that it does not require an uniform electric field along the field line.

5.2 PASCHEN'S CRITERION

Another approach consists in using the Paschen's criterion. It requires the computation of the field lines. The electric field has to be uniform along a field line. This approach was used in [55] to determine the PDIV between two enamelled round copper wires. The field lines are considered as straight lines. They are computed using geometrical relations. Figure 80 displays the used 2D-model.

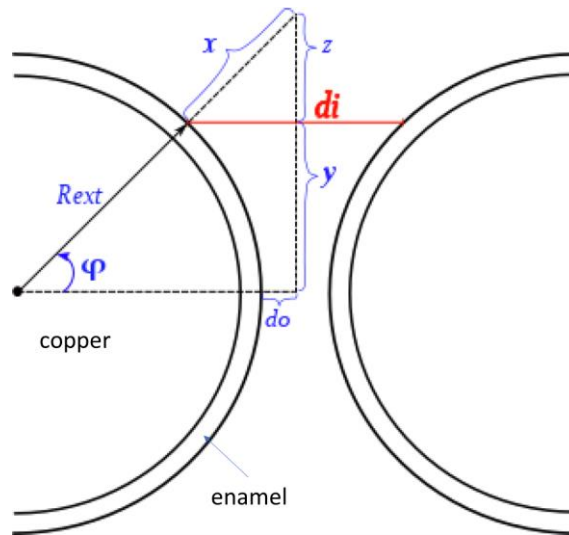


Figure 80: Parallel enamelled round wires; 2D-model [55]

This model is solved using finite elements. The voltage is then available on the whole model. The voltage difference at the extremities of a field line d_i is computed. The results are displayed in a Paschen's plot as presented in Figure 81. The abscissa axis is the product pd ($p = 1 \text{ bar}$) (i.e.: the field line length) and the ordinate axis is the voltage difference.

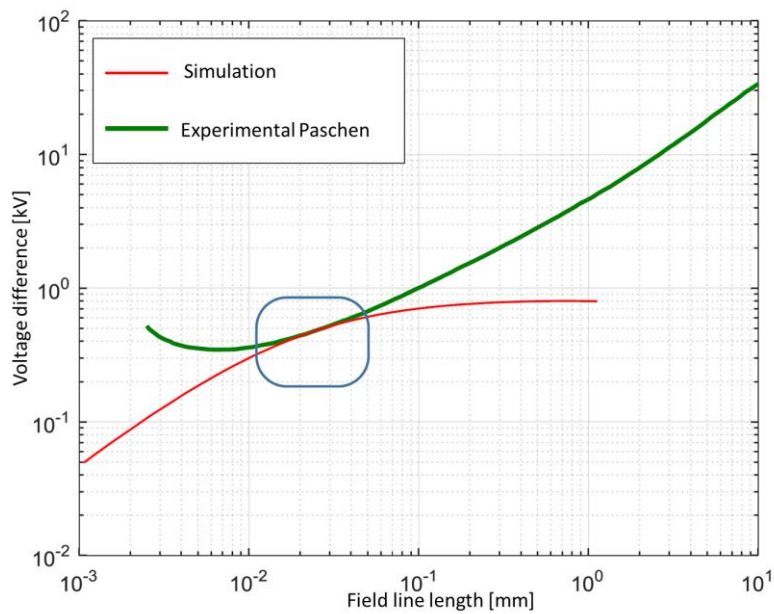


Figure 81: Example of simulated results versus the experimental Paschen's criterion [55]

Chapter 2: Physics of Partial Discharges (PD)

The intersection of the simulated curve (red line) with the Paschen's curve (green line) indicates that the field line at this intersection is probably subject to PD. In this case the field line of length $20 \mu m$ is the one on which PD may occur.

This approach is selected to evaluate PD activity in this work. That choice is made for mainly three reasons. First, it is simple to code. Second, it gives precise results. Third, only uniform fields are considered in this work. Chapter III will present the original developed method for precise field lines computation. Chapter IV will then detail an experimental study on the Paschen's criterion and will propose a correction adapted to enamelled round wires configurations. Finally, Chapter V will present the integration of the field lines computation module and the corrected Paschen's curve in an automatic tool to evaluate PD activity inside an electric motor slot under aeronautical environment.

This chapter has detailed the Partial Discharges (PD). The Paschen's law and some deviations which take into account the aeronautic environmental conditions have been given. The different experimental set-ups to detect and analysis the PD have been given. Results concerning the impact of frequency, voltage and temperature on insulation lifespan have been presented. At the end of this chapter two methods have been presented to evaluate the Partial Discharge Inception Voltage (PDIV). The Paschen's criterion has been retained. The next chapter deals with the computation of electric field lines. Field lines geometry and voltage drop are required to apply the Paschen's criterion.

Chapter 3: Electric field lines computation

1 INTRODUCTION

Our research for the evaluation of Partial Discharges (PD) leads us to the computation of electric field lines using *Matlab* software. However, in some configuration, strange results have been observed. These are field lines which are not perpendicular to iso-potential lines. In order to investigate the cause of such weirdness and to fully understand the methods used in *Matlab* software, we have to reinforce our knowledge on numerical methods used for the electric field lines computation in an electrostatic problem composed of both conductors and dielectric materials.

After the presentation of electrostatic formulations, the Whitakker's method is illustrated on a simple example. From the presentation of the Horowitz's method, we propose an improvement in the computation of field lines. This improvement makes it possible to present a more synthetic field map: the field lines are drawn so that their density is proportional to the intensity of the electric field. Finally, an example is treated with the Whitakker's method implemented in *Matlab* and the proposed method which allows them to be compared.

2 THE ELECTROSTATIC PROBLEM

2.1 PRESENTATION OF THE FIELD OF STUDY

The problem consists of two enameled round wires in close contact in air. It is a configuration representative of a contact between two adjacent wires in a stator slot in the presence of a default (air bubble or bad impregnation) in the surrounding impregnating resin.

The copper areas are obviously not modelled since there is no electric field in conductor materials. Boundary conditions (i.e.: voltages) are applied on the copper areas contours.

The air and the enamel are considered charge carrier free.

The wires are considered infinitely long in the machine active length dimension and the voltage drops are neglected. Due to invariance along this dimension and symmetries the problem is reduced to a 2D-electrostatic problem with only a quarter of the wires being modelled.

Figure 82 displays the 2D-problem.

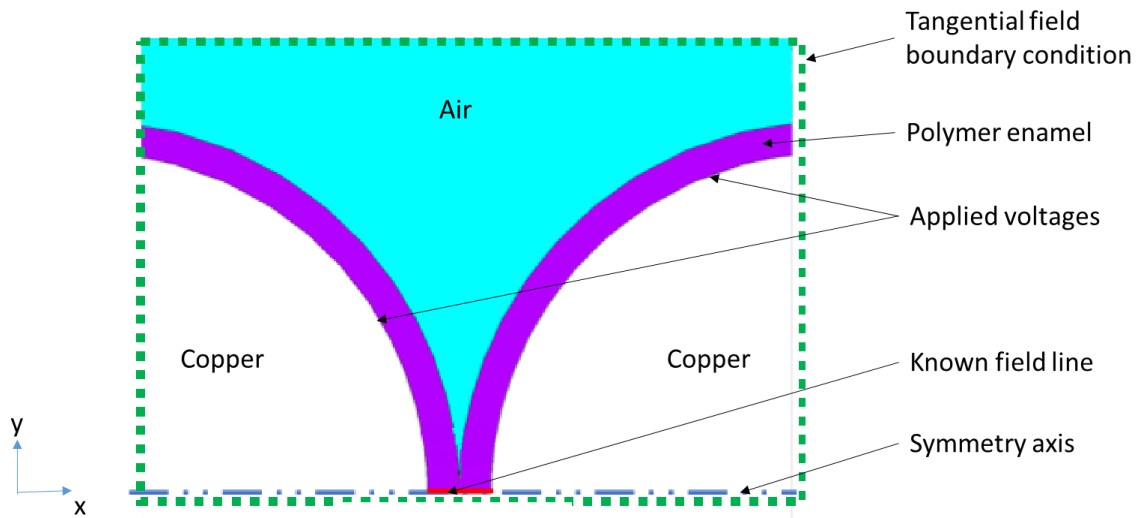


Figure 82: Enamelled wires 2D-electrostatic problem

In such electrostatic problem, the materials are characterized with their dielectric constant. The dielectric constant of air is 1. The dielectric constant of the enamel is greater than 1 and depends on the polymer used. In this chapter, the dielectric constant of the enamel will be taken as 3.5.

2.2 ELECTROSTATIC EQUATIONS AND FORMULATIONS

The basis of electromagnetism are the Maxwell's equations. These are recap in Table 16.

$\text{Curl } \vec{H} = \vec{j} + \frac{\partial \vec{D}}{\partial t}$	Eq 39
$\text{Curl } \vec{E} = -\frac{\partial \vec{B}}{\partial t}$	Eq 40
$\text{div } \vec{B} = 0$	Eq 41
$\text{div } \vec{D} = \rho$	Eq 42

Table 16: Complete Maxwell's equations [42]

Five field vectors are introduced: the electric field intensity \vec{E} , the magnetic field intensity \vec{H} , the electric flux density \vec{D} , the magnetic flux density \vec{B} and the current density \vec{j} . The volume charge density of the dielectric medium in which the field is considered is noted ρ .

The fields produced by a power frequency alternating voltage are not electrostatic. However, they are considered quasi-stationary: the fields time variation is neglected. Besides, in this work both air and

Chapter 3: Electric field lines computation

polymer insulation materials are considered free of charge carrier. Table 17 gives the simplified Maxwell's equations which comes into play in the considered electrostatic problem.

$Curl \vec{E} = 0$	Eq 43
$div \vec{D} = 0$	Eq 44

Table 17: Maxwell's equations used for a charge carrier free electrostatic problem

Because \vec{E} is curl free, it can be expressed as a gradient of a scalar potential. This scalar is the electric potential V :

$$\vec{E} = -grad V \quad Eq 45$$

The electric flux density \vec{D} is derived from the electric field intensity \vec{E} and the medium properties:

$$\vec{D} = \epsilon_r * \epsilon_0 * \vec{E} = \epsilon * \vec{E} \quad Eq 46$$

With ϵ_0 the vacuum dielectric constant, ϵ_r the medium relative dielectric constant (equals 1 in air). The medium is considered isotropic thus ϵ is a constant.

By injecting Eq 45 and Eq 46 into Eq 44 one gets:

$$\begin{aligned} div(\epsilon * (-grad V)) &= 0 & Eq 47 \\ div(grad V) &= 0 \\ \nabla^2 V &= 0 \end{aligned}$$

Equation Eq 47 is called the Poisson's equation. It is the scalar potential formulation of a charge carrier free electrostatic problem.

As \vec{D} is divergent free it thus can be expressed as the curl of an electric vector potential \vec{u} :

$$\vec{D} = curl \vec{u} \quad Eq 48$$

By injecting Eq 48 in Eq 43 one gets:

$$\begin{aligned} curl(curl \vec{u}) &= 0 & Eq 49 \\ grad(div \vec{u}) - \nabla^2 \vec{u} &= 0 \end{aligned}$$

The Coulomb's gauge applied to the vector potential \vec{u} is defined as follow:

$$div(\vec{u}) = 0 \quad Eq 50$$

Applying the Coulomb's gauge in Eq 49 results in:

$$\nabla^2 \vec{u} = 0 \quad \text{Eq 51}$$

Equation Eq 51 is the vector potential formulation of a charge carrier free electrostatic problem.

There are thus two formulations for solving the electrostatic problem. The first uses a scalar potential V . The second uses a vector potential \vec{u} . Each formulation has its advantages and disadvantages.

2.3 ADVANTAGES AND DISADVANTAGES OF EACH FORMULATION

2.3.1 Vector potential

In case of a 2D-problem in a (x,y) plane, the electric vector potential \vec{u} is written as:

$$\vec{u} = u \cdot \vec{z} \quad \text{Eq 52}$$

With:

$$\|\vec{z}\| = 1$$

The main advantage of the vector potential is that it directly gives the electric field lines. Field lines are in fact level curves (i.e.: contour) of a scalar function u . Such function is usually called the stream function [111]. By injecting Eq 52 in Eq 48 one gets:

$$\begin{cases} \frac{du}{dx} = -D_y \\ \frac{du}{dy} = D_x \end{cases} \quad \text{Eq 53}$$

Using the relationship between the electric field \vec{E} and the electric flux density \vec{D} (Eq 46), Eq 53 can be expressed under the form:

$$\begin{cases} \frac{du}{dx} = -\varepsilon * E_y \\ \frac{du}{dy} = \varepsilon * E_x \end{cases} \quad \text{Eq 54}$$

With E_x and E_y respectively the projections of \vec{E} along \vec{x} and \vec{y} axis in a 2D-system.

The vector potential formulation is complex to execute in an electrostatic problem with multiple conductors. It requires to put in place a network of branches and cuts all across the field of study [112], [113]. However, [113], [114] have successfully put in application that formulation to solve an electrostatic problem with multiple conductors. Their work has been done almost at the same time we started our researches on this topic.

Besides, none of the software at our disposal uses the vector potential formulation.

2.3.2 Scalar potential

The formulation with the scalar potential V is the simplest to use. Contrary to the vector potential u , there is no need to introduce cuts if multiple conductors are present in the domain of study. That is because the solution using a V formulation is unique. The scalar potential is also easy to handle for the computation of equipotential lines.

The main inconvenient of the V formulation is that it does not give directly the electric field lines. Additional steps are consequently required. Two main methods were found in the literature to compute field lines by using a numerical calculation software (such as *Matlab*) from the scalar potential solution.

The formulation with the scalar potential V was finally chosen for several reasons. First, the finite elements software at our disposal (*Ansys Emag*, *Ansys Maxwell*, *Femm* or *Jmag*) are using the scalar potential formulation. Then, it is simple to manipulate. Finally, methods exist in the literature to compute field lines from the scalar potential solutions. They constitute a strong base to start our work.

3 ELECTRIC FIELD LINES COMPUTATION DERIVED FROM A SCALAR POTENTIAL FORMULATION

3.1 BALLISTIC METHOD

The first method to compute field lines from a scalar potential formulation solution is presented by [115]. By definition, the electric field \vec{E} is parallel to a field line \vec{l} . In a direct orthonormal system, the cross-product of this two quantities is null:

$$\vec{l} \times \vec{E} = 0 \quad \text{Eq 55}$$

$$l_x * E_y - l_y * E_x = 0$$

With l_x and l_y respectively the projections of \vec{l} along \vec{x} and \vec{y} axis in a 2D-system.

From Eq 55 it comes:

$$\frac{E_y}{E_x} = \frac{l_y}{l_x} \quad \text{Eq 56}$$

E_x , E_y are the field components over the mesh. These are known.

Starting at any point, the field line \vec{l} can be computed by incrementing Eq 56 given an arbitrary displacement Δ_x along x axis. Thus, the vertical displacement Δ_y along y axis is expressed as follow:

$$\Delta_y = \Delta_x * \frac{E_y}{E_x} \quad \text{Eq 57}$$

Let us express equation Eq 57 between two consecutive points $M_i(x_i, y_i)$ and $M_{i+1}(x_{i+1}, y_{i+1})$:

$$(y_{i+1} - y_i) = (x_{i+1} - x_i) * \frac{E_{y,i}}{E_{x,i}} \quad \text{Eq 58}$$

Let us define a constant step increase Δ_{step} at each iteration, so that:

$$\Delta_{step} = \frac{(y_{i+1} - y_i)}{E_{y,i}} = \frac{(x_{i+1} - x_i)}{E_{x,i}} \quad \text{Eq 59}$$

It is thus possible to express the $M_{i+1}(x_{i+1}, y_{i+1})$ coordinates from $M_i(x_i, y_i)$ data (coordinates and field components) and Δ_{step} :

$$\begin{aligned} x_{i+1} &= x_i + \Delta_{step} * E_{x,i} \\ y_{i+1} &= y_i + \Delta_{step} * E_{y,i} \end{aligned} \quad \text{Eq 60}$$

When chosen arbitrary, the starting point may not be the start of the field line. It is then necessary to integrate Eq 60 backward to complete the line.

This method is called a ballistic method. The mesh is swept and field lines are started in elements which do not already contain a field line. The field lines are computed by integration. The integration process is stopped if one of the following condition is checked:

- the field line enters a forbidden region (for instance the limit of the domain);
- the field line reaches a null field;
- the field line loops back onto itself;
- the field line has too many segments. This is a safety measure in case the previous conditions do not work properly.

By doing so, there is the same density of field line all over the model. It does not allow to represent the electric field intensity.

As an illustration, let us consider an electrostatic problem made of two infinitely long cylinder oppositely. Due to the symmetries, only a quarter of the field of study is considered as displayed on Figure 83. The mesh is represented with black crosses. It is made of rectangular elements (dotted red line). The blue line delimits the conductor contour.

Chapter 3: Electric field lines computation

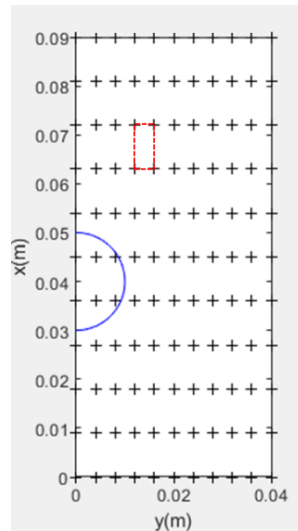


Figure 83: System of 2 infinite cylinders oppositely charges - field of study represents one quarter of the system - mesh (dots) and half conductor contour (blue)

Let us apply the Whittaker ballistic method on that system. The algorithm noted above is implanted in a Matlab script.

The orientation vector of the electric field is computed on all mesh nodes, except for the ones located inside the conductor. The starting points are chosen on the contour of the domain. Figure 84 displays the computed orientation vectors and the starting points (circles). The starting points are arbitrary chosen on the limit of the field of study.

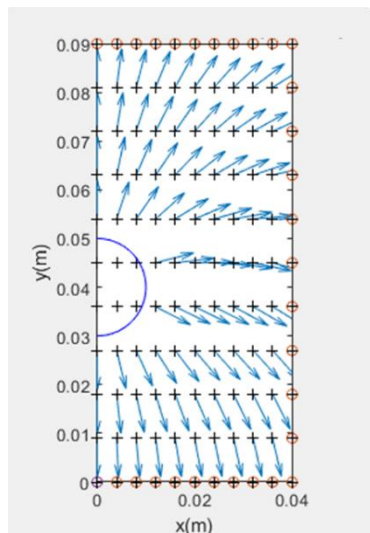


Figure 84: Electric field orientation vectors and starting points (red circles)

Let us designate the starting point $Q(x_0, y_0)$ of a field line. Then, the next point on the line $M_1(x_1, y_1)$ is computed by iteration from point Q . The iteration is backward because the starting points are on the end of the field lines:

$$x_1 = x_0 - \Delta_{step} * E_{x,0} \tag{Eq 61}$$

Chapter 3: Electric field lines computation

$$y_1 = y_0 - \Delta_{step} * E_{y,0}$$

With $E_{x,0}$ and $E_{y,0}$ the electric field orientation vector components along x and y axis respectively on starting point Q. The step increase Δ_{step} at each iteration is taken equal to the grid spacing along x axis dx . Figure 85 displays the field lines after one iteration backward from starting points.

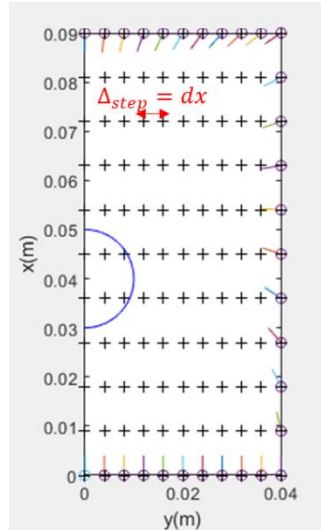


Figure 85: Field lines after a first iteration backward

It can be seen that the M_1 points do not coincide with a mesh node. The electric field orientation vectors are interpolated on the extra M_1 points using the *interp2* function.

At each iteration, the field lines extend. The i^{th} iteration between two consecutive points $M_i(x_i, y_i)$ and $M_{i+1}(x_{i+1}, y_{i+1})$ correspond to:

$$\begin{aligned} x_{i+1} &= x_i - \Delta_{step} * E_{x,i} \\ y_{i+1} &= y_i - \Delta_{step} * E_{y,i} \end{aligned} \tag{Eq 62}$$

The computed field lines after 11 iterations are displays on Figure 86.

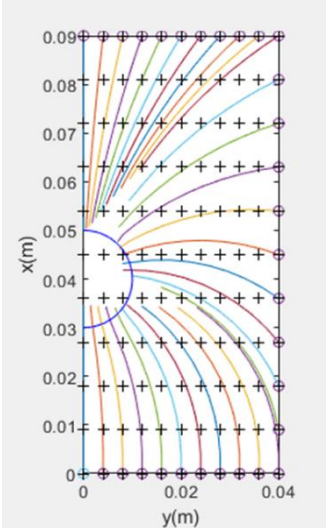


Figure 86: Computed field lines after 11 backward iterations

In this method, the starting points are chosen arbitrarily. In the next presented method, the choice of the starting points is a key step in order to represent a field intensity with the density of field lines.

3.2 FLUX TUBES BASED METHOD

The objective is to represent the strength of the electric field by the density of the electric flux lines [111]. The core of the method is the choice of the field lines starting points.

A predetermined amount of flux $\delta\Phi$ has to be present between two adjacent lines a and b :

$$\delta\Phi = \int_a^b E \cdot n \cdot ds \tag{Eq 63}$$

Where n is the normal vector and s is the path between the lines a and b . This path is chosen as the contour of scalar potential V . Figure 87 illustrates the equation Eq 63.

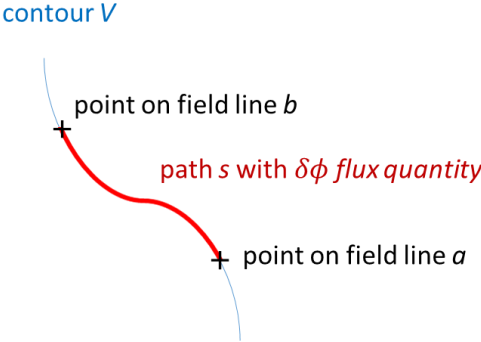


Figure 87: Illustration of flux quantity $\delta\Phi$ located between two consecutive field lines a and b

Chapter 3: Electric field lines computation

Such as in Whittaker's method, a uniform mesh is applied. The electric field is calculated on the whole meshed domain using linear interpolations. In a simple case, all the field lines pass through a single V contour. The contour results in a series of points $s_i = \{x_i, y_i\}; i=1, \dots, l$. The total flux through the contour of potential V is:

$$\phi_V = \int_{s_1}^{s_l} E ds = \frac{1}{2} \sum_{i=1}^l (E_i + E_{i+1}) |s_{i+1} - s_i| \quad \text{Eq 64}$$

Figure 88 displays the contour V discretization in a uniform meshed domain. Here the total number of points is $l=5$.

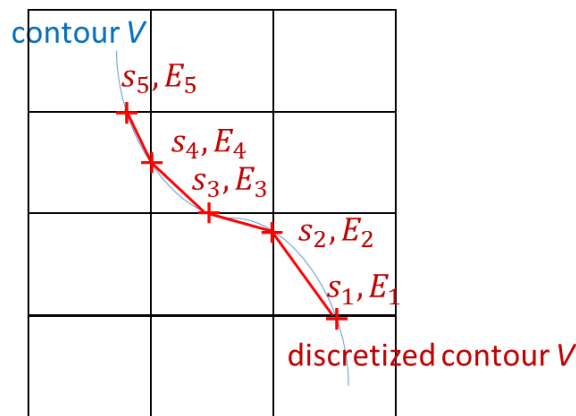


Figure 88: Contour discretization in an uniform mesh

The field lines starting points on contour V results in a second series of points $s_j = \{x_j, y_j\}; j=1, \dots, N$. Such points satisfy the following equation:

$$\int_{s_j}^{s_{j+1}} E ds = \delta \Phi \quad \text{Eq 65}$$

Starting from the s_1 point of the contour V , the s_i contour point which is in proximity of the next field line starting point is identified by this equation:

$$\int_{s_1}^{s_i} E ds < \delta \Phi < \int_{s_1}^{s_{i+1}} E ds \quad \text{Eq 66}$$

The s_j field line starting point on contour V segment s_i, s_{i+1} is defined as:

$$\int_{s_i}^{s_j} E ds = \delta \Phi - \int_{s_1}^{s_i} E ds = \phi_0 \quad \text{Eq 67}$$

Then one can express Eq 67 as:

$$\frac{1}{2} (E_i + E_j) |s_j - s_i| = \phi_0 \quad \text{Eq 68}$$

Let $a = \frac{|s_j - s_i|}{|s_{i+1} - s_i|}$ be the fractional distance from contour point s_i to field line starting point s_j . As the electric field \vec{E} is linear along the grid, one finally gets Eq 69 [111]:

$$a = \phi_0 / E_i |s_{i+1} - s_i| \quad \text{Eq 69}$$

Starting points s_j of field lines on contour V are finally determined [111]:

$$s_j = \{x_j, y_j\} \quad \text{Eq 70}$$

$$s_j = \{(1 - a) * x_i + a * x_{i+1}, (1 - a) * y_i + a * y_{i+1}\}$$

The field lines are then built from their starting point by integrating as in Whittaker's method [111]. As the same flux quantity $\delta\Phi$ is present between two adjacent lines, the electric field strength is represented by the concentration of field lines. The same termination criteria as in Whittaker's method are used.

However, an electric machine slot filled with conductors is a more complex case. It mainly happens that all the field lines do not pass through a single V contour. Let us consider two conductors at potential of V_1 and V_2 respectively. A field line starting from V_1 contour is identified by l_{n1}^1 ; $n1=1, \dots, N1$. The same procedure described in the simple case is applied to V_1 contour. However, the intersections of l_{n1}^1 field lines with V_2 contour have to be tracked. To do that, each segment of l_{n1}^1 is checked to verify whether or not it intersects with V_2 contour. The intersection points are added to V_2 contour points series. Now, one can apply the same procedure with V_2 contour adding some steps:

Step 1: choose as a starting point of field lines from V_2 contour (l_{n2}^2 ; $n2=1, \dots, N2$) one of the intersection point of a l_{n1}^1 field line with V_2 contour;

Step 2: integrate from that point until (a) another intersection point of a l_{n1}^1 field line with V_2 contour is reached or (b) the integral exceed the fixed flux quantity $\delta\Phi$. In case (b), the next point as to be determined the same way s_j point is in the simple case;

Step 3: repeat step 2 until the whole V_2 contour is swept;

Step 4: integrate backward from the first intersection point to find the remaining starting points.

Figure 89 illustrates the field lines computed between two conductors at potential V_1 and V_2 using the presented algorithm.

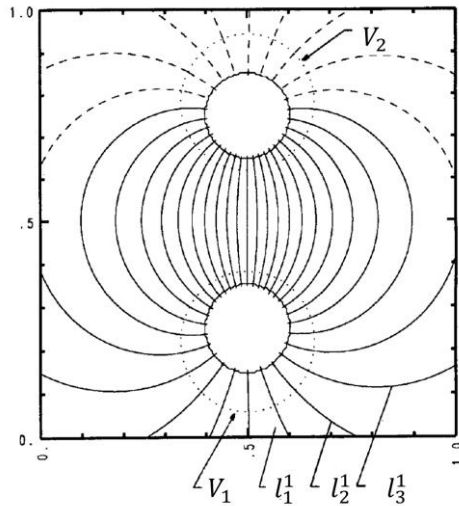


Figure 89: Electric field lines from two infinitely long wires of opposite charge in free space. V_1 and V_2 are potential contours. The solid field lines were drawn from V_1 . The dashed field lines were drawn from V_2 [111]

4 PROPOSED METHOD

The proposed method we developed is an upgrade of the method presented by Horowitz [111]. A flux function is built from the electric field components on all the nodes. The field lines correspond to iso-values of this scalar function. The proposed method does not require a uniform mesh. The calculation is done on the same mesh on which the scalar potential V is computed.

4.1 ELECTRIC FIELD AND ELECTRIC FLUX

The 2D-finite element model on Ansys Mechanical APDL uses 8 nodes elements. On each element, the coordinates and the scalar potential solution are expressed as a combination of each nodes data with a defined shape function. Shape functions are expressed in the local coordinate system (u,v) of the element. It is a coordinate system attached to the element which define the location of each node.

$$\begin{cases} x_e(u, v) = \sum_{i=1}^8 N_i(u, v) \cdot x_e(i) \\ y_e(u, v) = \sum_{i=1}^8 N_i(u, v) \cdot y_e(i) \\ V_e(u, v) = \sum_{i=1}^8 N_i(u, v) \cdot V_e(i) \end{cases}$$

Eq 71

With:

$$\begin{cases} N_i(u, v) = 1 \text{ at node } i \\ N_i(u, v) = 0 \text{ elsewhere} \end{cases}$$

With x_e and y_e the coordinates in the global coordinate system (x, y) of the nodes of an element e . For an 8 nodes elements, the shape functions N are given in [116].

The electric field on the nodes of an element is derived from the voltage values on the node using Eq 45. It requires the expression of partial derivatives in the global system.

First, the partial derivatives of a function in the local system (u, v) can be expressed from its partial derivatives in the global system (x, y) :

$$\begin{pmatrix} \frac{\partial}{\partial u} \\ \frac{\partial}{\partial v} \end{pmatrix} = \begin{bmatrix} \frac{\partial x}{\partial u} & \frac{\partial y}{\partial u} \\ \frac{\partial x}{\partial v} & \frac{\partial y}{\partial v} \end{bmatrix} \begin{pmatrix} \frac{\partial}{\partial x} \\ \frac{\partial}{\partial y} \end{pmatrix} = J \begin{pmatrix} \frac{\partial}{\partial x} \\ \frac{\partial}{\partial y} \end{pmatrix} \quad \text{Eq 72}$$

With:

$$J = \begin{bmatrix} J_{11} & J_{12} \\ J_{21} & J_{22} \end{bmatrix}$$

With J the Jacobian matrix. It is computed from the known shape functions partial derivatives in the local system when putting Eq 71 in Eq 72.

Then, the partial derivatives of a function in the global system (x, y) can be expressed from its partial derivatives in the local system (u, v) :

$$\begin{pmatrix} \frac{\partial}{\partial x} \\ \frac{\partial}{\partial y} \end{pmatrix} = \begin{bmatrix} \frac{\partial u}{\partial x} & \frac{\partial v}{\partial x} \\ \frac{\partial u}{\partial y} & \frac{\partial v}{\partial y} \end{bmatrix} \begin{pmatrix} \frac{\partial}{\partial u} \\ \frac{\partial}{\partial v} \end{pmatrix} = I \begin{pmatrix} \frac{\partial}{\partial u} \\ \frac{\partial}{\partial v} \end{pmatrix} \quad \text{Eq 73}$$

With:

$$I = \begin{bmatrix} I_{11} & I_{12} \\ I_{21} & I_{22} \end{bmatrix}$$

$$I = J^{-1}$$

It is matrix I which is use in practise because the data have to be expressed in the global system. It is computed as follow:

$$I = J^{-1} = \frac{1}{\det(J)} \begin{bmatrix} J_{22} & -J_{12} \\ -J_{21} & J_{11} \end{bmatrix} \quad \text{Eq 74}$$

With:

$$\det(J) = J_{11}J_{22} - J_{12}J_{21}$$

The electric field components on the nodes of an element e can finally be expressed in the global system by combining Eq 71 and Eq 73:

$$\begin{cases} E_{x,e} = -\frac{\partial V_e}{\partial x} = -\sum_{i=1}^8 \left(I_{11} \frac{\partial N_i}{\partial u} + I_{12} \frac{\partial N_i}{\partial v} \right) \cdot V_e(i) \\ E_{y,e} = -\frac{\partial V_e}{\partial y} = -\sum_{i=1}^8 \left(I_{21} \frac{\partial N_i}{\partial u} + I_{22} \frac{\partial N_i}{\partial v} \right) \cdot V_e(i) \end{cases} \quad \text{Eq 75}$$

The electric flux components are computed from electric field components using Eq 46.

4.2 EQUIPOTENTIAL LINES

The next step consists in forming equipotential lines. These are contours on which the voltage value is constant. Equipotential lines are obtained by regrouping nodes with the same voltage value. Let us see the steps to compute an equipotential line at voltage V .

A test is done on each edge of each element to check whether or not it is crossed by the equipotential line V . As can be seen on Figure 90, each edge is composed of three nodes. There are three possible outcomes:

- The voltage V is lower or bigger than any of the three nodes voltage. The edge is not intersected by the equipotential line V ;
- The voltage V is equal to one of the three nodes voltage. The equipotential line intersects the edge at the corresponding node of voltage V ;
- The voltage V is between any of the three nodes voltage. The edge is intersected by the equipotential line at a point which is interpolated.

Figure 90 illustrates an equipotential intersecting two edges of an element. On one edge the intersection point is an already existing node (node 6). The second edge intersection point has to be interpolated (red cross). The local numbering of the nodes is rearranged compared to Ansys 8 nodes reference element to facilitate the programming.

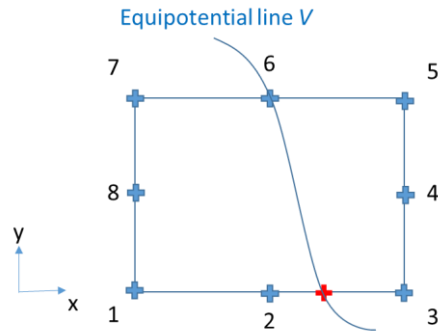


Figure 90: Equipotential line V intersecting an element edges

A second order polynomial is used for the interpolation. The following equation gives the parametric expression of the polynomial:

$$z(t) = a_{1,z} + a_{2,z} * t + a_{3,z} * t^2 \quad \text{Eq 76}$$

With:

$$t \in [0,1]$$

The parameter t represents the edge on which the interpolation is performed.

Figure 91 displays Eq 76 along a parameterized edge:

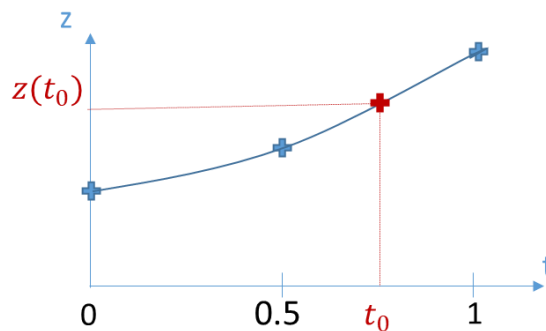


Figure 91: Illustration of a second order polynomial interpolation over a parameterized edge

For instance, on Figure 90 the interpolation is done on the edge containing the nodes (1,2,3). The nodes are parameterized according to the local numbering order: $t=0$ for node 1, $t=0.5$ for node 2 and $t=1$ for node 3. By solving Eq 76 in term of voltage it is possible to derived the polynomial coefficients:

$$V(t) = a_{1,V} + a_{2,V} * t + a_{3,V} * t^2 \quad \text{Eq 77}$$

With:

$$\begin{cases} V(0) = a_{1,V} = V_0 \\ V(0.5) = a_{1,V} + a_{2,V} * 0.5 + a_{3,V} * 0.25 = V_{0.5} \\ V(1) = a_{1,V} + a_{2,V} + a_{3,V} = V_1 \end{cases}$$

In the considered example, $(V_0, V_{0.5}, V_1)$ are respectively the finite elements voltage solution on nodes (1,2,3) in Figure 90. The three polynomial coefficients $(a_{1,V}, a_{2,V}, a_{3,V})$ are thus determined.

$$V(t_0) = V = a_{1,V} + a_{2,V} * t_0 + a_{3,V} * t_0^2 \quad \text{Eq 78}$$

With V the voltage of the considered equipotential line V .

The obtained parameter t_0 is injected back into Eq 77 to determine the interpolated node coordinates, electric field components and electric flux components. As in Eq 78, the associated polynomial coefficients are deduced from the known nodes data.

4.3 FLUX FUNCTION

At this point, equipotential lines made of nodes at the same scalar potential V are determined. The coordinates and fields components are determined on all these nodes. The number of equipotential lines depends on the accuracy from which the electric scalar potential problem is solved. The finer the mesh used to solve the problem, the higher the number of equipotential lines that can be accurately determined.

For each equipotential line a geometrical reference is defined on its barycentre. The points on the line are located by using polar coordinates in this reference. A starting point Q is chosen for instance by means of the angular coordinates. Figure 92 illustrates the barycentre reference attached to an equipotential line V . Point G is the barycentre. A point M located on the equipotential line is identified by its curvilinear abscissa $s(M)$.

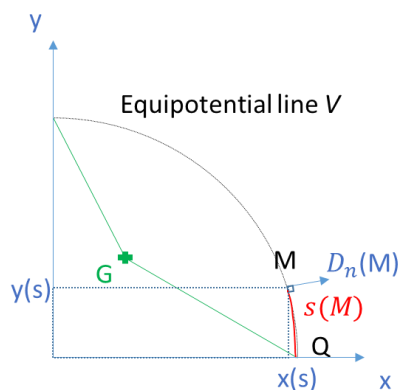


Figure 92: Barycentre system associated to an equipotential line V

A flux function $\Phi(M)$ of points on each equipotential is defined as the flux per meter crossing the line between the starting point Q and point M :

$$\Phi(M) = \int_Q^M D_n ds \quad \text{Eq 79}$$

D_n is the normal electric flux density on the equipotential line, ds is the elemental curvilinear length of the equipotential line. Each point M on the line is parameterized by the curvilinear abscissa $s(M)$ and:

$$\begin{cases} s(M) = \int_Q^M ds \\ x(M) = x(s) \\ y(M) = y(s) \\ \Phi(M) = \Phi(s) \end{cases} \quad \text{Eq 80}$$

The trace of a flux tube on the equipotential line is delimited by two points P_i and P_{i+1} which are given by the predetermined flux per meter $\delta\Phi$:

$$\delta\Phi = \int_{P_i}^{P_{i+1}} D_n ds \quad \text{Eq 81}$$

The properties of these points are:

$$\begin{cases} P_1 = Q \\ \Phi(P_1) = 0 \\ \Phi(P_i) = \Phi(P_{i-1}) + \delta\Phi = (i-1)\delta\Phi \end{cases} \quad \text{Eq 82}$$

All the points P_i on the equipotential line are determined by inverting the previous functions:

$$s(P_i) = \Phi^{-1}((i-1)\delta\Phi) \quad \text{Eq 83}$$

Figure 93 illustrates the flux tubes computation using Eq 80, Eq 81, Eq 82 and Eq 83:

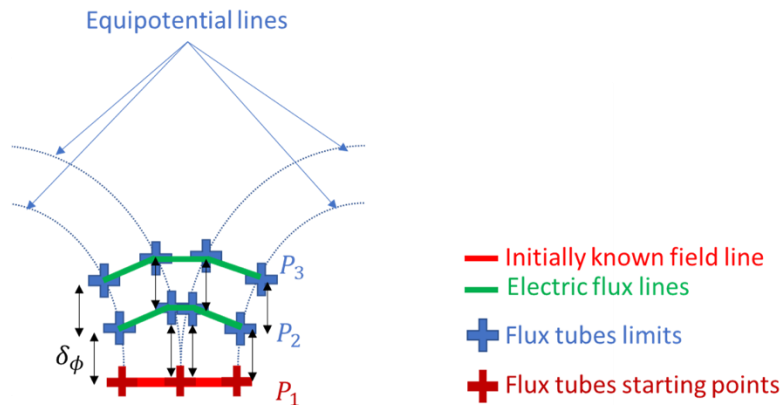


Figure 93: Flux tubes computation

The determination of points P_i is done on all equipotential lines. If the starting point Q on each equipotential line is correctly chosen then the electric flux lines are defined by iso- Φ lines. The starting point has to be chosen on a field line crossing all the equipotential lines present in the domain.

4.4 ILLUSTRATIVE EXAMPLES

In this paragraph the proposed method is used to compute electric field lines in the studied electrostatic problem. Table 18 gives the parameters used.

Wires' parameters		
R_{int}	Round wire copper radius	0.75 mm
e	Enamel overcoat thickness	70 μm
ϵ_r	Enamel dielectric constant	3.5
Applied voltages		
V_1	Left wire voltage amplitude	1000 V
V_2	Right wire voltage amplitude	0 V
Equipotential lines parameters		
V_{imp}	Imposed potentials intervals	$\left[0; \frac{V_1}{4}; \frac{2 * V_1}{4}; \frac{3 * V_1}{4}; V_1\right]$
N_{imp}	Imposed number of computed equipotential lines on each potential interval	[25; 25; 25; 25]

Table 18: Parameters used in the illustrative example

It can be seen that there are one hundred equipotential lines which will be formed. The voltage amplitude is divided into four intervals. A same number of twenty-five equipotential lines per voltage interval is chosen.

The finite element software used is *Ansys Mechanical APDL*. The used mesh is displayed on Figure 94. The computation time is given as an order of magnitude. It is obtained using tic-toc on *Matlab*. It changes depending on the system computing speed. Thus, the computation time presented on Figure 94 is the sum of the loading times of data transfer between *Ansys* and *Matlab*, the meshing time and the resolution time.

Chapter 3: Electric field lines computation

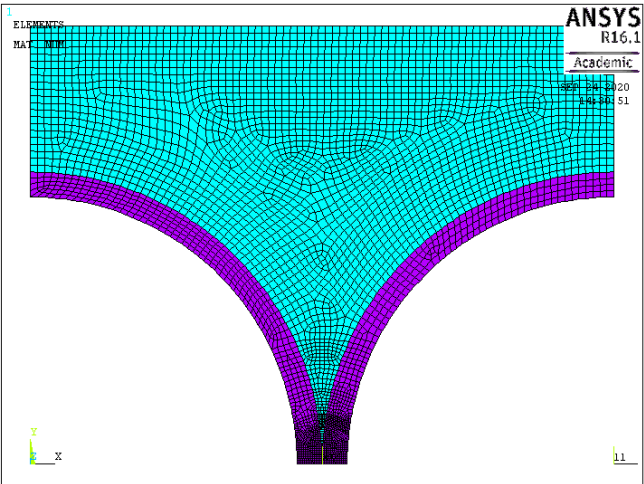
Mesh		Number of elements: 4144
		Computation time: 12.6 s

Figure 94: Used mesh (white: copper, purple: enamel, green: air)

The significant results are given on Figure 95 and Figure 96

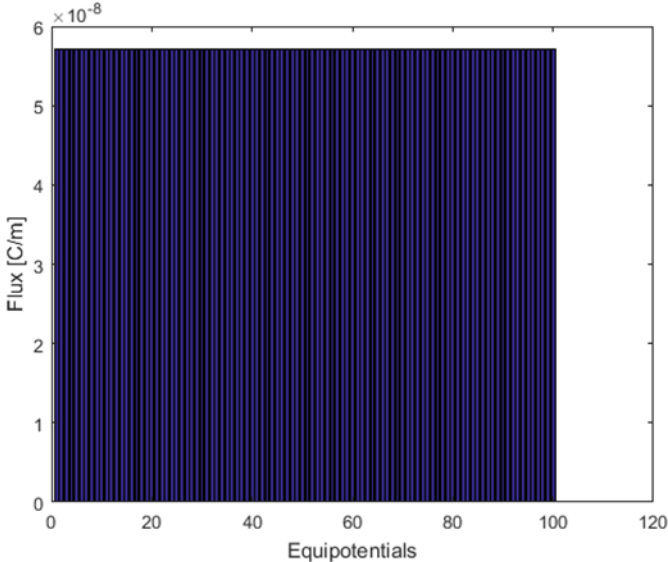


Figure 95: Total electric fluxes crossing each equipotential line

The electric flux across each equipotential line is constant. The starting point of the twenty field lines displayed on Figure 96 are chosen by dividing the total electric flux crossing each equipotential line by nineteen. That is because there is already one known field line that is the reference line chosen on the symmetry axis.

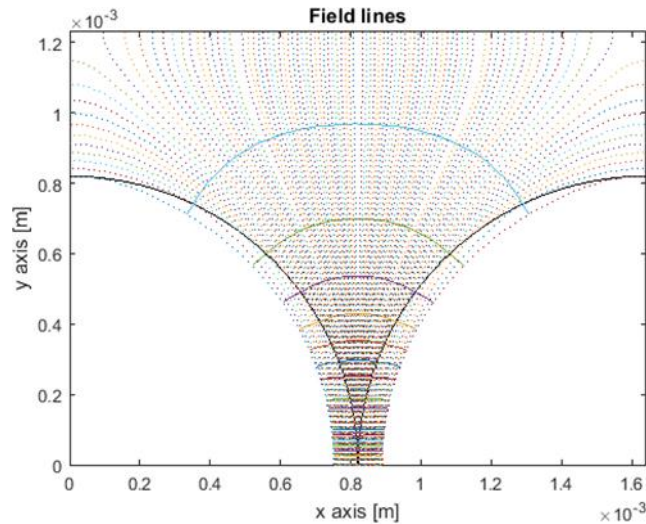


Figure 96: Electric field lines obtained with the mesh of Figure 94

The post processing time is the time required to build the field lines starting from the finite elements solution. It is of 9.11 s.

In this approach, the density of the field lines is linked to the electric field amplitude.

5 ANOTHER METHOD USING *MATLAB* FUNCTIONS

Another method to plot electric field lines from scalar potential solution is developed using *Matlab* functions. It is likely a Whittaker based approach [115]. The different steps in order to obtain such results are presented.

5.1 BUILDING THE ADDITIONAL MESH

The mesh created by the finite element software cannot be used directly by *Matlab* functions. Indeed, it has to be uniform. So the first step consists in building a second uniform mesh. The finite element (FEM) computed nodes coordinates (X, Y) and scalar potential V lists are imported. Axis vectors X_a, Y_a are built from X, Y lists such that:

- $X_a \in [X_{min}, X_{max}]$ and $Y_a \in [Y_{min}, Y_{max}]$
- X_a and Y_a results in a N uniformly spaced values

The *linspace* function is used so that:

$$X_a = \text{linspace}(X_{min}, X_{max}, N)$$

$$Y_a = \text{linspace}(Y_{min}, Y_{max}, N)$$

A new mesh is generated from these axis vectors. It is made of identical rectangles.

The *meshgrid* function is used:

$$[X_g, Y_g] = \text{meshgrid}(X_a, Y_a)$$

The X_g, Y_g matrix contain the coordinate of all the points of the new mesh. This mesh is referred as *Matlab* mesh.

5.2 ELECTRIC FIELD

The *Matlab* mesh is different from the one generated with the FEM software. Multiple points of the FEM mesh are deleted. Besides, the *Matlab* mesh adds some points. The voltage solution on these points are linearly interpolated from the existing ones.

The *griddata* function is used:

$$V_g = \text{griddata}(X, Y, V, X_g, Y_g, 'linear')$$

The V_g matrix contain the scalar potential values on all points in *Matlab* mesh.

The electric field components over the *Matlab* mesh is computed based on Eq 45.

The *gradient* function is used. It computes only the voltage drops over the mesh between two consecutive points.

$$[\delta V_{g,x}, \delta V_{g,y}] = \text{gradient}(-V_g)$$

Field lines starting points are chosen on one of the wire external contour (i.e.: on the enamel overcoat).

The starting points coordinates are designated by (X_0, Y_0) .

The field lines are built using the *stream2* function. This function generates field lines over the *Matlab* mesh following Whittaker methodology [115].

$$\text{FieldLines} = \text{stream2}(X_g, Y_g, \delta V_{g,x}, \delta V_{g,y}, X_0, Y_0)$$

5.3 COMPARISON WITH THE PROPOSED METHOD

The proposed method and the method based on *Matlab* functions are compared. The parameters are given in Table 18. The Figure 94 mesh configuration is used. For *Matlab* functions, the additional mesh generated with *meshgrid* has a resolution of 600*600.

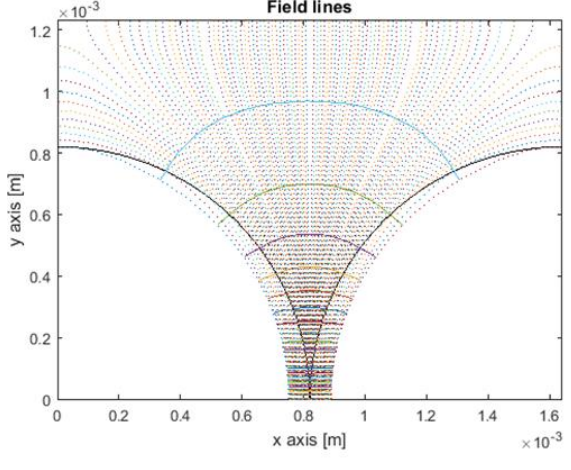
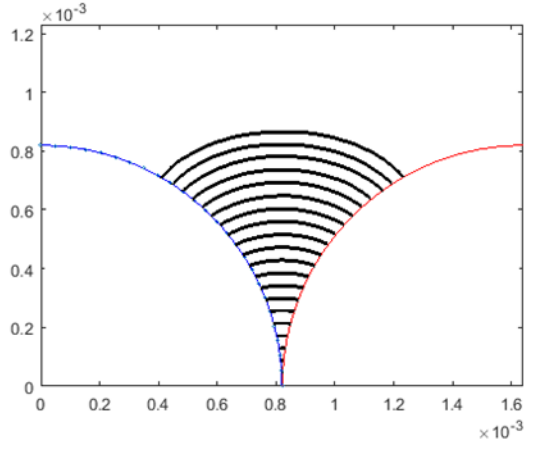
Proposed method	Matlab functions
	
20 field lines	20 field lines
Post processing time: 9.11 s	Post processing time: 1.4 s

Figure 97: Proposed method versus Matlab functions to obtain electric field lines

The post process refers to all the steps from the finite element solution to the field lines. *Matlab* algorithm is much more efficient than the developed approach. It is almost ten time faster.

In PD evaluation, only the part of the electric field line in the air gap is considered. Besides, the electric field along the field lines has to be uniform. Figure 98 displays the electric field amplitude. It can be seen that the electric field in the air gap is quite constant along the obtained field lines.

Chapter 3: Electric field lines computation

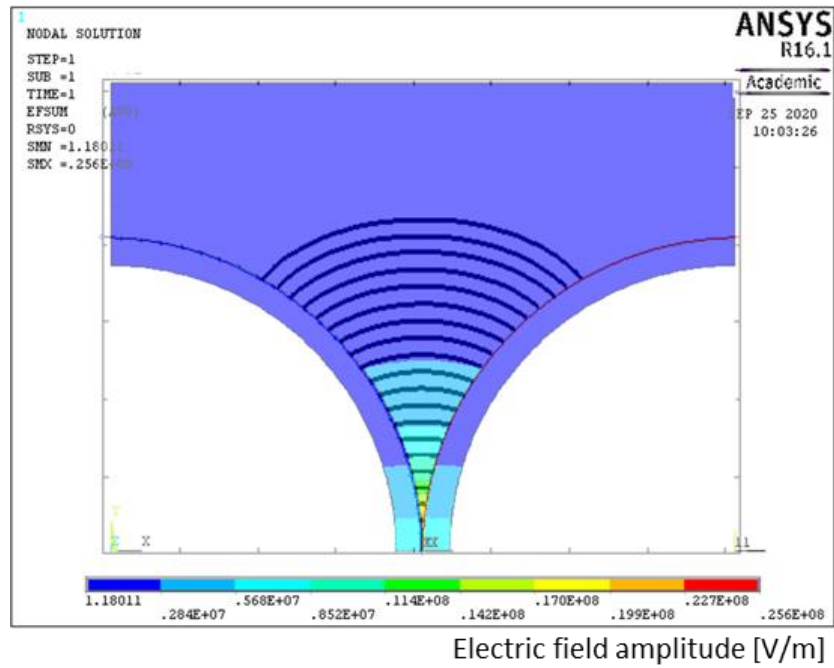


Figure 98: Electric field amplitude [V/m] obtained with finite elements

So the Paschen's criterion could be applied on the part of the field lines in the air gap to evaluate the PDIV. The PDIV is evaluated at 1040 V at 20°C, 1 bar pressure. The voltage on the enamel overcoat contours at the interface with the air is picked up at PDIV. Figure 99 displays the computed voltage drops along each part of field lines in air for the two approaches. The points intersecting with the Paschen's curve indicates field lines on which PD activity is likely to occur.

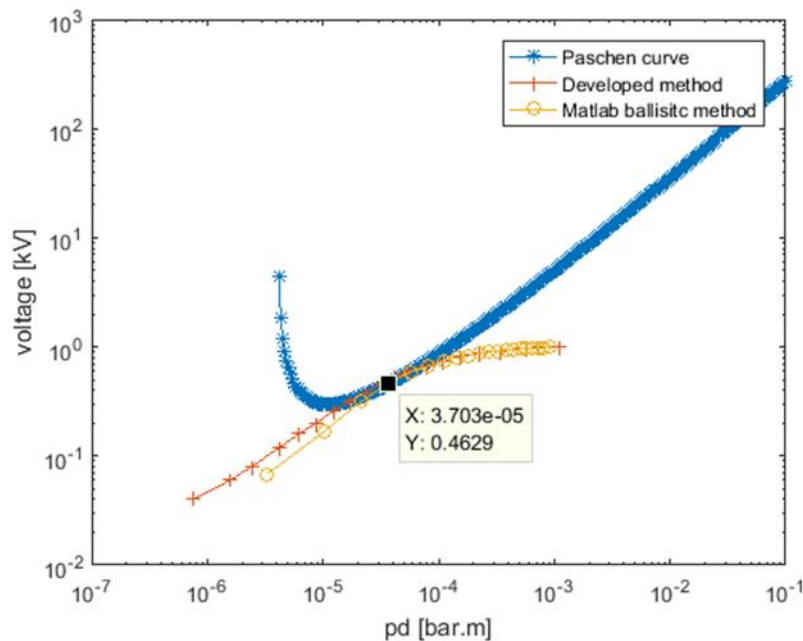


Figure 99: Computed voltage drops along field lines in air ($p=1$ bar) obtained with the two compared methods; $\gamma=0.01$

The results coincide for field lines longer than $10\ \mu\text{m}$. Both methods evaluate a PD activity on the field line of $37\ \mu\text{m}$ length in the gap. The additional inflection point on the orange curve for field lines of a few micrometers length could be due to a resolution issue and do not have to be taken into consideration.

In the tool to evaluate PD risk, the *Matlab* approach will be used. It is much faster than the developed method and gives similar results for the field lines of interest (i.e.: a few dozens of micrometers). However, *Matlab* functions are black boxes. Strange results have already been obtained with some configuration due to numerical errors. Numerical errors are much easier to deal with in the developed method because there is no black box. The whole code is accessible and modifiable.

6 CONCLUSION

The method using *Matlab* functions to plot electric field lines is most likely based on Whittaker's approach [115]. The work presented in this chapter clarifies the functions used by *Matlab*.

The method presented by Horowitz [111] make it possible to plot field lines with the electric field strength being represented by the density of lines. In this chapter, this method has been upgraded. A flux function is defined which iso-values directly give the field lines. For now, starting with the scalar potential solution obtained with Ansys Emag and using our proposed method, the computation times are long. However, it must be possible to significantly reduce the computation time by implanting the proposed method in a field calculation code. The main advantage of the proposed method is that it reuses the initial *Ansys Emag* mesh on which the scalar solution is first obtained.

Due to high computation times, the method using *Matlab* functions is used for now to derive field lines on a simplified problem with two conductors. The results given by the two methods are in good agreement for field lines in air longer than $10\ \mu\text{m}$. In the evaluation of PD using the Paschen's criterion, smaller field lines are not of interest.

In the next chapter, the validity of the Paschen's criterion for a configuration of two enamelled round wires in contact is investigated.

Chapter 4: Correction of the Paschen's criterion

1 MOTIVATIONS

1.1 CONFIGURATION DIFFERENT FROM THE INITIAL ONE

The Paschen's criterion has been presented in Chapter 2. It defines the required electric field strength in a gas gap in order to produce a self-maintained electronic avalanche. This criterion has been established for two metallic plane electrodes facing each other in an uniform electric field [81], [82].

In the literature, the Paschen's criterion has been widely used to determine the Partial Discharges Inception Voltage (PDIV) in the Electrical Insulation Systems (EIS) of electric devices (rotating machines, power electronics, connectors,...) [44], [55], [117], [118]. A representative configuration encountered in rotating machines EIS is two round enamelled wires in close contact. A 2D-finite elements model has been developed with *Ansys Mechanical APDL* (Figure 82). It has provided results showing non-uniform electric field in some air gap areas, as presented on Figure 98. Consequently, the conditions in which the Paschen's criterion has been established are not present in all the air gap surrounding the two neighbouring wires. The use of this criterion in the configuration of two enamelled wires in close contact, as it is the case in stator slots, is then questionable and need to be clarified.

1.2 EXPERIMENTAL OBSERVATION

Figure 100 confronts the observation of PD induced damage between two enamelled round wires in close contact in air (under normal pressure and temperature conditions) and the well-known Paschen's curve.

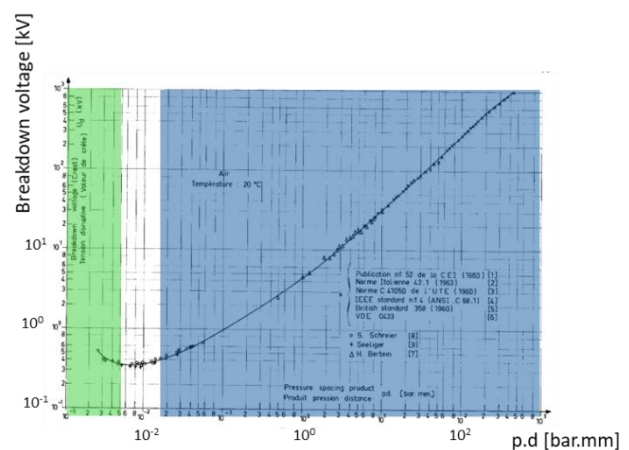
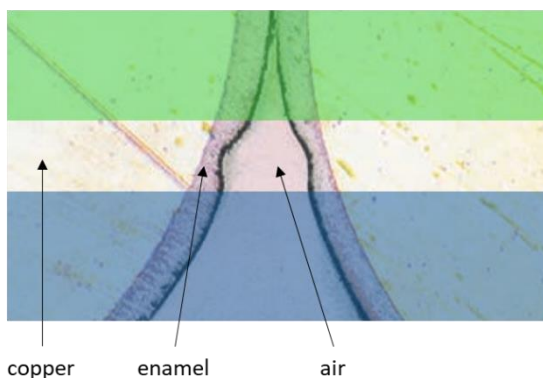


Figure 100: Left) Round enamelled wires damaged by PD [40]. Right) Paschen's curve in air [81]

As clearly shown in Figure 100, PD damage is neither located in small air gap zones (coloured in green) nor in large ones (coloured in blue), but in the intermediate air gap zone (coloured in white). This is coherent with the existence of a minimum which is well known in the Paschen's curve.

However differences have been observed by [44] between experimental and theoretical results obtained by using a 2D-finite element model. A correction was proposed by fitting the original Paschen's curve by coupling the numerical model with experimental results. This approach uses the secondary electron emission coefficient γ as a parameter, as it could be different from a material to another (Figure 101).

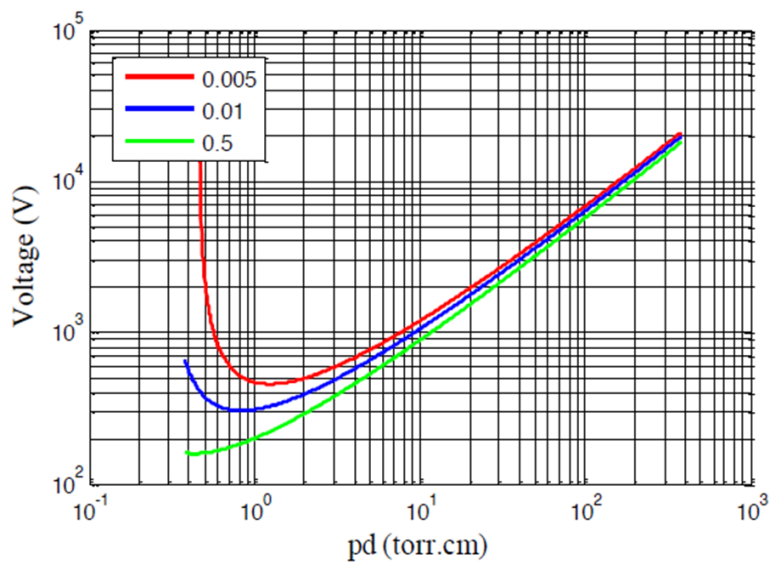


Figure 101: Paschen's curves in air plotted for three different γ values [44]

The introduction of two polymer layers may modify the mechanisms brought out by Paschen. This could even change the well-known Paschen's curve shape. However, in this work, the hypothesis consists in considering that the Paschen's curve shape is conserved (the theory is considered to be always applicable). In that case, the enamel layers only modify the breakdown voltage values. Such vertical translation of the Paschen's curve (at a given temperature and humidity rate) depends on the secondary electronic emission coefficient. In that way, the study will be focused on the evolution of the electronic secondary emission coefficient γ (also referred as Townsend's second coefficient) as a function of the copper diameters and the enamel nature used by the wire manufacturers.

2 EXPERIMENTAL APPROACH

2.1 SAMPLES

Investigation over four different enamelled copper wires were performed with (see Table 19):

- a (THEIC) Polyester-imide enamelled copper wire, overcoated with Polyamide-imide;
- a (THEIC) Polyester-imide enamelled copper wire, overcoated with a Polyamide-imide layer and overcoated with a self-bonding Polyamide layer;
- a Polyamide-imide copper, overcoated with a corona resistant Polyamide-imide layer;
- a Polyamide-imide copper, overcoated with a corona resistant Polyester-imide layer;

Three different copper diameters were investigated: 0.5 mm, 0.71 mm and 1 mm. Table 19 recaps the wires designations and layers order. The first named layer is in contact with the copper, the last named is the external layer, in contact with the air. These four magnet wires are overcoated with an external layer made with different polymers: Polyamide-imide, self-bonding Polyamide, corona-resistant Polyamide-imide and corona-resistant Polyester-imide.

Item	Polymer coating	Designation (number of layer)	Thermal class [°C]
Magnetemp CA 200	THEIC-modified Polyesterimide / Polyamide imide	PEI-THEIC / PAI (2)	200
Magnebond CAR-200	THEIC-modified Polyesterimide/Polyamide imide/self-bonding aromatic Polyamide	PEI-THEIC / PAI / self-bond PAI (3)	210
KMKED 22A	Polyamide-imide/ corona resistant Polyamide imide	PAI / PAI-PD (2)	220
KMKED 20E	Polyamide-imide / corona resistant Polyesterimide	PAI / PEI-PD (2)	220

Table 19: Recap of tested magnet wires

The samples consist in two parallel enamelled round wires in close contact. Their length is approximatively 3.5 cm. These kind of samples has been chosen instead of twisted pairs that are too complex samples. Indeed the contacts (gaps) between the wires are not well controlled and may vary along the wire and also from one sample to another. Moreover, this needs a 3D-modelling that is too complex and time-consuming to perform.

On one extremity of each wire, the enamel is removed in order to connect the samples to the high voltage power supply (and to the earth for the second wire). Three samples per diameter were tested. At both extremities of the samples, the gaps between the wires are filled with a glue, in order to avoid any discharge in this area and to be sure that PD will occur only just along the part of the wires in contact. The samples have been carefully examined by using a digital microscope (Keyence VHX1000) in order to verify whether there is no air gap between the two wires (Figure 102.b). If any small gap is detected, the sample is removed and a brand new one is built up and examined again. To detect small gaps, the sample is illuminated from below and carefully examined on all its length. If any bubble (where PD may appear) is observed in the the glue at both sample extremities, the sample is removed as well.

Figure 102 shows a typical sample. We may notice that small 'particles' are observed on the surface of the samples. This is not dust, as the samples have been carefully dusted off by blowing and cleaned with ethanol before testing. These are *protrusions* in the external layer of the wires. These protrusions appear during the wire manufacturing process presented in Chapter 1 paragraph 4.1.1 Turn-to-turn insulation. Such protrusions, that may reach 40 μm length and 20 μm tall for the larger ones, may probably modify the field distribution in air and consequently reduce the PDIV. We may however take them into account, as they are representative of defects in commercial wires, but when bigger ones are located close to the contact area, the sample is rejected. All these precautions are needed to obtain samples close to ideal ones modelled in our 2D-finite element simulations.

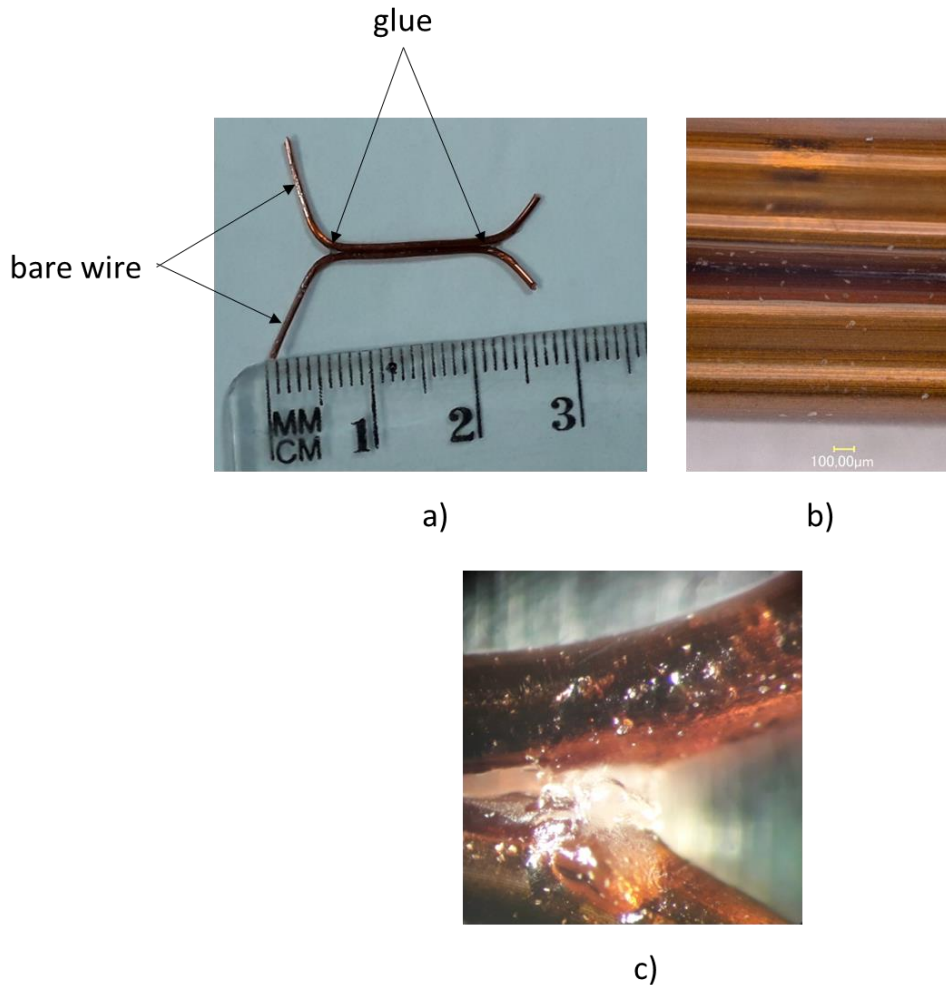


Figure 102: a) 0.71 mm 200°C studied sample; b) zoom on contact between the 2 wires; c) zoom on one glued extremity

2.2 EXPERIMENTAL PROTOCOL

Samples were tested under normal pressure and temperature conditions in a Faraday's cage to measure their respective PDIV. The experimental set-up followed, as well as we can, the IEEE standard [119]. Figure 65 displays the used setup for PD electric detection.

In order to compare both measurement and simulation, it is absolutely necessary to get the real sizes of each wire (copper diameter, enamel thickness, eccentricity) to introduce them into the simulation. These data may indeed vary from one sample to another (the standard allows a tolerance in the enamel thickness – see Annex 1). After each PDIV measurements, all samples were consequently encapsulated in Varykleer (Buehler) acrylic resin under pressure (2 bar) during twenty minutes. Encapsulated samples were then cut by using a circular saw (STRUERS SECOTOM 10) equipped with Buehler's grinder (ref 11-4217-010). Finally, the sections were polished by using at first 68 μm grains

diameters, then 22 μm ones. Samples were then observed with a digital microscope in order to get the exact sizes. Figure 103 shows an example of an observed sample.

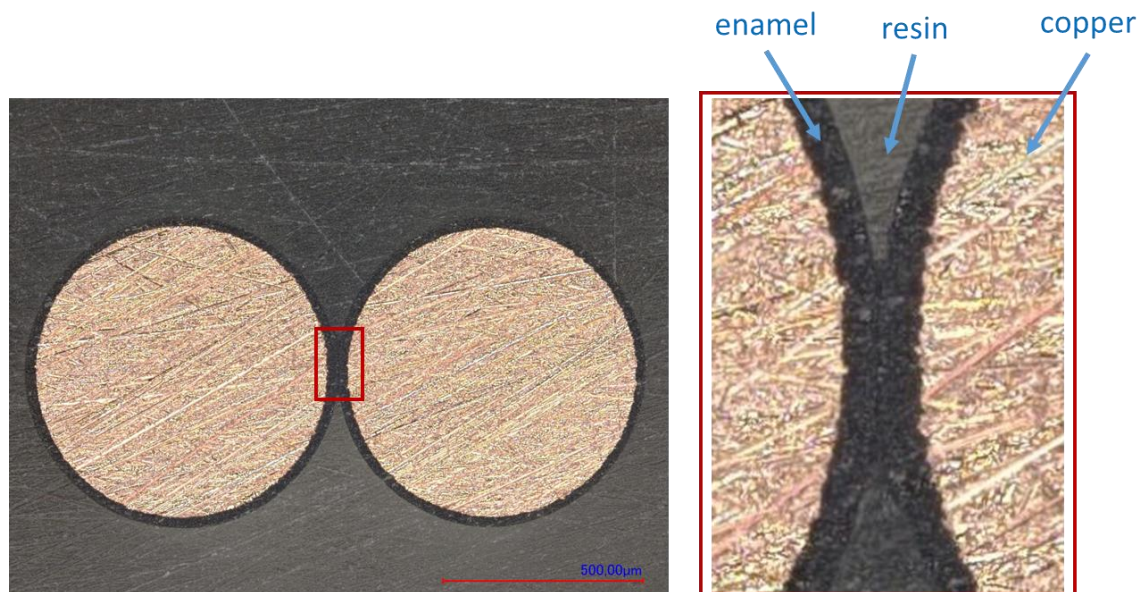


Figure 103: left) Encapsulated 200°C 0.71 mm magnet wires sample; right) Zoom in the contact area

The treatment of PDIV data were done using a two-parameters Weibull's law code [120]. A mixed numerical and finite element method [28], [121] was used to fit the original Paschen's curve with the obtained Weibull's PDIV for samples with the same copper diameter and for the same wire manufacturer. The finite element model was built with *Ansys APDL*®. The enamel profile is modelled by picking out the enamel thickness of the samples every 10 degrees by using the microscope. A spline is used to connect the points. The finite element modelling thus represents the true experimental configuration. The nodal voltage solution of this model is exported to a numerical calculation code developed on *Matlab*® 2017. This code computes the electric field lines and the voltage drops along field lines. These voltage drops are then compared to the Paschen's curve to determine whether or not there is a risk of PD appearance. The method iterates the secondary electron emission coefficient (γ) until the Paschen's curve intersects the computed voltage drops along the field lines curves

3 RESULTS

3.1 PDIV RESULTS

The PDIV (50Hz sine waveform - rms values) of the studied samples are presented in Table 20:

Chapter 4: Correction of the Paschen's criterion

Manufacturer	Copper diameter [mm]	Sample number	PDIV [Vrms]
Magnetemp CA 200	0.5	1	541; 552; 559; 536; 546; 539; 530; 559
		2	549; 534; 558; 554; 553; 563; 556; 556
		3	561; 566; 533; 557; 541; 543; 523; 544
	0.71	1	524; 539; 546; 529; 535; 541; 538; 533
		2	572; 568; 579; 580; 566; 570; 581; 574
		3	582; 588; 641; 600; 602; 631; 634; 687
	1	1	676; 696; 667; 686; 682; 702; 710; 679
		2	717; 685; 751; 737; 748; 787; 778; 749
		3	691; 713; 747; 735; 720; 759; 704; 730
KMKED 20E	0.5	1	572; 567; 546; 547; 558; 536; 530; 555
		2	546; 548; 518; 537; 539; 532; 539; 519
		3	548; 544; 539; 533; 537; 538; 541; 546
KMKED 22A	0.5	1	595; 629; 622; 604; 617; 625; 640; 631
		2	560; 575; 611; 565; 613; 607; 580; 641
		3	568; 545; 526; 559; 579; 543; 595; 549
Magnebond CAR-200 NAT	0.5	1	674; 698; 717; 719; 733; 748; 763; 788
		2	666; 672; 684; 690; 690; 691; 712; 716
		3	767; 775; 781; 805; 817; 822; 825; 877

Table 20: Experimental PDIV versus wire diameter and kind of enamel (T=23°C, RH=36%)

Eight measurements for each sample have been done successively. When the PDIV is reached, the voltage is no longer maintained in order to avoid any damage cause by PD that may modified the enamel surface and then the other remaining measurements.

For each sample, the experimental PDIV were analysed by using a two-parameters Weibull's code [122]. It gives the PDIV characteristic values (i.e.: at 63.2% of probability) and the corresponding regressive voltage with 90% confidence bounds. For each manufacturer and for a fixed copper diameter, the confidence intervals are displayed and the estimated Weibull's PDIV is determined. Such plot is shown on Figure 104 that gives an example for three 200 °C samples made with the same magnet wires (copper diameter: 0.5 mm).

Chapter 4: Correction of the Paschen’s criterion

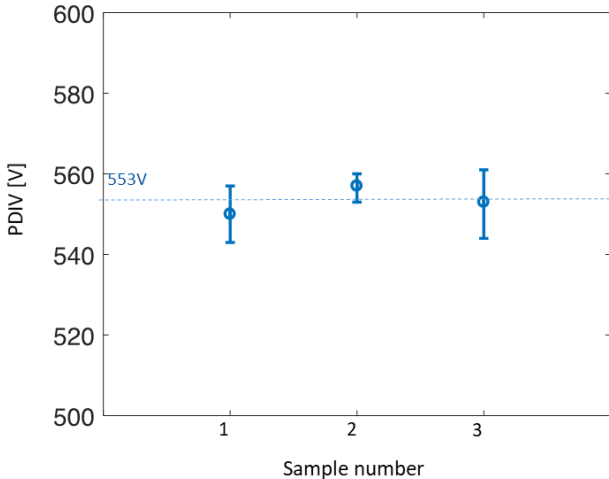


Figure 104: Measured PDIV - 0.5mm copper diameter (PEI overcoated with PAI, 200°C wire, T=23°C; RH=36%)

The PDIV values reported in Figure 104 show three characteristic PDIV close together. The average value is determined (dotted line). The average PDIV for each copper diameter and each wire manufacturer are recapitulated on Table 21.

Enamel	Copper diameter [mm]	Average PDIV [Vrms]
PEI-THEIC/PAI	0.5	553
	0.71	580
	1	721
PEI-THEIC/PAI/PA-self-bonding	0.5	768
PAI/PAI-PD	0.5	588
PAI/PEI-PD	0.5	546

Table 21: Average PDIV versus manufacturer and copper diameter

It should be noticed that the highest PDIV value is obtained with the 0.5 mm copper diameter PEI-THEIC/PAI/PA self-bonding wire. That wire has three layers of insulation leading to a higher enamel thickness, then the higher PDIV. The external additional layer is used as a varnish and may be polymerized by different technics (self heating by Joule’s effect, oven, UV).

These average PDIV values will be applied as boundary conditions on the 2D-finite element model in the proposed method (Figure 106).

3.2 DIELECTRIC CONSTANT MEASUREMENTS

The equivalent dielectric constant of each enamel were measured by using a Novocontrol Alpha-A dielectric spectrometer [123]. This device is able to determine the dielectric constant in a wide range of temperature and frequency.

We used our magnet wires samples. For that, they were metallized (gold sputtering - pressure 10^{-5} mbar) in order to form a cylindrical coaxial capacitor as illustrated on Figure 105. It is a vacuum metallization; the resulting gold deposit has a thickness of about 125 nm.



Figure 105: Gold metallization of an enamelled copper wire. Left) Equivalent 2D-coaxial capacitor - R_1 : external radius; R_2 : copper radius; e : enamel whole thickness; Right) Real sample for test in the Novocontrol.

At first, the parasitic capacitance is evaluated using both 2D- and 3D-finite elements model. Due to the limitation in the number of elements, a wire of $100 \mu\text{m}$ length is considered.

The capacitance values are derived from the total electric energy of the models:

$$C_{2D}[F.m] = \frac{2 * E_{2D} [J.m]}{V^2} \quad \text{Eq 84}$$

$$C_{3D}[F] = (C_{2D} + C_{par}) = \frac{2 * E_{3D} [J]}{V^2} \quad \text{Eq 85}$$

In these relationships, C_{2D} and E_{2D} are the respectively the linear capacitance and the electric energy on the 2D-model, V is the applied voltage peak value. C_{3D} and E_{3D} are the capacitance and electric energy in the 3D-model. C_{par} represents the parasitic capacitance.

Let us consider one configuration presented in Table 22.

Chapter 4: Correction of the Paschen's criterion

Copper radius	522 μm
Enamel thickness	36 μm
Enamel dielectric constant	4.07
Applied voltage	1 V_{rms}
Wire length	$L_{tot} = 100 \mu\text{m}$

Table 22: Test configuration for parasitic capacitance evaluation

The C_{2D} and C_{3D} are computed using Eq 84 and Eq 85. The main results are given in the Table 23 below:

	2D-model	3D-model
Electric energy	$E_{2D}=0.339497 \cdot 10^{-8} \text{J.m}$ $E_{2D} * L_{tot}=0.339497 \cdot 10^{-12} \text{J}$	$E_{3D}=0.36652 \cdot 10^{-12} \text{J}$
Capacitance	$C_{2D} * L_{tot} = 0.34 \text{pF}$	$C_{3D} = 0.37 \text{pF}$

Table 23: 2D- and 3D-capacitance evaluations

The parasitic capacitance is low (8% of the total capacitance) for a 100 μm -long wire, so that we can reasonably neglect it in the case of wire length of several centimetres. So the results given by the Novocontrol are directly the wanted coaxial equivalent capacitance.

The voltage (1 V_{rms}) is applied to the copper core via the pin. The sample is deposit on a grounded electrode. The sample is adapted to the Novocontrol electrode dimensions, that is the reason why in Figure 105 it is bent. The equivalent capacitor corresponds to a coaxial capacitor of total length $L_{tot} = 2 * L$.

To get a good measurement with the Novocontrol, the sample capacitance has to be bigger than 100 pF. The 2D-finite element model of the enamelled wire is used to determine the required total length L_{tot} . With $L_{tot}=5 \text{ cm}$, the evaluated capacitance is 170 pF, considering an enamel with a dielectric constant of 3.5.

A coaxial capacitor analytical formulation is given by Eq 86. The parameters are defined on Figure 105.

$$C = \varepsilon_0 * \varepsilon_r * \frac{2 * \pi * L_{tot}}{\ln\left(\frac{R_1}{R_2}\right)} \quad \text{Eq 86}$$

With C the capacity of the sample, ε_r the wanted enamel dielectric constant.

However, to the Novocontrol requires a diameter D because it considers a disc capacitor Eq 87:

$$C = \varepsilon_0 * \varepsilon_r * \frac{\pi * \left(\frac{D}{2}\right)^2}{e} \quad \text{Eq 87}$$

With e being the enamel thickness.

By identification, it comes that the equivalent diameter of the sample seen by the Novocontrol is:

$$D = 2 * \sqrt{\frac{2 * e * L}{\ln\left(\frac{R_1}{R_2}\right)}} \quad \text{Eq 88}$$

This value is given to the Novocontrol prior to the measurements.

Finally, the dielectric constant is derived from the capacitance computation Eq 87. The enamel thickness e is obtained using a digital microscope. Table 24 gives the computed dielectric constants at 20°C and 50 Hz:

Wire (0.5 mm)	Polymer coating	ϵ_r (20°C, 50 Hz)	Capacitance (20°C, 50 Hz) [pF]
Magnetemp CA 200	PEI-THEIC/PAI	3.3	162.81
Magnebond CAR-200 NAT	PEI-THEIC/PAI/PA self-bonding	4.4	122.27
KMKED 22A	PAI/PAI-PD	3.8	108.08
KMKED 20E	PAI/PEI-PD	4.2	126.84

Table 24: Samples computed dielectric constants at 20°C, 50 Hz

These values are in range to the ones found in the literature [124]. The measured dielectric constants will be introduced into the 2D-finite element model in the proposed method (Figure 106).

4 MIXED EXPERIMENTAL AND NUMERICAL APPROACHES

The experimental data are introduced into a numerical code which iterates the secondary electron emission coefficient value γ in order to make the Paschen's curve intersect the simulated voltage drop across field lines length curves. The experiments were conducted under normal temperature and pressure conditions. Thus, the computed γ are only valid at atmospheric pressure and 20°C.

The algorithm of the mixed experimental and numerical proposed approach is presented in Figure 106.

Chapter 4: Correction of the Paschen's criterion

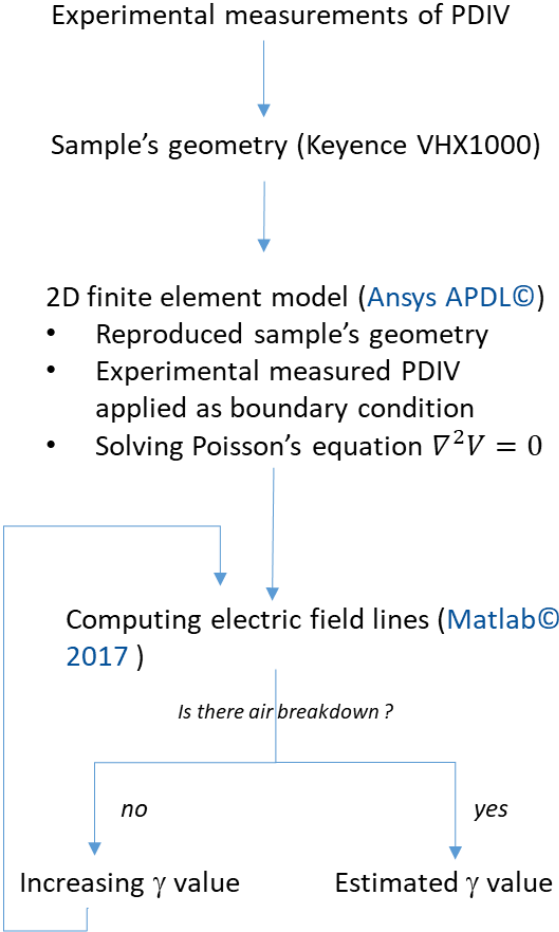


Figure 106: Algorithm, combining experimental and numerical approaches, used to determine γ

Field lines are computed by using Matlab approach presented in Chapter 3, paragraph 5: Another method using *Matlab* functions. Figure 107 displays an example of field lines between two 0.71 mm copper diameter wires in close contact.

Chapter 4: Correction of the Paschen's criterion

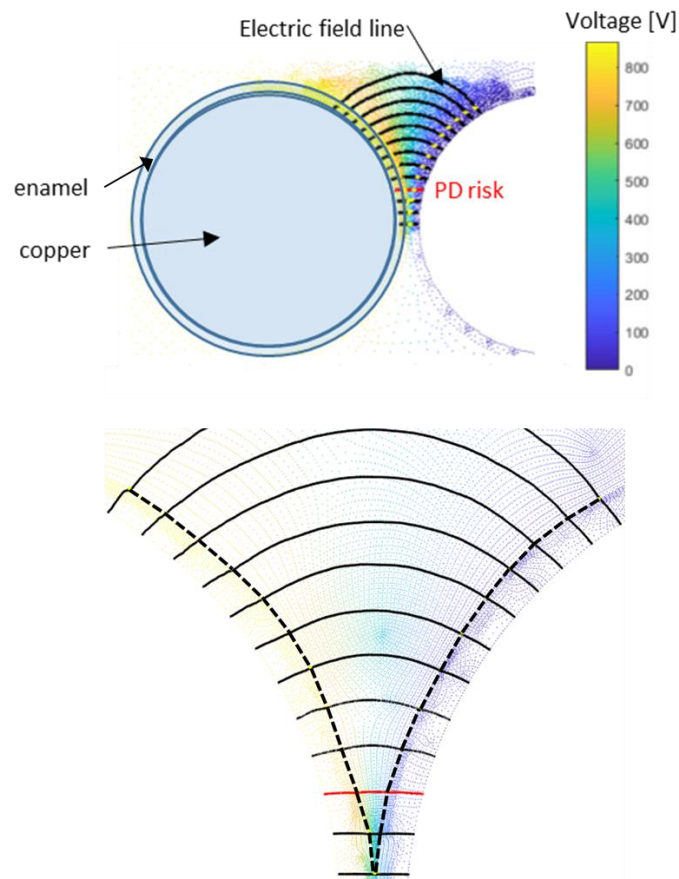


Figure 107: Top) Electric field lines. Bottom) Zoom. 0.71 mm copper diameter wire meshing. Dot lines represent the external wire contour

Figure 108 displays the corresponding voltage drop versus field lines length in the Paschen's plot ($p=1$ bar, $T=20$ °C). Two Paschen's curves computed with two values of γ are displayed. For $\gamma=1.1 \cdot 10^{-3}$ the Paschen's curve intersects the simulated one for an applied voltage corresponding to the experimental PDIV. Thus, PD appear on the red field line corresponding to the intersection point (Figure 109-bottom).

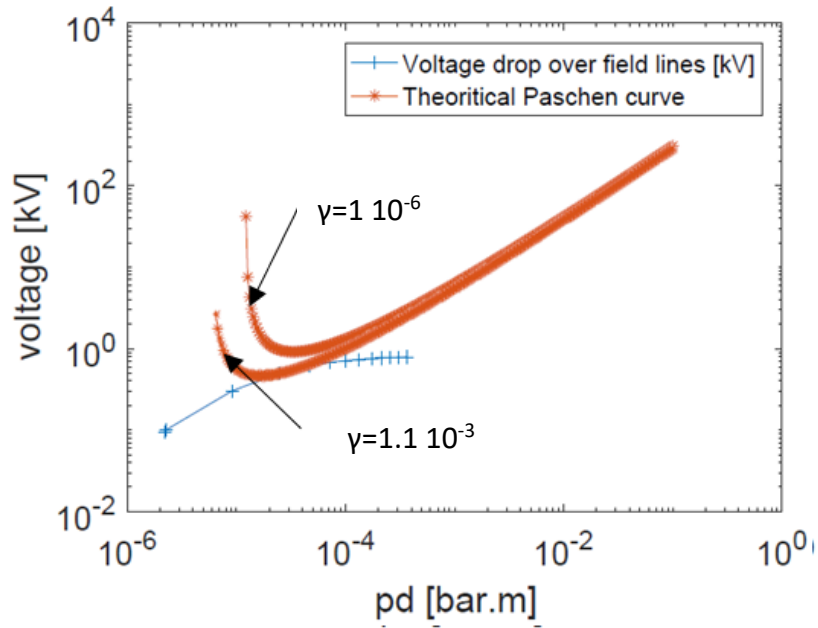


Figure 108: Corresponding voltage drop versus field lines length (in air, $p=1$ bar, $T=20^{\circ}\text{C}$)

5 SINGLE LAYER INSULATION

Most of the commercial enamel overcoating the copper wires are composed of multiple layers of polymers. The dielectric constant of each layer may be different. The slot insulation may also be multi-layered. Previously, we have considered a unique insulating layer, taking into account the equivalent global permittivity of all the layers. In order to verify whether this assumption is valid, we have estimated the PDIV for a multi layers insulation and a single one (with an equivalent dielectric constant). The simulated system is composed of two enamelled round wires in close contact, as presented in Figure 82. Table 25 gives the parameters values.

Parameter	Value
Copper diameter	0.5 mm
Enamel thickness	31.5 μm
Multi layered configuration:	
• Dielectric constant layer 1	• 3.5
• Dielectric constant layer 2	• 4.5
Single layered configuration:	
• Equivalent dielectric constant	• 3.94

Table 25: Multi layers versus single layer enamel parameters

In the case of multi-layered enamel, each layer has the same thickness. The given enamel thickness in Table 25 is the total thickness (layer 1 + layer 2).

The equivalent dielectric constant is derived from the capacitance calculation. The capacitance associated to layer 1 (C_{layer1}) and layer 2 (C_{layer2}) of the enamel are connected in series. The equivalent capacitance (C_{eq}) is expressed as follow:

$$\frac{1}{C_{eq}} = \frac{1}{C_{layer1}} + \frac{1}{C_{layer2}} \quad Eq\ 89$$

In both configurations, 2-layers and 1-layer, the same geometry has been considered. The capacitances C_{layer1} and C_{layer2} are computed on half the enamel thickness. In the capacitance computation, the only variable is the material dielectric constant. Eq 89 can be written as follow:

$$\frac{1}{\epsilon_{eq}} = \frac{1}{2 * \epsilon_{layer1}} + \frac{1}{2 * \epsilon_{layer2}} \quad Eq\ 90$$

The PDIV for both configurations was evaluated under normal temperature and pressure conditions by using the 2D-finite element model introduced in Chapter 3 and a secondary electron emission coefficient $\gamma=9 \cdot 10^{-4}$. Figure 109 displays the voltage drop across the field lines at 1 bar.

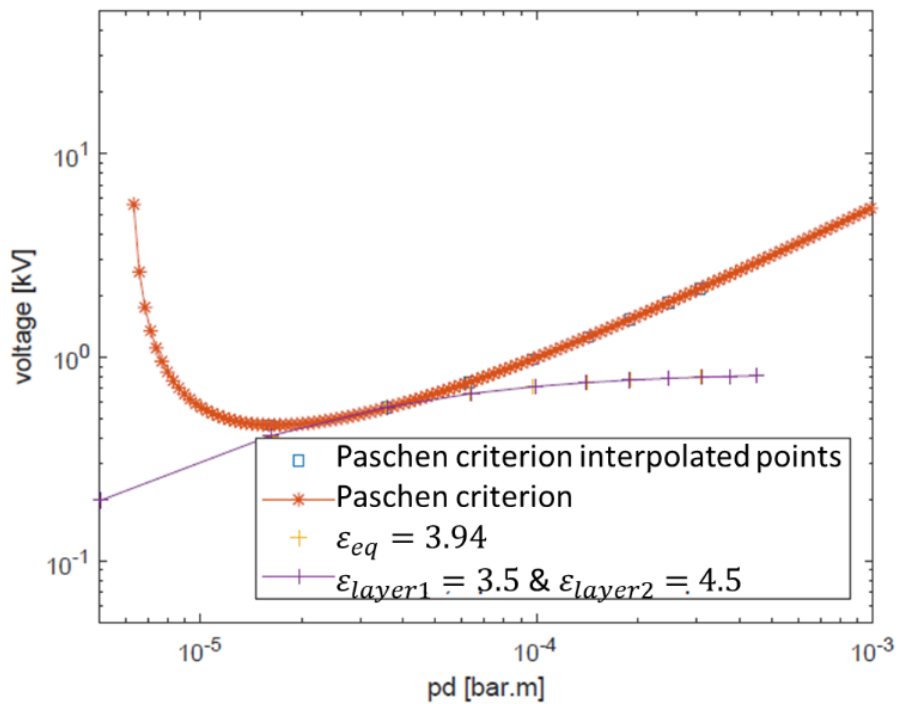


Figure 109: Voltage drop across field lines in air gap with a multi-layers enamel versus an equivalent single layered enamel. Applied voltage is 840 V_{peak}

Clearly, the results given by the model in the air gap by considering an equivalent single layer insulation are the same that the one considering a multi-layered one (the dots are superimposed).

In the PD evaluation tool, the multi-layered enamel and the multi-layered slot insulation will thus be considered as an equivalent single layer, as this do not affect the voltage repartition in the air, so that

the PDIV is unchanged. However, slot insulation may be composed of different layers having great differences between their permittivity, i.e.: organic (polymer) and non-organic layers (polymer filled with ceramic, mica,...). In that case, the same modelling has to be performed to be sure of the veracity the of one layer assumption.

6 SECONDARY ELECTRON EMISSION COEFFICIENTS

The impact of the wire radius in the secondary electron emission coefficient γ is presented in Figure 11 for a Magnetemp CA 200 wire. The γ coefficient is computed for three different copper diameters: 0.5 mm, 0.71 mm and 1 mm. The γ values displayed in Figure 110 result from a Weibull's law applied to treat the γ values computed of all samples for each copper diameter.

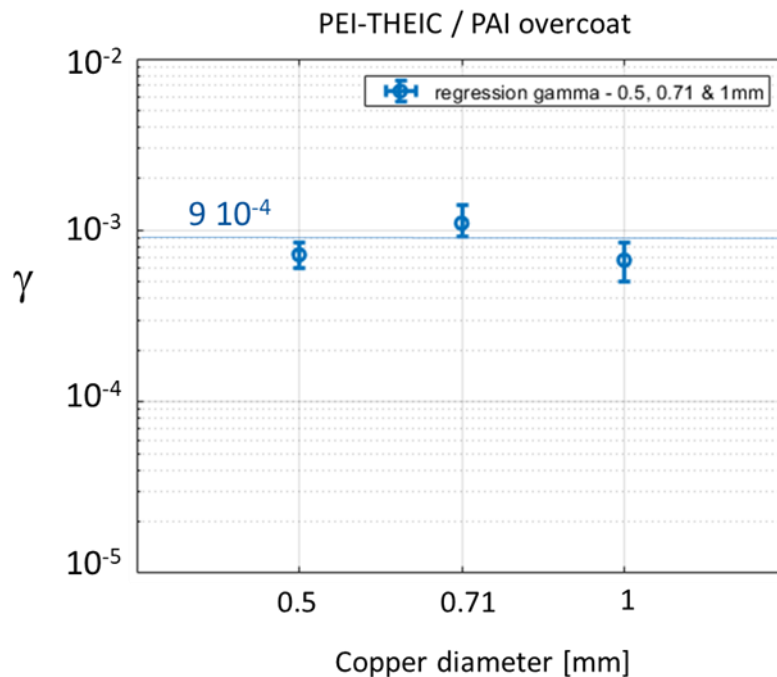


Figure 110: Secondary electron emission coefficient for 0.5 mm, 0.71 mm and 1 mm copper diameter (PAI overcoat, $T=23^{\circ}\text{C}$, $RH=36\%$)

The three γ coefficients found for a PAI overcoat enamel are close together. The observed differences may be due to the random distribution of defects (protusions) and the difference in the external layer structure (even if they are made with the same monomer, the final structure depend on the deposit and polymerization process that may be different versus wire diameter). In Figure 111 we have drawn the effect of changing the γ value on the Paschen's curve. As clearly shown, from 6.7×10^{-4} to 11×10^{-4} , the resulting Paschen's curve is quite the same (Figure 111). The difference between the lowest an

highest Paschen's minimum values is less than 7% (i.e.: 32V). The mean value is $\gamma_{PAI}=9 \cdot 10^{-4}$. It is almost one decade lower than the traditional γ value found in the literature for metallic electrodes ($\gamma = 0.01$). A similar value is obtained by [125].

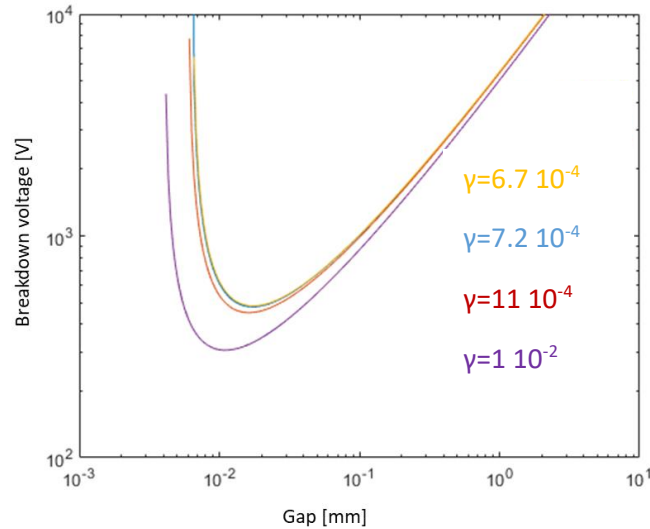


Figure 111: Paschen's curves in air for 3 γ coefficients

6.1 IMPACT OF THE INCOMING ANGLE OF BOMBARDING IONS

The impact of the ions incident angle of attack has been investigated in [126]. A monochromatic H_g^+ ion beam was used to bombard different kinds of electrodes. The energy of the incoming ion beam was adjusted from 5 to 25keV. Three angles of attack were tested: 0° , 30° and 45° . The higher the angle, the higher γ . The difference is amplified with the energy of the incoming ion beam.

In our experiments, it is assumed that the positive ions move along the field lines. Therefore, they are impacting the wire with a null incidence angle (i.e.: perpendicular to the bombarded area). We have investigated the incidence angle (Δ) of straight lines. It is calculated between the straight field line and the normal to the tangent at the point of impact. Copper diameters from 0.5 to 5mm were investigated. Figure 112 displays the field lines in the air gaps computed using the 2D-numerical model. The red field lines are subject to PD. The incoming angle Δ is introduced. Table 26 recaps the evolution of the incoming angle as a function of the wire copper diameter. It appears that the bigger the wire diameter, the closest to a straight line the field line in the air gap where PD occur.

Chapter 4: Correction of the Paschen's criterion

However, it is not certain that the positive ions move along the electric field lines. Their trajectory may be perturbed by complex interactions and by particles distribution in the air gap. Their mass may also reinforce these perturbations.

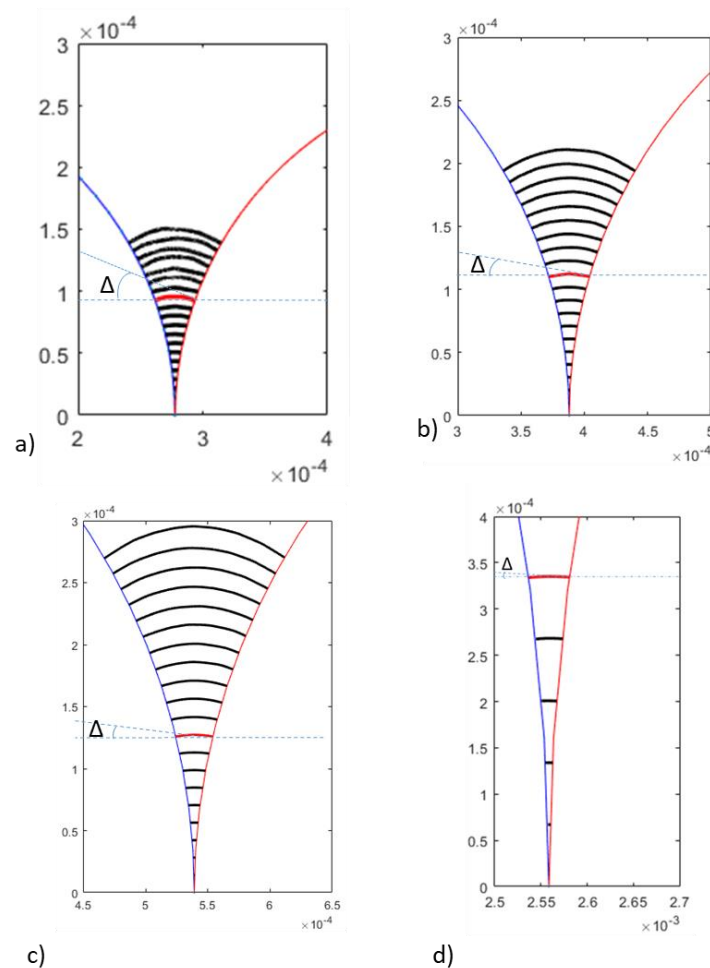


Figure 112: Field lines in air gap between two enamelled copper wires; Red lines are subject to PD; Δ is the incidence angle of positive ions following a straight field line ; Copper diameters of 0.5 mm (a), 0.71 mm (b), 1 mm (c) and 5 mm (d); Axes are in meter

Copper diameter [mm]	Length of the field line where PD occur	Incidence angle Δ (with straight field line) [degree]
0.5	32 μ m	23°
0.71	32 μ m	11°
1	37 μ m	8°
5	43 μ m	4°

Table 26: Incidence angles for copper diameters between 0.5 and 5mm - Evaluated at PDIV considering an average grade 2 insulation thickness (see Annex 1)

Let us evaluate the energy of a positive ion impacting the enamel layer for the configuration corresponding to Figure 112 c). The enamel thickness is $e=39.25 \mu\text{m}$ and the evaluated PDIV is 970 Vpeak. The resulting voltage drop in the air gap is evaluated using Eq 92 and equals 604 Vpeak. A

positive nitrogen ion N_2^+ is considered in the air gap. We suppose that this ion is accelerated from one side of the air gap to the other without any collision. Thus, only the electric force is applied to this ion. That force is a conservative one, so the mechanical energy of the ion is constant. The mechanical energy is the sum of the kinetic energy and of the potential energy. Initially, we consider that the ion starts with zero kinetic energy. Thus, the mechanical energy equals the potential energy alone. The potential electric energy of the ion is of 604 eV. That energy is fully converted to kinetic energy when the ion crashes on the enamel layer on the other side of the air gap. In [126], a 30° incidence angle has an impact on the γ coefficient for an energy bigger than 5 keV. We may reasonably consider that for enamelled wires of diameters ranging from 0.5 to 5 mm, γ will only depend on the external layer chemistry (and do not depend on the copper wire diameter). Consequently, if γ is estimated from an experiment performed with one wire, this value may be used for enamelled wires having the same external polymer layer but having another copper diameter.

6.2 INFLUENCE OF THE ENAMEL CHEMISTRY

The influence of the enamel chemistry is presented in Figure 113 for 0.5 mm enamelled wires. Different wires were tested with different external layers ($p=1 \text{ bar}$; $T = 23 \text{ }^\circ\text{C}$). The results show that γ naturally depends on the enamel overcoat. From left to right, γ values are: $7.2 \cdot 10^{-4}$, $5.5 \cdot 10^{-4}$, $6.2 \cdot 10^{-4}$ and $5.5 \cdot 10^{-5}$.

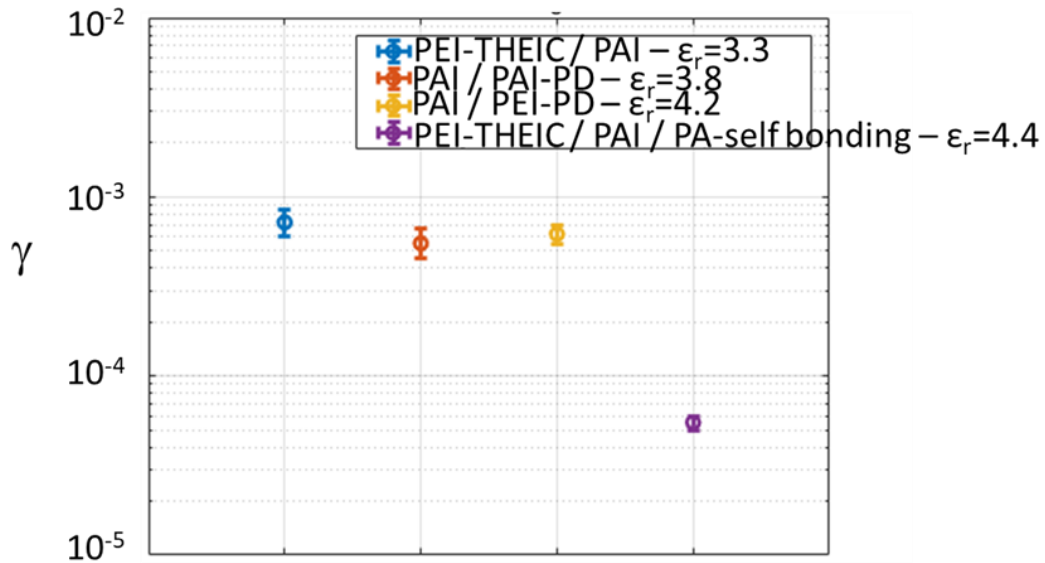


Figure 113: γ versus external enamel layer nature - copper diameter 0.5 mm – $T=23^\circ\text{C}$, $RH=34\%$

For PAI, PAI-PD and PEI-PD external overcoats, the obtained values are very close together while for self-bonding PA it is almost one decade lower. In the particular case of self-bonding PA, the polymerization is not achieved. We can reasonably consider that this value may change after the curing process.

As a conclusion, preliminary measurements of such important coefficient has to be performed prior to any modelling.

7 ADDITIONAL EXPERIMENTATION

In the experiments previously described, no proof has been found to dismiss the Paschen's theory in our samples. However, another experimentation has been performed in order to check that both Paschen's theory and our proposed methodology are applicable. The idea consisted in determining the PDIV between two enamelled round wires in parallel to rebuilt the Paschen's curve.

7.1 SET UP

Samples were prepared with 3 mm copper diameter wires overcoated with PAI (wire length about 3 cm). The choice of the diameter was mainly due to the great rigidity of the samples, allowing an easy manipulation. The two pieces of enamelled wires were manually positioned and glued. One on the micrometre screw and the other on the support (see Figure 114). The screw and the support are

electrically isolated. The gap is approximately obtained by interleaving wedges of the wanted thickness in between the wires. Then the two wire samples are glued on the micrometre screw measuring contacts. Once the glue is dry, the wedge was removed and the potential was brought by two needles to the copper cores on the edge. The needles were equipped with small springs to ensure a good electrical contact with the copper. Some glue was finally applied at each wire extremities to avoid any discharge in these areas. If bubbles were found inside the glue, the sample was removed. It is assumed that the wires are infinitely long so that the 2D-finite element model is relevant to determine the field lines and the voltage drops in air for the corresponding gap value. A particular attention was also paid to be sure that the two wires were perfectly parallel. This has been checked by using an electronic microscope. In this condition, the electric field may still be calculated with a 2D-finite element model, while if the wires are not parallel, the electric field is strongly modified and need to be modelled by a 3D-finite element model (see an example in Figure 115).

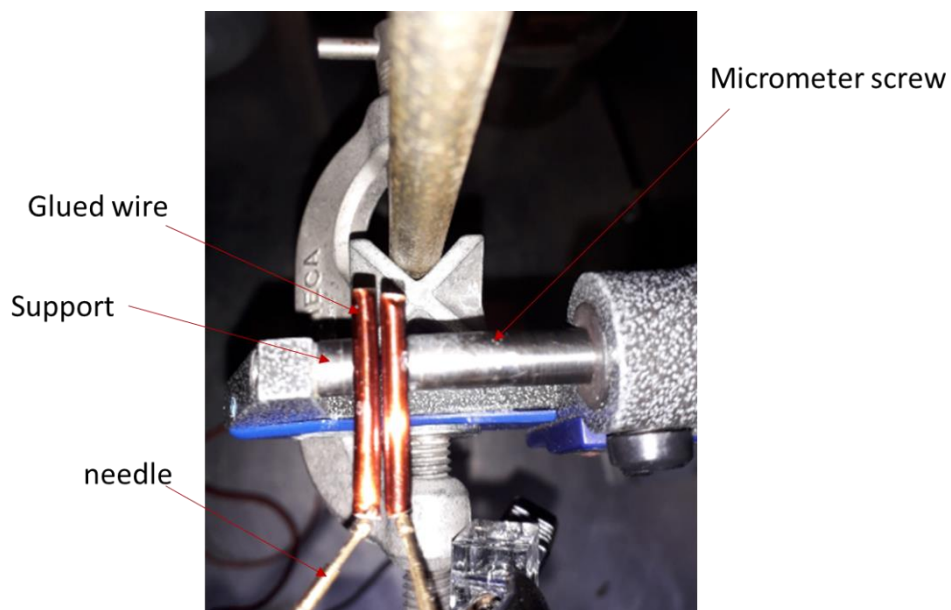


Figure 114: Experimental sample holder for rebuilding the Paschen's curve with two parallel enamelled wire samples

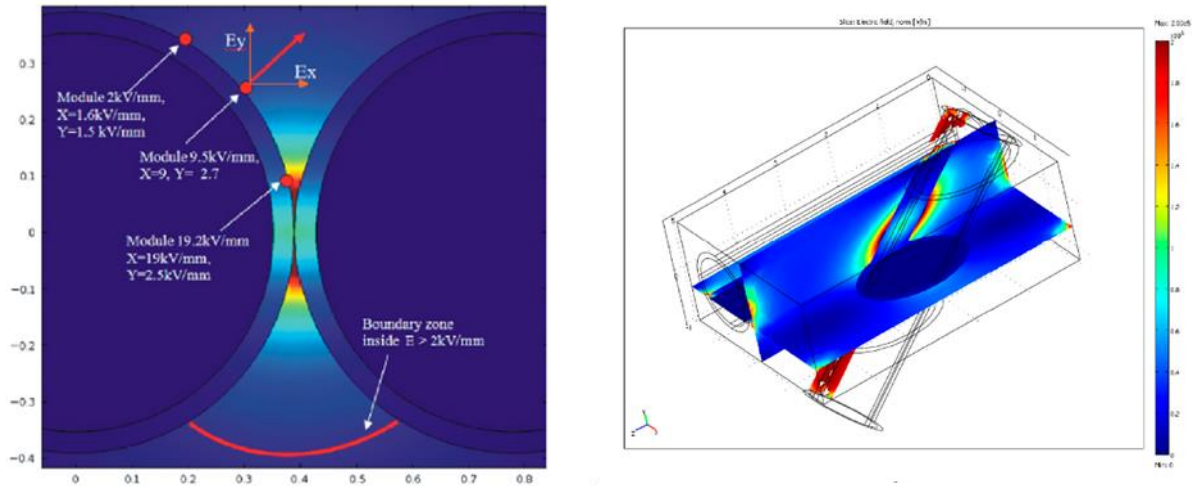


Figure 115: Electric field calculation between to enamelled wires in close contact [127]. Left) parallel wires: $E_{max}=19.2$ kV/mm; Right) non-parallel wires: $E_{max}= 2$ kV/mm. 0.7 mm enamelled wires; enamel thickness: $100 \mu\text{m}$; dielectric constant: 4.2; Applied voltage: 2 kVpeak.

The micrometre screw was used to obtain the parallelism. If the wires were not satisfactorily fixed (as shown in Figure 116 where the gap is not constant), they were removed to built-up another ones. A very large number of attempts were necessary to obtain suitable samples!

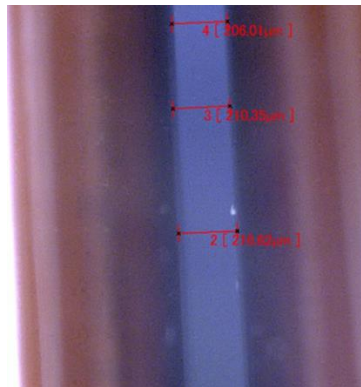


Figure 116: Gap observed with an electronic microscope in between two non-rigorously parallel enamelled wires

7.2 RESULTS

The measured PDIV and the corresponding gap values are presented in Table 27.

Measured gap [$\mu\text{m} \pm 2\mu\text{m}$]	PDIV [Vrms]
30 μm	634; 589; 631; 616; 593; 611; 619; 600
100 μm	887; 859; 893; 921; 885; 880; 922; 942
140 μm	985; 1033; 1080; 972; 1007; 993; 1014; 1004
210 μm	1318; 1319; 1221; 1301; 1299; 1253; 1191; 1248

Table 27: Experimental PDIV for different values of the gap in between the two parallel enamelled wires

Chapter 4: Correction of the Paschen’s criterion

Figure 117 displays a cross section of the tested 3mm diameter PAI overcoated wires. The enamel thickness entered in the numeric model is close to 50 μm (see Figure 117). The dielectric constant is taken equal to 3.5.

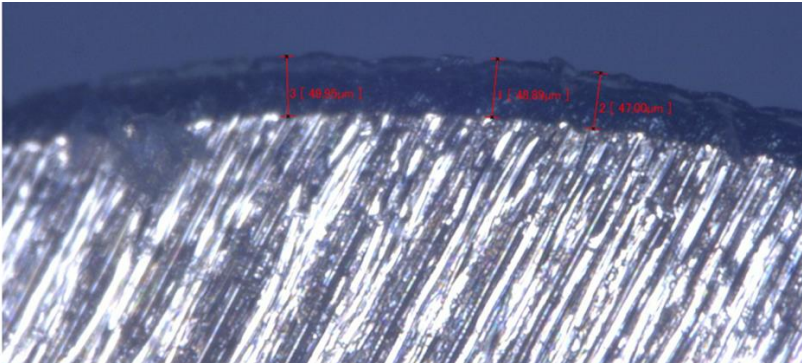


Figure 117: Cross section of a 3mm copper diameter wire (PAI overcoat)

The experimental PDIV were treated using the 2 parameters Weibull’s law. The characteristic PDIV at 63% along with the 90% boundary intervals were determined. These data were entered in the previously introduced numeric model. The electric field lines was thus computed. The voltage drops along the field line crossing the air gap were collected. It is designated as the breakdown voltage V_{bd} .

Table 28 recaps the voltage drops (peak values) of the field lines crossing the air gaps.

Measured gap [μm]	V_{bd} in air [Vpeak]
30	437
100	1000
140	1210
210	1612

Table 28: Breakdown voltages of air gap between parallel enamelled wires versus gap thickness

Figure 118 displays two Paschen’s curves plotted with two γ values coefficients: $\gamma_{metal} = 0.01$ and $\gamma_{PAI} = 9 \cdot 10^{-4}$ (mean value calculated for different diameter of PAI overcoated wires – see Figure 110). The computed air breakdown voltages, calculated from the measured PDIV, are positioned on the graph.

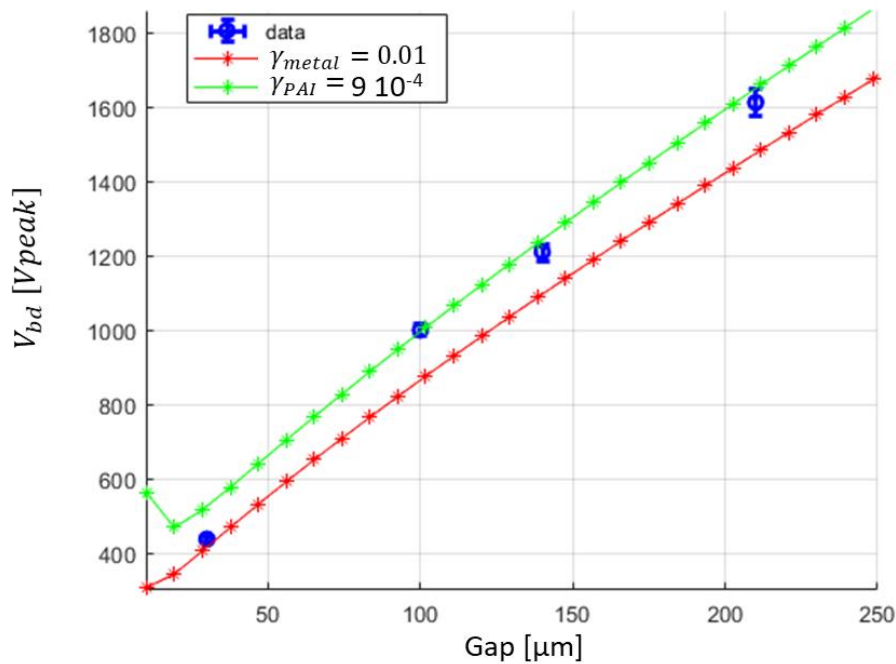


Figure 118: V_{bd} of air gap between parallel enamelled wires versus gap thickness

As clearly shown in Figure 118, experimental air breakdown voltage data obtained with PAI overcoated wires fit well with the theoretical Paschen's curve plotted by using the γ value obtained with this kind of wire. Concerning the measurement performed for the lower gap (i.e.: 30 μm), the effect of surface irregularities and/or defects may strongly affect (by lowering) the PDIV. This value should not be considered in the same way as the others.

8 CONCLUSIONS AND PERSPECTIVES

In this chapter it has been demonstrated that the Paschen's criterion is still valid in a configuration of two enamelled round wires in close contact. A methodology to determine the secondary electron emission coefficient of enamelled round wires was proposed. It combines both experimental data and numerical models. This coefficient is obtained by fitting the Paschen's curve with a computed voltage drops along straight field lines curve. Close results have been obtained for the same overcoating enamel (PAI) with different copper diameters, i.e.: $\gamma=7.2, 11$ and $6.7 \cdot 10^{-4}$ for 0.5, 0.71 and 1 mm respectively. It can be concluded that if a secondary electron emission coefficient is found by using this proposed method on a sample having a given copper diameter, this coefficient could be used to predetermine the PDIV of wires having others copper diameters but made with the same overcoating enamel. This study has also shown that this method has to be applied each time the wire enamel

Chapter 4: Correction of the Paschen's criterion

chemistry is changed or if the same thermal class wire is used but provided by different manufacturers. However, the developed numerical model is a static one. Physical dynamic effects, such as memory effect [128], are not taken into account in the model. Our model is thus only valid when the first discharges occur.

In the next chapter, the corrected Paschen's criterion is used to evaluate PDIV and compute sizing graphs for the insulation layers.

Chapter 5: Tool to predict PD activity in machine slot

This chapter presents the Partial Discharge Evaluation Tool (PDET) that has been developed. It has been coded with Matlab. It provides recommendations regarding the sizing of the Electrical Insulation System inside a stator slot. As it is considered only one phase per slot, the hot spot for Partial Discharges (PD) activity are turn/turn and turn/slot contacts. It could be naturally upgraded to treat the case of slots embedding more than a single phase.

This chapter starts by considering the impact of both temperature, frequency and pressure. Then the Partial Discharge Evaluation Criterion (PDEC) will be given. It will take into account the variable environmental conditions which should be withstood by the motor in a non-pressurized area. Simplified Analytical Models (SAMs) of turn/turn and turn/slot contacts will be developed. These SAMs will be validated with 2D Finite Elements Models (2D FEMs). Parametric studies will be done by using the SAMs in order to compute design graphs for the enamel and slot liner insulation design. Finally, the graphs will be arranged into the PDET. The solutions provide the minimal thicknesses necessary to withstand the determined electric stresses in both turn/turn and turn/slot contacts.

1 DIELECTRIC CONSTANT EVOLUTION WITH TEMPERATURE AND FREQUENCY

In inverter fed motors, the dielectric properties of insulators may change as a function of both working temperature and converter frequency. To study the impact on the PDIV, some enamelled wires have been characterised by using a dielectric spectrometer (Novocontrol Alpha-A). The measurement method was presented in Chapter 4. Figure 119 displays the evolution of the dielectric constant as a function of both applied temperature and frequency for two different enamelled wires.

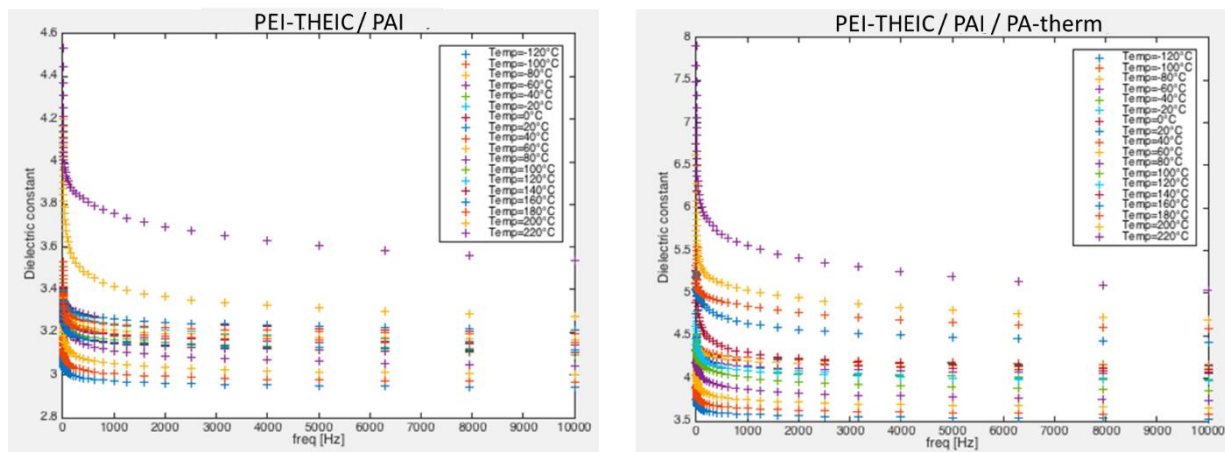


Figure 119: Evolution of the dielectric constant as a function of both applied temperature and frequency for two enamelled wires (PEI-THEIC/PAI and PEI-THEIC/PAIS/PA-therm)

It can be seen that the dielectric constant ϵ_r is classically inversely dependent on the frequency. This evolution is strongly dependent on the nature of the material. Thus, it is absolutely necessary to characterise the dielectric materials following a similar approach presented on Chapter 4, prior to any

modelling, as no general model can be used. Even if the data sheets of different commercial enamelled wires indicate that they are made with the same enamels, it is necessary to proceed to such dielectric characterization as it is well known that polymers properties are strongly dependent on their thermo-mechanical history which may be different from one manufacturer to another.

2 PARTIAL DISCHARGE EVALUATION CRITERION

In stator slot, where enamelled wires having diameters ranging from 0.5 to 5 mm are used under normal conditions of temperature and pressure, the PD risk was evaluated to take place in gaps of about 30 μm length (Chapters 2,3 and 4).

The strong environmental variations along the mission profile of an aircraft have been highlighted in Chapter 2. Some deviations to the Paschen's curve are then taken into account (Table 12). Such deviations have been verified experimentally for gaps of about 1 mm with a variable pressure. However, it has been pointed out that for a same pd product (with p the pressure in the gap and d the gap length) the breakdown voltage is not the same either the gap length is fixed and the pressure varies or the pressure is fixed and the gap length varies [129]. Moreover, deviations to the Paschen's curve have been observed for micro gaps smaller than 10 μm at room temperature [130], [131].

The authors in [132] have presented an approach to evaluate the PDIV in a planar geometry with many length scales. It was experimentally observed that for small pressure values the breakdown voltage versus pd product curve shows an extended flat region rather than a narrow dip. Multiple curves are plotted, each one associated to a gap length.

The corrected Paschen's criterion implanted in the PDET was derived from [132]. The standard Paschen's equation was used. However, the narrow dip on the left of the minimum is replaced by a flat region. The temperature was taken into account by defining an equivalent pressure as recommended by Dunbar [87]. Figure 120 displays the breakdown voltage as a function of pressure curves for different gap length at a temperature of 180 °C. The secondary electron emission coefficient is taken equals to 0.01 for further comparison with experimental data obtained with metallic electrodes (Figure 121).

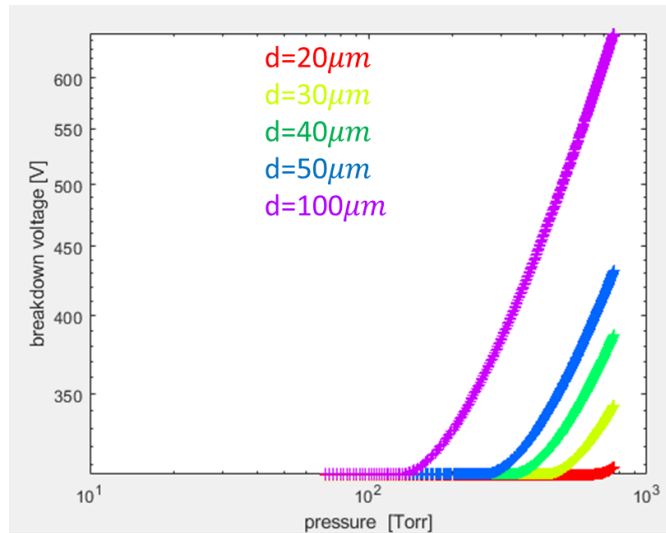


Figure 120: Breakdown voltage as a function of pressure for several gap length ($T = 180^{\circ}\text{C} - \gamma = 0.01$)

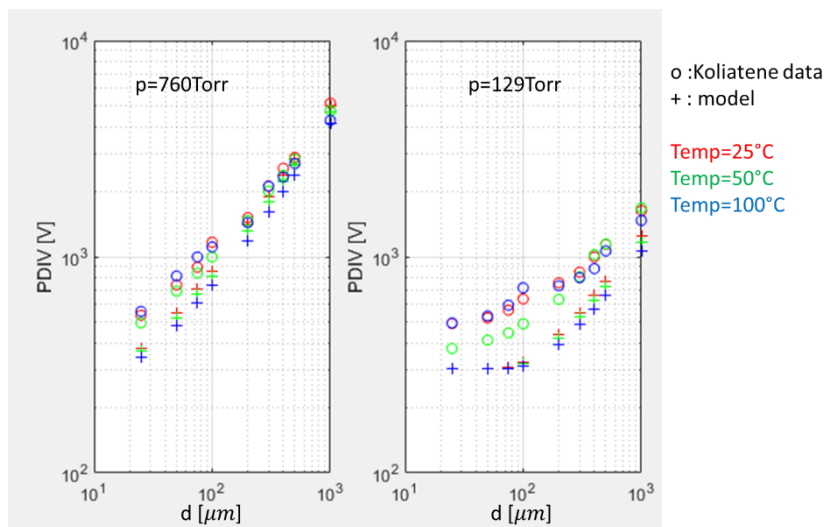


Figure 121: Comparison between the corrected Paschen's criterion and experimental data from [84] - $\gamma = 0.01$

The model is in good agreement with the experimental data.

The criterion is defined with $\gamma_{PAI} = 9 \cdot 10^{-4}$. The criterion is designated as the Partial Discharge Evaluation Criterion (PDEC).

3 PARTIAL DISCHARGE INCEPTION VOLTAGE (PDIV) DECREASE FOR A COMBINED VARIATION OF TEMPERATURE AND PRESSURE

The Partial Discharge Evaluation Criterion (PDEC) was used to produce a graph which indicates the decrease in PDIV level due to a combined variation of temperature and pressure (Figure 122). The

system into consideration was composed of two enamelled round wires in close contact. That was designated as turn/turn close contact. The copper diameter of the wire was 0.5 mm, the enamel thickness overcoating the copper was $30\mu\text{m}$. The enamel dielectric constant was 3.5.

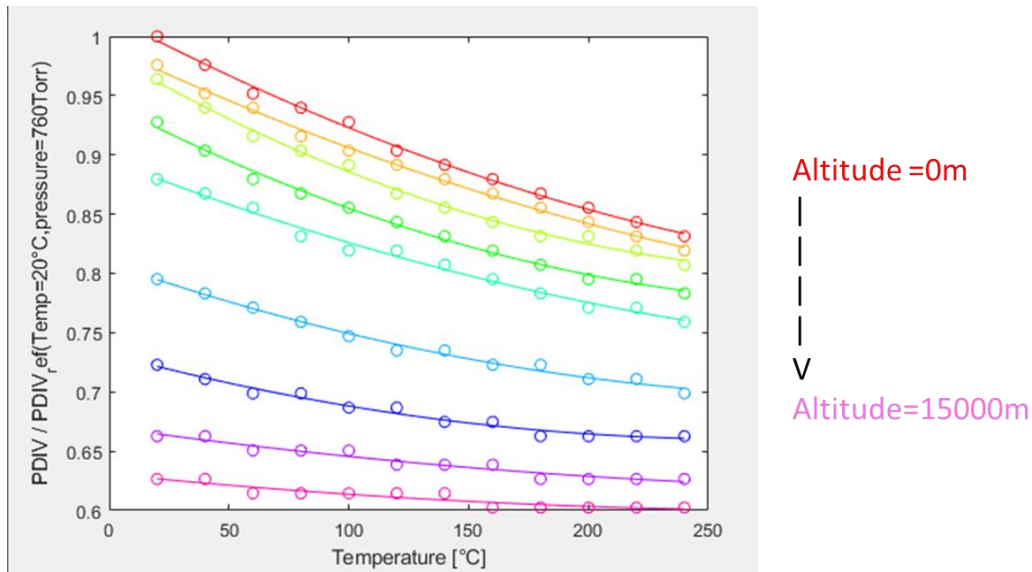


Figure 122: PDIV decrease for a combined variation of temperature and pressure

The PDIV is maximum at normal temperature and pressure conditions (i.e.: 20 °C, 760 Torr). This PDIV is designated as PDIV_{ref} . Using the graph in Figure 122, it is possible to evaluate the PDIV level between two enamelled round wires in close contact for any point on the mission profile. It is directly derived from PDIV_{ref} obtained with a numerical model.

It was assumed that the decrease of the PDIV level with temperature and pressure is the same considering the turn/slot close contact.

4 WIRE DESIGN GRAPHS

4.1 SIMPLE ANALYTICAL MODEL FOR ELECTRIC FIELD IN AIR GAP COMPUTATION

A Simple Analytical Model (SAM) was developed. It is a simplified vision of the 2D-Finite Elements Model (2D FEM) of turn/turn close contact. It requires no finite element computation that makes it much faster. The electric field line where PD takes place was approximated to a straight line. The lines length in the gap between two round conductors was determined by using geometric relations. The field line was delimited with a tube. The tube was considered thin enough so that the materials are considered as planar capacitances. Figure 123 illustrates the idea of flux tube and the resulting analytical circuit model representing the turn to turn configuration. We must notice that this

assumption is consider as valid only at PDIV, as for applied voltages much higher than the PDIV, electric field lines involved in the PD area may not necessary be all straight lines.

The wire grade refers to the standard enamel thickness applied on a wire given the copper radius. In the model, grades 1, 2 and 3 were considered. The data were taken from catalogue [36].

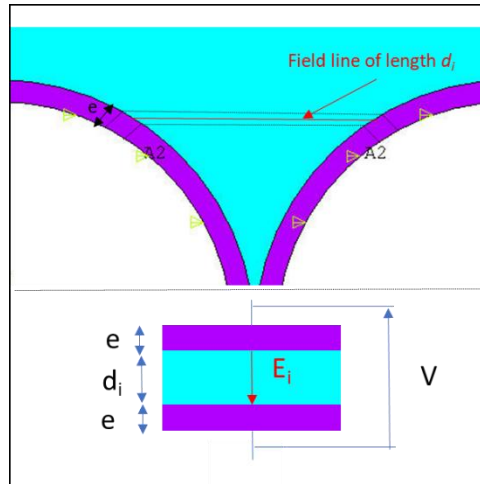


Figure 123: Top) example of straight field line and associated tube; below) resulting SAM circuit model

In the analytical model, the electric field \vec{E} and electric field density \vec{D} are purely normal. They are noted E and D respectively. The D field is conservative on the interfaces air/polymer:

$$D_{air} = D_{diel} \tag{Eq 91}$$

$$E_{air} \cdot \epsilon_0 = E_{diel} \cdot \epsilon_0 \cdot \epsilon_{r, enamel}$$

With E_{air} and E_{diel} the electric field respectively in the air gap and in the dielectric overcoating the conductors, D_{air} and D_{diel} the electric field density in the air gap and the dielectric respectively, ϵ_0 and ϵ_r the dielectric constants of vacuum and the dielectric respectively.

It is thus possible to derive the electric field in the air gap as a function of the applied voltage V , the geometric and dielectric parameters:

$$E_{air} = \frac{V}{d_i + 2 \cdot e \cdot \frac{1}{\epsilon_{r, enamel}}} \tag{Eq 92}$$

The copper radius comes in the computation of d_i . Field lines length in air d_i are computed using geometrical relations as in [55].

4.2 VALIDATION OF SIMPLE ANALYTICAL MODEL WITH FINITE ELEMENTS

Figure 124 displays the evaluation of the PDIV as a function of the enamel thickness for both 2D FEM and SAM. The wire copper radius and associated enamel thicknesses are extracted from [36]. The enamel dielectric constant was $\epsilon_{r, enamel} = 3.5$. The PDIV was evaluated under normal temperature and pressure conditions (i.e.: 20 °C, 760 Torr) by using the PDEC.

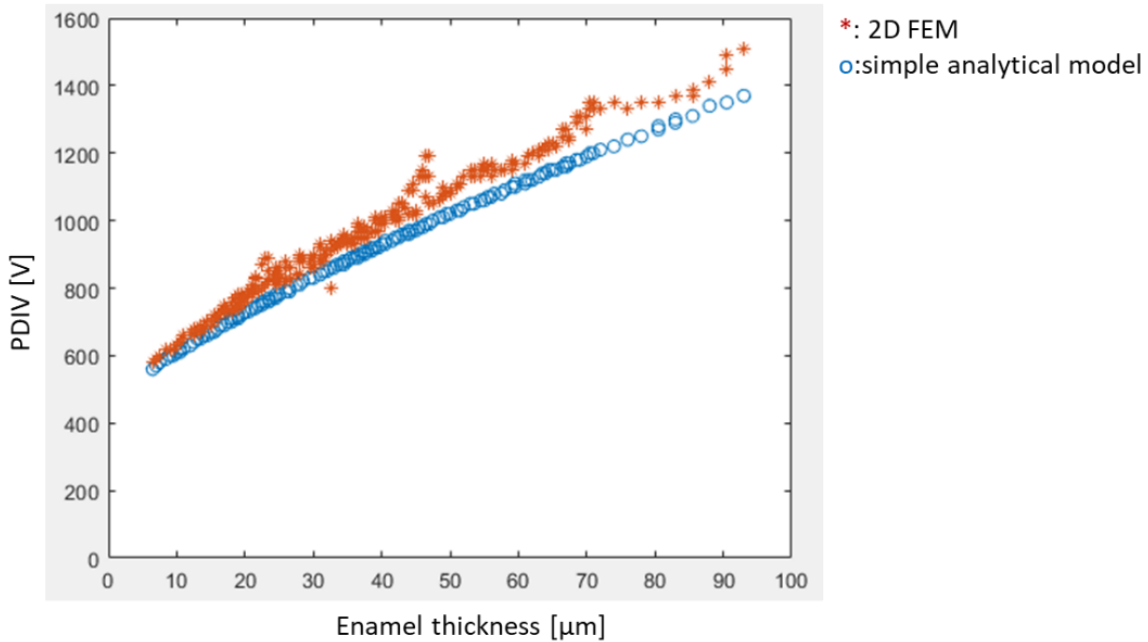


Figure 124: Evaluation of the PDIV as a function of the enamel thickness - 2D-FEM model versus SAM - $\epsilon_{r, enamel} = 3.5$

Field lines from 2D-FEM are computed by using Matlab approach presented in Chapter 3, paragraph 5: Another method using *Matlab* functions. It can be seen important variations on some consecutive 2D FEM points. These are due to numerical errors mainly introduced by:

- the same mesh used for each configuration.
- the variation of the field lines length for each configuration. This is due to, firstly, to the same number of field lines to be computed, and secondly, the same angular coordinate of each field line starting point. In some configurations, field lines that lengths are close to the Paschen's minimum, may not be computed. That leads to an overestimated PDIV value.

The SAM gives an evaluation of the PDIV very close to the one obtained with the 2D-FEM. Besides, the SAM returns undervalued results compared to the 2D-FEM. It means that the design choices resulting from the SAM will be slightly oversized. As an example, for an enamel thickness of 30 μm , the oversize is about 3%, at 90 μm , it is about 10%.

The main advantage of the SAM is its speed of execution. The results presented on Figure 124 requires only few minutes of computation compared to dozens of hours in the case of 2D-FEM ! To study the impact of parameters presented on Table 2 on the wire design, multiple variations have to be tested. Therefore, the simple analytical model was used in this chapter for the computation of the wire design model.

4.3 ENAMEL THICKNESS AS A FUNCTION OF APPLIED VOLTAGE

The SAM was used to realize a parametric study on the impacting parameters for the turn/turn insulation design. These parameters are indicated on Table 29:

Parameters	Designation
Partial Discharge Inception Voltage	<i>PDIV</i>
Enamel dielectric constant	$\epsilon_{r, enamel}$
The grade of the wire	<i>grade</i>

Table 29: Impacting parameters in wire insulation design

The parameter *grade* in the model takes into account this standardized overcoat thickness associated to a copper diameter. It is defined as follow:

Grade	Tolerance
0	min grade 1
1/5	max grade 1
2/5	min grade 2
3/5	max grade 2
4/5	min grade 3
1	max grade 3

The catalogue [36] was swept. For each configuration of copper radius and enamel thickness, the maximal voltage that the wire can stand was evaluated with the simple analytical model illustrated on Figure 123. The impact of the material was investigated by changing the dielectric constant values. Figure 125 displays the evolution of the enamel thickness as a function of the PDIV occur in the air gap. The PDIV in the air gap were evaluated using the introduced Partial Discharge Evaluation Criterion (PDEC) under normal conditions of temperature and pressure with the secondary electron emission coefficient $\gamma = 9 \cdot 10^{-4}$.

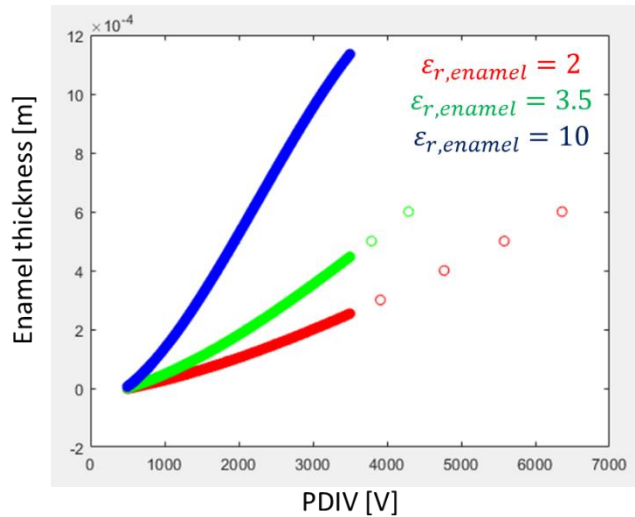


Figure 125: Enamel thickness as a function PDIV - PDIV evaluated using the PDEC under normal temperature and pressure conditions - ($\gamma = 9 \cdot 10^{-4}$)

The required enamel thickness e was interpolated over the $PDIV$ domain using a 3rd order polynomial. The polynomial coefficients are dependant on the material dielectric constant.

$$e = a_1(\epsilon_{r, enamel}) * PDIV^3 + a_2(\epsilon_{r, enamel}) * PDIV^2 + a_3(\epsilon_{r, enamel}) * PDIV + a_4(\epsilon_{r, enamel}) \quad Eq 93$$

The evolution of the a_i ($i \in [1:4]$) polynomial coefficients was investigated for dielectric constant values ranging from 1 to 10. Most of the polymer used for the enamel overcoat have dielectric constant in this interval. Figure 126 displays the evolution of the a_i polynomial coefficients as a function of the dielectric constant. It was obtained under normal temperature and pressure conditions (i.e.: 20 °C, 760 Torr).

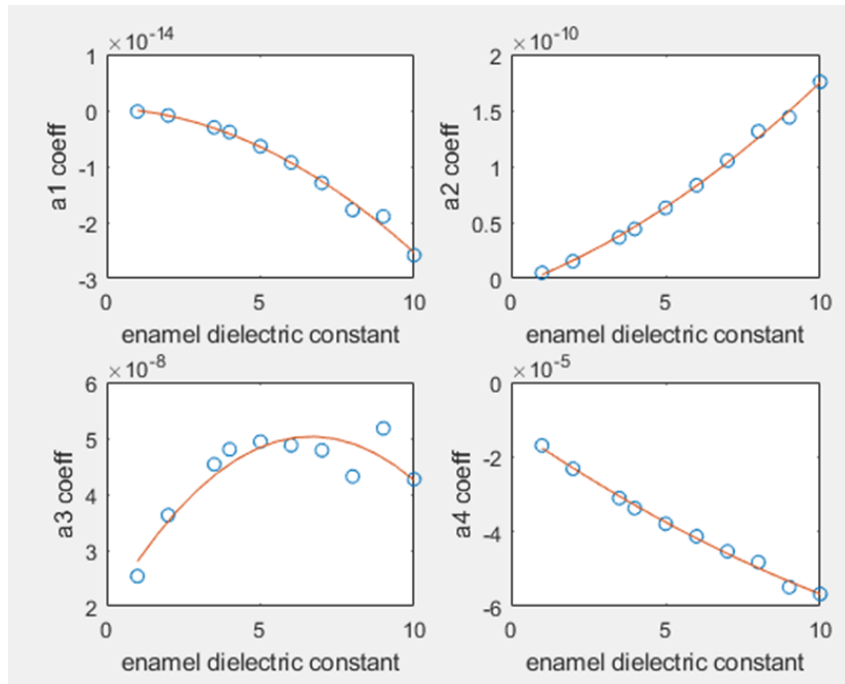


Figure 126: Evolution of a_i polynomial coefficients as a function of enamel dielectric constant – (20°C, 760Torr)

A second order polynomial (red line) was used to interpolate the evolution of a_i coefficients (blue dots) over the domain of dielectric constant. The dependency of the a_i coefficients with the enamel dielectric constant $\epsilon_{r, enamel}$ is expressed as follow:

$$a_i = c_{i,1} * \epsilon_{r, enamel}^2 + c_{i,2} * \epsilon_{r, enamel} + c_{i,3} \quad Eq 94$$

With: $i \in [1,4]$

$\epsilon_{r, enamel} \in [1,10]$

4.4 COPPER DIAMETER AS FUNCTION OF COMPUTED ENAMEL THICKNESS

Figure 127 displays the copper radius as a function of the enamel thickness given by the grade tolerance (min/max). The data were taken from catalogue [36].

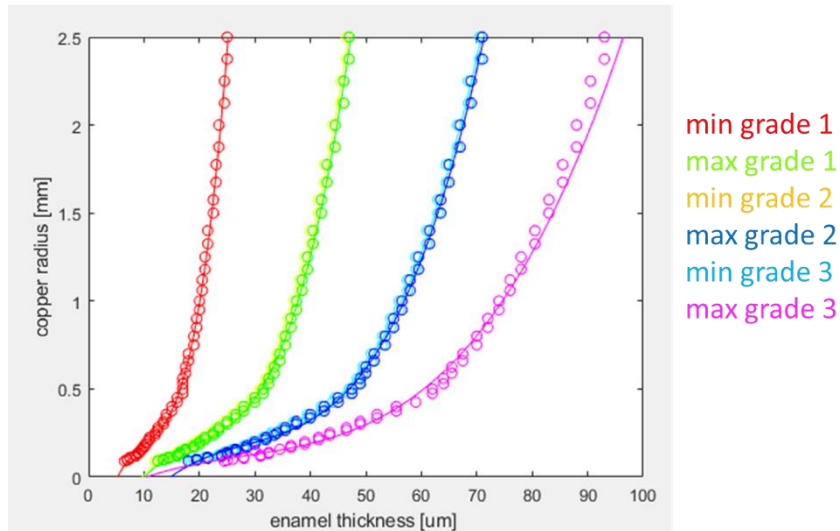


Figure 127: Copper radius versus enamel thickness for all grade tolerances in [36]

It can be seen that the tolerances max grade 1 and min grade 2 are overlapping. It is the same for the tolerances max grade 2 and min grade 3.

The discrete data from the catalogue (dots) can be interpolated with a 3rd order polynomial. The coefficients of such polynomial are dependent on the wire grade.

$$R_{copper} = b_1(grade) * e^3 + b_2(grade) * e^2 + b_3(grade) * e + b_4(grade) \quad Eq 95$$

4.5 VALIDATION

The results given by the wire design model were confronted to the ones using the simple analytical model. The catalogue [36] was swept considering a min grade 2 insulation, (i.e.: grade=2/5). The enamel dielectric constant was taken as $\epsilon_{r, enamel} = 4.2$.

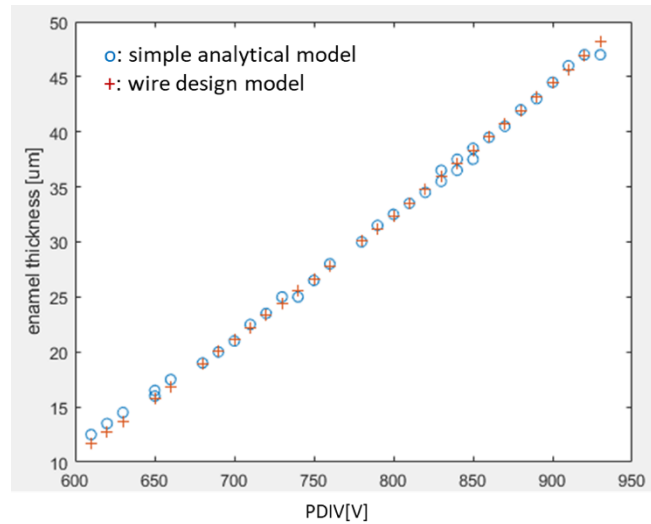


Figure 128: Enamel thickness as a function of PDIV - blue circles are simple analytical model results; red crosses are wire design model results – (grade=2/5; $\epsilon_{r, enamel} = 4.2$)

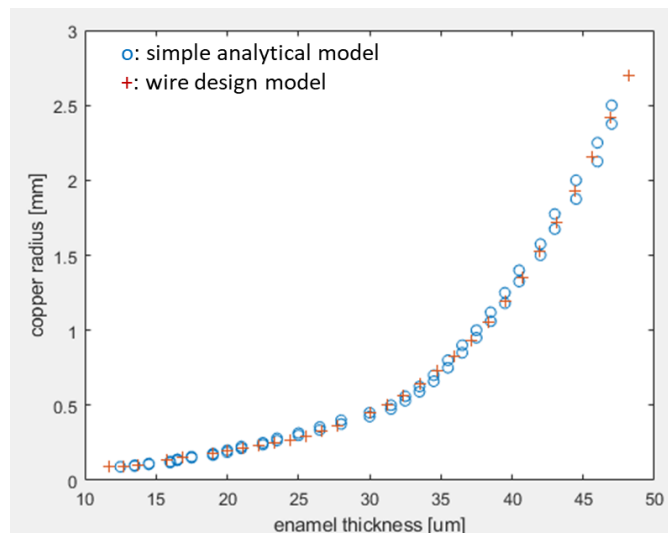


Figure 129: Copper radius as a function of the enamel thickness - blue circles are simple analytical model results; red crosses are wire design model results – (grade=2/5; $\epsilon_{r, enamel} = 4.2$)

Figure 128 and Figure 129 shows that the wire design model generated using polynomial forms gives results in very good agreement with the ones obtained using the simple analytical model.

The main advantage of the wire design graphs is that they directly return an enamel thickness whatever the inputs and, in addition, the applied voltage domain is continuous.

5 SLOT INSULATION DESIGN GRAPHS

The same approach was carried on for the slot liner design evaluation. This case is more complex due to the presence of two different insulation materials: the enamel and the slot liner. Table 30 presents the impacting parameters on the slot liner thickness choice.

Parameters	Designation
Partial Discharge Inception Voltage	$PDIV$
Enamel dielectric constant	$\epsilon_{r, enamel}$
The grade of the wire	$Grade$
Enamel thickness	E
Slot liner dielectric constant	$\epsilon_{r, liner}$

Table 30: Impacting parameters on slot insulation design

5.1 SIMPLE ANALYTICAL MODEL FOR ELECTRIC FIELD IN AIR GAP COMPUTATION

The electric field lines in this model were approximated to straight line too. The lines length in the gap between a round conductor and the slot liner was determined using geometric relations, as in [55]. The field lines were delimited with a tube. The tube is considered thin enough so that the materials are considered as planar capacitances. Figure 130 illustrates the idea of flux tube and the resulting Simple Analytical Model (SAM) representing the turn/slot configuration.

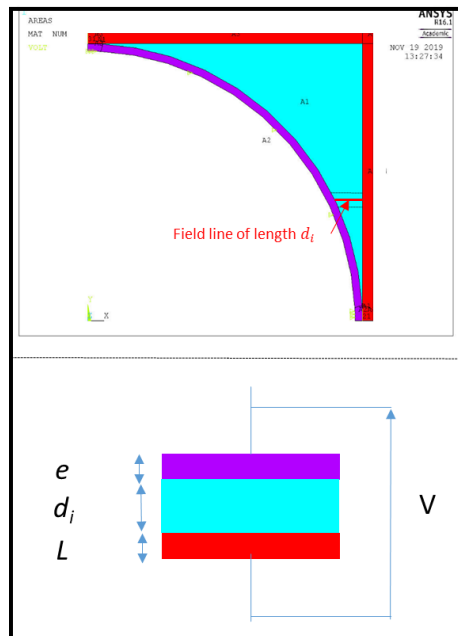


Figure 130: Top) Example of straight field line and its associated tube; below) SAM. (red: slot insulator, purple: enamel, blue: air)

In the SAM, the electric field \vec{E} and electric field density \vec{D} are purely normal. They are noted E and D respectively. The D field is conservative on the interfaces air/polymer:

$$\begin{aligned} D_{air} &= D_{enamel} \\ E_{air} \cdot \epsilon_0 &= E_{enamel} \cdot \epsilon_0 \cdot \epsilon_{r,enamel} \end{aligned} \tag{Eq 96}$$

$$\begin{aligned} D_{air} &= D_{liner} \\ E_{air} \cdot \epsilon_0 &= E_{liner} \cdot \epsilon_0 \cdot \epsilon_{r,liner} \end{aligned}$$

With E_{air} , E_{enamel} and E_{liner} the electric fields respectively in the air gap, in the enamel and in the slot liner, D_{air} , D_{enamel} and D_{liner} the electric field densities in the air gap, the enamel and the liner respectively, ϵ_0 , $\epsilon_{r,enamel}$ and $\epsilon_{r,liner}$ the dielectric constants of vacuum, enamel and liner respectively.

Based on Eq 96 it is possible to derive the electric field in the air gap as a function of the applied voltage V , the geometric and dielectric parameters:

$$E_{air} = \frac{V}{d_i + e \cdot \frac{1}{\epsilon_{r,enamel}} + L \cdot \frac{1}{\epsilon_{r,liner}}} \tag{Eq 97}$$

5.2 VALIDATION OF SIMPLE ANALYTICAL MODEL WITH FINITE ELEMENTS

Figure 131 presents a comparison between the simple analytical model (solid lines) and the 2D-finite element model (FEM) in the evaluation of the PDIV as a function of insulation configuration. The wire configuration was fixed. The wire copper radius was 0.5 mm, the enamel thickness was $e = 40\mu m$ and the enamel dielectric constant was $\epsilon_{r,enamel} = 3.5$. The PDIV was determined under normal temperature and pressure conditions using the PDEC.

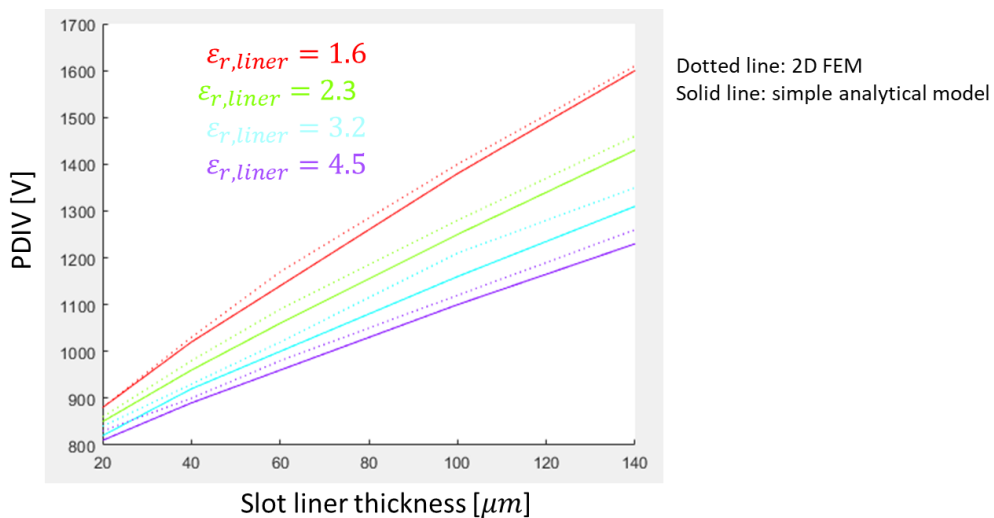


Figure 131: Evaluation of the PDIV as a function of the slot liner thickness - 2D-FEM model versus simple analytical model – ($e=40\mu m$, $\epsilon_{r,enamel} = 3.5$)

The simple analytical model gives results close to the one obtained with the 2D-FEM. The evaluation of the PDIV is slightly undervalued compared to 2D FEM. As an example, for $\epsilon_{r,liner} = 3.2$, the oversize is only 4% for a 140 μm -thick slot liner. The simple analytical model was used in this chapter for the study of the impacting parameters on the slot liner design mainly because of its fast computation time.

5.3 SLOT LINER THICKNESS AS A FUNCTION OF APPLIED VOLTAGE AND INSULATION MATERIALS

Figure 132 displays the evaluation of the required slot liner thickness depending on the PDIV and the wire insulation parameters. The wire insulation parameters are its enamel dielectric constant $\epsilon_{r,enamel}$ and its thickness e . The slot liner dielectric constant was fixed at $\epsilon_{r,liner} = 4.5$. The PDIV was determined under normal temperature and pressure conditions using the PDEC.

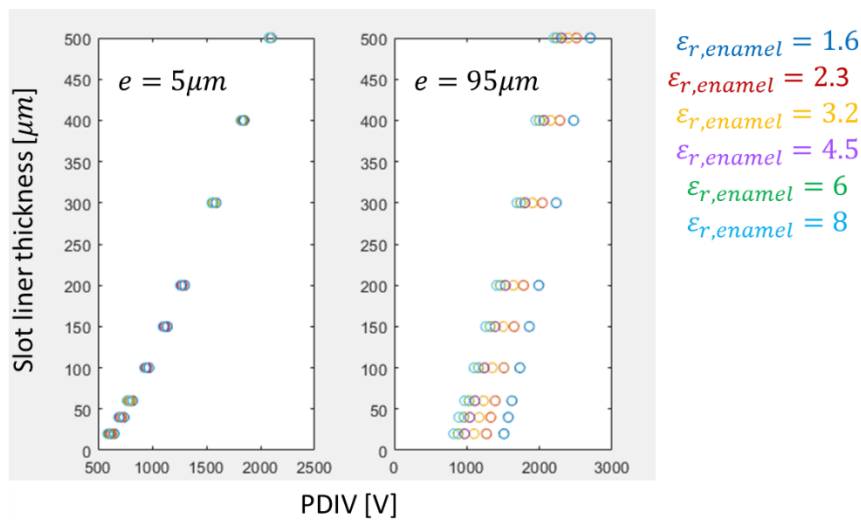


Figure 132: Evaluated slot liner insulation as a function of PDIV for different wire insulation configurations (thickness e and permittivity $\epsilon_{r,enamel}$) – ($\epsilon_{r,liner} = 4.5$)

A 2nd order polynom was used to interpolate the slot liner thickness L as a function of the PDIV. The polynomial coefficients are dependent on the enamel thickness e and dielectric constant $\epsilon_{r,enamel}$ and of the slot liner dielectric constant $\epsilon_{r,liner}$.

$$L = a_1(e, \epsilon_{r,enamel}, \epsilon_{r,liner}) * PDIV^2 + a_2(e, \epsilon_{r,enamel}, \epsilon_{r,liner}) * PDIV + a_3(e, \epsilon_{r,enamel}, \epsilon_{r,liner}) \quad \text{Eq 98}$$

The polynomial coefficients are dependent on three parameters. Therefore, three imbrications were required to fully spell out Eq 98.

The first imbrication expresses the a_i ($i \in [1:3]$) polynomial coefficients as a function of $\varepsilon_{r,liner}$. A polynomial form was also used here. The polynomial coefficients are named “first imbrication polynomial coefficients”.

The second imbrication expresses the “first imbrication polynomial coefficient” as a function of e . Another polynomial has been used, resulting in the apparition of “second imbrication polynomial coefficients”.

Finally, the third imbrication expresses the “second imbrication polynomial coefficients” as a function of $\varepsilon_{r,enamel}$.

By going up from the third imbrication to the first one, equation Eq 98 was fully determined.

Figure 133 illustrates the described imbrications:

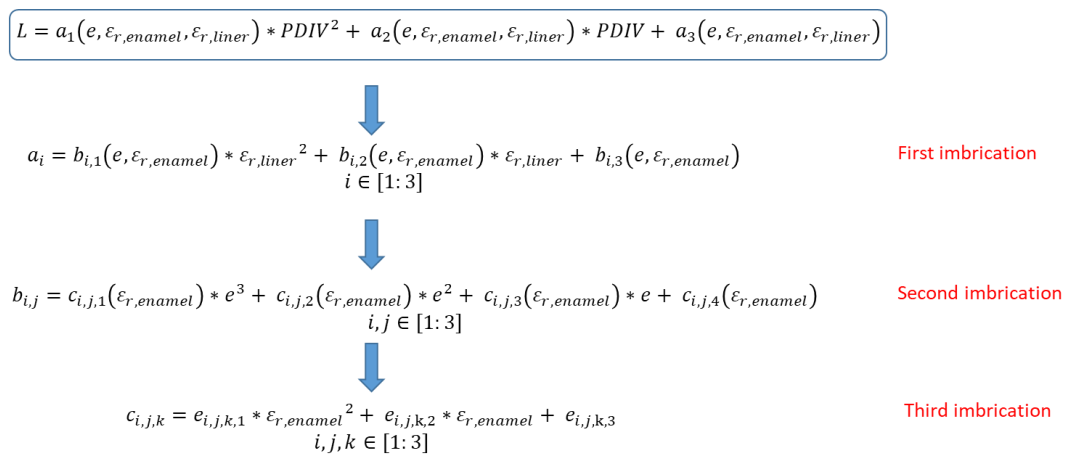


Figure 133: Imbrications equations

5.3.1 First imbrication

Figure 134 displays the evolution of a_i ($i \in [1:3]$) polynomial coefficients present in Eq 98 as a function of $\varepsilon_{r,liner}$. The enamel thickness is $e = 5\mu m$.

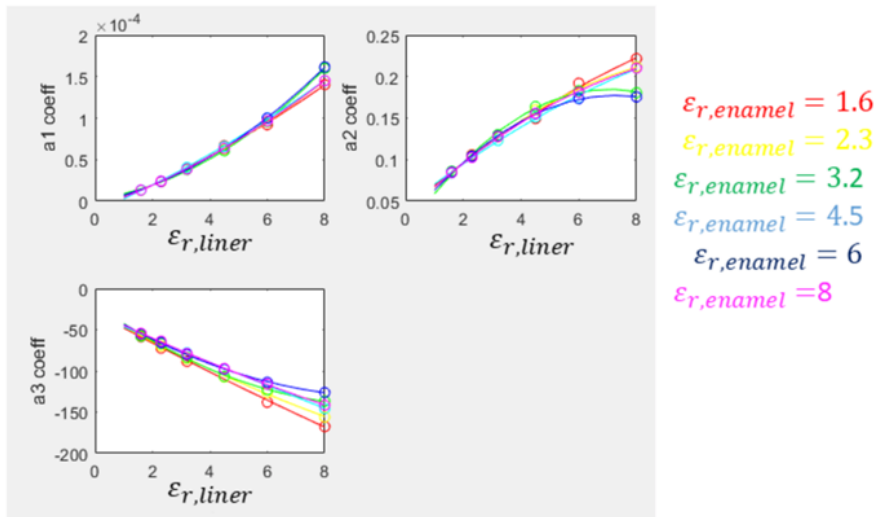


Figure 134: a_i ($i \in [1:3]$) polynomial coefficients as a function of $\epsilon_{r,liner}$ - $e=5\mu\text{m}$

The a_i ($i \in [1:3]$) coefficients are interpolating over the $\epsilon_{r,liner}$ domain using a second order polynomial.

$$a_i = b_{i,1}(e, \epsilon_{r, enamel}) * \epsilon_{r, liner}^2 + b_{i,2}(e, \epsilon_{r, enamel}) * \epsilon_{r, liner} + b_{i,3}(e, \epsilon_{r, enamel}) \tag{Eq 99}$$

With $i \in [1:3]$

The $b_{i,j}$ ($i, j \in [1:3]$) are the “first imbrication polynomial coefficients”.

5.3.2 Second imbrication

Figure 135 displays as an example the evolution of $b_{1,1}$ coefficient presents in Eq 99 as a function of the enamel thickness e for different $\epsilon_{r, enamel}$.

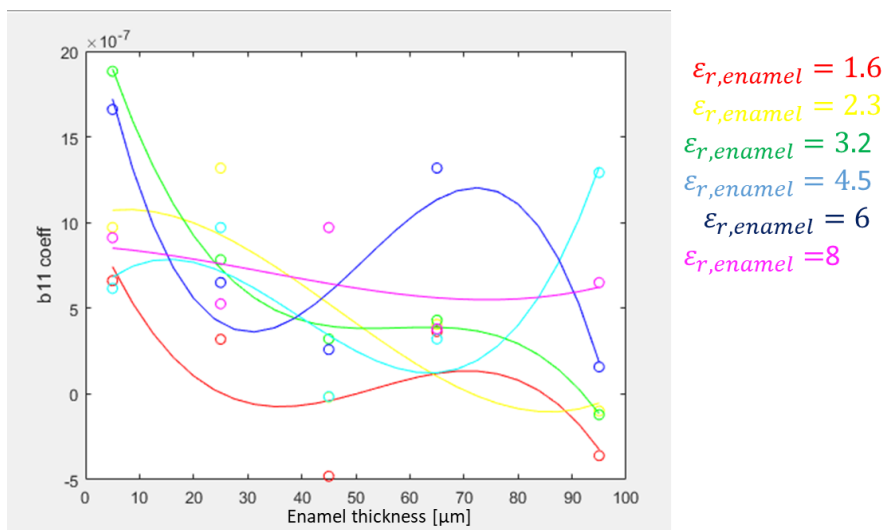


Figure 135: $b_{1,1}$ coefficients as a function of enamel thickness

The $b_{i,j}$ ($i \in [1:3]$) coefficients were interpolating over the $\epsilon_{r,liner}$ domain using a third order polynomial.

$$b_{i,j} = c_{i,j,1}(\varepsilon_{r, enamel}) * e^3 + c_{i,j,2}(\varepsilon_{r, enamel}) * e^2 + c_{i,j,3}(\varepsilon_{r, enamel}) * e + c_{i,j,4}(\varepsilon_{r, enamel}) \tag{Eq 100}$$

With $i, j \in [1:3]$

The $c_{i,j,k}$ ($i, j \in [1:3]$ and $k \in [1:4]$) are the “second imbrication polynomial coefficients”.

5.3.3 Third imbrication

Figure 136 presents as an example the evolution of $c_{3,j,k}$ ($j \in [1:3]$ and $k \in [1:4]$) coefficients in Eq 100 as a function of $\varepsilon_{r, enamel}$.

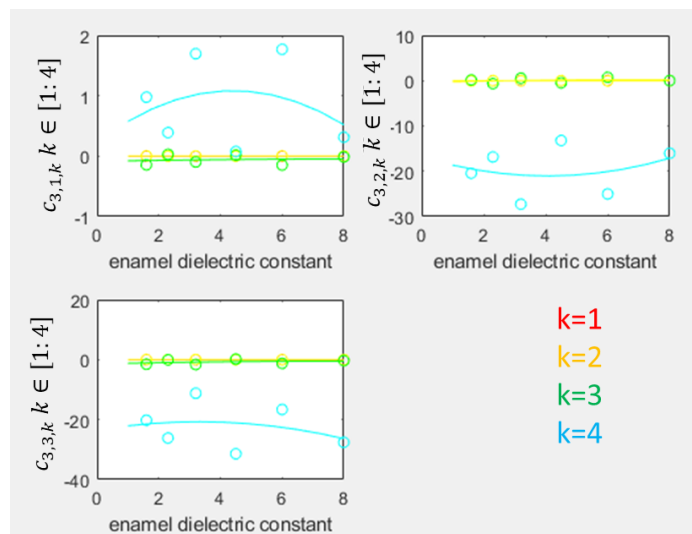


Figure 136: $c_{3,j,k}$ coefficients as a function of $\varepsilon_{r, enamel}$

The $c_{i,j,k}$ ($i, j \in [1:3]$ and $k \in [1:4]$) are finally interpolated over $\varepsilon_{r, enamel}$ using second order polynomial forms.

5.4 VALIDATION

The results given by the slot insulation design model were then compared to the ones using the simple analytical one. The wire copper radius was $R_{copper} = 0.5 \text{ mm}$, the enamel thickness was $e = 31.5 \mu\text{m}$ and the enamel dielectric constant was $\varepsilon_{r, enamel} = 4.2$. The slot insulation was taken as $\varepsilon_{r, liner} = 3.5$.

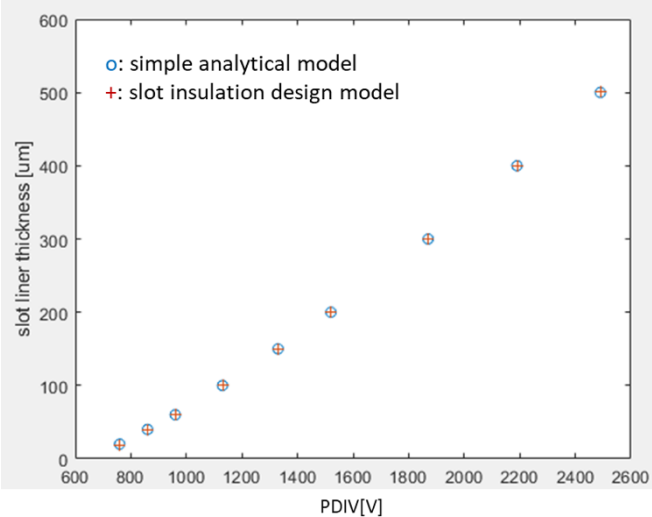


Figure 137: Slot liner thickness versus PDIV - blue circles are simple analytical model results; red crosses are wire design model results - $R_{copper} = 0.5\text{ mm}$; $e = 31.5\text{ }\mu\text{m}$; $\epsilon_{r, enamel} = 4.2$; $\epsilon_{r, liner} = 3.5$

Figure 137 shows that the results given by the slot insulation design model are in very good agreement with the ones given by the simple analytical model.

As for turn/turn insulation, the main advantages of the slot insulation design model is that it directly returns a slot liner thickness whatever the inputs and moreover the applied voltage domain is continuous. An abacus can therefore be produced.

6 EVALUATION OF THE ELECTRIC STRESSES UNDER NORMAL TEMPERATURE AND PRESSURE CONDITIONS

6.1 TURN/TURN ELECTRIC STRESS

The transient regime determines the maximum turn/turn electric stress. In transient regime, voltage phase terminals have to withstand pulses train of amplitude V_{step} as illustrated in Figure 138.

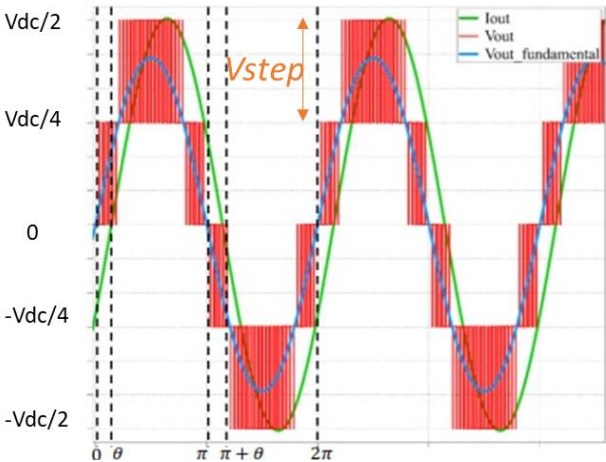


Figure 138: Example of both output voltage (phase to ground) and current waveforms of a 5-level ANPC obtained with PLECS software. V_{dc} is the bus voltage.

The effect of the impacting parameters on the the motor terminals overshoots have been presented in Chapter 1, paragraph 6 Impact of power electronics. The power cable length between the inverter output and the motor terminals is considered shorter than 1 m. Thus, only the rising time remains impacting. In the example of Figure 138, the multilevel converter enables to reduce the voltage pulse amplitude.

The impact of the rising time of inverter voltage pulse was derived from [60] results. Figure 139 presents a simple evaluation of voltage overshoot at phase terminals expressed as a percentage of the inverter voltage pulse amplitude.

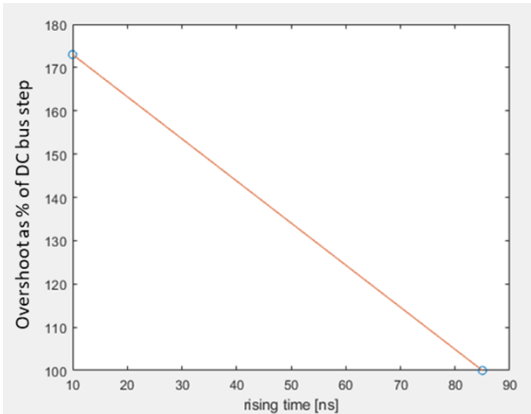


Figure 139: Overshoot at phase terminals expressed as a percentage of inverter voltage pulse amplitude as a function of the rising time

Overshoot start to appear for rising time shorter than 80 ns. It was considered that during transient the first conductor of the phase receives 70% of the transient phase voltage [56]. The voltage front does not reach the other conductors during a fraction time of transient regime [62].

6.2 TURN/SLOT ELECTRIC STRESS

The maximal electric stress between turn and slot insulation is the nominal phase peak voltage.

A linear voltage repartition was considered all over a phase. There was one single phase per slot. The number of conductors inside a slot represent the number of passing of the phase inside the slot. The machine active length was considered long enough so that the end winding length was neglected.

The voltage on the i^{th} conductor of the phase in the slot is expressed as:

$$V_{cond,i} = V_{peak} * \left(1 - \frac{L_i}{L_{tot}}\right)$$

With L_i the length of the phase in the slot lugs for the i^{th} conductor, L_{tot} the total phase length and V_{peak} the phase to neutral peak voltage.

7 PARTIAL DISCHARGE EVALUATION TOOL (PDET)

The perimeter of the PDET is only the stator slot. The PDET provides solution(s) in order to get a PD-free stator slot. These(this) correspond(s) to minimal required insulation thicknesses to withstand the electric stresses in both turn/turn and turn/slot close contacts.

The solutions are derived from graphs computed using the presented Simple Analytical Model (SAM) validated with 2D-Finite Elements Model (2D FEM) in the case of a uniform electric field.

The developed PDET scope is:

- inside a rectangular stator slot;
- only one phase in the slot;
- considered slot is the phase entrance;
- round enamelled wires constitute the turns;
- turns in close contact with each other and with the slot insulation;
- a catalogue of round enamelled copper wires is already integrated.

Obviously, the scope of this study may be changed to take into account other configurations: flat wires, trapezoidal slots, more than one phase per slot,...

7.1 PDET ALGORITHM

Figure 140 illustrates the PDET organigram. There are five main steps. Each step is managed by a function. These steps are automatically executed when PDET is running.

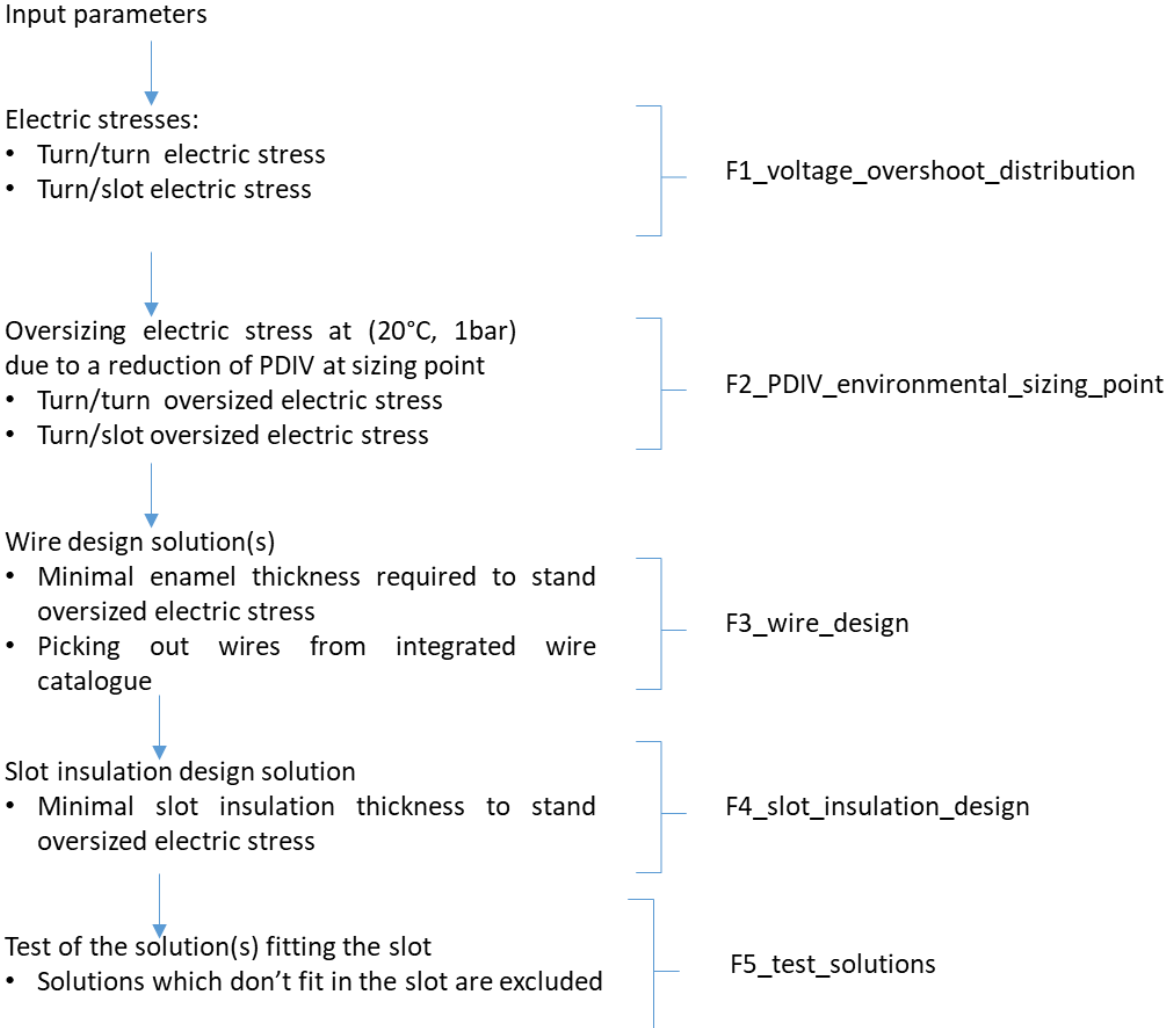


Figure 140: PDET organigram

F3_wire_design and *F4_slot_insulation_design* uses the graphs above presented. In *F2_PDIV_environmental_sizing_point* function, the graph on Figure 122 is applied on turn/turn and turn/slot evaluated electric stresses. It comes the oversized electric stresses at (20°C, 1bar) to ensure that the solution takes into account the decrease in PDIV with temperature increase and pressure decrease.

7.2 INPUTS

The inputs are listed on Table 31.

Input	Description	Unit
Motor		
<i>nb_phase</i>	Number of electric phases of the motor	
<i>nb_slot</i>	Total number of slots in the stator	
<i>nb_cond</i>	Number of conductors per slot. The conductors are the passages of a phase in the slot	
<i>L_slot</i>	Slot width	[m]
<i>h_slot</i>	Slot height	[m]
<i>kfill</i>	Filling factor	
Converter		
<i>ma</i>	Maximal modulation width	
<i>Vemot_max_cond1</i>	Equivalent 1 conductor / slot / phase peak voltage	[V]
<i>nb_level</i>	Number of levels of the converter	
<i>rise_time</i>	Switch component rise time	[ns]
Sizing point		
<i>Temp0</i>	Stator operating temperature	[°C]
<i>h0</i>	Operating altitude	[m]
Material		
<i>val_epsr_enamel</i>	Enamel dielectric constant	
<i>val_epsr_cale</i>	Slot insulation dielectric constant	
<i>val_cale_min</i>	Minimal slot insulation thickness	[μm]
Wire		
<i>R_cu</i>	Copper radius – 0 if no selected wire (default)	[m]
<i>e</i>	Enamel thickness – 0 if no selected wire (default)	[m]

Table 31: PDET inputs

The user may use the tool with a pre-selected wire configuration. PDET will then check that the selected wire can withstand turn/turn electric stress. It will design the slot insulation to withstand the electric stress between turn/slot. It will finally check that the solution fits in the slot.

The DC bus voltage is evaluated from the parameters *Vemot_max_cond1*, *ma* and *nb_cond*. At iso power, increasing the number of conductors of the phase reduces the current density on the conductors. On the other hand, the phase voltage increases.

$$\begin{aligned}
 V_{emot_max} &= V_{emot_max_cond1} * nb_{cond} \\
 V_{inv_max} &= V_{emot_max}/ma \\
 V_{dc} &= 2 * V_{inv_max}
 \end{aligned}
 \tag{Eq 101}$$

The wires are in close contact with each other and with the slot liner. That is because of the assumptions made for the elaboration of the wire design and slot insulation graphs. These graphs are established for round enamelled wires.

A default minimal slot liner thickness is fixed at 20µm. It may be a constraint given by the user.

8 ILLUSTRATIVE EXAMPLE

As an example, let us consider the configuration presented on Table 32. No wire is preselected.

	Parameters	Designation	Value
Inverter	Maximal modulation width	<i>ma</i>	1.15
	Equivalent 1 conductor / slot / phase peak voltage	<i>Vemot_max_cond1</i>	450 V
	Number of levels	<i>nb_level</i>	5
	Voltage pulse amplitude		
	Voltage pulse rising time	<i>rise_time</i>	200 ns
Motor	Number of phases	<i>nb_phase</i>	3
	Number of slots	<i>nb_slot</i>	36
	Number of conductors	<i>nb_cond</i>	4
	Slot width	<i>L_slot</i>	8 mm
	Slot pitch	<i>h_slot</i>	46 mm
	Filling factor	<i>kfill</i>	0.5
Sizing point	Temperature	<i>Temp</i>	180°C
	Altitude	<i>h0</i>	8000 m
Materials	Enamel dielectric constant	<i>ε_{r, enamel}</i>	3.5
	Slot liner dielectric constant	<i>val_epsr_enamel</i>	4.5
	Minimal slot liner thickness	<i>val_epsr_cale</i>	20 µm

Table 32: Tool inputs - Example values

Referring to PDET organigram in Figure 140, the first step is the determination of the electric stresses for turn/turn and turn/slot contacts. That is detailed in above §6: Evaluation of the electric stresses under normal temperature and pressure conditions. The second step is to determine the overvalued electric stresses at (20 °C, 1 bar) corresponding to the impact of the sizing point. For that, the graph on Figure 122 is used.

Figure 141 displays PDET window where the electric stresses are computed. The tab pages on the top (Inputs, Electric stresses, Wire design, Slot liner design and Solutions) are the steps to compute in successive order. The DC bus voltage computed using Eq 101 is $V_{dc}=3130$ V. The inverter voltage pulse amplitude is $V_{step}=782.6$ V. The turn/turn and turn/slot electric stresses are respectively designated by *PDIVO_turn_turn* and *PDIVO_turn_slot*. The rise time of 200 ns is slow enough so that no additional overshoot is considered. The turn/turn electric stress thus correspond to 70% of V_{step} . The turn/slot electric stress is the nominal voltage of the first conductor. The graph on Figure 141 displays the PDIV evolution as a function of the temperature on the ground (triangles) and at 8000 m (crosses). The blue

curves correspond to turn/slot contact, the red curves to turn/turn contact. To be able to stand the identified electric stresses at 180°C, 8000 m (green circles) the insulation has to be oversized at 20 °C, on the ground (purple circles). Table 33 gives the electric stresses and the resulting overvalued stresses at (20°C, 1bar) due to the sizing point environmental conditions.

Interface	Electric stresses	Oversized electric stresses at (20°C, 1bar) due to sizing point impact
Turn/turn	547.8 V	807.8 V
Turn/slot	1800 V	2640 V

Table 33: Calculated overvalued voltages

The third step is the evaluation of wire solution(s). Figure 142 displays PDET Wire design window.

The left graph on Figure 142 is the enamel thickness design graph corresponding to the used material. The right graph is the used catalogue. For each copper radius, there are six possible enamel thicknesses. These correspond to the tolerances min and max of grade 1, grade 2 and grade 3 wires. PDET returned a required enamel thickness of 27.65 µm using the left graph. That results in five possible wires configuration (Table 34). Each configuration has an enamel thickness close to the required one.

Copper radius [mm]	Enamel thickness [µm]	Grade
0.425	29.5	0.2 (i.e.: max grade 1)
0.3750	28	0.4 (i.e.: min grade 2)
0.1675	28	0.6 (i.e.: max grade 2)
0.1675	28.5	0.8 (i.e.: min grade 3)
0.1060	28	1 (i.e.: max grade 3)

Table 34: Wire solutions

The two solutions corresponding to a copper radius of 0.1675 mm are quite the same as explained with Figure 127. The enamel thickness given by PDET is the minimal required thickness to withstand both overshoot and sizing point conditions.

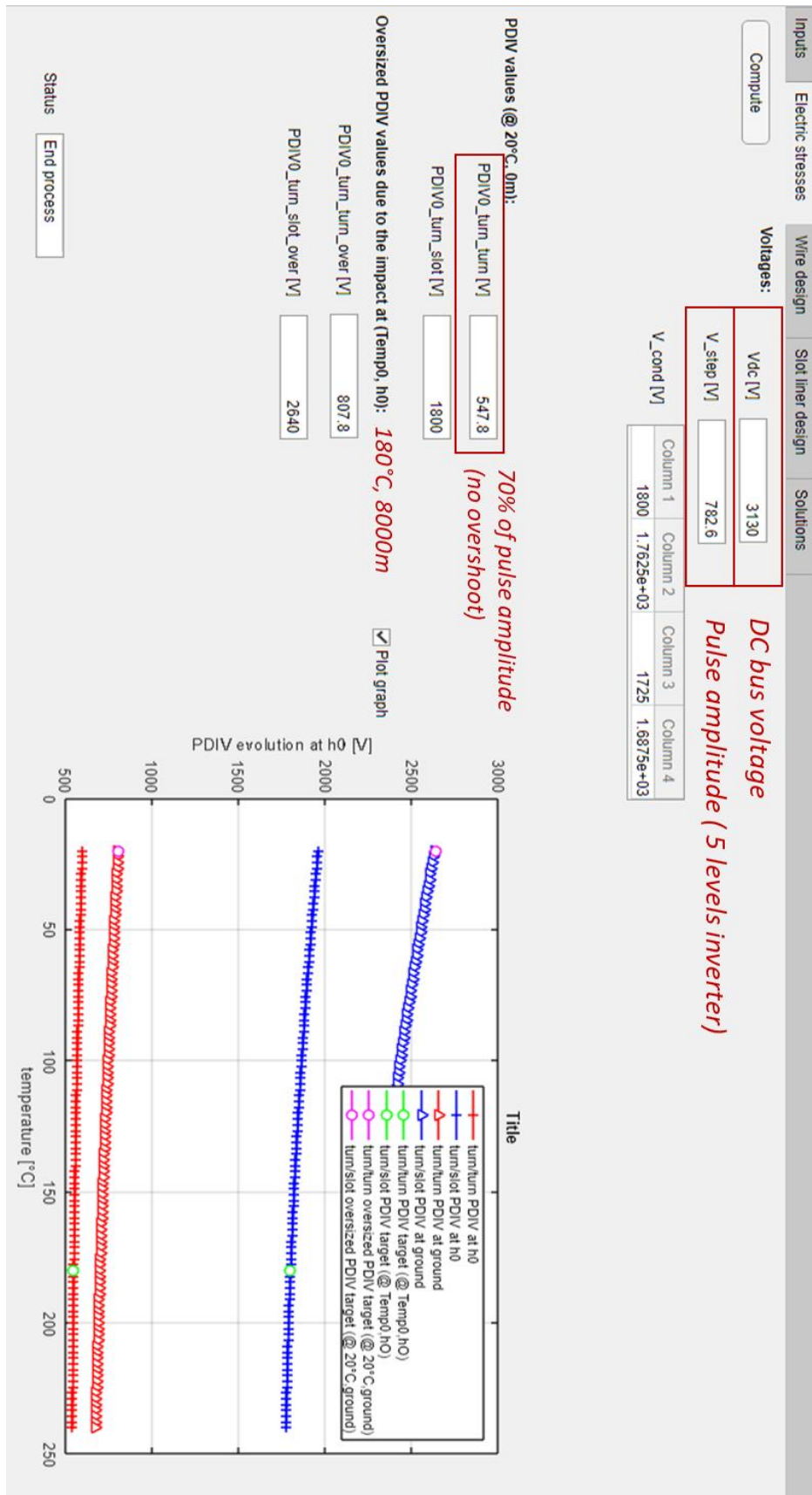


Figure 141: PDET - Electric stresses window

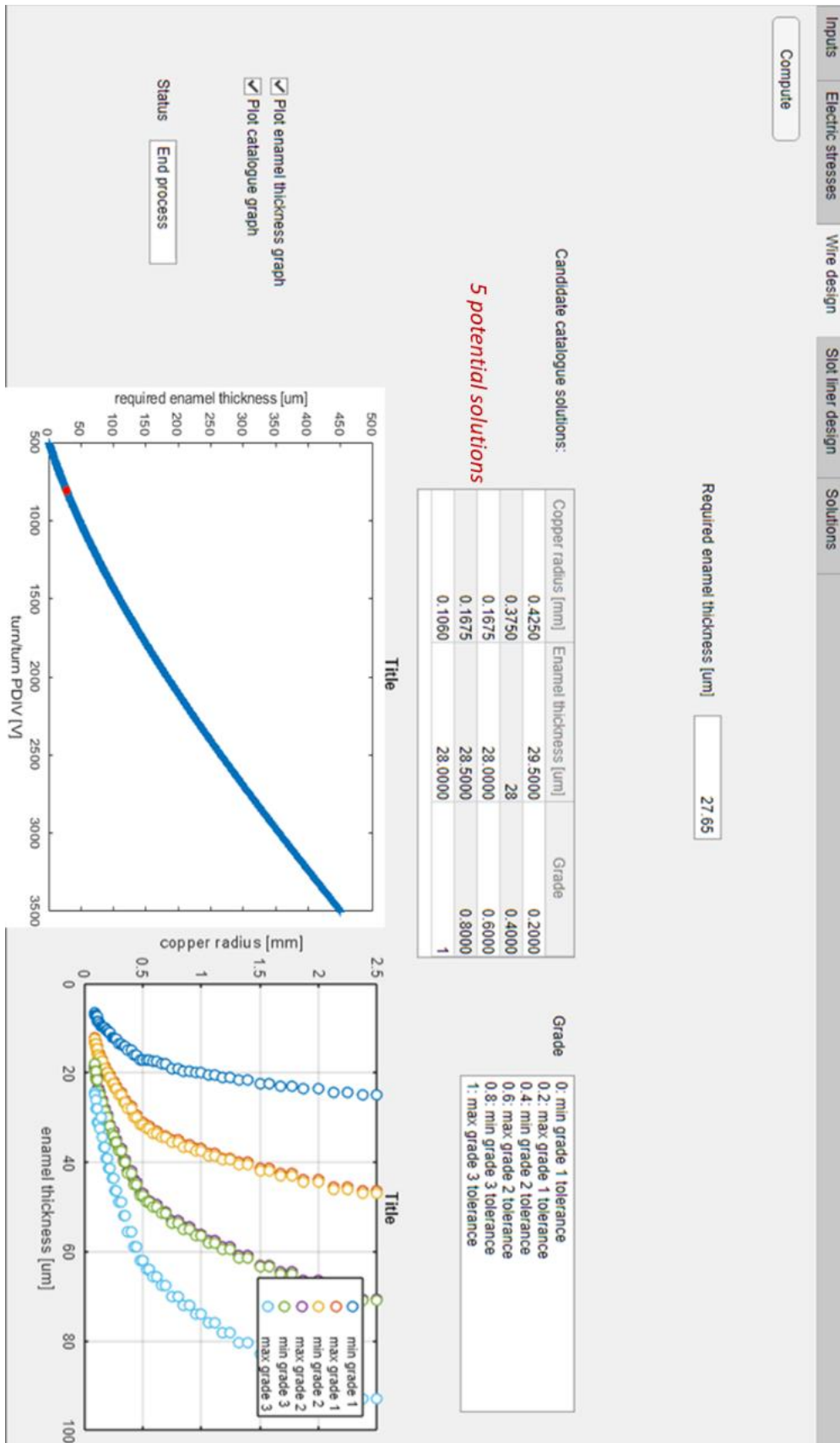


Figure 142: PDET - Wire design window

Chapter 5: Tool to predict PD activity in machine slot

The fourth step is the evaluation of the minimal required liner thickness to withstand the turn/slot electric stress at sizing point conditions. Figure 143 displays PDET Slot liner design window. The graph provides a slot liner thickness of 716.4 μm .

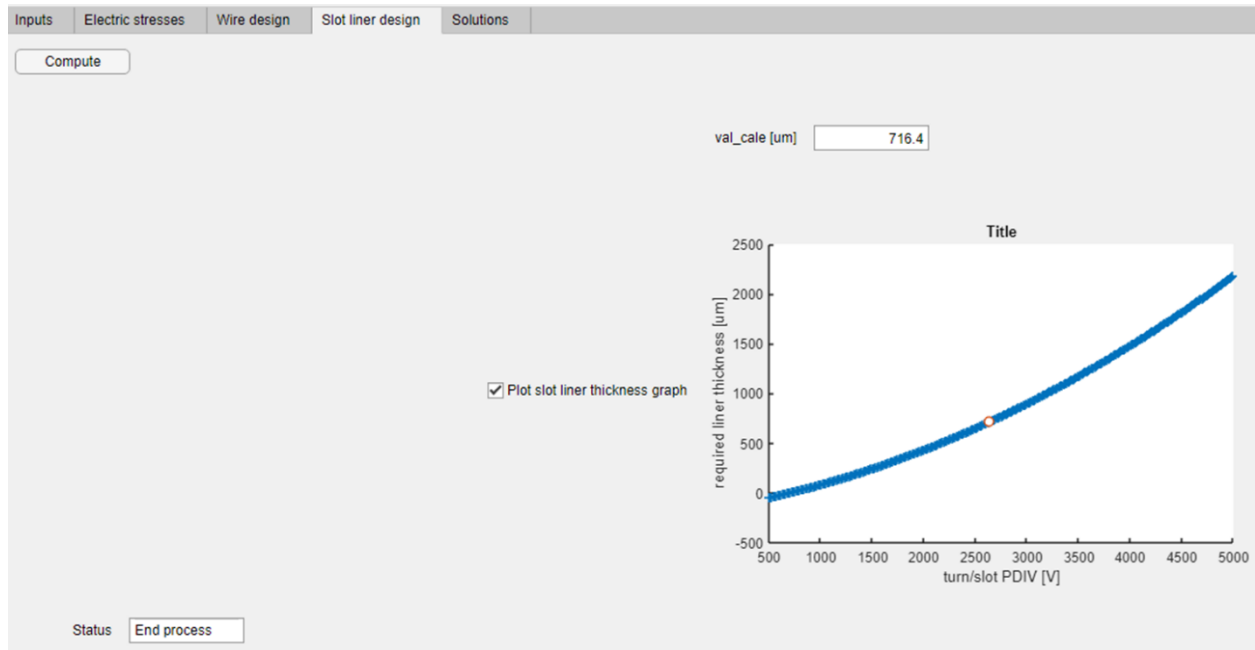


Figure 143: PDET - Slot liner design window

The final step consists in checking if the wire solutions are fitting in the slot considering a liner thickness of 716.4 μm . The fitting solutions are displayed on Figure 144:

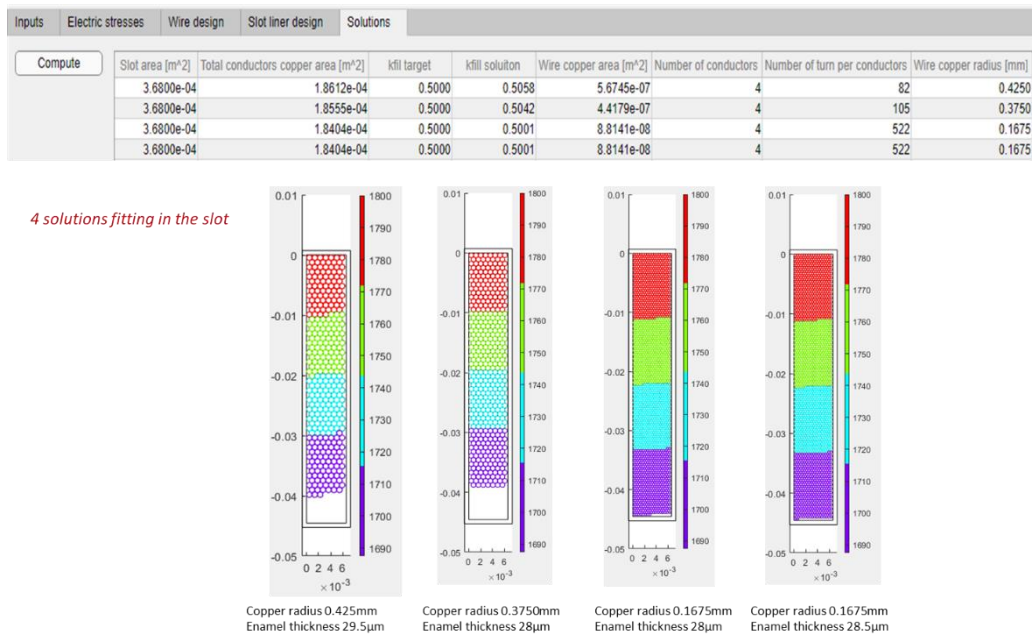


Figure 144: PDET - Solutions window

The color bar on the plots represent the nominal voltage [V] on each conductor. As four conductors are considered in this example, there are four colors. The outer rectangle is the slot. The inner rectangle is the free space in the slot once the liner is inserted. Each blank circle is the copper area of the wires. The colored contour is the enamel overcoat. Each conductor is subdivided depending the copper radius of the solution so that the filling factor is close to 0.5. From the five original solutions only four fit in the slot.

Table 35 recap the solutions:

	Copper radius [mm]	Enamel thickness [μm]	Grade	Number of wires per conductor
Wire	0.425	29.5	0.2 (i.e.: max grade 1)	82
	0.3750	28	0.4 (i.e.: min grade 2)	105
	0.1675	28	0.6 (i.e.: max grade 2)	522
	0.1675	28.5	0.8 (i.e.: min grade 3)	522
Liner		Liner thickness		
		716.4 μm		

Table 35: PDET solutions

In case no solution fits the slot, different actions are possible:

- Changing the material parameters alone (i.e.: the insulation materials) ;
- Changing inverter parameters alone;
- Changing motor parameters alone;
- Changing sizing point alone;
- A combination of the previous four possible actions.

Therefore, several actions to suppress PD have an impact on the whole powertrain sizing. The strong connection with the other WP has been clearly shown.

9 CONCLUSION

This chapter has presented the tool coded on *Matlab* which automatically size the insulation in a stator slot to avoid PD risk. First, the criterion to evaluate PDIV was presented. That criterion takes into account a combined variation of temperature and altitude for different field lines length. That criterion has been used to produce a graph to quantify the PDIV decrease (compared to 20 °C, 1 bar conditions) due to changing environmental conditions (sizing point).

Chapter 5: Tool to predict PD activity in machine slot

Then, Simple Analytical Models (SAMs) of the turn/turn and turn/slot contacts have been presented and validated by 2D-Finite Element Models (2D-FEMs). The SAMs have been used to compute graphs which give the minimal required insulation thickness to withstand electric stresses considering the chosen materials and taking into account a transient voltage overshoot. Besides, the electric stresses are overestimated in order to take into account the decrease in PDIV at the sizing point.

Finally, it came out that multiple actions are possible to avoid PD. Some of them may actually have a real impact on the whole powertrain sizing.

General conclusion and perspectives

This PhD work has consisted in studying the Electrical Insulation System (EIS) of rotating machines fed by inverters that will equip future hybrid propulsion aircrafts. It is a part of the European H2020 project HASTECS (**H**ybrid **A**ircraft **r**e**S**earch on **T**hermal and **E**lectrical **C**omponents and **S**ystems).

Partial Discharges (PD) phenomenon represents a great deal in the design of future rotating machines fed by inverter. On one hand, new faster components made out of SiC and GaN technologies will considerably improve the performances of the inverters. On the other hand, they will generate harder voltage fronts at the motor terminals which lead to higher transient voltage overshoots. PD will be more likely to appear and the insulation lifespan will be reduced due to both voltage overshoots and high switching frequency. That is the reason why it is absolutely necessary to take into account such a phenomenon when designing the motor to avoid any PD appearance, rather than searching for solutions in a motor already produced to remove them.

It was appeared relevant in this project to integrate both inverters and motors in the nacelles. That will reduces the voltage overshoots at motor terminals by using a power harness length shorter than 2 m. Nevertheless, in an aeronautical non-pressurized environment where equipment are submitted to great temperature and pressure variations, the Partial Discharge Inception Voltage (PDIV) will be considerably affected, as it is very sensitive to them.

It has appeared that the choices for the EIS will considerably impact the design of the cooling system. Polymer materials widely used in EIS have very low thermal conductivity. Therefore, an oversizing of the EIS results in much more thermal resistance in the path of the heat flux to be evacuated by the cooling system. New insulating materials having higher thermal conductivity are nowadays under study (not only for aircraft electric devices). These are composites made of a polymer matrix in which ceramic particles are inserted. Such particles are used in micro- or nano-sizes. The proportion of ceramic introduced in the polymer material is completely adjustable. It improves thermal properties but also have a negative impact on mechanical properties.

Experimental works about the relevant use of the well-known Paschen's criterion in motor EIS design have been carried on during this PhD work. PDIV measurements have been performed on samples of PEI/PAI overcoated round copper wires (polymers able to support the estimated motors working temperature). A correction of the secondary electron emission coefficient has been proposed for the configuration of two parallel enamelled round copper wires in close contact (representative of two neighbouring conductors in a machine slot). This corrected coefficient has been found to be almost

ten times lower compare to the value found in the literature obtained with metallic planar electrodes. That leads to higher PDIV levels in the case of enamelled round wires.

The Paschen's criterion requires the complete knowledge of electric field lines geometry. A numerical code has then been developed on Matlab to drawn electric field lines from a 2D-Finite Elements (2D-FEM) solution of an electrostatic problem. The originality of the proposed method is that only the scalar potential solution is required and the density of displayed lines is analogous to the field intensity. It has been compared to a ballistic approach already implanted on Matlab. It results that the Matlab function is much faster. Both methods give similar results for the considered 2D-electrostatic problem. The development of the proposed method provided better understanding on scalar potential formulation and the notions of electric flux tubes.

Simple Analytical Models (SAM) of the turn/turn and turn/slot configurations have been established. Results given by the SAM have been verified with the corresponding 2D-FEM. The SAM enabled parametric studies which has lead to design graphs. They indicate the minimal insulation thicknesses to ensure a PD-free slot in order to withstand the nominal electric stresses.

Finally, the design graphs have been implanted in tool specifically developed in this work: the Partial Discharge Evaluation Tool (PDET). It is a fully automatic tool which dimensions the EIS inside a stator slot to avoid PD appearance. This tool can be implanted in an optimization loop of the whole powertrain. For now, the tool perimeter is inside a stator slot with only one phase, but it may be upgraded to treat more than one phase per slot. The conductors are made of enamelled round wires in close contacts. The hot spots are the turn/turn and turn/slot electric stresses. The stresses were automatically evaluated from the inverter and motor parameters. The decrease in PDIV due to a combined variation of pressure and temperature was also considered.

PDET provides PD-free solutions for Type I-EIS motors. It is obviously transposable to Type II-EIS motors (high voltage motors). In case of Type II-EIS motors (able to support PD), the PDET will provide an EIS design that will limit the PD amplitude.

The work carried on during this PhD work offers multiple perspectives:

- The use of flat wire for windings. In such geometry, SAM are not valid anymore. Besides, the electric field is slightly non uniform. Design graphs will have to be derived from 2D-FEM and the degree of uniformity of the electric field will have to be carefully checked in order to apply the corrected Paschen's criterion.

General conclusion and perspectives

- The consideration of multiple phases per slot. An additional insulation layer will be required to insulate the different phases. The maximum electric stress will be now found between two different phases.
- The addition of cooling pipes embedded in the slot for a more efficient cooling inside the winding. The coolant may be composed of glycoled water, which is an electric insulating liquid. However, the pipes are usually conductors. That will add new zones where the electric stress has to be carefully investigated. Hollow wires may also be investigated.
- The end winding is the zone where electric stress may also be high. Indeed, in this area, the different phases overlap. Besides, there is triple points at the exit of the slot between the metallic carcass of the motor, the air, and the insulation. Tackle such configuration will need to develop a 3D-modelling.

Publications

P. Collin, D. Malec, Y. Lefevre, "Tool to Design the Primary Electrical Insulation System of Low Voltage Rotating Machines Fed by Inverters", In 2018 IEEE Electrical Insulation Conference (EIC) (pp. 8-13). IEEE

P. Collin, D. Malec, Y. Lefevre, "Outil d'aide au design du système d'isolation primaire de machines tournantes basse tension alimentées par onduleur", In SFE Grenoble 2018

"Design of Electric Machine Taking Into Account the Partial Discharges Phenomena for Future Hybrid Propelled Aircrafts", P.Collin, S.Touhami, D.Malec, Y.Lefevre, J.F.Llibre, More Electric Aircraft, February 6-7, 2019, Toulouse

"Concernant la pertinence de l'utilisation du critère de Paschen pour l'estimation de la tension d'apparition des décharges partielles (TADP) lors du design du système d'isolation électrique de moteurs alimentés par onduleur", P. Collin, D. Malec, Y. Lefevre, Jeunes Chercheurs en Génie Electrique, 11-14 juin, 2019, Oléron

"About the relevance of using Paschen's criterion for partial discharges inception voltage (PDIV) estimation when designing the electrical insulation system of inverter fed motors", P. Collin, D. Malec, Y. Lefevre, Electrical Insulation Conference, June 16-19, 2019, Calgary

"A general method to compute the electric flux lines in the slots of electric machines for the evaluation of partial discharges risk", P. Collin, D. Malec, Y. Lefevre, Compumag, July 15-19, 2019, Paris

"Tool to predict and avoid Partial Discharges in stator slot of rotating motors fed by inverter", P. Collin, D. Malec, Y. Lefevre, Aerospace Europe Conference, February 25-28, 2020, Bordeaux

Annex

Nominal conductor diameter [mm]	Minimum increase due to the insulation thickness [mm]			Maximal overall diameter [mm]		
	Grade 1	Grade 2	Grade 3	Grade 1	Grade 2	Grade3
0,180	0,013	0,025	0,036	0,204	0,217	0,229
0,190	0,014	0,027	0,039	0,216	0,228	0,240
0,200	0,014	0,027	0,039	0,226	0,239	0,252
0,212	0,015	0,029	0,043	0,240	0,254	0,268
0,224	0,015	0,029	0,043	0,252	0,266	0,280
0,236	0,017	0,032	0,048	0,267	0,283	0,298
0,250	0,017	0,032	0,048	0,281	0,297	0,312
0,265	0,018	0,033	0,050	0,297	0,314	0,330
0,280	0,018	0,033	0,050	0,312	0,329	0,345
0,300	0,019	0,035	0,053	0,334	0,352	0,360
0,315	0,019	0,035	0,053	0,349	0,367	0,384
0,335	0,020	0,038	0,06	0,372	0,391	0,408
0,355	0,020	0,038	0,057	0,392	0,411	0,428
0,375	0,021	0,040	0,060	0,414	0,434	0,453
0,400	0,021	0,040	0,060	0,439	0,459	0,478
0,425	0,022	0,042	0,064	0,466	0,488	0,508
0,450	0,022	0,042	0,064	0,491	0,513	0,533
0,475	0,024	0,045	0,067	0,519	0,541	0,562
0,500	0,024	0,045	0,068	0,544	0,566	0,587
0,530	0,025	0,047	0,071	0,576	0,600	0,623
0,560	0,025	0,047	0,071	0,606	0,630	0,653
0,600	0,027	0,050	0,075	0,649	0,674	0,698
0,630	0,027	0,050	0,075	0,679	0,704	0,728
0,670	0,028	0,053	0,080	0,722	0,749	0,774
0,710	0,028	0,053	0,080	0,762	0,789	0,814
0,750	0,030	0,056	0,085	0,805	0,834	0,861
0,800	0,030	0,056	0,085	0,855	0,884	0,911
0,850	0,032	0,060	0,090	0,909	0,938	0,968
0,900	0,032	0,060	0,090	0,959	0,989	1,081
0,950	0,034	0,063	0,095	1	1	1,074
1,000	0,034	0,063	0,095	1,062	1,094	1,124
1,060	0,034	0,065	0,098	1,124	1,157	1,188
1,120	0,034	0,065	0,098	1,184	1,217	1,248
1,180	0,035	0,067	0,100	1,246	1,279	1,311
1,250	0,035	0,067	0,100	1,316	1,349	1,381
1,320	0,036	0,069	0,103	1,388	1,422	1,455
1,400	0,036	0,069	0,103	1,468	1,502	1,535
1,500	0,038	0,071	0,107	1,570	1,606	1,640
1,600	0,038	0,071	0,107	1,670	1,706	1,740
1,700	0,039	0,073	0,110	1,772	1,809	1,844
1,800	0,039	0,073	0,110	1,872	1,909	1,944
1,900	0,040	0,075	0,113	1,974	2,012	2,048
2,000	0,040	0,075	0,113	2,074	2,112	2,148
2,120	0,041	0,077	0,116	2,196	2,235	2,272
2,240	0,041	0,077	0,116	2,316	2,355	2,392
2,360	0,042	0,079	0,119	2,438	2,478	2,516
2,500	0,042	0,079	0,119	2,578	2,618	2,656
2,650	0,04	0,081	0,123	2,730	2,772	2,811

Annex

2,800	0,043	0,081	0,123	2,880	2,922	2,961
3,000	0,045	0,084	0,127	3,083	3,126	3,166
3,150	0,045	0,084	0,127	3,233	3,276	3,316
3,350	0,046	0,086	0,130	3,435	3,479	3,521
3,550	0,046	0,086	0,130	3,635	3,679	3,721
3,750	0,047	0,089	0,134	3,838	3,883	3,926
4,000	0,047	0,089	0,134	4,088	4,133	4,176
4,250	0,049	0,092	0,138	4,341	4,387	4,431
4,500	0,049	0,092	0,138	4,591	4,637	4,681
4,750	0,050	0,094	0,142	4,843	4,891	4,936
5,000	0,050	0,094	0,142	5,093	5,141	5,186

Annex 1: Enamel thickness tolerances picked from [37]

References:

- [1] 'Agenda 21 (Rio Declaration on Environment and Development)', 1992, p. 79.
- [2] 'IEA World energy outlook 2018'. International Energy Agency, Jul. 2018.
- [3] 'ITF Transport outlook 2017'. International Transport Forum , OECD iLibrary, 2017.
- [4] 'OPEC World Oil Outlook 2040'. Organization of the Petroleum Exporting Countries, Sep. 2018.
- [5] 'WHO Health and sustainable development - Transport and health risks'. World Health Organization, 2019.
- [6] 'The cost of air pollution – Health impacts of road transport'. ISBN 978-92-64-210448, OECD iLibrary, 2014.
- [7] J. P. RODRIGUE, C. COMTOIS, and B. SLACK, *The geography of transports systems*, 4th edition. New York Routledge Edition, 2017.
- [8] 'World Energy Model'. International Energy Agency, Version 2018.
- [9] 'Les énergies renouvelables en France : les chiffres clés 2018'. Ministère de la Transition écologique et solidaire, May 24, 2018.
- [10] 'Quelle est la source d'énergie la plus utilisée dans le monde ?' ENGIE, Mar. 29, 2019.
- [11] 'Historique évolution du cours du baril (159 litres) de pétrole WTI'. france-inflation.com, 2020.
- [12] 'Road transport: Reducing CO2 emissions from vehicles'. European Commission, 2019.
- [13] 'Aviation carbon offset programmes'. IATA, 2008.
- [14] E. Féraud, 'En Suède, la "honte de prendre l'avion" pousse les voyageurs à favoriser le train'. Géo, Apr. 16, 2019.
- [15] L. Faleiro, J. Herzog, B. Schievelbusch, and T. Seung, 'INTEGRATED EQUIPMENT SYSTEMS FOR A MORE ELECTRIC AIRCRAFT – HYDRAULICS AND PNEUMATICS', *Hydraul. Pneum.*, p. 10.
- [16] M. Palomeque, 'A320 - Dual hydraulic loss'. Safety first #4, Jun. 2017.
- [17] J. Robinson, 'Collins Aerospace building \$67M electric aircraft lab', *Wings Mag.*, Apr. 2019.
- [18] B. Sarlioglu and C. T. Morris, 'More Electric Aircraft: Review, Challenges, and Opportunities for Commercial Transport Aircraft', *IEEE Trans. Transp. Electrification*, vol. 1, no. 1, pp. 54–64, Jun. 2015, doi: 10.1109/TTE.2015.2426499.
- [19] R. Hemmati, F. Wu, and A. El-Refaie, 'Survey of Insulation Systems in Electrical Machines', in *2019 IEEE International Electric Machines & Drives Conference (IEMDC)*, San Diego, CA, USA, May 2019, pp. 2069–2076, doi: 10.1109/IEMDC.2019.8785099.
- [20] 'Electric flight - Bringing zero-emission technology to aviation'. Airbus.
- [21] 'The future is electric'. Airbus, Jul. 17, 2018.
- [22] 'CityAirbus'. Airbus.
- [23] 'HASTECS'. <http://www.laplace.univ-tlse.fr/HASTECS> (accessed Jan. 09, 2020).
- [24] J. Thauvin, 'Exploring the design space for a hybrid-electric regional aircraft with multidisciplinary design optimisation methods', Institut National Polytechnique de Toulouse, 2018.
- [25] 'Hybrid Aircraft Academic reSearch on Thermal & Electrical Components and Systems (HASTECS), Project selected from CFP in Cleansky II (H2020) framework' . .
- [26] M. Pettes-Duler, X. Roboam, and B. Sareni, 'Integrated design process and sensitivity analysis of a hybrid electric propulsion system for future aircraft', Salerno, Italy, May 2019.
- [27] Y. Lefevre, S. El-Aabid, J.-F. Llibre, C. Henaux, and S. Touhami, 'Performance assessment tool based on loadability concepts', *Int. J. Appl. Electromagn. Mech.*, vol. 59, no. 2, pp. 687–694, Mar. 2019, doi: 10.3233/JAE-171059.
- [28] P. Collin, S. Touhami, D. Malec, Y. Lefevre, and J. F. Llibre, 'Design of Electric Machine Taking Into Account the Partial Discharges Phenomena for Future Hybrid Propelled Aircrafts', 2019.

References:

- [29] N. Erroui, G. Gateau, and N. Roux, 'Continuous-caliber semiconductor components', in *2018 IEEE International Conference on Industrial Technology (ICIT)*, Lyon, Feb. 2018, pp. 658–663, doi: 10.1109/ICIT.2018.8352256.
- [30] A. Zeaiter and M. Fenot, 'Thermal Sensitivity Analysis of a High Power Density Electric Motor for Aeronautical Application', in *2018 IEEE International Conference on Electrical Systems for Aircraft, Railway, Ship Propulsion and Road Vehicles & International Transportation Electrification Conference (ESARS-ITEC)*, Nottingham, Nov. 2018, pp. 1–6, doi: 10.1109/ESARS-ITEC.2018.8607393.
- [31] R. Wrobel, S. J. Williamson, J. D. Booker, and P. H. Mellor, 'Characterizing the in situ Thermal Behavior of Selected Electrical Machine Insulation and Impregnation Materials', *IEEE Trans. Ind. Appl.*, vol. 52, no. 6, pp. 4678–4687, Nov. 2016, doi: 10.1109/TIA.2016.2589219.
- [32] S. Touhami, Y. Bertin, Y. Lefèvre, J.-F. Llibre, C. Henaux, and M. Fenot, 'Lumped Parameter Thermal Model of Permanent Magnet Synchronous Machines', p. 7.
- [33] F. Accorinti *et al.*, 'High-efficiency cooling system for highly integrated power electronics for hybrid propulsion aircraft', in *2019 IEEE 28th International Symposium on Industrial Electronics (ISIE)*, Vancouver, BC, Canada, Jun. 2019, pp. 870–877, doi: 10.1109/ISIE.2019.8781086.
- [34] M. E. Banda, D. Malec, and J.-P. Cambonne, 'Simulation of Space Charge Impact on Partial Discharge Inception Voltage in Power Busbars Dedicated to Future Hybrid Aircrafts', *Circuits Syst.*, vol. 09, no. 11, pp. 196–212, 2018, doi: 10.4236/cs.2018.911018.
- [35] 'EIC 60034-18-41, "Partial discharge free electrical insulation systems (Type I) used in rotating electrical machines fed from voltage converters – Qualification and quality control tests," 2014.'
- [36] 'Enamelled copper wire, SONA' . .
- [37] 'enamllled_copper_wire.pdf'.
http://www.universalmetals.com.pk/pdf/enamllled_copper_wire.pdf (accessed Jan. 15, 2020).
- [38] A. Anton, 'Émaux isolants et fils émaillés', *Tech. Ing.*, vol. D2330, p. 19, 2009.
- [39] J. Pyrhonen, T. Jokinen, and V. Hrabovcová, *Design of rotating electrical machines*. Chichester, West Sussex, United Kingdom ; Hoboken, NJ: Wiley, 2008.
- [40] 'Magnet Wire – Selection and Use Directions for Magnet Wire',
https://www.ecmenzies.com.au/images/productpdf/COROCUdatasheet_1.pdf .
- [41] Y. Agari, A. Ueda, and S. Nagai, 'Thermal conductivity of a polymer composite', *J. Appl. Polym. Sci.*, vol. 49, no. 9, pp. 1625–1634, Sep. 1993, doi: 10.1002/app.1993.070490914.
- [42] R. Arora and W. Mosch, 'High Voltage and Electrical Insulation Engineering'. A John Wiley & Sons, Inc., Publication, 2011.
- [43] M. Chapman, N. Frost, and R. Bruetsch, 'Insulation Systems for Rotating Low-Voltage Machines', in *Conference Record of the 2008 IEEE International Symposium on Electrical Insulation*, Vancouver, BC, Jun. 2008, pp. 257–260, doi: 10.1109/ELINSL.2008.4570323.
- [44] J. Moeneclaey, 'Méthode de conception des bobinages des actionneurs électriques adaptés aux nouvelles contraintes de l'avionique', University of Artois, Béthune, 2015.
- [45] 'Resins and Varnishes 2013 - VON ROLL - PDF Catalogs | Technical Documentation | Brochure'.
<https://pdf.directindustry.com/pdf/von-roll/resins-varnishes-2013/12485-556569.html> (accessed Jan. 21, 2020).
- [46] 'Design and Testing of Insulation for Adjustable Speed Drives - PDFHALL.COM'.
https://pdfhall.com/design-and-testing-of-insulation-for-adjustable-speed-drives_5b69f350097c4775388b45ee.html (accessed Jan. 22, 2020).
- [47] G. C. Stone, Ed., *Electrical insulation for rotating machines: design, evaluation, aging, testing, and repair*. Piscataway, NJ : Hoboken, NJ: IEEE ; Wiley-Interscience, 2004.
- [48] S. Nategh, A. Krings, O. Wallmark, and M. Leksell, 'Evaluation of Impregnation Materials for Thermal Management of Liquid-Cooled Electric Machines', *IEEE Trans. Ind. Electron.*, vol. 61, no. 11, pp. 5956–5965, Nov. 2014, doi: 10.1109/TIE.2014.2308151.

References:

- [49] W. Sixel, M. Liu, G. Nellis, and B. Sarlioglu, 'Cooling of Windings in Electric Machines via 3D Printed Heat Exchanger', in *2018 IEEE Energy Conversion Congress and Exposition (ECCE)*, Portland, OR, Sep. 2018, pp. 229–235, doi: 10.1109/ECCE.2018.8557845.
- [50] Y. Ohki, 'Development of epoxy resin composites with high thermal conductivity', *IEEE Electr. Insul. Mag.*, vol. 26, no. 1, pp. 48–49, Jan. 2010, doi: 10.1109/MEI.2010.5383936.
- [51] P. Rodgers, V. Eveloy, and L. El Sayed, 'Candidate thermally enhanced polymer composite materials for cooling of electronic systems', in *20th International Workshop on Thermal Investigations of ICs and Systems*, Greenwich, London, United Kingdom, Sep. 2014, pp. 1–6, doi: 10.1109/THERMINIC.2014.6972495.
- [52] S. Diahm, 'Modulation of the dielectric breakdown strength in polyimide nanocomposites by deep traps tailoring in interphase regions', *IEEE Trans. Dielectr. Electr. Insul.*, vol. 26, no. 1, pp. 247–252, Feb. 2019, doi: 10.1109/TDEI.2018.007540.
- [53] C. Abadie, T. Lebey, and T. Billard, 'On-line non-intrusive partial discharges detection in aeronautical systems', Université Toulouse 3 Paul Sabatier, 2017.
- [54] H. Foch, F. Forest, and T. Meynard, 'Onduleurs de tension - Structures. Principes. Applications', p. 21, 1998.
- [55] L. Benmamas, 'Méthodes d'évaluation du risque de décharges partielles dans le bobinage de machines électriques destinées à la traction automobile', University of Paris-Saclay, Gif-sur-Yvette, 2017.
- [56] M. Kaufhold, H. Aninger, M. Berth, J. Speck, and M. Eberhardt, 'Electrical stress and failure mechanism of the winding insulation in PWM-inverter-fed low-voltage induction motors', *IEEE Trans. Ind. Electron.*, vol. 47, no. 2, pp. 396–402, Apr. 2000, doi: 10.1109/41.836355.
- [57] B. Taghia, B. Cougo, H. Piquet, D. Malec, A. Belinger, and J.-P. Carayon, 'Advanced analysis of transient overvoltage in electromechanical chain fed by SiC inverter', *Electrimacs 2017*, p. 8, 2017.
- [58] A. Ong, J. Carr, J. Balda, and A. Mantooth, 'A Comparison of Silicon and Silicon Carbide MOSFET Switching Characteristics', in *2007 IEEE Region 5 Technical Conference*, Fayetteville, AR, USA, Apr. 2007, pp. 273–277, doi: 10.1109/TPSD.2007.4380318.
- [59] L. Dupont, S. Lefebvre, and Z. Khatir, 'Characterisation of Silicon Carbide Schottky diodes and COOLMOSTM transistors at high temperature', *35th Annu. IEEE Power Electron. Spec. Conf.*, p. 6, 2004.
- [60] V. Mihaila, 'Nouvelle Conception des bobinages statoriques des machines à courant alternatif pour réduire les effets négatifs des dV/dt .', Artois, 2011.
- [61] B. Taghia, B. Cougo, H. Piquet, D. Malec, A. Belinger, and J.-P. Carayon, 'Overvoltage at motor terminals in SiC-based PWM drives', *Math. Comput. Simul.*, vol. 158, pp. 264–280, Apr. 2019, doi: 10.1016/j.matcom.2018.09.009.
- [62] P. Bidan, T. Lebey, and C. Neacsu, 'Development of a new off-line test procedure for low voltage rotating machines fed by adjustable speed drives (ASD)', *IEEE Trans. Dielectr. Electr. Insul.*, vol. 10, no. 1, pp. 168–175, Feb. 2003, doi: 10.1109/TDEI.2003.1176584.
- [63] R. Bartnikas and E. McMahon, 'Engineering dielectrics - Volume 1 - Corona measurements and interpretation', *Am. Soc. Test. Mater.*, no. STP669, 1979.
- [64] F. H. Keuger, 'Partial discharge detection in high voltage equipment', *Butterworth-Heinemann*, pp. 78–85, 1990.
- [65] R. Bruetsch, M. Tari, K. Froehlich, T. Weiers, and R. Vogelsang, 'Insulation Failure Mechanisms of Power Generators', p. 7.
- [66] 'Lichtenberg figure', *Wikipedia*. Jan. 25, 2020, Accessed: Feb. 12, 2020. [Online]. Available: https://en.wikipedia.org/w/index.php?title=Lichtenberg_figure&oldid=937573574.
- [67] C. Mayoux, 'Aging of polymeric insulating materials in power cables', *IEEE Trans. Dielectr. Electr. Insul.*, vol. 4, no. 6, pp. 665–673, Dec. 1997, doi: 10.1109/94.654573.
- [68] G. Nayak, Y. Du, R. Brandenburg, and P. J. Bruggeman, 'Effect of air flow on the micro-discharge dynamics in an array of integrated coaxial microhollow dielectric barrier discharges', *Plasma Sources Sci. Technol.*, vol. 26, no. 3, p. 035001, Feb. 2017, doi: 10.1088/1361-6595/aa56a4.

References:

- [69] M. Q. Nguyen, 'Étude de l'impact des contraintes aéronautiques sur les systèmes d'isolation des moteurs de conditionnement d'air', University of Toulouse, Toulouse, 2012.
- [70] G. Stone, 'Partial Discharges in Electrical Insulation' . .
- [71] J. Kurimský, I. Kolcunová, and R. Cimbala, 'Understanding surface partial discharges in HV coils and the role of semi-conductive protection', *Electr. Eng.*, vol. 92, no. 7–8, pp. 283–289, Dec. 2010, doi: 10.1007/s00202-010-0184-0.
- [72] 'Corona discharge', *Wikipedia*. Feb. 03, 2020, Accessed: Feb. 13, 2020. [Online]. Available: https://en.wikipedia.org/w/index.php?title=Corona_discharge&oldid=938928794.
- [73] 'Ozonation of Polymers'. <https://polymerdatabase.com/polymer%20chemistry/Ozone.html> (accessed Feb. 13, 2020).
- [74] 'Failures in Three-Phase Stator Windings'. <https://easa.com/resources/failures-in-three-phase-stator-windings> (accessed Feb. 13, 2020).
- [75] C. Julie, 'Étude des mécanismes anti-cancéreux induits par milieux activés par jet de plasma froid : vers une nouvelle approche thérapeutique.', Toulouse 3 Paul Sabatier, 2018.
- [76] E. SILL, 'Étude et caractérisation des décharges partielles et du vieillissement du polyimide en environnement aéronautique', Toulouse 3 Paul Sabatier, 2012.
- [77] C. Van De Steen, 'Modélisation des propriétés de transport des ions moléculaires de krypton et xénon pour l'optimisation des générateurs de plasma froids utilisant les gaz rares', Université Toulouse 3 Paul Sabatier, Toulouse, 2018.
- [78] I. Popescu and E. Badareu, *Gaz Ionisés, Décharges Electriques dans les Gaz*, Dunod. Paris, 1968.
- [79] E. R. B. Adamson and A. Dissertation, 'SECONDARY ELECTRON EMISSION COEFFICIENT FROM LEXAN: THE LOW ENERGY CROSSOVER', p. 78.
- [80] O. Eichwald, M. Yousfi, and O. Ducasse, 'Breakdown criteria in air: an overview supported by predictive simulations', p. 6.
- [81] F. Paschen, 'Ueber die zum Funkenübergang in Luft, Wasserstoff und Kohlensäure bei verschiedenen Drucken erforderliche Potentialdifferenz', *Ann. Phys.*, vol. 273, no. 5, pp. 69–96, 1889, doi: 10.1002/andp.18892730505.
- [82] T. W. Dakin, G. Luxa, G. Oppermann, J. Vigreux, G. Wind, and H. Winkelkemper, 'Breakdown of Gases in Uniform Fields Paschen Curves for Nitrogen, Air and Sulfur Hexafluoride', *Electra*, 1974.
- [83] H. H. Wittenberg, 'Gas Tube Design', *Electron Tube Des. RCA Electron Tube Div.*, pp. 792–817, 1962.
- [84] F. Koliatene, 'CONTRIBUTION A L'ETUDE DE L'EXISTENCE DES DECHARGES DANS LES SYSTEMES DE L'AVIONIQUE', Toulouse 3 Paul Sabatier, 2009.
- [85] 'RTCA DO-160, Environmental Conditions and test Procedures for Airborne Equipment' . .
- [86] F. W. Peek, *Dielectric Phenomena in High Voltage Engineering*, McGraw Hill. 1929.
- [87] W. G. Dunbar and J. W. Seabrook, 'High Voltage Design Guide for Airborne Equipment', *Boeing Aerosp. Co.*, p. 217, 1976.
- [88] V. L. Bychkov, S. A. Volkov, and I. V. Kochetov, 'Ionization process in the humid air of the lower troposphere', *Russ. J. Phys. Chem. B*, vol. 5, no. 6, pp. 940–945, Dec. 2011, doi: 10.1134/S1990793111060054.
- [89] P. Mikropoulos, C. Stassinopoulos, and B. Sarigiannidou, 'Positive Streamer Propagation and Breakdown in Air: the Influence of Humidity', *IEEE Trans. Dielectr. Electr. Insul.*, vol. 15, no. 2, pp. 416–425, Apr. 2008, doi: 10.1109/TDEI.2008.4483460.
- [90] G. Robles, J. Fresno, J. Martínez-Tarifa, J. Ardila-Rey, and E. Parrado-Hernández, 'Partial Discharge Spectral Characterization in HF, VHF and UHF Bands Using Particle Swarm Optimization', *Sensors*, vol. 18, no. 3, p. 746, Mar. 2018, doi: 10.3390/s18030746.
- [91] B. Cella, 'On-line partial discharges detection in conversion systems used in aeronautics', University of Toulouse, 2015.
- [92] T. Balachandran, S. Sirimmana, A. Jin, and K. S. Haran, 'Partial Discharge Testing of Form-Wound Air-Core Armature Windings for a High-Frequency PMSM for Electric Aircraft Applications', in *2018 IEEE International Conference on Information and Automation for*

References:

- Sustainability (ICIAfS)*, Colombo, Sri Lanka, Dec. 2018, pp. 1–6, doi: 10.1109/ICIAfS.2018.8913342.
- [93] J. M. Wetzler and P. C. T. van der Laan, 'Prebreakdown currents: Basic interpretation and time-resolved measurements', *IEEE Trans. Electr. Insul.*, vol. 24, no. 2, pp. 297–308, Apr. 1989, doi: 10.1109/14.90288.
- [94] R. Ross, 'Graphical methods for plotting and evaluating Weibull distributed data', in *Proceedings of 1994 4th International Conference on Properties and Applications of Dielectric Materials (ICPADM)*, Brisbane, Qld., Australia, 1994, vol. 1, pp. 250–253, doi: 10.1109/ICPADM.1994.413986.
- [95] J. S. White, 'The Moments of Log-Weibull Order Statistics', *Technometrics*, pp. 373–386, 1969.
- [96] J. C. Fothergill, 'Ageing, Space Charge and Nanodielectrics: Ten Things We Don't Know About Dielectrics', in *2007 IEEE International Conference on Solid Dielectrics*, Winchester, UK, Jul. 2007, pp. 1–10, doi: 10.1109/ICSD.2007.4290739.
- [97] R. Rui and I. Cotton, 'Impact of low pressure aerospace environment on machine winding insulation', in *2010 IEEE International Symposium on Electrical Insulation*, San Diego, CA, USA, Jun. 2010, pp. 1–5, doi: 10.1109/ELINSL.2010.5549718.
- [98] S. Palit, D. Varghese, H. Guo, S. Krishnan, and M. A. Alam, 'The Role of Dielectric Heating and Effects of Ambient Humidity in the Electrical Breakdown of Polymer Dielectrics', *IEEE Trans. Device Mater. Reliab.*, vol. 15, no. 3, pp. 308–318, Sep. 2015, doi: 10.1109/TDMR.2015.2431998.
- [99] E. McMahon and J. Perkins, 'Surface and Volume Phenomena in Dielectric Breakdown of Polyethylene', *IEEE Trans. Power Appar. Syst.*, vol. 82, no. 69, pp. 1128–1136, Dec. 1963, doi: 10.1109/TPAS.1963.291505.
- [100] J. V. Champion, S. J. Dodd, A. S. Vaughan, and S. J. Sutton, 'THE EFFECT OF VOLTAGE, TEMPERATURE AND MORPHOLOGY ON ELECTRICAL TREEING IN POLYETHYLENE BLENDS', *IEEE Dielectr. Mater. Meas. Appl. Conf. Publ.*, no. 473, p. 6, 2000.
- [101] M. Szczepanski, 'Development of methods allowing the test and the comparison of low-voltage motors insulation systems running under partial discharges (fed by inverter)', p. 214.
- [102] R. Acheen, C. Abadie, T. Lebey, T. Billard, and S. Duschesne, 'Comparison of the Electrical Ageing Under Sinusoidal and Square-Wave Stresses', San Antonio, TX, 2018, pp. 353–356.
- [103] 'IEEE Guide for the Statistical Analysis of Electrical Insulation Voltage Endurance Data'. ANSI/IEEE Std 930, 1987.
- [104] N. Lahoud, J. Faucher, D. Malec, and P. Maussion, 'Electrical Aging of the Insulation of Low-Voltage Machines: Model Definition and Test With the Design of Experiments', *IEEE Trans. Ind. Electron.*, vol. 60, no. 9, pp. 4147–4155, Sep. 2013, doi: 10.1109/TIE.2013.2245615.
- [105] 'Qualification and type tests for Type I electrical insulation systems used in rotating electrical machines when fed from voltage converters'. IEC 60034-18-CD International Standard, 2012.
- [106] 'Qualification and acceptance tests for partial discharge resistant electrical insulation systems (Type II) used in rotating electrical machines when fed from voltage converters'. IEC 60034-18-42 TS, International Standards, 2008.
- [107] P. Maussion, A. Picot, M. Chabert, and D. Malec, 'Lifespan and aging modeling methods for insulation systems in electrical machines: A survey', in *2015 IEEE Workshop on Electrical Machines Design, Control and Diagnosis (WEMDCD)*, Torino, Italy, Mar. 2015, pp. 279–288, doi: 10.1109/WEMDCD.2015.7194541.
- [108] K. Petcharakas, 'A contribution to the streamer breakdown criterion', in *11th International Symposium on High-Voltage Engineering (ISH 99)*, London, UK, 1999, vol. 1999, pp. v3-19-v3-19, doi: 10.1049/cp:19990689.
- [109] A. Pedersen, T. Christen, A. Blaszczyk, and H. Boehme, 'Streamer inception and propagation models for designing air insulated power devices', in *2009 IEEE Conference on Electrical Insulation and Dielectric Phenomena*, Virginia Beach, VA, USA, Aug. 2009, pp. 604–607, doi: 10.1109/CEIDP.2009.5377740.

References:

- [110] G. Eriksson, 'Easy Evaluation of Streamer Discharge Criteria', *Proc. 2012 COMSOL Conf. Milan*, p. 7, 2012.
- [111] E. J. Horowitz, 'A general field-line plotting algorithm', *Comput. Phys.*, vol. 4, no. 4, p. 418, 1990, doi: 10.1063/1.168384.
- [112] Z. Ren, '2-D dual finite-element formulations for the fast extraction of circuit parameters in VLSI', *IEEE Trans. Magn.*, vol. 39, no. 3, pp. 1590–1593, May 2003, doi: 10.1109/TMAG.2003.810548.
- [113] G. Parent, S. Duchesne, and P. Dular, 'Determination of Flux Tube Portions by Adjunction of Electric or Magnetic Multivalued Equipotential Lines', *IEEE Trans. Magn.*, vol. 53, no. 6, pp. 1–4, Jun. 2017, doi: 10.1109/TMAG.2017.2661401.
- [114] G. Parent, M. Rossi, S. Duchesne, and P. Dular, 'Determination of Partial Discharge Inception Voltage and Location of Partial Discharges by Means of Paschen's Theory and FEM', *IEEE Trans. Magn.*, vol. 55, no. 6, pp. 1–4, Jun. 2019, doi: 10.1109/TMAG.2019.2902374.
- [115] T. M. Whittaker, *Mon Weather.*, 1977.
- [116] G. Dhatt and G. Touzot, *Une présentation de la méthode des éléments finis*, Les Presses de l'Université Laval. Québec, et Maloine, Paris, 1981.
- [117] F. Pauli, N. Driendl, L. Yang, and K. Hameyer, 'Corona resistant enameled wires as a solution for electrical motor winding systems supplied by high du/dt inverter voltage: An insulation life-time estimation', *IEEE Submitt.*, p. 7, 2019.
- [118] N. Hayakawa and H. Okubo, 'Partial discharge characteristics of inverter-fed motor coil samples under ac and surge voltage conditions', *IEEE Electr. Insul. Mag.*, vol. 21, no. 1, pp. 5–10, Jan. 2005, doi: 10.1109/MEI.2005.1389265.
- [119] 'IEC 60270 (2000-12), High-voltage test techniques — Partial discharge measurements'.
- [120] W. Weibull, 'A Statistical Distribution Function of Wide Applicability', *J. Appl. Mech.*, no. 18, pp. 293–297, 1951.
- [121] P. Collin, D. Malec, and Y. Lefevre, 'Tool to Design the Primary Electrical Insulation System of Low Voltage Rotating Machines Fed by Inverters', *2018 IEEE Electr. Insul. Conf. EIC*, pp. 8–13, 2018, doi: 10.1109/EIC.2018.8481037.
- [122] M. Szczepanski, D. Malec, P. Maussion, B. Petitgas, and P. Manfe, 'Prediction of the lifespan of enameled wires used in low voltage inverter-fed motors by using the Design of Experiments (DoE)', in *2017 IEEE Industry Applications Society Annual Meeting*, Cincinnati, OH, Oct. 2017, pp. 1–6, doi: 10.1109/IAS.2017.8101798.
- [123] H. Xu, Y. Zhang, and F. Zheng, 'Study on measuring method of dielectric spectroscopy for polymer dielectrics', in *2009 IEEE 9th International Conference on the Properties and Applications of Dielectric Materials*, Harbin, China, Jul. 2009, pp. 922–925, doi: 10.1109/ICPADM.2009.5252247.
- [124] F. Aymonino, 'Contribution à l'étude du comportement des systèmes d'isolation des machines tournantes à courant alternatif fonctionnant sous très hautes températures (200-400°C)', University of Toulouse Paul Sabatier, Toulouse, 2008.
- [125] M. G. D. L. Calle, J. M. Martínez-Tarifa, Á. M. G. Solanilla, and G. Robles, 'Uncertainty Sources in the Estimation of the Partial Discharge Inception Voltage in Turn-to-Turn Insulation Systems', *IEEE Access*, vol. 8, pp. 157510–157519, 2020, doi: 10.1109/ACCESS.2020.3018870.
- [126] H. Ismail, 'Étude du taux de pulvérisation et du coefficient d'émission électronique secondaire de cibles métalliques polycristallines bombardées par des ions Hg⁺, dans un domaine d'énergie allant de 5 à 30 keV', *Rev. Phys. Appliquée*, vol. 5, no. 5, pp. 759–764, 1970, doi: 10.1051/rphysap:0197000505075900.
- [127] M. Florkowski, B. Florkowska, and P. Zydron, 'Partial Discharges in Insulating Systems of Low Voltage Electric Motors Fed by Power Electronics—Twisted-Pair Samples Evaluation', *Energies*, vol. 12, no. 5, p. 768, Feb. 2019, doi: 10.3390/en12050768.
- [128] N. Naudé, A. Belinger, S. Dap, and N. Gherardi, 'Memory effects in Atmospheric Pressure Townsend Discharges in N₂ and air', p. 4, 2015.

References:

- [129] D. Marić, N. Škoro, P. D. Maguire, C. M. O. Mahony, G. Malović, and Z. L. Petrović, 'On the possibility of long path breakdown affecting the Paschen curves for microdischarges', *Plasma Sources Sci. Technol.*, vol. 21, no. 3, p. 035016, Jun. 2012, doi: 10.1088/0963-0252/21/3/035016.
- [130] P. G. Slade and E. D. Taylor, 'Electrical breakdown in atmospheric air between closely spaced (0.2 μm -40 μm) electrical contacts', *IEEE Trans. Compon. Packag. Technol.*, vol. 25, no. 3, pp. 390–396, Sep. 2002, doi: 10.1109/TCAPT.2002.804615.
- [131] A. Peschot, N. Bonifaci, O. Lesaint, C. Valadares, and C. Poulain, 'Deviations from the Paschen's law at short gap distances from 100 nm to 10 μm in air and nitrogen', *Appl. Phys. Lett.*, vol. 105, no. 12, p. 123109, Sep. 2014, doi: 10.1063/1.4895630.
- [132] P. Carazzetti and H. R. Shea, 'Electrical breakdown at low pressure for planar microelectromechanical systems with 10- to 500- μm gaps', vol. 8, p. 9.